Diss. ETH Nr. 9439

TURBULENCE WITHIN AND ABOVE AN URBAN CANOPY

vorgelegt von

MATHIAS WALTER JAKOB ROTACH

Dipl. Natw. ETH Zürich

geboren am 31. März 1960

von Herisau AR

1

Acknowledgements

First of all, I would like to express my gratitude to my "Doctorfather" Prof. Atsumu Ohmura. He gave me all possible freedom to find my own way into the wide field of turbulence. And he had always an open door when problems were to be discussed or decisions to be made. I am especially grateful that he always "found" some money to make it possible that I could attend a workshop or a conference. And last but not least, he made it possible that I could join the ETH Greenland Expedition in summer 1990: many pages of this thesis were originally written under the midnight sun or, later in the year, in candle light (when electricity was short).

The two "Co-Referees", Profs. H.C. Davies and T.R. Oke gave me many constructive comments and instrumental suggestions for the final draft of this thesis. Their help and encouragement is greatly appreciated.

And then, there is this other man, Karl Schroff. Without him, almost nothing would have been possible concerning the measurements. His hands and understanding solved countless problems and made my extra wishes to become reality. It was a great pleasure to be his technical assistant - not only because I could learn a lot.

Many thanks are also due to Drs. Heinz Blatter and H.P. Schmid, the former and present "boss" of the urban climate group. Heinz with his "critical skepticism" and HP with his "refreshing enthusiasm" were always the right address for feed-back and suggestions, for discussions and plans. And HP, the "Canadian" saved me from being the "lonely turbulence guy" in the department. Be it in the office or in a bar, at my place or at his, I always enjoyed these stimulating discussions (not only on turbulence...), the jokes and the laughs. And finally, he did a great job in making this thesis readable and understandable, in finding hidden or obvious mistakes and in encouraging me in its last weeks and days.

Many other people were important for the realization of this thesis: Pierluigi Calanca, who joined my curiosity for the performance of the sonic anemometers (and made significant contributions to the respective chapter of this thesis); Roberto Mazzoni, with whom I shared the office, hard- and software and many pleasant days; Carolyn Schmid-Porter, who found an incredible amount of language mistakes and misprints in the manuscript; Hansjürg Frei, who constructed the measurement tower and had to erect it twice (...); Peter Schuhmacher with whom I shared the ups and downs of being a young innocent scientist when the urban climate project started; Gaby Schädler and Thomas Leutenegger, the diploma students who brought fresh wind into the department structures and Urs Sutter, with whom I "shared" work in a very comfortable way: he typed large parts of the manuscript. To all these people and to

(Sonja): ...Forests make a harsh climate milder. In countries with a mild climate people spend less energy in the struggle with nature, and so man is gentler and more capable of tender feeling. In such countries people are beautiful, sensitive and flexible in spirit - their speech is elegant, their movements graceful. Science and fine arts flourish among them; their philosophy is cheerful and there is great refinement and courtesy in their attitude towards women.

(Astrov): ...I can see your ironic expression, and I believe that what I say doesn't seem at all serious to you, and ... and maybe it is just crankiness. .. All the same when I go walking by the woods that belong to the peasants, the woods I saved from being cut down, or when I hear the rustling of the young trees I planted with my own hands, I'm conscious of the fact that the climate is to some extent in my power too, and that if mankind is happy in a thousand years' time, I'll be responsible for it even though only to a very minute extent. When I plant a little birch tree and then see it growing green and swaying in the wind, my heart fills with pride, and I ... [Sees the workman who has brought a glass of vodka on a tray.] *However ...* [Drinks.] *It's time for me to go. After all, that's probably just my crankiness. Permit me to take my leave!*

Anton Chekhov
UNCLE VANIA, act one

4

Seite Leer /
Blank leaf

Table of Contents

8

Zusammenfassung

Die Turbulenzstruktur nahe einer städtischen Oberfläche wird in einer experimentellen Fallstudie untersucht. Dazu werden Messungen an je einem Turm über Dachniveau (20 m) und in der angrenzenden Strassenschlucht während fast zweier Jahre herangezogen. Neben der Untersuchung der mittleren Profile von Windgeschwindigkeit, Temperatur und spezifischer Feuchte liegt das Schwergewicht dieser Arbeit auf der Charakterisierung der Turbulenzstruktur in diesen untersten Schichten der städtischen Atmosphäre (Canopy- oder Bestandsschicht und "Roughness Sublayer"). Zwei Ultraschall-Anemometer, eingesetzt in verschiedenen Höhen-Kombinationen liefern dazu die zeitlich hochaufgelösten Werte der drei Windgeschwindigkeits-Komponenten und der Temperatur.

Da eine konsistente Beschreibung der Turbulenz im betrachteten Höhenbereich bis heute fehlt, wird in numerischen Modellen oft die Monin-Obukhov-Aehnlichkeits-theorie für die Bodennahe Grenzschicht (surface layer) verwendet, obwohl die Voraussetzungen dafür nicht erfüllt sind. Die Resultate werden deshalb ebenfalls unter diesem Aspekt diskutiert. Die wichtigste Charakteristik der Turbulenz im Roughness Sublayer ist die festgestellte Abnahme des Impulsflusses je näher die Oberfläche erreicht wird. Auf einer Höhe nahe der Nullflächenverschiebung wird im Mittel kein Impulsfluss mehr beobachtet. Druckunterschiede im Strömungsnachlauf (wake) von einzelnen Gebäuden führen dabei zum Aufbrechen der organisierten Scherströmung in kleinere Wirbel. Die verschiedenen Beiträge zum Impulsfluss werden mit Hilfe einer Quadranten Analyse untersucht. Vorallem innerhalb der Strassenschlucht und unmittelbar darüber erfolgt der Impulsfluss vorwiegend durch Abwärtstransport von Ueberschuss-Impuls (sogenannte Sweeps). Je näher an der "Oberfläche", desto stärker ist die Tendenz zu grossen, sich teilweise aufhebenden Beiträgen der vier Quadranten. Durch die nahe Dachoberfläche (Erwärmung und Abkühlung) ergibt sich für den turbulenten Transport von sensibler Wärme eine komplizertere vertikale Struktur.

Wenn das Konzept der lokalen Skalierung angewendet wird, können für den Roughness Sublayer viele der halbempirischen Funktionen zur Beschreibung der Turbulenz (in der Bodennahen Grenzschicht) unverändert übernommen werden. Die Energiespektren der einzelnen Geschindigkeitskomponenten und die Cospektren für Impuls- und Wärmefluss sind nicht nur von einer einzelnen Längenskala abhängig (Messhöhe oder Mischungsschichthöhe), sondern werden zusätzlich durch die Bebauungsgeometrie bestimmt. Die Peak-Frequenzen entsprechen auf allen Höhen Wellenlängen, die viel kleiner sind als über homogenem Terrain beobachtet. Während die "-5/3-Steigung" im hochfrequenten Bereich der Spektren recht gut erhalten bleibt

(Roughness Sublayer), kann aufgrund des Verhältnisses der spektralen Dichten von longitudinalen und vertikalen Geschwindigkeits-Komponenten trotzdem nicht von einem Inertial Subrange gesprochen werden.

Innerhalb der Canopy-Schicht ist die Turbulenz stark von der Stabilität der Ueber-Dach-Strömung abhängig. Insbesondere die Profile der vertikalen Geschwindigkeits-Varianzen und der turbulenten kinetischen Energie unterscheiden sich drastisch zwischen neutralen und stark instabilen Situationen. Der Luftaustausch zwischen der Canopy-Schicht und der darüberliegenden "freien" Strömung geschieht zu einem grossen Teil aufgrund von vereinzelten Luftstössen, die in die Strassenschlucht einzudringen vermögen. Darüber hinaus scheinen aufsteignde "Blasen" von warmer Luft aus der Strassenschlucht ebenfalls zum Luftaustausch beizutragen.

Abstract

The structure of Turbulence close to an urban surface is investigated in an experimental case study. For this purpose, measurements of almost two years duration on a tower located on the roof-top of a building and on another tower situated within the adjacent street canyon are used. Apart from the description of mean profiles of wind speed, temperature and specific humidity, the main emphasis of this study is put on the characterization of turbulence in the lowest two layers of the urban atmosphere (canopy layer and roughness sublayer). Two ultrasonic anemometers, used in various height configurations, provided the required turbulence data of the three wind speed components and temperature.

Due to the lack of a consistent theory for the description of turbulence in the considered height range, Monin-Obukhov similarity theory for the surface layer is often used in numerical models although the conditions for which it is valid are clearly not met. The results of the present study are therefore also discussed with a view to this aspect. The outstanding characteristic of turbulence in the roughness sublayer is found to be the decrease of Reynolds stress when approaching the "surface". At a height close to the zeroplane displacement height turbulent momentum transport vanishes on average. Pressure effects in the wake of single buildings lead to the break-up of the organized shear flow into smaller, less correlated eddies. Using the conditional sampling technique (quadrant analysis), the various contributions to the transport of momentum are investigated. Within the street canyon and directly above it, sweeps clearly dominate over ejections. The tendency to large, partly offsetting contributions from the four quadrants is increasing when approaching the "surface". The turbulent transport of sensible heat shows a more complex vertical structure due to the vicinity of the roof (heating and cooling).

If the concept of local scaling is applied, it is possible to adopt many of the semi-empirical functions evaluated for the inertial sublayer for the use in the roughness sublayer. Energy spectra for the velocity components and also cospectra for Reynolds stress and sensible heat flux are not only dependent on a single length scale (measurement height or mixed layer height), but are also determined by the building geometry. At all heights, the peak frequencies correspond to a wave length considerably smaller than observed over homogeneous terrain. Although the "-5/3" slope in the high frequency range of the spectra is preserved (even in the roughness sublayer), this constitutes no true inertial subrange since the ratio of vertical to longitudinal spectral densities does not approach the value 4/3 as required by theory.

Within the canopy the structure of turbulence is strongly dependent on the stability of the flow above roof level. In particular, profiles of vertical velocity variance and turbulent kinetic energy vary significantly for near-neutral and strongly unstable situations. The exchange of air between the canopy and the roughness sublayer above is dominated by intermittent bursts that may penetrate into the canyon. In addition, it seems that also "bubbles" of warm canyon air contribute to the ventilation of a street canyon.

Symbols and Abbreviations

a	accuracy (in equation. 5.1)
a_{ij}	flow distortion matrix
A	an area
A_r	area covered with roughness elements
A_b	area covered with buildings
c_s	speed of sound
c_{ij}	transformation matrix for the sonic array into an orthonormal frame of reference
c_p	specific heat of air
c_s	speed of sound
Co_{ij}	cospectral density between variables i and j
d	the zeroplane displacement
D	separation of roughness elements
e	turbulent kinetic energy
e_a	water vapour pressure
e_w	saturation water vapour pressure
e_{w_s}	$e_w(373.16 \ K)$
E	exuberance
f	$= nz/\bar{u}$, non-dimensional frequency
f_c	coriolis parameter
f_m	peak frequency
f^*	$= n(z-d)/\bar{u}$
g	acceleration due to gravity
G	the cross spectrum
h	height of main roughness elements
h_b	height of buildings
h_k	geometric roughness
H_i	height of roughness element i
H	turbulent flux of sensible heat (also: hyperbolic hole)
$I_{i,H}$	the indicator function
$I_{u,v,w}$	Turbulence intensity
J_s	function that depends on the shape of the spectrum of horizontal turbulent energy
k	von Kármán constant
K_i	eddy diffusivity for property i
l	mixing length
l_r	breadth of roughness elements
l_0	distance constant of a cup anemometer

L	Obukhov length
L_m	length scale
L_v	latent heat of condensation
L_ε	dissipation length scale
M_{jk}	$= \overline{u^i u^k}$, i=1,2,3,.. (statistical moments)
n	natural frequency
p	atmospheric pressure
$p(\ )$	joint probability density function
q	specific humidity
$q*$	surface layer humidity scale
Q	the quadrature spectrum
Q_E	turbulent flux of latent heat
Q_H	turbulent flux of sensible heat
r_{ij}	estimate of the flow distortion matrix
R	gas constant for dry air
R_c	$= \overline{uw}/\sigma_u\sigma_w$, the correlation coefficient for longitudinal and vertical wind components
R_f	flux Richardson number
R_i	gradient Richardson number
RI	run test index
s	silhouette area
s_i	normalized coordinate frame spanned by the misaligned sonic array
S	lot area
S_i	spectral energy density of property i
S_L	effect of latent heat on temperature change
S_q	effect of evaporation and condensation on moisture change
S_R	effect of solar radiation on temperature
$S_{i,H}$	stress fraction for quadrant i and hole size H
ΔS_H	difference between stress fractions due to sweeps and ejections
t_j	orthonormal coordinate system of the sonic array
T	temperature
T_a	averaging time
T_s	measured deviation from the mean temperature (in contrast to the actual T')
T_S	373.16 K
u	longitudinal velocity component
u_f	convective velocity scale
u_i	wind velocity components, (Appendix A2: fluctuating velocity components)
$u*$	friction velocity
$u*_c(38m)$	scaling velocity calculated from profile data at z=38m

$\hat{u}$	$= u'/\sigma_u$, scaled velocity component
U_i	mean velocity component in the direction i (Appendix A2)
v	lateral velocity component
V	strength of a wind vector
w	vertical velocity component
z	measurement height
z_h	height up to which horizontal inhomogeneity is non-negligible
z_i	mixed layer height
z_r	reference height
z_0	roughness length
z_*	height of the roughness sublayer
z'	$=z-d$

Greek

α	deviation angle between the wind vector and the nearest sensor axis of the sonic (Appendix A2)
α_k	Kolmogorov constant
β	Bowen ratio
β_{ij}	angle between s_i and t_j
γ	ratio of ejections to sweeps at hole size zero (also: azimuth angle, Appendix A2)
γ_d	dry adiabatic lapse rate
ε	dissipation rate of turbulence kinetic energy (also: elevation angle, Appendix A2)
η	Kolmogorov microscale
θ	potential temperature
θ_*	surface layer temperature scale
$\theta_{*c}(38m)$	scaling temperature calculated from profile data at z=38m
$\vartheta_{i,H}$	time fraction for quadrant i at hole size H
κ	wavenumber
λ	wavelength
λ_m	peak wave length
Λ_s	characteristic length scale of the horizontal turbulence
ρ	density of air
σ_i	standard deviation of property i
τ	$= \overline{\rho}(u'w'^2 + v'w'^2)^{1/2}$, total Reynolds stress
τ_i	integral time scale

Φ_i semi-empirical dimensionless function for property i

Ψ_m surface layer stability correction term for momentum

Special Symbols and Operators

$\mathbb{F}[\,]$ Fourier transform

$(\,)'$ deviation from temporal mean

$(\,)''$ deviation from spatial mean

$\overline{(\,)}$ time average operator

$\langle\,\rangle$ spatial average operator

$[\,]$ conditional average

$\widetilde{(\,)}_i^{**}$ measured wind component

$\widetilde{(\,)}_i^{*}$ measured wind component by the sonic, corrected for transducer shadowing

$\widetilde{(\,)}_i$ as $\widetilde{(\,)}_i^{*}$ but in an orthogonal frame of reference.

$(\,)_h$ heat

$(\,)_m$ momentum

$(\,)_q$ specific humidity

$(\,)_\theta$ potential temperature

$(\,)^{IS}$ inertial sublayer

$(\,)_c$ calculated

$(\,)^{ext}$ extrapolated

$(\,)_{u,v,w}$ wind components

$(\,)_{WT}$ wind tunnel

Abbreviations

CL   canopy layer
FFT   fast Fourier transform
PBL   planetary boundary layer
RS   roughness sublayer
SAM   source area model
SL   surface layer
TKE   turbulent kinetic energy
TP   dew point
TVM   temperature variance method (determination of d)
UCL   urban canopy layer
URS   urban roughness sublayer

1. Introduction

The urban climate has been extensively investigated over the years. Firstly, it has been recognized as a specific type of 'local' or 'regional' climate with anomalies that are anthropogenic and that therefore are attributable to, and may be affected by urban planning. The primary scope of urban climate research centered around questions of the type: 'what would the climate be like at this particular location, if there were no city here ?' To this end, the parameters of the urban climate (and their distribution) were compared with their corresponding "rural" properties, so as to provide measures for the strength of the urban anomaly. The main findings were that: the urban environment was found to be warmer than its surroundings ("urban heat island"), especially at night; the air motion is generally slower due to the higher friction over the very rough urban surface; the water budget is altered due to the higher percentage of paved ground, leading to generally lower evaporation rates (latent heat fluxes). A complete review of these characteristics can be found in Kratzer (1956), Oke (1974 and 1979) and Landsberg (1981). In harmony with the type of question mentioned above urban climate studies generally describe a mesoscale phenomenon, even though the processes leading to it certainly have been recognized as being very local in origin . The principal aim was to determine, what the influence of a "warm, rough spot" with a diameter of a few tens of kilometers" is on the large-scale air flow; whether the formation of clouds is enhanced by rising (warmer) air; etc.

In recent years another aspect of urban climate has become increasingly important: air pollution. The extraordinarily high concentration of sources of pollutants within an urban area demands· an adequate understanding of dispersion processes in order for example to analyse or forecast the contribution of a single source (or a cluster of sources) to the total pollution. Transport of any property in the atmosphere is always associated with *advection* and *dispersion* and this latter process is one of the key unsolved problems of urban pollution modelling. The turbulent state of the lower layer of the atmosphere (i.e. the layer of the atmosphere under consideration) governs to a large measure the effectiveness of dispersion. Unfortunately, knowledge of turbulent transport and the use of physical models to describe turbulence characteristics close to the surface are restricted by and large to a very special idealized type of surface which is flat and homogeneous. To express it pointedly, we would be able to describe dispersion of pollutants in a flat, open desert if there were sources there, but at locations where sources of pollutants are likely to be found, the prerequisites for the application of theories for the description of turbulence are often violated. This is

especially true for urban areas, where pollution levels are high but the application of the classical turbulence "laws" becomes questionable.

1.1 Objectives

At present very little is known about the characteristics of turbulence over a rough urban surface. This is mainly due to the following:

- The flow close to an urban surface has to be considered fully three-dimensional so that, in order to obtain a horizontal average of the variables of interest, a large experimental effort is needed just to obtain a survey of the relevant phenomena.
- There is no consistent turbulence theory covering the lowest few tens of meters above an urban surface and, considering the complex structure of turbulence around a single building (i.e. a roughness element) exposed to a "well behaved flow", it does not seem likely that it will be possible in the near future to set up a comprehensive theory based on physical arguments

Despite these problems, it is nevertheless one of the aims of this study to provide information on the nature of turbulence close to a rough urban surface. Due to financial and temporal constraints, the experimental part of the work was designed as a *case study*. The urban street canyon and adjacent buildings are characteristic elements of urban morphology. Therefore, the instrumental setup was designed to provide measurements of mean variables and turbulence statistics in vertical profiles within a street canyon and above an adjacent building. Thus, it is possible to address the following questions:

- What are the characteristics of the mean and turbulent flow fields close to a rough urban surface ?
- To what extent can the well known surface layer theories be applied to turbulence in its lower portion (roughness sublayer).
- What aspects of turbulence are most sensitive to horizontal inhomogeneity (considering two limiting positions: roof and canyon) and to what extent? Is there a (scaling- or other) framework to account for horizontal inhomogeneity?
- Can any scaling variables be determined for profiles of mean flow in the vicinity of roughness elements and turbulence properties ?

A significant related issue is whether the observed patterns are intrinsic to *canopy/roughness sublayer* turbulence or must be treated as strictly configurational and specific to the present site. This question, in particular, points out the importance of identifying coherent structures in urban turbulence and the need for information on what type of future experiments are required and potentially meaningful.

1.2 Lack of Foundation

Related results on canopy- and roughness sublayer-flow found in the literature are mostly restricted to studies over forests or other types of vegetation. It is clear that these (although similarly rough) surfaces may have thermal and mechanical properties that differ from urban surfaces and thus the use of analogies is limited. On the other hand, wind tunnel studies on the flow over rough surfaces proved to be very useful for comparison as long as characteristics of the neutrally stratified flow were considered. Also in terms of the data analysis very few (or hardly any) of the commonly used empirical or semi-empirical formulas for corrections (e.g. of overspeeding of cup anemometers) could be applied, since they all rely on homogeneous turbulence. Often, best-fit parameterisations have been used instead. Also, many of the "rule-of-the-thumb"-approximations, used to assess certain influences (e.g. the upwind fetch for a turbulence measurement is ≈ 100 z, where z is the measurement height) cannot be used as long as the structure of the turbulence is not a priori clear.

Seite Leer /
Blank leaf

THEORY AND CONCEPTS

2. The Homogeneous Planetary Boundary Layer

Many of the results of the present measurements will be discussed in the light of theories and concepts for the *homogeneous* boundary layer (or, more precisely, the surface layer), using them as a "frame of reference". These theories will therefore be discussed in some detail in this chapter.

In the natural sciences atmospheric flows are usually described by using equations for the conservation of momentum, energy (the first law of thermodynamics), mass (the continuity equation) and scalar quantities (e.g. specific humidity), together with constitutive equations such as the equation of state for ideal gases. In general, this set of partial differential equations cannot be solved analytically. Depending on the scale (in time and space) of the problem under consideration, the equations are simplified in various ways by neglecting terms that are order(s) of magnitude smaller than the others. The Planetary Boundary Layer (PBL) is that part of the atmosphere, where the flow is directly affected by its lower boundary, the earth's surface. Here, friction retards the motion near the surface (such that $u \rightarrow 0$ as $z \rightarrow 0$). Thus it plays an important role and cannot be neglected as in many free atmosphere approximations. In addition, the flux of solar radiation through the earth-atmosphere system exhibits a strong discontinuity at the earth's surface. Both the large vertical wind shear and the thermal effects from surface heating provide the energy for the turbulence that is typically observed in the PBL.

To describe the state of the atmosphere, the following variables are required: the velocity vector $\vec{u} = (u_1, u_2, u_3)$, temperature T (or potential temperature Θ), pressure p, density ρ and the specific humidity q. In order to separate processes of different scales, these variables are commonly split into mean and fluctuating parts. This split is commonly obtained by defining

$$x(t) = \bar{x} + x'(t) \tag{2.1}$$

where

$$\bar{x} = \frac{1}{T_a} \int_0^{T_a} x(t) \, dt' \tag{2.2}$$

is the time average of x over the time interval of length T_a (based on the ergodic hypothesis) and x' is an instantaneous deviation from it. By (2.1) and (2.2) $\overline{x'}$ must be identically zero and for the product of two variables we find

$$\overline{xy} = \overline{x} \cdot \overline{y} + \overline{x'y'}. \tag{2.3}$$

If this decomposition is applied to the above mentioned conservation equations and the gas law together with several reasonable simplifications we obtain the well known *Boussinesq* set of equations for the mean motions in the turbulent boundary layer:

$$\frac{d\overline{u}_1}{dt} = f_c\overline{u}_2 - \frac{1}{\rho}\frac{\partial \overline{p}}{\partial x} - \frac{\partial(\overline{u_1'u_3'})}{\partial z} \tag{2.4}$$

$$\frac{d\overline{u}_2}{dt} = -f_c\overline{u}_1 - \frac{1}{\rho}\frac{\partial \overline{p}}{\partial y} - \frac{\partial(\overline{u_2'u_3'})}{\partial z} \tag{2.5}$$

$$\frac{d\overline{u}_3}{dt} = -g - \frac{1}{\rho}\frac{\partial \overline{p}}{\partial z} \tag{2.6}$$

the equations of motion,

$$\frac{d\overline{T}}{dt} = -\overline{w}\gamma_d - \frac{\partial\overline{w'T'}}{\partial z} + S_R + S_L \tag{2.7}$$

the first law of thermodynamics,

$$\frac{d\overline{q}}{dt} = -\frac{\partial\overline{w'q'}}{\partial z} + S_q \tag{2.8}$$

the moisture budget equation,

$$\overline{p} = \overline{\rho}R\overline{T}(1 + 0.61\overline{q}) \tag{2.9}$$

the equation of state and

$$\frac{\partial\overline{u}_1}{\partial x} + \frac{\partial\overline{u}_2}{\partial y} + \frac{\partial\overline{u}_3}{\partial z} = 0 \tag{2.10}$$

the continuity equation.

The substantial derivative d/dt is defined as

$$\frac{d}{dt} = \frac{\partial}{\partial t} + \overline{u}_1\frac{\partial}{\partial x} + \overline{u}_2\frac{\partial}{\partial y} + \overline{u}_3\frac{\partial}{\partial z}.$$

(For details in the notation see Symbols and Abbreviations). S_R describes the effect of solar radiation on temperature, S_L the effect of latent heat on temperature change and S_q the effect of evaporation and condensation on moisture change. γ_d is the dry adiabatic lapse rate, f_c the Coriolis parameter and g the acceleration due to gravity.

Subtracting equations (2.4) - (2.6) from their respective complete form in $u_i = \overline{u}_i + u_i'$, yields the prognostic equations for perturbations u_i'. In most PBL

problems, these are of limited importance due to the very short time scale of turbulence phenomena, but they can be used to derive prognostic equations for variances $\overline{u_i^2}$ (and other second-order terms). This is achieved by simply multiplying the equations for u_i' by $2 u_i'$ and averaging again. Finally, the halved sum of the three budget equations for $\overline{u_i^2}$ yields the budget equation for turbulent kinetic energy per unit mass $\overline{e}$ (TKE),

defined as $\overline{e} = \frac{1}{2}\left(\overline{u_1'^2} + \overline{u_2'^2} + \overline{u_3'^2}\right)$, which may be written close to the surface in the following form (Panofsky and Dutton, 1984):

$$\frac{d\overline{e}}{dt} = - \overline{u_1'u_3'}\frac{\partial \overline{u}_1}{\partial z} - \overline{u_2'u_3'}\frac{\partial \overline{u}_2}{\partial z} + g\frac{\overline{u_3'T'}}{T}\left(1 + \frac{0.07}{\beta}\right) - \frac{1}{\rho}\frac{\partial(\overline{u_3'p'})}{\partial z} - \frac{\partial(\overline{eu_3'})}{\partial z} - \epsilon. \qquad (2.11)$$

The first two terms one the right hand side of (2.11) describe the rate of production of TKE by the mean wind shear; the third term is the rate of destruction of turbulence in stable stratification (or production in unstable stratification); the fourth term describes how TKE is redistributed by pressure perturbations; the fifth term represents the (vertical) turbulent transport of TKE and the last term represents dissipation (i.e. the irreversible conversion into heat). Equation (2.11) is valid only if vertical velocity fluctuations are of the same order of magnitude as the horizontal, and if vertical gradients are much larger than horizontal gradients (the latter assumption is fulfilled most of the time throughout the PBL due to its nearness to a solid boundary which induces a distinct vertical structure).

The factor $1 + 0.07 / \beta$ is added to describe the production of convective energy due to water vapour (c.f. Panofsky and Dutton, 1984). Here, β represents the Bowen Ratio, the ratio of sensible to latent turbulent heat fluxes at the surface. Depending on the relative height within the PBL, different simplifications are valid for (2.11). The relative importance of shear induced turbulence and destruction through convective processes is expressed by the Flux-Richardson-Number

$$R_f = \frac{\left[-g\frac{\overline{u_3'T'}}{T}\left(1 + \frac{0.07}{\beta}\right)\right]}{\left[-\overline{u_1'u_3'}\frac{\partial \overline{u}_1}{\partial z} - \overline{u_2'u_3'}\frac{\partial \overline{u}_2}{\partial z}\right]}. \qquad (2.12)$$

If the kinematic sensible heat flux $\left(\sim \overline{u_3'T'}\right)$ is positive (upward), R_f becomes negative. This is the case if the air is unstably stratified. The opposite is true for a stable flow (sensible heat flux is negative, downward, $R_f > 0$). Large negative Richardson numbers indicate strong convection (mechanical turbulence being unimportant). As R_f approaches zero ("forced convection") shear induced turbulence becomes more and

more important . A positive Richardson number indicates that mechanical turbulence can persist, but is damped by the stratification as long as $R_f < R_f{}^{crit} \approx 0.25$ (Panofsky and Dutton, 1984). The (mathematically idealized) situation where $R_f = 0$ corresponds to natural stratification. In practice, "neutral" or rather "near neutral" has to be defined, e.g. $|R_f| < 0.05$.

2.1 Concepts and Simplifying Assumptions

Equations (2.4 - 2.10) can be simplified by making assumptions about the evolution of the variables or their horizontal variability. Before briefly discussing these concepts that are frequently used throughout the text, we have to deal with a problem inherent in equations (2.4 - 2.10).

2.1.1 The Closure Problem

With the Boussinesq approximation we are left with seven equations and eleven unknowns. In addition to the seven principal variables such as pressure and density etc., also mean covariances, or turbulent fluxes (e.g. $\overline{u_1 T'}$), have to be specified. It is clear that - similar to the conservation equations for variances - equations for the fluxes can be derived. Unfortunately, these contain third order moments such as $\partial/\partial z \left(\overline{u_i u_j^2} \right)$ for which we would again need new equations. The higher the order of moments included in the equations (say n), the higher the order of unknown moments (n+1)will be. This is called *the closure problem*. It implies that at the level of desired complexity, the process of introducing new equations including still higher order moments has to be stopped and *assumptions* have to be made concerning the remaining unknowns. The simplest way to do this is to neglect the turbulence terms in (2.4 -2.10), an approach we call zero-order closure. Stull (1988) points out that *similarity theory* (see next section) can be viewed as a type of zero - order closure since no parameterisations of turbulence are retained in this framework. This, however, implies that the turbulent fluxes are *known* in order to diagnose mean quantities from similarity relations - a condition that is very rarely fulfilled (e.g. in modelling applications). If the turbulent fluxes are related to (or parameterised by) mean quantities we speak of *first-order closure*. A prominent example is the so-called K-theory that relates the turbulent transport of a quantity, π, through an eddy diffusivity (or transfer coefficient) K to the gradient of the mean $\overline{\pi}$ in the respective direction. As an example, the vertical turbulent flux of sensible heat, $\overline{\rho c_p u_3 T'}$, can be parameterised by

$$\overline{\rho c_p u_3 T'} = -\overline{\rho} c_p K_h \frac{\partial \overline{T}}{\partial z} \qquad (2.13)$$

where the subscript 'h' stands for "heat"; a further subscript indicating that K_h stands for vertical exchange has been dropped for convenience, since in the horizontally homogeneous PBL only vertical turbulent fluxes are important. The negative sign in (2.13) arises from the definition of the axes: A positive gradient (increasing with height) is associated with a downward flux (or K is kept positive). There is some experimental evidence that K_h and K_q (for moisture) seem to be some 30% smaller than K_m (momentum) in the neutral limit. Usually, in dispersion modelling the transfer coefficient for a quantity χ (e.g. a chemical compound), K_χ, is set equal to K_h. The so-called *Mixing-Length* concept can be used to describe the vertical variation of K_i by introducing the mixing length l to yield (see e.g. Ohmura and Rotach, 1986)

$$K_i = l^2 \left| \frac{\partial \overline{u}}{\partial z} \right| \tag{2.14}$$

which holds for purely mechanical turbulence. In the surface layer (see Section 2.3) it is often assumed that $l = kz$, where k is the von Kármán constant (with a value of approximately 0.4). More often, the vertical variation K_i is described using similarity relations (e.g. Stull, 1988). K-theory has, however, some limitations. Specifically, it is restricted to small eddy transport and to locations where no sources or sinks of the transported property are important. However, large eddies can transport a property χ directly (with only little mixing) to a certain height z, where large upward motions might be associated with large values of χ, giving a positive flux, while the local gradient may also be positive, implying a downward flux (e.g. Panofsky and Dutton, 1984). Because of these limitations of K-theory, higher order closure schemes are frequently used (especially in numerical models), i.e. the third order moments appearing in the equations for the second order moments are parameterised using the latter or even mean values.

2.1.2 Homogeneity

The equations of mean and turbulent flow can be considerably simplified if it can be assumed that its properties do not change in space. Obviously, this assumption cannot hold in the boundary layer for the vertical direction, since the flow is clearly stratified due to the vicinity of the solid boundary. Homogeneity, if any, can therefore only mean *horizontal homogeneity in* the boundary layer. This means that the horizontal derivatives $(\partial/\partial x, \partial/\partial y)$ vanish (see e.g. the restrictions to the TKE Budget (2.11)). It has to be noted, however, that the concept of homogeneity again refers to the scale of the problem: even a huge, flat desert surface is inhomogeneous very close to the

surface, near z_0. On the other hand, even a forest or urban surface may be considered homogeneous if one sufficiently far from the surface. In the past the problem of homogeneity has usually been dealt with by prescribing the "required fetch" (i.e. a distance rather than an area): if the surface characteristics do not change distinctly for a sufficiently large upwind distance (usually given in terms of the measuring height z, e.g. 100 z) and if one is high enough above the surface (see Section 2.3), the flow can be considered horizontally homogeneous. This is the reason why most of the famous boundary layer experiments were performed in large uniform prairies or deserts.

Clearly, at small heights the concept of homogeneity will never apply above complex surfaces such as cities or forests. Schmid (1988) has therefore reversed the argument by establishing a measure of representativeness (of e.g. an observation) over complex terrain. He provides a method to estimate the so-called *Source Area* for observations at a given height and for given flow characteristics (wind speed, stability etc). This source area is the (two dimensional) upwind part of the surface that influences the observation (divided into different weighting regions) and is obtained using a reversed diffusion approach. The measurement is now considered representative for the surface domain of interest to a degree that corresponds to the fraction of surface variability found within the source area. In this sense, the "required fetch" conditions are equivalent to a representativeness approaching 100%. If in the following, expressions like "homogeneous fetch", "ideal fetch conditions" or "ideal terrain" are used, such a 100% representativeness condition is anticipated.

2.1.3 Stationarity

Stationarity can be viewed as "homogeneity in time". Thus, the statistical characteristics of a stationary flow do not change with time. This is an equally idealized mathematical concept ($\partial/\partial t = 0$) as homogeneity is in the spatial sense. Through the diurnal cycle of energy supply (solar radiation) and changing synoptic patterns, the condition of stationarity is, strictly speaking, never fulfilled. It can be approached, however, by choosing an appropriate averaging time. Mean values over time periods on the order of one minute can even be considered stationary if they are obtained in situations of strong winds and thick cloud cover (a common example for a situation likely to be stationary). On the other hand, a five-hour average is certainly influenced by the diurnal cycle. Spectral estimates of long term runs (Fig. 2.1) indicate that there is a gap in the energy spectrum of atmospheric motions at a wavenumber of $10^{-4}m^{-1}$, corresponding roughly to a period of one hour (Panofsky and Dutton,1984). Since even with an appropriate averaging time, unstationarity cannot be excluded (e.g. at sunrise or sunset) measurements have to be examined for stationarity (see Section 5.2).
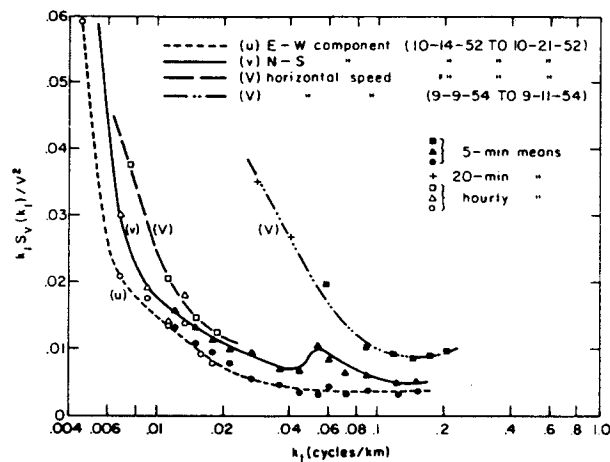
Figure 2.1   Indications of a spectral gap around 0.1 cycles km^{-1} (about 1 cycle h^{-1}).
Adapted from Panofsky and Dutton (1984).

2.1.4 Isotropy

A flow is isotropic if its statistics are invariant to rotation and reflection of the coordinates. It is easy to show that variances of the three velocity components must be equal in case of isotropy. This condition is never met in the PBL for appropriate averaging times and thus, motions at turbulence scales in this part of the atmosphere are not isotropic. The concept of isotropy, however, has great importance for spectral considerations (see Chapter 12) since the smallest eddies are found to be isotropic, a phenomenon which is called *local isotropy*. The wavenumber (or frequency) range in the one-dimensional energy spectrum (e.g. longitudinal) for which local isotropy holds is called the *inertial subrange*. It lies between the *energy containing subrange* where the energy input into the system takes place and the *dissipation subrange*. There is much evidence, that atmospheric data in the wavenumber range $\eta < 1/\kappa_1 < z/10$, where η is the Kolmogorov microscale (on the order of 10^{-3}m), fall into the the inertial subrange. Spectral densities in the inertial subrange are very easy to describe and can provide important information for the description of the flow.

2.1.5 Taylor's Hypothesis

Usually, turbulence observations are performed at a fixed location and provide time series but not spatial information. This spatial information, however, is very important for the description of scales within the PBL. For example, the wavelength of the maximum energy containing eddies is related to the PBL height, an important length scale within the boundary layer. Especially in complex terrain one might be interested to identify the spatial structures producing departures from e.g. spectra obtained over

homogeneous surfaces. It is therefore desirable to be able to convert time series into "space series" (and vice versa). This is possible if eddies move faster over a distance equivalent to their diameter than they change their character, or, in other words if turbulence is "frozen". If this can be assumed, Taylor's hypothesis states simply that the time-space conversion can be obtained through

$$x = \bar{u} \cdot t .$$ (2.15)

Similar expressions exist for the wavenumber-frequency conversion and so forth. Panofsky and Dutton (1984) mention several conditions where Taylor's hypothesis fails, especially the fact that strong vertical wind shear can distort eddies as they move. As a criterion, they give a threshold frequency $(f < \partial \bar{u}/\partial z)$ for which Taylor's hypothesis is likely to fail. Willis and Deardorff (1976) suggest as a condition for the applicability $\sigma_H < 0.5\bar{u}$, where σ_H is the standard deviation of the mean wind speed $\bar{u}$. Thus Taylor's hypothesis should work in stable boundary layers or if turbulence intensity is not too large as compared to mean wind speed.

2.2 Similarity Theory

If it is not possible to derive equations based on first principles to predict or diagnose the variables governing a turbulent flow the *similarity theory* provides a useful tool to derive empirical relationships for the variables of interest. It is based on the principle that a non-dimensionalized ("scaled") variable can be described by a universal function of dimensionless groups of variables, as long as all important variables (for the problem in question) are taken into account. The mathematical procedure to determine the number of required dimensionless groups and their possible form is the *dimensional analysis*, based on *Buckingham's theorem*. This states that for a number of n variables with r physical units (such as m, s, K), (n-r) independent dimensionless groups are possible (cf. e.g. Munn, 1966). Another way to put this, is to state that r key variables, chosen such that no dimensionless group can be formed from them, is sufficient to describe the system. Once the relevant dimensionless groups are found, observations must provide the empirical constants to describe the shape of the desired functional dependence between the variables. Similarity theory can therefore never come up with "physical laws" for the description of turbulent flows, but nevertheless provides useful empirical relations.

The crucial step in any dimensional analysis is the proper choice of the relevant variables. The last step of the procedure, however, provides an 'a posteriori'

justification of the chosen selection: an unimportant dimensionless group can be identified when the other groups do not change with respect to the former and if too few variables are chosen, this will be indicated by large scatter in the postulated relations. In the very simple case where (n - r) equals 1, dimensional analysis can even provide us with relationships between the variables of which the powers are known and only a proportionality constant has to be experimentally determined. As an example of dimensionless analysis, such a simple case shall be demonstrated in the following: In the inertial subrange of the turbulent energy spectrum, energy is neither produced nor dissipated (see Section 2.1.4) and in a stationary turbulent flow the rate of energy "transported" through the inertial subrange (from large eddies to small eddies), or the spectral energy density S (units $[m^3s^{-2}]$), is only dependent on the wavenumber κ ($[m^{-1}]$) and on the amount of energy that can be dissipated (at wavelength smaller than η), ε ($[m^2s^{-3}]$). Thus, we have three variables and two physical units and therefore only one dimensionless group is possible:

$$\alpha_k = S^a \, \kappa^b \, \varepsilon^c \,. \tag{2.16}$$

The equations for the units are

$$0 = 3a - b + 2c \qquad\qquad m \tag{2.17}$$
$$0 = -2a \quad\;\; - 3c \qquad\qquad s \tag{2.18}$$

From (2.18) it follows immediately that c = -2/3a and then from (2.17) that b = 5/3a. Rearranging (2.16) in order to obtain a relation of the form s = f(κ,ε), and choosing a=1 leads to

$$s = \alpha_k \, \varepsilon^{2/3} \, \kappa^{-5/3} \,. \tag{2.19}$$

This is the well known shape of the energy spectrum in the inertial subrange. α_k is the so-called Kolmogorov constant. A step by step description for the dimensionless analysis together with frequently used scaling variables can be found in Stull (1988).

2.2.1 Monin - Obukhov Similarity

In the surface layer (SL), the lowest part of the PBL (see next section), turbulence characteristics and the vertical distribution of mean variables turn out to be relatively simple. The various simplifications described in the previous sections (homogeneity, stationarity) and a comparison of the order of the magnitudes of the terms in the Boussinesq set of equations leads to a situation where e.g. (2.4) reduces to

$$\frac{\partial}{\partial z}\left(\overline{u_1'u_3'}\right) \approx 0. \tag{2.20}$$

Turbulent fluxes of momentum, sensible heat and moisture are thus almost constant throughout the SL (they vary by about 10%) but they are large and determine the flow characteristic in the SL. One of the important consequences of a constant stress with height is that neither the wind direction changes with height, so that the coordinate system can always be turned in a way that $\bar{u}_2 = 0$ and the mean wind is described by $\bar{u}_1$ only. For a homogeneous surface, the problem is therefore essentially one-dimensional.

The similarity theory for the SL, originally presented by Monin and Obukhov (1958) requires three "key" or scaling variables due to dimensional arguments. Because of the importance of the turbulent fluxes of momentum and sensible heat, they chose the scaling variables for velocity and temperature:

$$u_* \equiv \left(-\overline{u_1'u_3'}\right)^{1/2} = \left(\frac{\tau}{\rho}\right)^{1/2} \tag{2.21}$$

$$\theta_* = \frac{-\overline{T'u_3'}}{u_*} = \frac{-\left(Q_H/\rho c_p\right)}{u_*} \tag{2.22}$$

where τ is the surface shear stress and Q_H the surface heat flux. The quantity u_* is called the friction velocity, while θ_* is the scaling temperature. As a third key variable a length scale is required for which the height z is an appropriate choice. As a second length scale, Monin and Obukhov introduced the so-called Obukhov Length L, defined as

$$L = \frac{-u_*^2\,\bar{T}}{\theta_*\left(1+ \frac{0.07}{\beta}\right)\cdot k \cdot g} \tag{2.23}$$

where k is the von Karman constant, introduced by convention (or for comparison to mixing length theory) and the factor $(1+ 0.07/\beta)$ was included later as a correction for humidity effects. The Obukhov length L is (due to the constancy of the turbulent fluxes) essentially constant throughout the SL and its magnitude can be interpreted as the height where thermal and shear forcing for the turbulence balance (Ohmura and Rotach, 1986). For many problems in the SL the ratio z/L is the only dimensionless group that is important and similarity relations turn out to be relatively simple. The ratio

z/L can be shown to be a measure for the static stability (i.e. the thermal stratification) similarly as the Richardson number (cf. (2.12), (2.21), (2.22) and (2.23)) and since the latter is dimensionless too, similarity theory requires that R_f be a function of z/L. Businger et al. (1971) have given such relationships for the *Gradient Richardson number* R_i, an approximation of R_f based on K-Theory (the numerical constants are adopted after Högström, 1988)

$$R_i = \frac{0.95 \, z/L \, (1-19.3 \, z/L)^{1/2}}{(1-11.6 \, z/L)^{1/2}} \quad \text{(unstable)} \tag{2.24.a}$$

$$R_i = \frac{z/L \, (0.95 + 7.8 \, z/L)}{(1+6 \, z/L)^2} \quad \text{(stable)} \tag{2.24.b}$$

where

$$R_i = \frac{\frac{g}{T} \left(\frac{d\overline{T}}{dz} - \gamma_d\right) \left(1 + \frac{0.07}{\beta}\right)}{\left(\frac{\partial \overline{u}}{\partial z}\right)^2} = \frac{K_m}{K_h} R_f \tag{2.25}$$

A survey of important surface layer relations will be given in the following. Specific discussions on the value of experimentally determined constants involved, can be found wherever these relations will be used for comparison in the subsequent analysis. All these relations refer to homogeneous SL turbulence (i.e. to ideal fetch conditions) and $\overline{u}$ will be used to denote the mean wind in the following (see above) instead of $\overline{u}_1$.

The dimensionless wind shear can be written as

$$\frac{d\overline{u}}{dz} \cdot \frac{kz}{u_*} = \Phi_m (z/L) \tag{2.26}$$

where k (von Kármán constant) is again introduced for convenience. It is common to choose Φ_m such that in the neutral SL (z/L = 0),

$$\Phi_m (0) = 1. \tag{2.27}$$

Equation (2.26) can easily be integrated to yield the well known "logarithmic wind profile"

$$\overline{u} (z) = \frac{u_*}{k} \ln \left(\frac{z}{z_0}\right), \tag{2.28}$$

where z_0 is the "roughness length", the height above the surface where $\bar{u}$ becomes zero (ideally) and can be used to characterize the surface. For Φ_m, various forms have been proposed e.g. by Businger et al. (1971) and Dyer and Hicks (1970), who found, however, different values for k. Högström (1988) has re-analyzed the von Kármán constant and found $k \approx 0.4$. He gave the reformulated functions Φ_m as follows

$$\Phi_m = (1 - 15.2 \ z/L)^{-\frac{1}{4}} \qquad \text{Dyer and Hicks (1970)}$$

$$\Phi_m = (1 - 19.3 \ z/L)^{-\frac{1}{4}} \qquad \text{Businger et al. (1971)} \qquad \text{unstable}$$

$$(2.29)$$

$$\Phi_m = (1 + 4.8 \ z/L) \qquad \text{Dyer and Hicks (1970)}$$

$$\Phi_m = (1 + 6 \ z/L) \qquad \text{Businger et al. (1971)} \qquad \text{stable}$$

Integrating (2.26) for non-neutral conditions yields

$$\bar{u}(z) = \frac{u*}{k} \left[\ln \left(\frac{z}{z_0} \right) - \psi_m \left(\frac{z}{L} \right) \right] \qquad (2.30)$$

where

$$\psi_m \left(\frac{z}{L} \right) = \int_{\xi_0}^{\xi} \left[1 - \Phi_m(\xi) \right] \frac{d\xi}{\xi} \quad , \quad \xi = z/L \qquad (2.31)$$

is the integrated form of Φ_m or the "diabatic departure from the logarithmic profile". ψ_m is usually given by an analytical expression (Paulson, 1970) depending on the functional form and the constants in Φ_m. Similar relations as (2.26) exist also for the non-dimensional profiles of potential temperature $\bar{\theta}$ and specific humidity $\bar{q}$:

$$\frac{d\bar{\theta}}{dz} \cdot \frac{k z}{\theta_*} = \Phi_h(z/L) \qquad (2.32)$$

$$\frac{d\bar{q}}{dz} \cdot \frac{k z}{q_*} = \Phi_q(z/L) \qquad (2.33)$$

where q_* is a humidity scale defined in analogy to θ_*

$$q_* \equiv \frac{\overline{u'_3 q'}}{u_*}. \qquad (2.34)$$

These equations can be integrated in a similar manner to (2.26).

The scaled standard deviation of vertical wind fluctuations is well described by

$$\frac{\sigma_w}{u_*} = \Phi_3 \left(z/L \right), \tag{2.35}$$

while the horizontal fluctuations are dependent on the height of the PBL, rather than the height of observation z, so that Monin-Obukhov scaling cannot be expected to apply there. For temperature fluctuations we find

$$\frac{\sigma_T}{\theta_*} = \Phi_T \left(z/L \right). \tag{2.36}$$

Considering the energy spectrum of surface layer flows, another length scale enters the problem: the wavelength λ (often expressed as the wavenumber κ). The spectral density of the vertical velocity may be expressed then

$$\frac{f\, S_w\, (f)}{u_*^2} = \Phi_w \left(z/L, \ \kappa \cdot L \right) \tag{2.37}$$

where f is the frequency. This formulation holds if Taylor's hypothesis can be applied. What was mentioned for the variances of horizontal velocity fluctuations also applies for the spectral density of horizontal wind component (at least in the energy containing subrange). They scale better with the PBL height and were therefore not subject to Monin-Obukhov scaling. In the inertial subrange, however, all three spectral densities obey Monin-Obukhov scaling (which is consistent with Kolmogorov theory) and can be expressed by (2.19).

2.3 Observed Boundary Layer Characteristics

The PBL can be subdivided into various sublayers according to two criteria: one is the height within the PBL and the other is a subdivision into various scaling regions. Starting with the latter, we can adopt a picture proposed by Holtslag and Nieuwstadt (1986), (Fig. 2.2). For a wide range of stabilities, the lowest 10% of the PBL is characterized by surface stress, surface heat flux and the height z. This part is usually called the *surface layer* and Monin-Obukhov scaling applies for many problems. If z/L becomes smaller than approximately -1, buoyant processes dominate shear induced turbulence and u_* becomes unimportant in the *free convection layer*. Higher up in the boundary layer, the fluxes tend to vary strongly in a stable situation, so that local

values are likely to be used as scaling variables (*local scaling*) and the height may become unimportant (*z-less scaling*). The upper part of the unstable PBL is still determined by the surface heat flux, while u_* becomes unimportant and the boundary layer height z_i replaces z (*mixed layer*). The *near neutral upper layer* is poorly understood at present so that no suggestions are given for scaling variables.
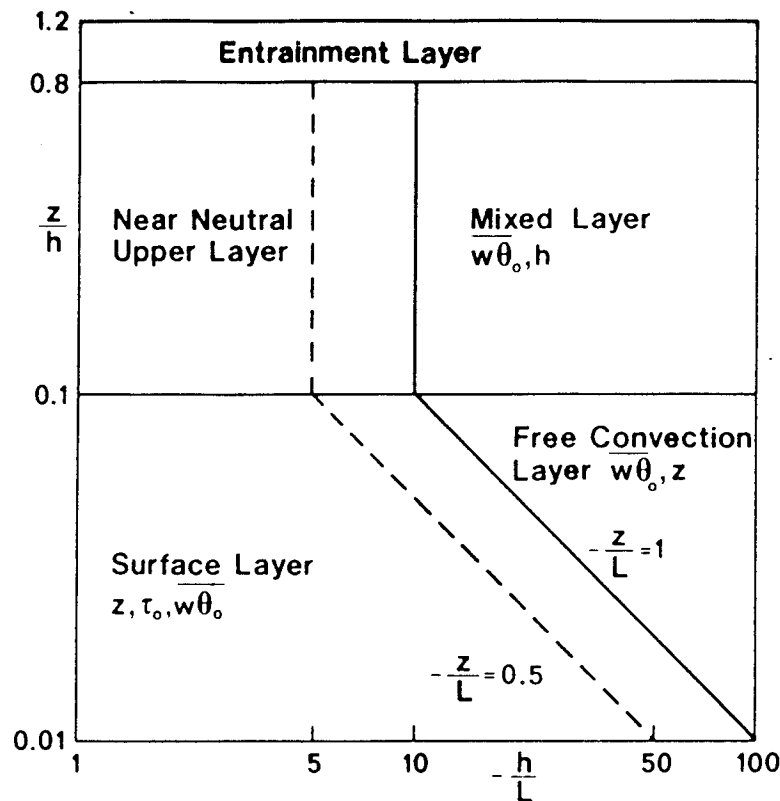

Figure 2.2   Definition of the scaling regions in the unstable atmospheric boundary layer. Basic scaling parameters for the turbulence are indicated. In this figure, τ_0 corresponds to the surface shear stress and $\overline{w\theta_0}$ to the kinematic heat flux. h denotes the mixing height. Adapted from Holtslag and Nieuwstadt (1986).

The boundary layer height exhibits a strong diurnal cycle over land and is, of course, dependent on synoptic and mesoscale features. As an example, Fig.2.3 shows. the evolution in a high pressure region. The boundary layer height is often defined as the height of the lowest (potential) temperature inversion. From Fig. 2.3 it is apparent that an observation at a fixed height may, depending on the local time, fall into different scaling regions.

The vertical structure of the PBL is strongly dependent on stability. Usually, the first few centimeters (in homogeneous terrain !, see Section 3.1) are called the *microlayer* or interfacial layer. Above that, we find a surface layer, regardless of stability. The SL is

characterized through a gradient of potential temperature that is either positive (stable), negative (unstable) or near zero ("neutral"). The layer above the SL is often called *Ekman Layer* if convective processes are unimportant (in a sense that does not rely on scaling considerations). Here, the wind direction changes with height towards the geostrophic direction in the so-called Ekman-spiral, which was first derived by Ekman for a stationary, homogeneous, neutral and barotropic atmosphere with no subsidence. These conditions are indeed sometimes fulfilled in the boundary layer so that the Ekman-spiral can be a useful approximation. This finding illustrates, on the other hand, the fact that the stability of the PBL is determined by the gradient of the potential temperature in the surface layer, a result that can be inferred from the definition of L using surface layer values.
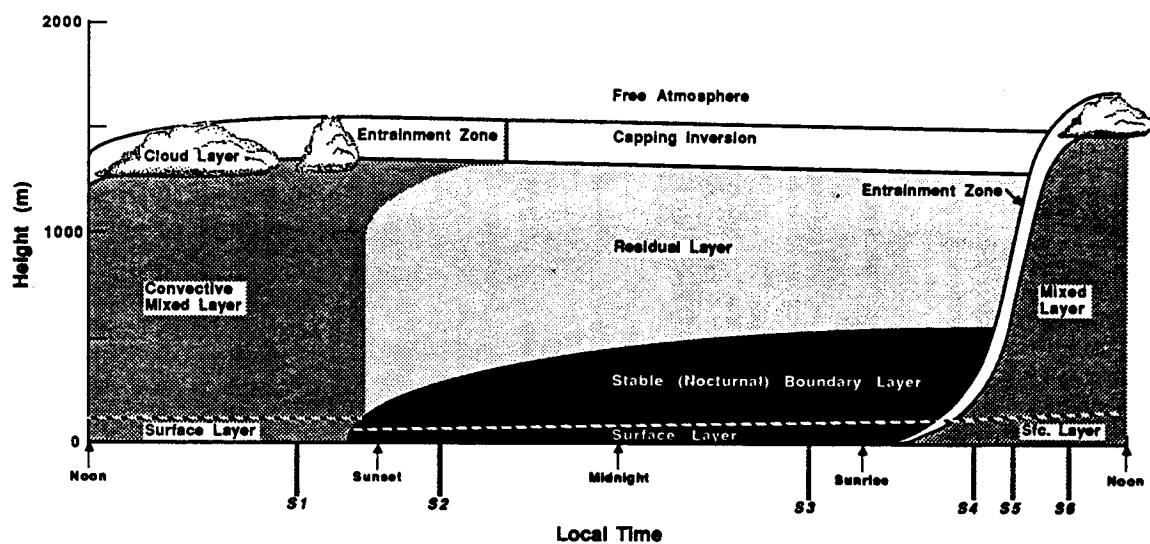

Figure 2.3   The evolution of the boundary layer within a high pressure zone. Adapted from Stull (1988).

Seite Leer /
Blank leaf

3. The Structure of the Lower Boundary Layer

The lowest part of the atmosphere adjacent to the ground[1] is called the *"canopy layer"* and consists of the air volume between the "roughness elements" - if there are any (and this is the case on almost every surface). These roughness elements can, in principle, be as large as houses or as small as sand grains, in which latter case the question of flow and turbulence within the canopy layer is quite academic, however. The lower part of the boundary layer, usually referred to as the "surface layer" is generally considered in two different sublayers: one, the *roughness sublayer* (or transition layer or turbulent wake layer) starts at the top of the canopy layer and ranges up to a certain height z_*, above which the influence of an individual roughness element cannot be distinguished anymore. The region above z_* is called the *inertial sublayer*, where the flow "sees" a surface of a certain roughness depending on size and distribution of the roughness elements. In the case of uniform, flat terrain the inertial sublayer is often called the "surface layer" since the roughness sublayer is then indistinguishably small. Flow and turbulence within the inertial sublayer can be described by semi-empirical functions using Monin-Obukhov Similarity (see Chapter 2). Fig. 3.1 summarizes the different regions of the lower boundary layer together with some suggestions for the height of the roughness sublayer.

The flow within the canopy layer (CL) and the roughness sublayer (RS) is essentially three dimensional. Measurements or model predictions for a single point in the horizontal plane can not lead to a general description of the flow. It is therefore appropriate to consider horizontal averages (Raupach and Shaw, 1982). Formally, an averaging operator can be defined (Raupach and Shaw,1982) as

$$\langle \Omega \rangle = \frac{1}{A} \int_R \int \Omega(x,y) \, dx \, dy, \qquad (3.1)$$

where Ω denotes a scalar field defined in the air but not at the points occupied by the roughness elements, and A is the area of a region R of the xy-plane. The angle brackets denote the horizontal average. In analogy to the decomposition of a time dependent scalar flow variable into its mean and turbulent parts we can write

$$\Omega(x,y,t) = \langle \Omega \rangle + \Omega''(x,y,t), \qquad (3.2)$$

---

[1] apart from a very thin laminar layer

where the double prime indicates a departure from the horizontal average. Raupach and Shaw (1982) show that the averaging operator (3.1) satisfies all but one of the commutation properties required of a turbulence averaging operator. The exception is that horizontal averaging and spatial differentiation do not commute in general: i.e. if Ω is not constant at the air - canopy element interface $\langle\partial\Omega/\partial x_i\rangle \neq \partial\langle\Omega\rangle/\partial x_i$ (for i =1, 2). This implies in particular that $\langle\partial\Omega''/\partial x_i\rangle \neq 0$ in the latter case. Raupach and Shaw (1982) further point out the importance of the sequence of temporal and spatial averaging. When the time averaging is applied first, an extra contribution to the Reynolds stress, the so called dispersive covariance $\langle\bar{u}_i''\bar{u}_j''\rangle$ is introduced. It arises from the spatial correlation of quantities averaged in time but varying with position. The total spatially averaged covariance then reads

$$\langle u_i''u_j''\rangle = \langle\bar{u}_i''\bar{u}_j''\rangle + \langle\overline{u_i'u_j'}\rangle \tag{3.3}$$

This dispersive covariance can, fortunately be neglected for many flows (see Chapter 7).

It has to be noted that it is very difficult in the real atmosphere to obtain data from a sufficient number of points in a horizontal plane in order to perform an averaging according to (3.1). Therefore, assumptions often have to be made about the horizontal variation of a certain variable, using e.g. wind tunnel results (where a sufficiently large density of measurements is possible).
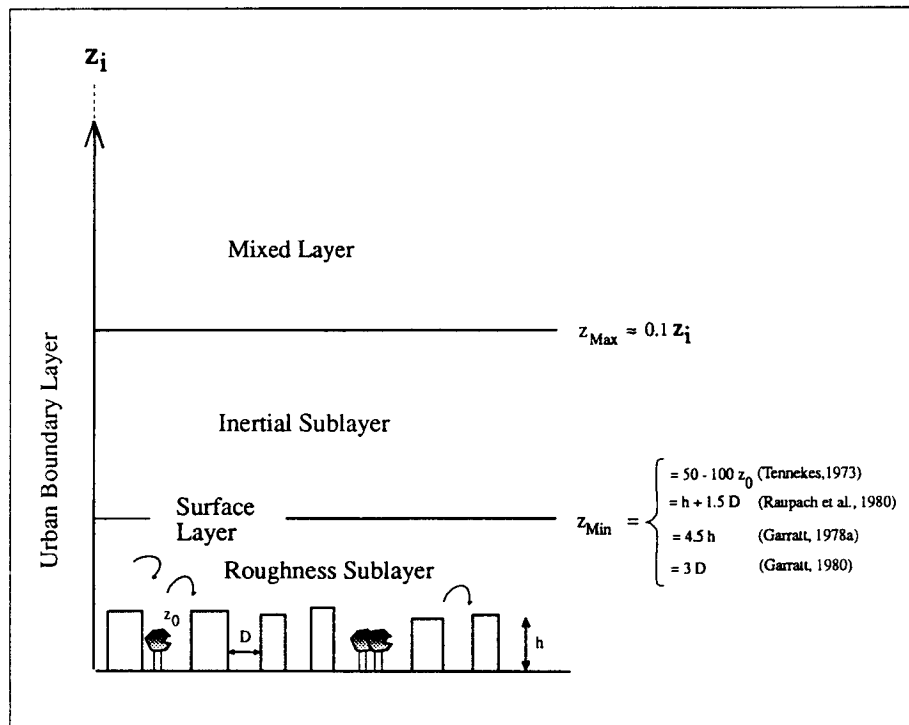

Figure 3.1   Boundary layer structure over a rough (urban) surface. z_i denotes the mixed layer height. Modified after Oke (1988).

3.1 The Canopy Layer

For roughness elements of uniform height, the canopy layer (CL) ranges from the ground ($z=0$) to the top of these roughness elements (trees, houses, bushes, plants etc.) at $z=h$ by definition. If there are different roughness elements, such as plants and bushes, or houses and trees etc. their averaged height ($z = \bar{h}$) is usually considered as the top of the CL. For the urban canopy layer (UCL), Oke (1988) refers to "about roof level" as a "definition"of its top.

Uniform plant or tree canopies have been widely investigated in recent years. (Thom, 1975; Raupach and Thom, 1981; Shaw et al., 1983; Gao et al., 1989). Turbulence within the CL is found to be highly intermittent (e.g. Baldocchi and Meyers, 1988), i.e. large contributions to the Reynolds stress within an averaging period occur during a relatively short period of time. Profiles of mean variables and higher order moments turn out to be characteristic for a certain type of canopy and depend on the density of the roughness elements and the vertical structure of the CL (e.g. the vertical distribution of the leaf area index for vegetation canopies). Organized structures of turbulence events have been shown to contribute to a large extent to both fluxes of heat and momentum within the CL (Gao et al., 1989).

The urban canopy layer (UCL) consists of many different structural elements such as street canyons, squares, parks, suburban residential districts and all possible combinations of these. This makes it very difficult to find a general description for the UCL as a whole. The various structures have to be considered separately; together with their respective interactions. Flow characteristics have especially been investigated for the case of an *urban street canyon*. This feature of urban morphology, however, cannot be considered as a true canopy layer (in the sense a forest canopy can, for instance) since the flow within the street canyon can exhibit certain flow characteristics that are only weakly related to above-roof atmospheric situations. A number of equally spaced (or randomly distributed) street canyons as an "ensemble" would be necessary to investigate the interactions between the UCL flow and the urban roughness sublayer. Exchange characteristics and the knowledge of transport processes within and out of an urban street canyon are nevertheless very important with respect to air quality control. Unfortunately, a street canyon's air volume is not only the place where most people spend their day but also a region where large amounts of pollutants are released: near the street level from the exhaust of motor vehicles and near the roof tops from chimneys. When the above-roof wind direction is perpendicular to the axis of the canyon, a vortex (Fig. 3.2) can develop within the canyon (Georgii et al., 1967; De Paul, 1984) with its strength and location essentially being dependent on the ratio

between the canyon's height and width. This vortex can also have the form of an along-axis spiral if the wind direction above roof level is not exactly orthogonal to the canyon (e.g. Yamartino and Wiegand, 1986). Most of the time, the horizontal wind speed within the canyon (as measured with an ordinary cup anemometer) is considerably reduced as compared to above-roof values. For long and straight street canyons, however, channeling can produce even higher wind speeds than above the roof when the flow is parallel to its axis (Hosker, 1984). These pictures can be considered "ideal cases" in the sense that real street canyons are usually "disturbed" by crossings, intersections or squares etc. which make the flow much more complex.

Table 3.1:   Several approaches for the estimation of z_*, the height of the roughness sublayer. h = mean element height, D = separation of roughness elements, l_r = breadth of roughness elements, z_0 = roughness length.

| formulation	criterion	type of experiment	authors
$z_* = h + D$	mean velocity variations	Wind tunnel, random surface	Mulheam and Finnigan (1978)
$z_* = h + 2D$	shear stress variations	Wind tunnel, random surface	Mulheam and Finnigan (1978)
$z_* = h + 1.5\ l_r$	wake diffusion effective	Wind tunnel, regular surface	Raupach et al. (1980)
$z_* = h + D$	horizontal inhomogeneity	Wind tunnel, regular surface	Raupach et al. (1980)
$z_* = 100\ z_0$	inertial sublayer considerations		Tennekes (1973)
$z_* \geq 3h$	horizontal inhomogeneity	Wind tunnel, regular surface	Sadeh et al. (1971)
$z_* = 3D$	non dimensional gradients of $\bar{u}$ and θ	field study, forest	Garratt (1980)
$z_* = 4.5\ h$	non dimensional gradients of $\bar{u}$	forest	Garratt (1978a)
$z_* = 3\ h$	non dimensional gradients of θ	forest	Garratt (1978a)
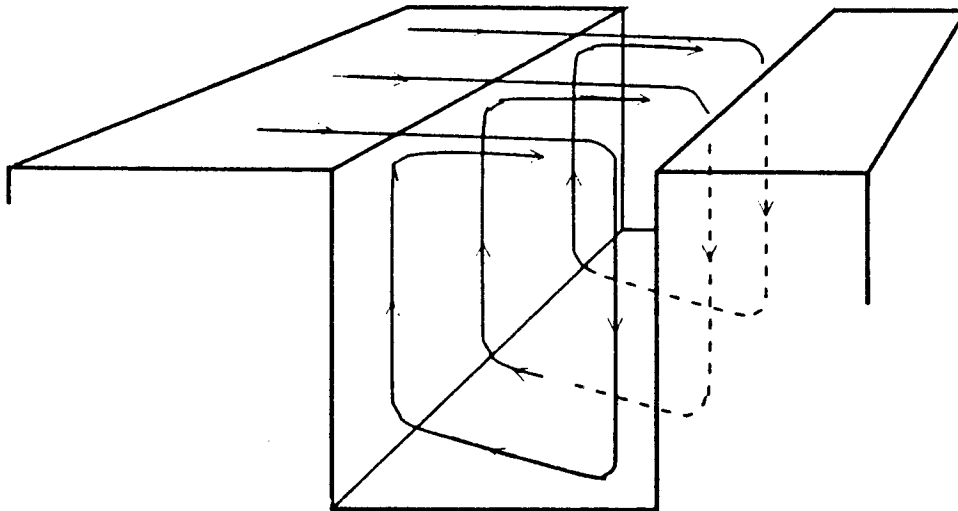
Figure 3.2   Schematic representation of a vortex within a street canyon. Adapted
from DePaul (1984).

3.2 The Roughness Sublayer

The roughness sublayer (RS) is, as mentioned above, the air volume just above the roughness elements, where the influence of individual elements can still be felt in the flow. One of the key problems with this layer starts with its definition or height range. Its lower boundary can be defined as the top of the CL ($z = h$) or , with respect to the wind profile of the inertial sublayer above, as $z = d + z_0$, where d is the displacement height and z_0 the roughness length (see Chapter 6). Its upper limit is physically the height $z = z_*$, where turbulent mixing has "merged" with the three-dimensional structure of the flow to an extent that horizontal variations vanish and the flow "sees" a homogeneous, rough surface. Note that for certain flow conditions the top of the RS is so high that an inertial sublayer cannot develop, or in other words the latter is "squeezed" between the RS and the mixed layer above. The height of the RS is dependent on the height of the roughness elements and their spatial distribution. Many suggestions have been made to express z_* as a function of the roughness element's height h and their separation distance D or the roughness length z_0. Some of these are compiled in Fig. 3.1. One difficulty in defining z_* arises from the fact that horizontal variability does not vanish at the same level for all properties. Table 3.1 lists several approaches for z_*, together with the criterion used and the type of experiment.

Wind tunnel studies provide a very good approach to investigate the character of horizontally averaged flow over surfaces with randomly distributed (e.g. Mulheam and Finnigan, 1978) or regularly arrayed (Antonia and Luxton, 1971; Raupach et al., 1980 and 1986) roughness elements. Here, profiles of mean wind speed show a smaller gradient than in the inertial sublayer. Thus, we have a layer where the eddy diffusivity K_m, defined through

$$u_*^2 = K_m \frac{\partial \langle \overline{u} \rangle}{\partial z'},$$

(3.4)

is considerably enhanced (u_* is consistently the value from the IS). This extra mixing in the RS is, at least partly, due to the superposition of turbulent wakes generated by individual roughness elements upon the shear flow. This general behaviour of horizontally averaged flow may not be observed at a single point (e.g. in the lee of a roughness element; see Raupach et al., 1980). Reynolds stress is found to decrease with height (larger negative values higher up) for most of the surfaces investigated (Antonia and Luxton, 1971; Mulheam and Finnigan, 1978; Raupach et al., 1980). This phenomenon is, however, attributed by most of the authors to erroneous measurements (see Chapter 7). The flow at different locations *along* the wind tunnel exhibits a self-preserving profile of the turbulence and velocity field increasingly with height over a rough surface. Hence, the turbulence structure is self-preserving even below the inertial sublayer (Raupach et al., 1986). Rather contradictory results are found when considering spectra of vertical and longitudinal velocity, respectively. While Mulheam and Finnigan (1978) report spectra of w (and partly of u) that collapse with inertial sublayer scaling for z ≥ 2h, Raupach et al. (1986) find the natural frequency to be much more appropriate. This indicates that the large structures (eddies of the size of the boundary layer depth) may dominate the energy distribution even in the roughness sublayer (see the discussion in Chapter 12). All results of these wind tunnel experiments were obtained in neutrally stratified flows.

In field studies, the RS has been widely studied over rough surfaces such as crop fields and forests. Gradients of mean wind speed have also been found to be smaller than in logarithmic profiles (e.g. Garratt, 1978b). This finding is consistent with wind tunnel results. The dimensionless gradients of momentum, heat and water vapour differ significantly from inertial sublayer predictions (Garratt, 1978a; Raupach, 1979). For most of the surfaces investigated it is found that

$$\Phi_i < \Phi_i^{IS}.$$

(3.5)

The extent of this departure (and sometimes even its sign) is, however, dependent on height and wind direction (Högström et al., 1989). Dimensionless gradients of wind speed and of temperature usually do not show the same departure from inertial sublayer predictions, especially at heights close to the rough surface (Garratt, 1978a; Högström et al., 1989). While Thom et al. (1975), Raupach (1979) and Denmead and Bradley (1985) report a dependence for $\Phi_m - \Phi_m^{IS}$ on stability, Garratt (1980) and Högström et al. (1989) find only a dependence on height (see Chapter 11 for a detailed discussion). The turbulence field close to a rough surface turns out to be quite intermittent (Shaw et al., 1983) and organized structures, such as repeated patterns in the time series of temperature and water vapour fluctuations can contribute more than 50% to the total transfer processes (Gao et al., 1989). Over different surfaces, the contributions of "sweeps" and "ejections" and "outward" and "inward interaction" (for their definition see Section 3.3) to the total momentum transfer can be substantially different.

The urban roughness sublayer (URS) is quite poorly understood at present. Most of the urban turbulence experiments are designed to avoid the URS (e.g. Clarke et al., 1982; Roth et al., 1989) or are restricted to turbulence intensities and non-dimensional velocity variances (e.g. Yersel and Goble, 1986). Högström et al. (1982) show spectra of longitudinal, lateral and vertical velocities respectively that were measured within an URS. These sparse possibilities for comparison will be discussed in detail together with the present results in the respective chapters below.

3.3 Conditional Sampling

From what was said in the foregoing section, it is clear that in a RS and CL turbulence is not locally governed (at least not entirely) and thus, gradient diffusion models are not likely to apply in these layers. Furthermore, there is some evidence (Finnigan,1979 a,b) that turbulence in the CL (and RS) is strongly influenced by coherent structures of larger scale from the overlying layers. A useful tool for investigating the nature and mechanisms of turbulent processes is the method of conditional sampling for Reynolds stress. Contributions to the total mean Reynolds stress originate from four different quadrants in the (u,w)-plane. Following Raupach (1981) they are termed as follows:

- outward interaction, $i = 1, u' > 0, w' > 0$
- ejections, $i = 2, u' < 0, w' > 0$
- inward interactions, $i = 3, u' < 0, w' < 0$
- sweeps, $i = 4, u' > 0, w' < 0$

Quadrants one and three give positive contributions and quadrants two and four negative contributions to the turbulent flux of momentum. Additionally, a hyperbolic hole H is defined (Fig. 3.3) excluding from the analysis a region of instantaneous values of $|u'w'|$ that are smaller than $H \cdot |\overline{u'w'}|$. Systematic variation of the hole size H allows the investigation of the contributions to the total Reynolds stress, whether they are large and sparse or small and frequent. If [··] denotes a conditional average, we have

$$[u'w']_{i,H} = \lim_{T_a \to \infty} \frac{1}{T_a} \int_0^{T_a} u'(t) \cdot w'(t) \cdot I_{i,H}(u'(t), w'(t)) \, dt \qquad (3.6)$$

where T_a is the averaging time and I the indicator function defined as

$$I_{i,H}(u',w') = \begin{cases} 1 & \text{if } (u',w') \text{ is in quadrant i and} \\ & |u'w'| \geq H \cdot |\overline{u'w'}| \\ 0 & \text{otherwise} . \end{cases} \qquad (3.7)$$

The stress fraction for quadrant i, $S_{i,H}$, is then

$$S_{i,H} = \frac{[u'w']_{i,H}}{\overline{u'w'}} \qquad (3.8)$$

and the time fraction, $\vartheta_{i,H}$, is the average of $I_{i,H}$ over the time period of interest

$$\vartheta_{i,H} = \overline{I_{i,H}(u',w')} \qquad (3.9)$$

Note that through (3.8) the sum of $S_{i,0}$ for i = 1,4 is one. Different quantities can be defined from the stress fractions. The difference ΔS_H between sweeps and ejections

$$\Delta S_H = S_{4,H} - S_{2,H} \qquad (3.10)$$

or their respective ratio

$$\gamma = \frac{S_{2,0}}{S_{4,0}} \qquad (3.11)$$

at hole size zero. Exuberance E (Shaw et al. 1983) is defined through

$$E = \frac{S_{1,0} + S_{3,0}}{S_{2,0} + S_{4,0}} \qquad (3.12)$$

Raupach (1981) points out that the stress fraction $S_{i,H}$ is related to the probability distribution of u' and w'. If $p(\hat{u}, \hat{w})$ is the joint probability density function of the rescaled velocity components

$$\hat{u} = \frac{u'}{\sigma_u}, \ \hat{w} = \frac{w'}{\sigma_w} \qquad (3.13)$$

and

$$R_c = \frac{\overline{u'w'}}{\sigma_u \sigma_w} = \overline{\hat{u}\,\hat{w}} \qquad (3.14)$$

the correlation coefficient, we find

$$S_{i,H} = \frac{1}{R_c} \int \int_{-\infty}^{\infty} \hat{u}\,\hat{w}\, p(\hat{u}\,\hat{w})\, I_{i,\rho H}(\hat{u}, \hat{w})\, d\hat{u}\, d\hat{w}. \qquad (3.15)$$

Furthermore, $p(\hat{u}, \hat{w})$ is completely specified by an infinite set of statistical moments (Raupach, 1981):

$$M_{jk} = \overline{\hat{u}^j\,\hat{w}^k}, \qquad j,k = 1,2,3,\dots \qquad (3.16)$$

and therefore such a set of moments also determines $S_{i,H}$. Raupach (1981) shows that $\Delta\,S_H$ can be described by a set of third order moments (j +k =3) and the special case of a hole size equal to zero will be adapted here (for detail see Raupach, 1981)

$$\Delta\,S_0 = \frac{1 + R_c}{R_c\,\sqrt{2\pi}}\left[\frac{2\,C_1}{1 + R_c^2} + \frac{C_2}{1 + R_c}\right] \qquad (3.17)$$

where

$$C_1 = (1 + R_c)\left(\frac{1}{6}(M_{03} - M_{30}) + (M_{21} - M_{12})\right)$$

$$C_2 = -\left(\frac{1}{6}(2 - R_c)(M_{03} - M_{30}) + (M_{21} - M_{12})\right) \qquad (3.18)$$

Thus, third order moments give important information about distinguishing the difference between sweeps and ejections.
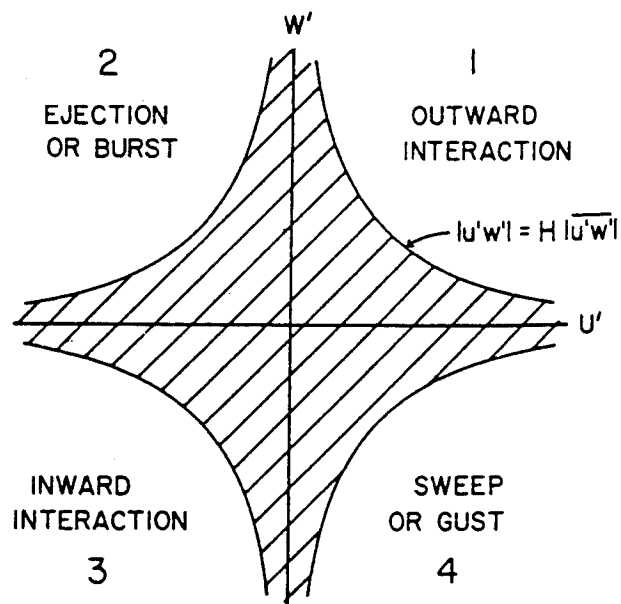

Figure 3.3   The definition of a hyperbolic hole in the u' - w' plane. Adapted from Shaw et al. (1983)

MEASUREMENTS

4. Case Study in the City of Zurich

Turbulence within and above an urban canopy layer was studied experimentally as a *case study* in the city of Zurich, Switzerland. This type of surface with its horizontal variability would require a dense network of observations in order to resolve the three dimensional structure of the flow and turbulence (e.g. Schmid and Oke, 1990), and the approach adopted here should be viewed as a first step in the direction of a deeper understanding of the processes contributing to turbulence in such an environment. These turbulence measurements were part of a larger scientific programme in urban climatology that consisted of:

- a network of 25 wind speed and wind direction sensors spread over the whole city and its surroundings (some stations also equipped with temperature and humidity sensors). Each of them was mounted some 5 m above the ambient roof level. It was designed to yield information on the mesoscale wind field close to the urban surface (Schuhmacher, 1991),

- three additional "mobile" wind and temperature stations, used to close gaps in the network for the specific investigation of local wind systems (Mazzoni, 1988),

- a "semi-mobile" 10m tower, equipped with four levels of wind speed and temperature sensors and one level of wind direction sensors, mounted for a certain time at three distinctly different sites of the city (commercial, industrial and residential) in order to study the variability of the mean vertical structure in the first few meters above roof level (Schädler, 1988), and

- last but not least, the "central station" of the network that will be described in detail below. The measurements from this site are the subject of analysis of the present study.

4.1 The Site

The city of Zurich is surrounded by some moderately high hills (about 200 - 400m higher than the city center). This topography is responsible for the mesoscale features of the flow over the city, together with the lake to the SE of the urban area (Schuhmacher, 1991). The site ("Anwand") is located in the center of the flat part of the urban area with no distinct terrain elevation within a radius of about 2 km (Fig. 4.1).

This part of the city is mixed residential / commercial area that can be considered typical for a *European* city. Blocks of buildings, a few small parks and schools, streets and squares can be found in the close vicinity. Buildings are fairly regularly distributed within the the closest ~ 300m and do no vary significantly in height (~20m). A plan

view of the site is given in Fig. 4.2. For the distribution of the building heights over the city see Fig. 4.3. The setup for the measurements consisted of two towers: one of them, located on the top of a five-story building, was 20m high and the other, erected on a "bridge" over the street next to that building, ranged from 5.5m above street level to the height of the lowest level of the roof tower. The whole experimental setup is shown schematically in Fig. 4.4. Figs.4.5 and 4.6 show photographs of the two towers to give a visual impression of the site.
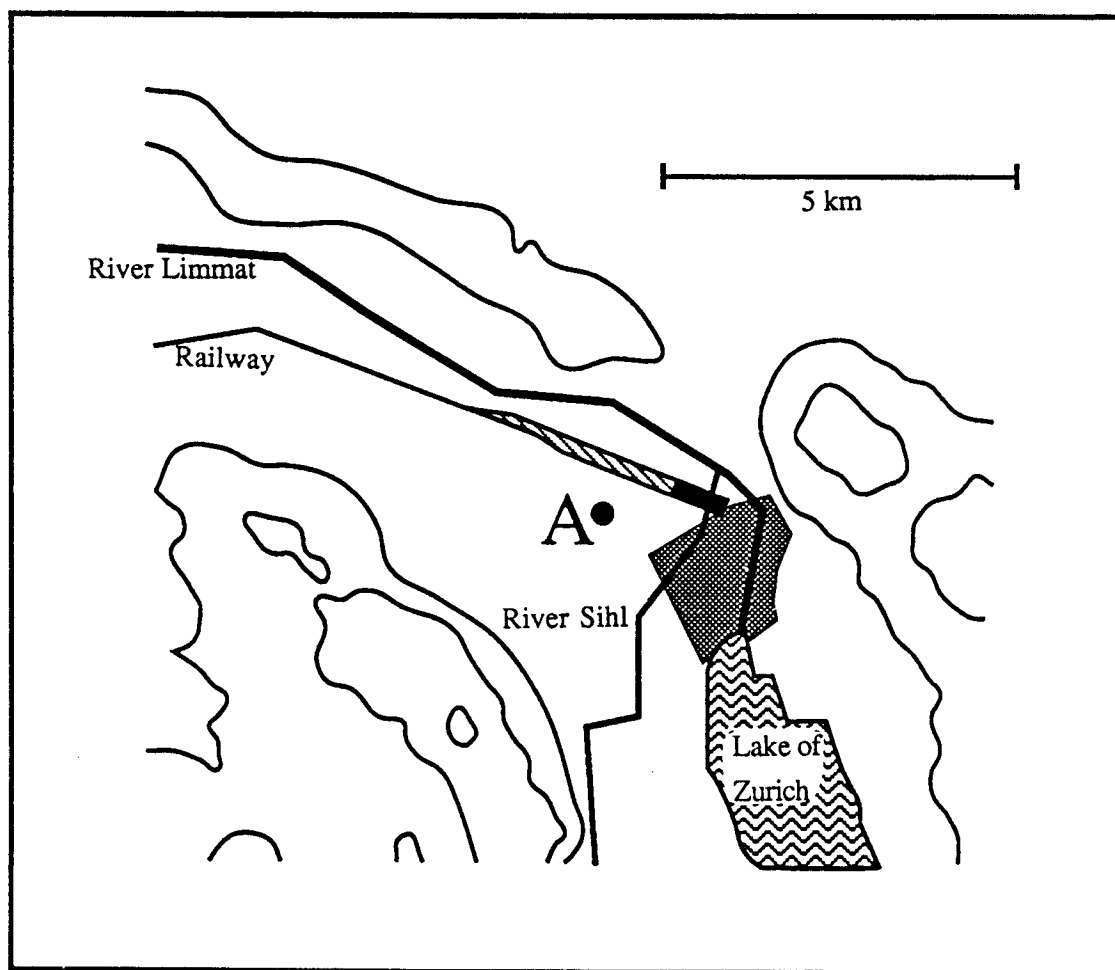

Figure 4.1   Schematic map of Zurich showing the Anwand site (A) and the city center (dark hatched). The surrounding hills are indicated by the solid (topographic) lines.
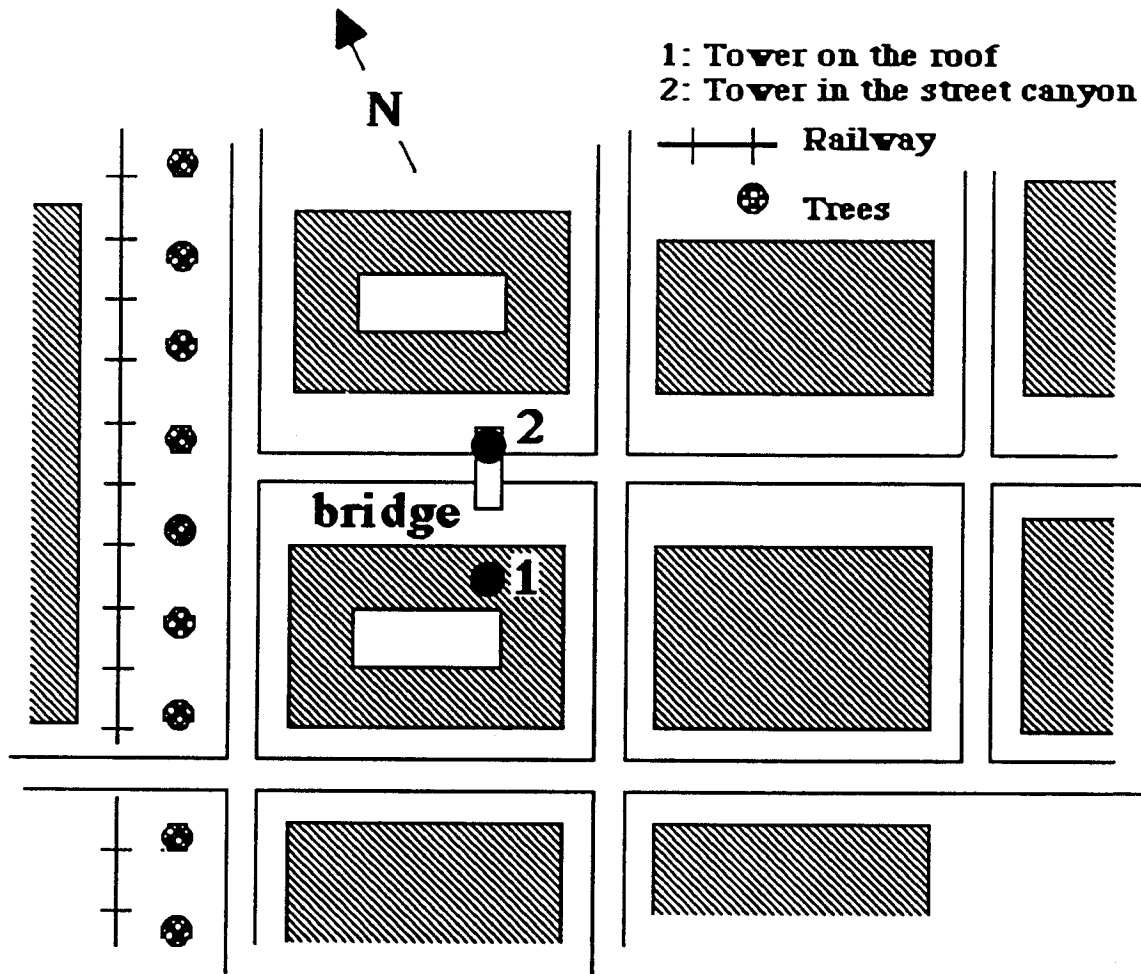
Figure 4.2   Plan view of the site where the measurements were taken.

4.2 Instrumentation

The roof-top tower was equipped with four levels of cup anemometers and one wind vane at 10m (Fig. 4.4). Temperature and specific humidity (i.e. dew point) was measured regularly at two levels (3m and 20m) and for certain time periods at three or four levels. For a detailed description of the instruments, calibrations (and specific problems) see Appendix A1. The tower's layout had the form of a triangle with a side length of 0.5m up to a height of 12m and from there to the top with a side length of 0.25m (see Fig. 4.5). The instruments were mounted on booms with a diameter of 0.04 m at a distance of 1.1m from the tower (at the top level, these distances were 0.25m larger). The levels were 3, 5, 10 and 20m, respectively above the roof.
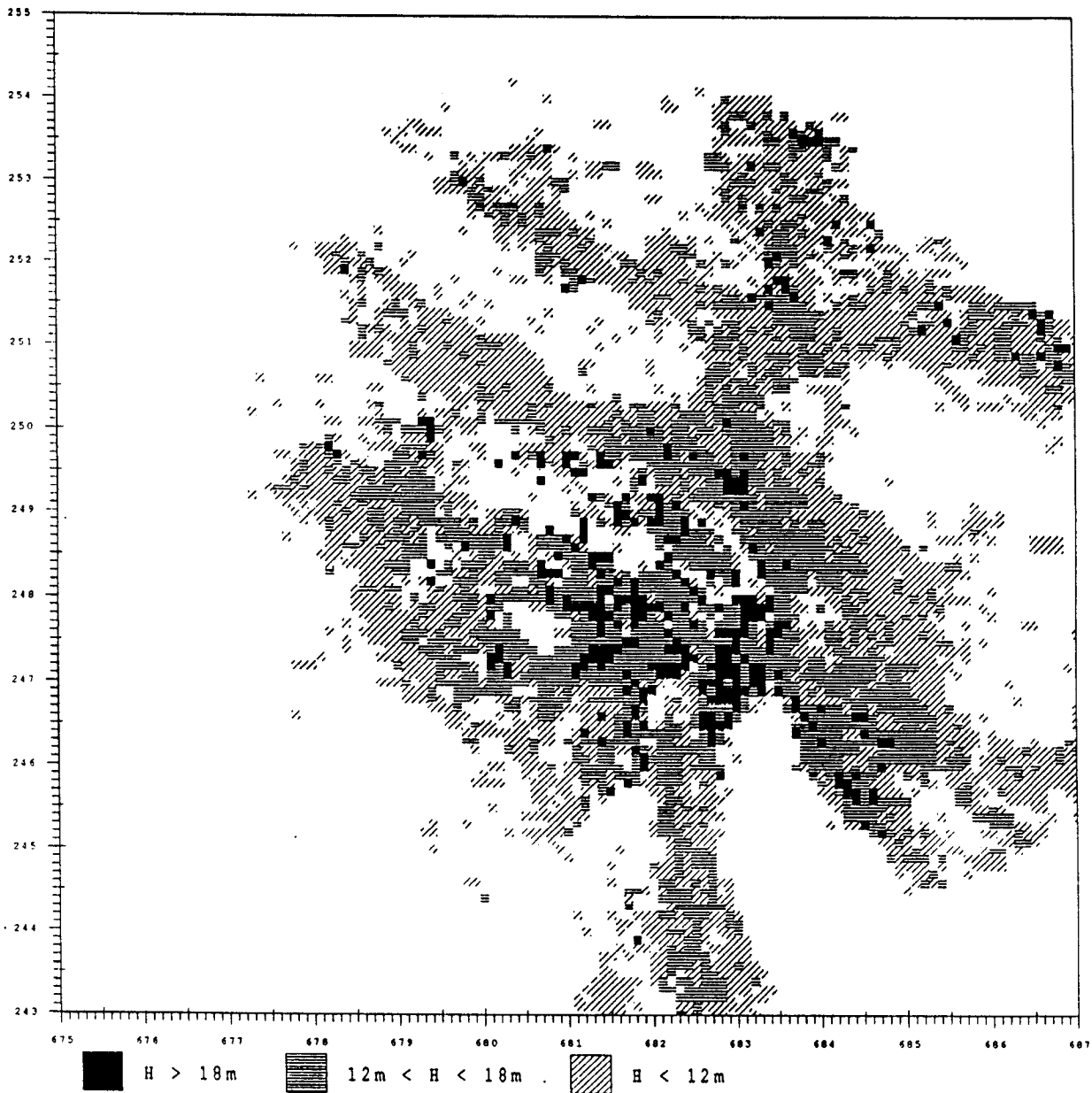
Figure 4.3   Distribution of building heights over the city of Zurich. White areas indicate "no information", i.e. no buildings are located within the respective spot (lake, forests, etc.).
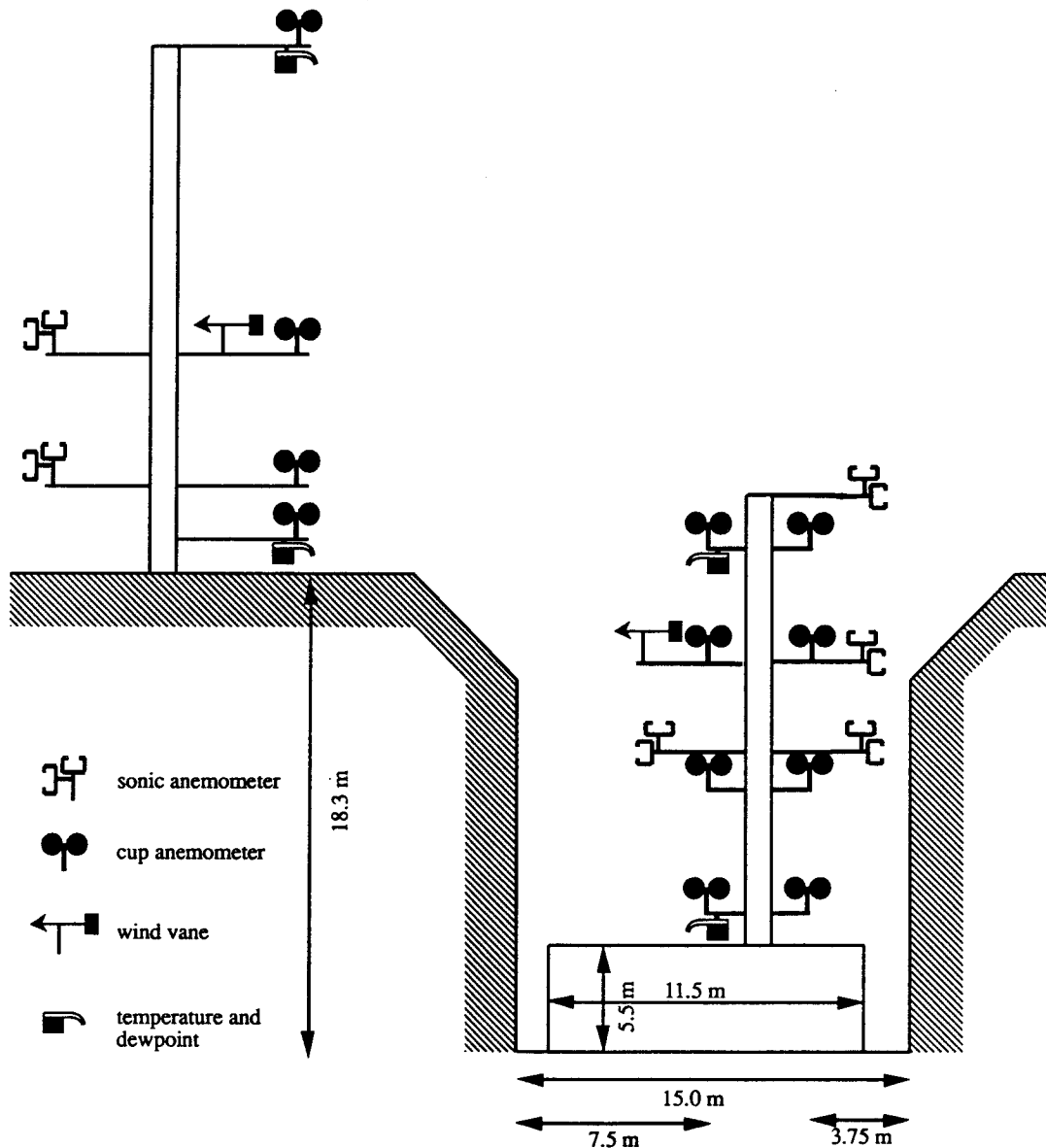
Figure 4.4   Schematic view of the site. The symbol for "sonic anemometer" denotes all (but not simultaneously) realized positions of measurements.

The tower within the street canyon was mounted on the "bridge" in such a way that two profiles of mean wind speed could be measured, one in the middle of the canyon and one (termed "wall profile") in a distance of three quarters of the canyon width from one of the walls (see Fig. 4.4).This tower had a rectangular shape with a width of 1.5m (cross canyon). Instruments were also mounted on booms of 0.04m diameter at a distance of 0.9m from the tower. The levels for wind speed measurements were 7.7, 12.2, 16,7 and 21.3m above street level on each side of the tower. The height of the top level corresponded to the lowest level on the roof-top tower. Temperature and specific humidity were observed regularly at the 7.7m and 21.3m levels of the middle profile. For a short period of time an additional temperature/humidity sensor was

mounted within the canyon at 14m. A wind vane was mounted at the 16.7m level of the middle profile.

The turbulence measurements were performed with two sonic anemometer systems. During the various stages of the study, they were mounted either at two levels on the roof-top tower, one at each tower, or both at the canyon tower (see below).

The performance of the instruments is discussed in detail in appendices A1 (profile instrumentation) and A2 (sonic anemometers). All required information on the type of the instruments, their calibration(s) and how the specific problems were handled can be found there.
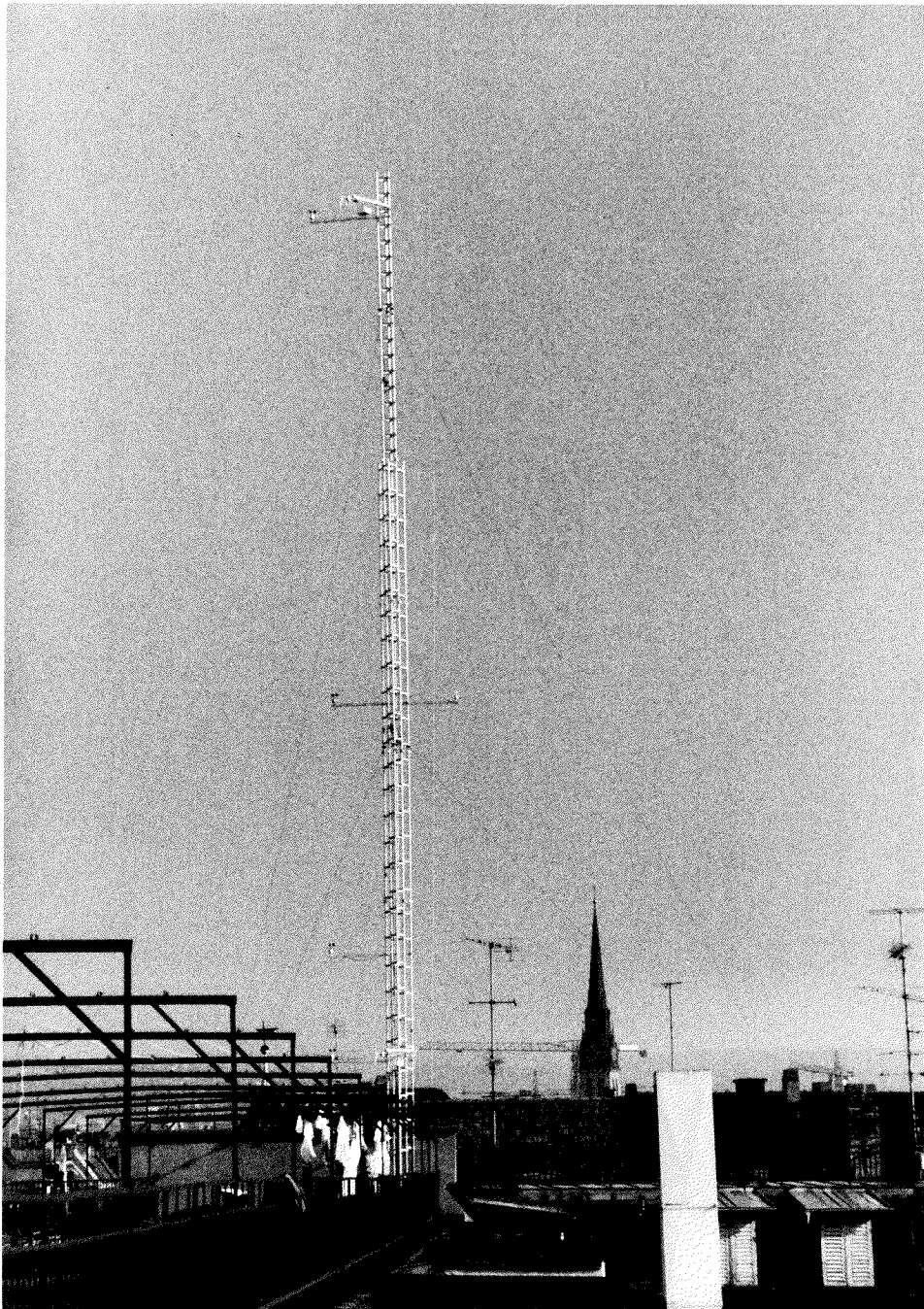

Fig. 4.5   The roof top tower

4.3 Measurement Programme

All measurements were taken between November 1986 and May 1988. Wind speed and wind direction were recorded throughout this period with some short interruptions. Table 4.1 lists the duration of the different configurations of the continuous temperature and humidity measurements at the two towers. Note that because of various problems with the dew point hygrometers, the actual amount of usable data is for certain periods considerably smaller than indicated in Table 4.1.

Table 4.2 shows date, configuration and number of obtained intervals of the various turbulence observations. The number of obtained intervals refers to the number of continuous measurements during a period of duration T_a, where T_a is the averaging period (see Section 5.1).

Figure 4.6   The tower within the street canyon.

Table 4.1:   Configurations of temperature and humidity measurements and their respective duration

Year	Days: from - to	Positions* of temperature observations	Positions* of dew-point observation
1986	210 - 300	campus**	campus**
1986	310 - 336	5, 8, 9, 12	5, 8, 9, 12
1986	338 - 341	5, 9, 12	5, 9, 12
1986	343 - 365	5, 8, 9, 12	5, 8, 9, 12
1987	1 - 222	5, 8, 9, 12	5, 8, 9, 12
1987	223 - 224	5, 8, 9	5, 8, 9
1987	225 - 232	5, 8, 10	5, 8, 10
1987	247 - 272	5, 6, 8, 9	5, 6, 8, 9
1987	274 - 365	8, 9, 11, 12	8, 9, 11, 12
1988	1 - 68	5, 8, 9, 12	5, 8, 9, 12
1988	70 - 99	5, 8, 9, 10, 12	5, 8, 9, 10, 12
1988	99 - 137	5, 9, 10, 11, 12	5, 9, 11, 12
1988	137 - 147	10, 10, 10, 10, 10 **	10, 10, 10, 10 **

*   "Positions" as shown in Fig.9.1
**   relative calibration period

Table 4.2   Configuration and duration of turbulence observations at the Anwand site.

No	3D Sonic		2 x 2D Sonic		Number of 50-Min. runs**		Date
	Position*	Height ab. street	Position*	Height ab. street	3D	2D	
1	10	23.3	10	23.3	15	3	10/11.03.87
2	10	23.3	10	23.3	15	15	16.06.87
3	11	28.3	10	23.3	4	4	7.10.87
4	11	28.3	10	23.3	4	4	5.11.87
5	4+	23.3	10	23.3	6	6	8/9.12.87
6	4+	23.3	2	13.0	11	11	16/17.3.88
7	3	16.7	2	13.0	3	3	23/24.3.88
8	3	16.7	2	13.0	9	9	27/28.3.88
9	3	16.7	2	13.0	1	1	29.3.88
10	6	13.0	2	13.0	15	15	4.-6.4.88
11	11	28.3	10	23.3	25	25	15.-25.4.88
13	11	28.3	10	23.3	15	15	6/7.5.88

*   as defined in Fig. A3.1
**   not yet subject to any rejection (due to errors, unstationarity,...)

5. Data Validation

5.1 Averaging Time

It has been shown in 2.1.3 that the averaging time T_a plays a crucial role in determining whether or not a turbulence time series may be considered stationary. In relation to atmospheric turbulence, the upper limit for T_a lies somewhere between 2 and 3 hours. Its optimal length, however, depends strongly on the process under consideration. Lumley and Panofsky (1964) give an estimate of the possible statistical uncertainty (error), introduced through the choice of a certain averaging time. It takes the form

$$T_a = \frac{2\tau_i \overline{\varphi'^2}}{a^2 \overline{\varphi^2}},$$ (5.1)

where T_a is the averaging time required to determine the mean quantity $\overline{\varphi}$ to an accuracy a, $\overline{\varphi'^2}$ is the ensemble variance of φ about its ensemble mean and τ_i is the integral time scale of φ. Wyngaard (1973) points out that "a" may not only be a measure of the error introduced through unstationarity, but in general through "non ideal" circumstances. Using equation (5.1) and a number of runs, the optimal T_a was found to be of the order of one hour for the present experiments.

The actual choice for T_a, however, was determined by another constraint. The data logger used to store the sonic data did not allow a continuous registration of more than approximately 100 minutes. After this time, the tape had to be spooled back and ca. 2 minutes of data were lost. In order to obtain as many uninterrupted time series as possible, it was decided to choose $T_a = 50$ minutes as an averaging interval.

5.2 Run Test

A proper averaging interval may be a necessary, but is never a sufficient condition to obtain stationary time series. As a test for stationarity, a run test (Bendat and Piersol, 1986) has therefore been applied to every averaging period (and component). The variance[1] is calculated in this run test, the averaging period is subdivided into a number of sub-intervals. For each of these sub-intervals, as well as for the whole

---

[1] Strictly speaking, all statistical moments would have to be tested with the same procedure since stationarity requires time independence of statistical moments. For the present study, the run test was only applied for the second order moments.

averaging period and each sub-interval variance $(\sigma_1, \sigma_2, ...)$ is checked to determine whether it is smaller or larger than the variance for the whole averaging period $\overline{\sigma}$. If $\sigma_1 \geq \overline{\sigma}$ and $\sigma_2 \leq \overline{\sigma}$ (i.e. if the sign of $(\overline{\sigma} - \sigma_i)$ changes for two subsequent sub-intervals) the run test index RI is augmented by one, and otherwise unaltered. Depending on the number of sub-intervals, a range for RI (RI_1, RI_2) can be calculated, within which the hypothesis, that the time series is unstationary can be rejected with a certain confidence level. Thus, if $RI_1 < Ri < RI_2$, the time series may be considered stationary. If either, $RI < RI_1$ or $RI > RI_2$, processes of significantly different time scales than the chosen averaging time dominate the time series. Due to the fact that the second order moment was chosen for the run test (see above), it was possible to detect whether or not the sub-intervals may be treated as "random observations". It was, however, not possible to detect possible trends within an averaging period. Therefore, each time series was "detrended" (linearly) before applying the run test.

5.3 Rejection of Data

Before being included in the analysis, each data point was routinely checked for physical plausibility and other causes of possible rejection. The criteria will be outlined in the following. Further constraints (e.g. the rejection of near neutral runs for certain applications) will be noted where necessary in the respective chapters.

5.3.1 Profile Data

In general, the profile data did not give much cause for rejection. This is however only partly true for the dew point (specific humidity) measurements. The following checks on physical plausibility were performed:

- Cup anemometer readings were tested for sudden drops to zero. This could happen either due to snow deposition on the cups or a failure in the electric circuit. Data were excluded from the analysis when smaller than 0.5 ms^{-1} (the threshold speed of the instruments)

- The temperature measurements only had to be tested for a failure in the electric circuit (e.g. wet cables). Physically meaningless data at a certain height could easily be detected by checking the gradients.

- Dew point data were most problematic. Due to the effects of improper mirrors and electrical problems, many hours of data were lost. Dew point measurements had to be rejected if they either read higher than the corresponding temperature measurement (!) or if one of the sensors showed a completely different daily course than all the others

5.3.2 Turbulence Data

For each run (i.e. an averaging period of 50 minutes) the following was tested:

a) Stationarity

Using the run test, each component was checked for stationarity. In the analysis for e.g. $\sigma_v/u*$, a run was included if the u-, v- and w-components passed the run test, irrespective of the stationarity of the temperature time series.

b) Error

In analogy to (5.1), the error due to "non-ideal conditions" was calculated for $\overline{u'w'}$, $\overline{v'w'}$ (both sonics) and $\overline{w'\theta'}$. The simplified form of (5.1) was used (after Wyngaard, 1973):

$$a^2_{\overline{u'w'},\overline{v'w'}} = \frac{z}{T_a\bar{u}}(\frac{\overline{(u'w')^2}}{u_*^4} - 1) \tag{5.2}$$

$$a^2_{\overline{w'\theta'}} = \frac{z}{T_a\bar{u}}(\frac{\overline{(w'\theta')^2}}{u_*^2\theta_*^2} - 1) \tag{5.3}$$

where T_a is the averaging period. If all errors were smaller than 25% a run was included.

c) Wind direction

The wind tunnel investigation of the sonic anemometers showed that certain angles of attack (with respect to the instrument's geometry) led to irreproducible and strongly distorted readings (see Appendix A2). If the mean wind, either at the roof top tower or within the canyon (depending on the sonic's position), was such that the flow approached the sonic with an angle of attack of $180° \pm 30°$ (see Appendix A2 for the definition of the angle), the run was excluded from analysis.

The influence of the tower itself on the measurements (i.e wind direction such that the instrument lies in the wake of the tower) was also tested. It turned out, however, that the results were insensitive to this restriction. Therefore, no runs were excluded because of tower shadowing.

d) 2x2D Sonics

Electronic problems with the 2D sonics resulting in sudden "outbursts" are outlined in Appendix A2. Although a correction was shown to be possible, runs were excluded

if the cumulative number of "outbursts" (the sum for all three components) exceeded 10.

5.4 Calculation of Spectral Estimates

The spectral representation of a time series may be obtained through the Fourier transform of its auto-correlation function or, equivalently (since the auto-correlation function is even), by taking the modulus square of the (complex valued) Fourier transform of the time series itself. It can be shown (e.g. Stull, 1988) that this latter definition corresponds to multiplying the Fourier transform of the time series by its complex conjugate. Similarly, the *cross spectrum* G of two time series A and B can be defined as

$$G_{AB}(n) = F[A(t)]^* \cdot F[B(t)]$$
$$= Co(n) + Q(n),$$

(5.4)

where $F[\ ]$ stands for the Fourier transform, n is the natural frequency and * denotes the complex conjugate. Since the correlation function of A and B is not even, the cross spectrum consists of a real part, the *cospectrum* Co and an imaginary part, the *quadrature spectrum* Q.

To use standard Fast Fourier Transform (FFT) routines, one is advised to set the number of data equal to an integer power of two. Thus the averaging time for the calculation of the spectra was chosen as 3328 seconds (approximately 55 minutes), the absolute maximum possible with respect to the problems discussed in Section 5.1. The series were then supplemented with zeros to yield a 4096 point time series. This so-called 'zero padding' is an often used approach to treat end effects due to non periodicity of real time series. In terms of the auto-correlation function, the additional zeros ensure that time lags smaller than 768 seconds (=4096-3328) are unspoiled by end effects. Before applying the FTT, the data set were subjected to a Parzen window.

The resulting spectral estimates were block-averaged into 32 "frequency bands", approximately equidistant in the frequency domain (Kaimal and Gaynor, 1983). Thus the high frequency range of the resulting spectral curves (the average spectral density calculated from many frequencies) shows much less scatter than the low frequency range. Due to the zero padding of the time series (see above) the lowest frequency was not included into the analysis.

RESULTS

Since the urban roughness sublayer and the canopy layer are poorly investigated, the results of the present measurements will be presented and discussed under different aspects. As a background, profiles of mean variables, averaged over characteristic time periods (e.g. "spring" or "all year") are shown in Appendix A3. The turbulence characteristics are presented as profiles covering the whole height range of observations from the mid canopy to the uppermost sonic level (10 m above roof), as long as the property under consideration is meaningful at all heights in both layers. If this is not the case (e.g. the dimensionless wind shear is not meaningful within the canopy) only the measurements from levels within the layer of interest are discussed. For the roughness sublayer, a method widely used in bio-meteorology has been adapted: although acknowledging that the semi-empirical relationships derived from similarity arguments and experimental evidence in the *inertial sublayer* cannot be expected to hold, turbulence statistics are compared to the latter. The *departures* from the inertial sublayer formulations can then be used to characterize the turbulence in the roughness sublayer. The scaling variables used (e.g. u_*, θ_* and L) are either the local values at the height under consideration (suggested by Högström et al. (1982) to be appropriate for an urban roughness sublayer), or an estimate of the respective inertial sublayer property.

It was pointed out in Chapter 3 that horizontally-averaged variables are needed in order to obtain valuable and consistent results. In the present observations, more than one position in the xy-plane has been measured only at two heights (5m above roof level and 13m above street, respectively). These two positions certainly do not yield the required horizontal averages. It can be argued, however, that for different wind directions, a fixed instrument on a boom represents a variety of horizontal positions relative to the respective upwind (and downwind) geometry if there is no predominant wind direction because of channeling of the flow due to topography or other processes. Since this is not the case at the present site, it is assumed that, as a first order approximation, the horizontal average can be replaced by an average over all wind directions.

An overview over all positions of measurements together with their respective height above street level is given in Fig. A3.1, which is reproduced in this paragraph for convenience. For simplicity, the measurement levels are numbered as depicted in Fig. A3.1.
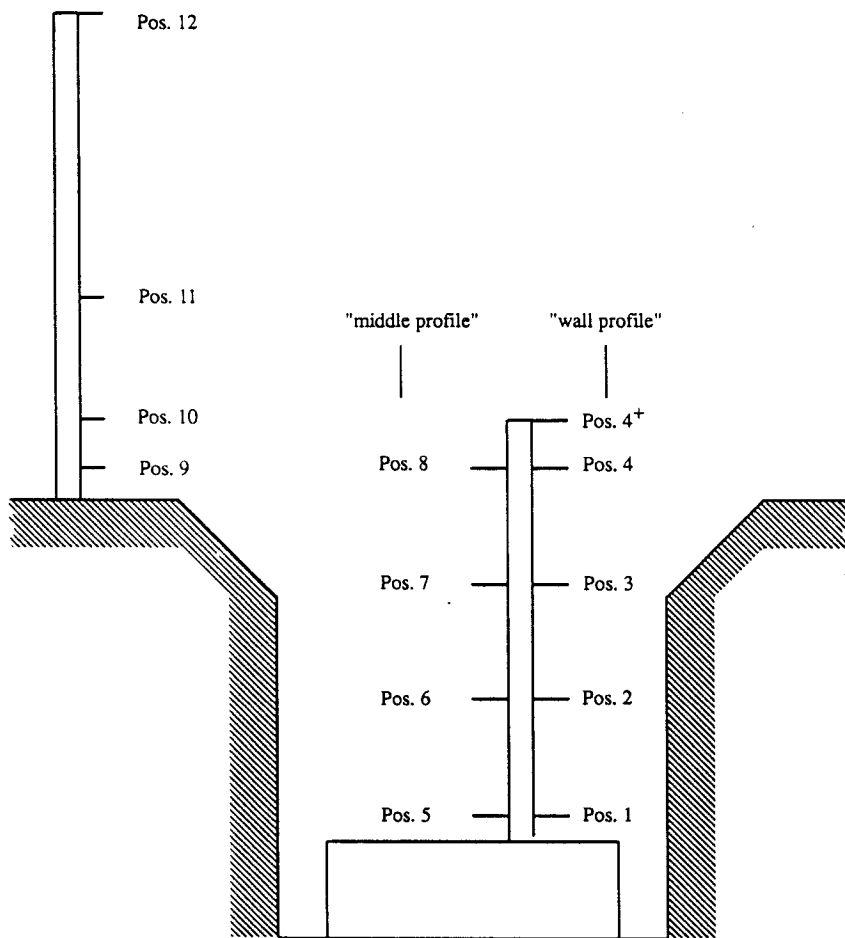
Figure A3.1   Schematic view of the Anwand site showing the definition for the
various positions (Pos.) of measurement with their respective numbers.

6. Zeroplane Displacement Height and Roughness Length

6.1 Zeroplane Displacement

The height of the measurement above the surface is of great importance for "ideal" surface layer (SL) experiments , because the earth's surface is the natural boundary of the air flow. For homogeneous fetch conditions, it is no problem to determine this measurement height. However, the problem becomes more serious for complex terrain, especially if there is no clear regularity as in a (European) urban area. From many studies over vegetated areas (such as crop or forest) the concept of an elevated "zeroplane" is known, and has been widely used with success (cf. e.g. Lettau 1969; Thom 1975). This concept states that if the vertical scale of the roughness elements exceeds a certain value that is dependent on their density, the flow behaves *as if* there were a (physical) boundary at a height z=d, where d is called the zeroplane displacement. This zeroplane displacement must clearly be greater than zero and in general not greater than the average height of the roughness elements in the upwind fetch. If the roughness elements in this *source area* for the measurement (as defined by Schmid, (1988) as the surface area that influences a measurement at a certain height) are not uniformly distributed and of different heights (non uniform fetch) the applicability of the zeroplane displacement concept is quite questionable. This is obvious in the case of an urban environment, where built up areas are surrounded by parks, open water etc., but also divided by streets, gardens and so on. Interpreting the zeroplane displacement height as the level of mean momentum absorption (Thom, 1971), i.e. looking at d in terms of the flux-gradient relation for momentum, will not necessarily be possible in such an environment. On the other hand, it is clear that also in complex terrain (i.e. in an urban RS) some "zeroplane" or reference level is required, since the height above the "surface" remains an important variable for the RS flow. For convenience, we will call the reference level in the urban RS zeroplane displacement too. In the following, the physical meaning of d is outlined, methods (and their problems) of determining d are discussed and a method is presented to find a reference level in the urban RS.

6.1.1 Physical Meaning of the Zeroplane Displacement

At first glance, d can be interpreted purely as a statistical best-fit *parameter*, that serves to extend the description of the steady, homogeneous SL to field conditions where the surface is covered with uniformly distributed roughness elements (such as in a crop field or a forest). In this context it is important to note that every surface can be characterized by such a distribution of roughness elements of a certain height h, and what is usually called "homogeneous, undisturbed flat terrain" (e.g. desert, calm waters) is nothing more than a case in the limit h ---> 0. This extension of the commonly used SL concept reflects the fact that the height above "ground" is an important SL scaling factor , which indicates the size of the largest (energy containing) eddies. If the roughness elements are not rigid (like trees or crop) or their density is rather small (as in the case of houses), it seems that this "virtual surface" lies well within the canopy, in its upper part (cf. e.g. Garratt (1978a), who found $d \approx 0.75$ h for a savannah type surface). This is equivalent to the finding that large eddies can to a certain extent penetrate the canopy.

Alternatively, Thom (1971) has shown for an artificial crop field in a wind tunnel experiment that the zeroplane displacement height can be identified as the level of mean momentum absorption by the rough surface (Raupach, 1979). This concept is consistent with the interpretation of $(d+z_o)$ as the height of a virtual momentum sink, since $u(d+z_o)=0$ by definition (Thom, 1971).

All these considerations on the concept of zeroplane displacement are based on the assumption that i) d is a property of the underlying surface and ii) the height of the zeroplane can be determined from wind profile or momentum absorption measurements alone and can therefore also be used to describe profiles of turbulence or mean properties of heat and water vapour. Hicks et al. (1979) raised the question (in contrast to the above statements) whether different values for d_M, d_H and d_E should be taken into consideration, in order to describe the flux-gradient relations for momentum, heat and water vapour consistently with the formulations for ideal terrain. This means that they assume that not only the flux-gradient relations (equations 2.26, 2.32 and 2.33, respectively), but also the constants in these formulations determined for ideal sites are valid and d_M, d_H and d_E are used to fit the experimental data to those equations. In other words, they state implicitly that there is no RS above very rough terrain and SL similarity can be used to describe the flow over such terrain. This implies, however, that d would have to be a function of height (as can be deduced from results by Garratt, 1978a), in order to make the flux-gradient relations obey their "ideal formulations" (e.g. Businger,1971, or Dyer and Hicks, 1970). Such a height dependence would

make it very difficult to find a physical interpretation of the zeroplane displacement, especially since the length scale z' (see equation 6.1) would become height dependent itself.

If we consider an experimental situation with a very homogeneous distribution of roughness elements which have varying thermal properties (e.g. large, irregularly distributed spots of "black sand" among the white one) over a very large fetch (a sandy desert, say), the concept of Hicks et al. (1979) would then lead to a value $d_M \approx 0$ and $d_E \approx 0$ but d_H would certainly become much larger than zero (in order to fit the data to the "ideal" flux-gradient relations). This shows that d_H in this case would be nothing more than a correction parameter (function) with no physical meaning. And it would clearly be no "height" as a level at which an important physical process takes place. Due to the lack of better knowledge it is often assumed that $d_M=d_H=d_E$ for all properties momentum, sensible heat and water vapour.

6.1.2 Commonly Used Methods to Determine the Zeroplane Displacement

Since it is common in SL work to describe fluxes in terms of profiles of mean quantities (flux-gradient-relations, see Chapter 2), the zeroplane displacement is often determined from the mean wind profile. Instead of equation (2.28) we consider the wind profile for neutral conditions

$$u(z) = \frac{u_*}{k} \ln\left(\frac{z'}{z_o}\right) \tag{6.1}$$

with

$$z' = z-d$$

and d is the zeroplane displacement that is defined as the the "true reference level of the logarithmic law" (Lettau, 1969) and can be determined from wind speed measurements at different levels. Various methods for the determination of d from wind profile measurements have been proposed (Lettau, 1957; Stearns, 1970; Lo, 1977) for "only neutral" cases or general stability. They all have in common that a certain minimizing procedure is applied when comparing measured profile data with (6.1), thereby using a set of estimates for u_*, z_o and d. Two main problems arise from this approach:

- two length scales, z_o and d, have to be determined from the same profile. This makes the "partition" between the two heights in some cases quite arbitrary. This especially when the profiles are not necessarily well behaved (e.g. in an urban RS, as in the present study).
- the logarithmic form of (6.1) is very sensitive to small deviations from the "ideal" values of wind speed. This can be seen through the following example: If one

calculates a wind profile by (6.1) with prescribed values of u_*, z_0 and d and then varies the wind speed of any level by a small amount (the uncertainty of a wind speed measurement, say), the possibility is very small to find more or less the prescribed values of u_*, z_0 and d from this "data set" by these methods.

The above procedures can therefore only be applied in a statistical sense: as many profiles as possible have to be considered, as long as they refer to the same source area. Since all surface properties in an urban area (i.e an irregular, complex terrain) are dependent on i) wind direction and ii) the source area (Schmid, 1988), which is related to the measurement height and therefore difficult to define, the requirement of many profiles corresponding to the same situation is very hard to meet. In a recent study, Schädler (1988) evaluated from wind profile data of a mobile 10m tower in Zürich u_*, z_0 and d according to those "profile methods". It was found that within the RS (and even if neutral conditions can be assumed) the profiles show large departures from the logarithmic form (6.1) for certain wind directions. The shapes of the profiles seem to be influenced very locally (but show a similar behaviour within certain sectors of wind direction). For sectors with "well behaved" profiles the evaluated values of z_0 and d lie between 0 and 4m below roof level in areas with mean building heights of the order of 20 m. This indicates that the ratio d/h is larger than about 0.7 for the building structures considered here.

Another method has been suggested to determine the zeroplane displacement height in terms of the geometrical properties of the upwind fetch. In a wind tunnel, Counihan (1971) systematically varied the distribution and number of roughness elements and fitted an empirical curve for d/h as a function of A_r/A (where h is the height of the roughness elements, A the total area and A_r the area covered with roughness elements). A similar curve can be found from the results of Kutzbach (1961), who evaluated d from experiments with different distributions of bushel baskets on a frozen lake surface. Fig. 6.1 gives a comparison of the two approaches after Clarke et al. (1982). It can be seen that the two experiments yield quite different results, especially in the region of lower roughness element density. Note that both studies determine their respective "reference d value" (in order to fit the empirical relationship to the surface geometry) by means of the logarithmic form of the wind profile. This can be done if profile measurements are available up to heights $z \gg z_0$ or $z > (2-4)h$ (see Chapter 3), which was the case in both studies.
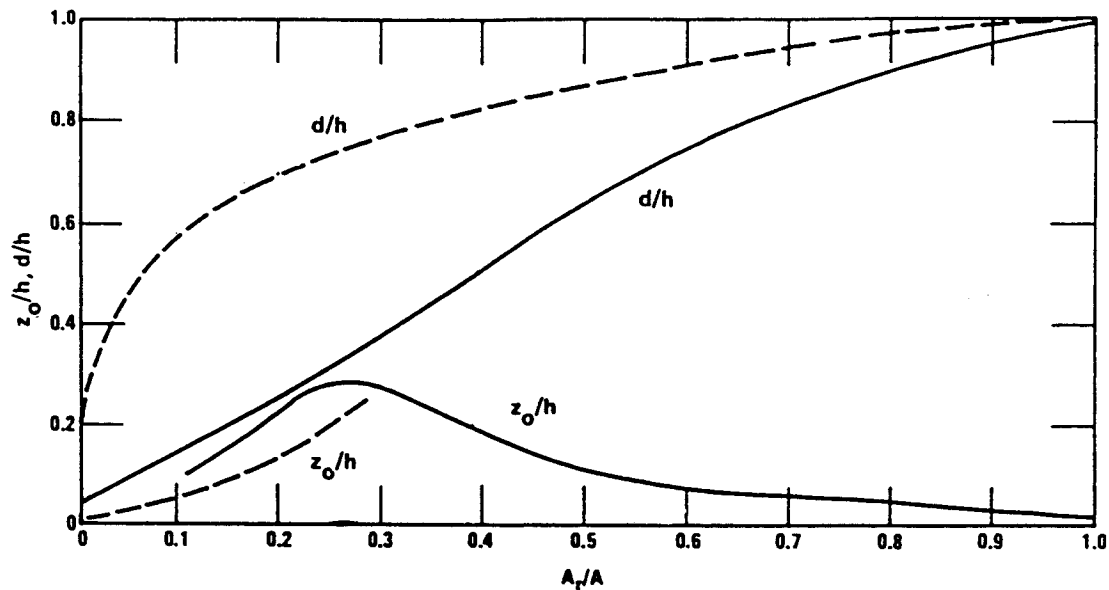
Figure 6.1   The ratios of z_0/h and d/h as a function of A_r/A from the empirical data
of Kutzbach (1961), dashed line and Counihan (1971), solid line.
Adapted from Clarke et al. (1982).

6.1.3 The Temperature Variance Method (TVM)

From what has been mentioned at the beginning of this section it follows that it is very difficult to determine a value for the zeroplane displacement d from profile measurements in general. In the case of the present study, two additional difficulties must be considered:

- when measurements are carried out within the RS, profiles for certain wind direction sectors are too much locally disturbed and show a shape that does not allow one to derive a value for d for that sector (Schädler, 1988).

- As it is one of the objectives of this study to investigate to what extent the flux-gradient relations are disturbed in the RS just above the very complex surface of a city, it does not seem to be appropriate to use these formulations (in the neutral cases) to determine d. Also, even for neutral conditions one cannot "a priori" expect the wind velocity gradients to be in equilibrium with the momentum fluxes. One part of the possible difference would then be "absorbed" in a wrong value for d.

To avoid the usage of such an implicit assumption, one can only rely on the geometric approaches described above. However, there are also some problems in their application:

- the different formulations yield quite different results

- a completely new data set (information on the distribution and height of roughness elements is required

- actual roughness features in urban areas differ significantly from the simple forms that have been used to derive the empirical formulations in the wind tunnel (Counihan, 1971) or from the bushel baskets (Kutzbach, 1961). This has been pointed out already by Clarke et al. (1982).

For these reasons, it seems worthwhile to look for an independent method to determine the zeroplane displacement. Results of Clarke et al. (1982) show that the functional dependence of σ_θ/θ_* on stability in an urban area is in good agreement with the "ideal" formulation from the Kansas data (Wyngaard et al., 1971, Tillman, 1972). Similarly, de Bruin et al. (1988) find the Kansas formulation to be a valid representation of their data in the case of a modestly rough terrain (Cabau region, The Netherlands) without distinct temperature inhomogeneities (in contrast to an irrigated field surrounded by hot dry terrain, where the temperature variance was found to be very much affected). These results show that under certain conditions (see below) the surface of an urban area can be considered "thermally homogeneous" even if it is dynamically very rough. Using results of Schmid (1988) one can put this in a more precise way: for a suburban area in Vancouver BC (Canada) a spectral analysis of the surface temperature showed that the dominant wave lengths of the spatial temperature variance spectrum correspond roughly to the distribution of roughness features (such as street width, block size, etc.). If the source area of a temperature measurement is much larger in diameter than the dominant wave length of the surface temperature distribution (or more generally: spatial features), the thermal regime can be considered "homogeneous". In this case, measurements of σ_θ/θ_* can be used to derive a value for the zeroplane displacement d. This method will be outlined in detail in the following. Its general idea states that for certain types of dynamically rough surfaces (de Bruin et al., 1988) the temperature variance distribution is affected very little and is well described by its "ideal-site" formulation. The height dependence of σ_θ/θ_* can therefore be used to determine the height (above the reference level) that the temperature variance field "sees" for different wind directions. Under the assumption that this reference level is equal for other properties of the flow such as momentum and water vapour the height of this reference level can be identified with the zeroplane displacement (as it will be termed in the following).

Similarity theory predicts for the dimensionless temperature variance in the unstable SL a -1/3 dependence on z/L only. This prediction has been experimentally verified, e.g. by Tillman (1972), who suggests

$$\frac{\sigma_\theta}{\theta_*} = -C_1 \left(C_2 - \frac{z}{L}\right)^{-1/3} \qquad\qquad (6.2)$$

For the parameter C_1 a value of 0.95 (after Wyngaard et al., 1971) is suggested and C_2 is determined by the neutral limit of the function. This neutral limit can be expressed as

$$\frac{\sigma_\theta}{\theta_*}\bigg|_{n.l.} = C_3, \qquad\qquad (6.3)$$

and thus

$$C_2 = \left(\frac{C_3}{C_1}\right)^{-3}. \qquad\qquad (6.4)$$

Tillman (1972) finds a value "larger than 2.5" for C_3, while Beljaars (1982) suggests a value of 3.5 and data from de Bruin et al. (1988) indicate $C_3 \approx 3$.

If instead of the height z in (6.2) the modified height z' according to (6.1) is introduced, it is possible to vary d in order to find the closest correspondence to (6.2). It is clear that measured data for σ_θ/θ_* can only be compared to (6.2) in a statistical sense, i.e. for a single value (or only a few) it makes no sense to calculate the "optimal" d. As much data as possible are therefore desired. For near neutral stability, however, two problems arise. Firstly, the measurements become quite inaccurate. This is due to the very small energy fluxes in general and due to the correction procedure that has to be applied to the temperature data because of water vapour effects (see Section A1.5). According to Schotanus et al. (1983) these corrections (especially for σ_θ) become doubtful in the near neutral limit. Secondly, the only available data on urban σ_θ/θ_* in the literature show a wide spread in the neutral limit while following closely the relation (6.2) in the unstable regime (Clarke et al., 1982). This might be due to the uncertainty in the measurements mentioned above, but could also be a characteristic of an urban environment. Near neutral measurements are therefore to be excluded from the analysis. However, this requirement ,raises a fundamental problem, since the variation of d affects the calculated value of the stability. Measurements that are included for small d (apparently more unstable) may become "near neutral" for larger d and will be excluded from further analysis. This, however, changes the data set so that it is difficult to compare the errors for different estimates of d. Especially single measurements with large deviations from (6.2) can change the calculated errors significantly if they are included in the analysis for small d but excluded above a certain threshold "stability". Thus they produce a sharp change in the error. This can possibly

lead to errors in the estimate of d. It is therefore important to vary d from the largest possible value (apparently "most neutral case") towards smaller ones and to exclude those measurements from the further analysis that fall into the "neutral range" for the largest d. This ensures that for every estimate of d the same data set is used and errors become comparable with each other.

A detailed description of the method and the restrictions used is given in the following:

- 15 min. samples of σ_θ, θ_* and L are used in order to maximize the number of data points. A subsequent comparison with the results from 30 min or 50 min samples show no significant differences in the obtained d if there are still enough data points.

- for every measurement the wind direction is determined from the wind vane reading (at 10m, on the tower) and it is attributed to one of 8 wind direction sectors of 45° width. 45° was chosen to keep the number of data points per sector high enough and since a ± 22.5° variation of wind direction corresponds to what one can typically expect over a rough surface.

- data are excluded from the analysis if the norm of $\xi^* = (z-D^*/L)$ is smaller than 0.015, where D^* is the largest value for d allowed (the height above street level, in the present case). They are also excluded if the estimated error of the turbulent flux of sensible heat (after Lumley and Panofsky, 1964, see Section 5.4) exceeds 30%. Results are very insensitive to this latter restriction, apart from the number of data! (This error estimate requires a height measurement, too. In order to calculate it, a constant value for d of 14 m has been used).

- the variation of d ranges from street level (d=0m) to roof level (d=18.3m). As an increment 0.5 m was used.

The error is calculated as

$$\text{err} = \left(\frac{1}{N} \sum_i^N \left(\frac{\sigma_\theta}{\theta_*} - \left(\frac{\sigma_\theta}{\theta_*} \right)_{(6.2)} \right)^2 \right)^{1/2}, \qquad (6.5)$$

where N is the number of data points for the respective wind direction sector and $\left(\sigma_\theta/\theta_* \right)_{(6.2)}$ is the value calculated by (6.2). The parameters used in (6.2) are $C_1 = 0.95$ (Wyngaard et al., 1971) and $C_3 = 3.5$ (Beljaars, 1982).

Table 6.1   d values for the different wind directions sectors of the Temperature Variance Method. The along street direction is 120° and 300°, respectively.

Sector	d (m)	err	Number of data points
1-45°	14	0.346	>>20
46-90°	15.5	0.376	>>20
91-135°	-	-	-
136-180°	16	0.199	11
181-225°	9	0.247	7
226-270°	13.5	0.637	>20
271-315°	10.5	0.262	9
316-360°	14	0.243	10

An example of errors "err" for the variation of d is given in Fig. 6.2. From the resulting d values (Table 6.1) it can be seen that there is a quite large difference between the wind direction sectors, with d ranging from 9 m to 16 m. This corresponds to d/h from 0.5 to 0.88 if we take the local roof level (18.3 m) as h. For the sector 91°-135° it was not possible to determine a value for d, since for this wind direction the sonic anemometer was situated in the lee of the tower and thus the measurements were distorted. Sectors 181°-225° and 271°-315° are calculated in fact from too few data points. Fig. 6.3a and 6.3b show all the σ_θ/θ_* data used for the determination of d as calculated with the respective optimal d (Fig. 6.3a) and with d=18m for all sectors (Fig.6.3b). Although the *visual* differences are obviously small, it will be shown in the following that the zeroplane displacement heights calculated using the TVM are in good agreement with values obtained from other methods.

These results are compared to those obtained by the geometric approach mentioned earlier in this section. A land use inventory for the city of Zurich with a resolution of 100 x 100 m was used for this purpose. The data available for each square were the following:

- number of buildings
- their average height
- fraction of built up area
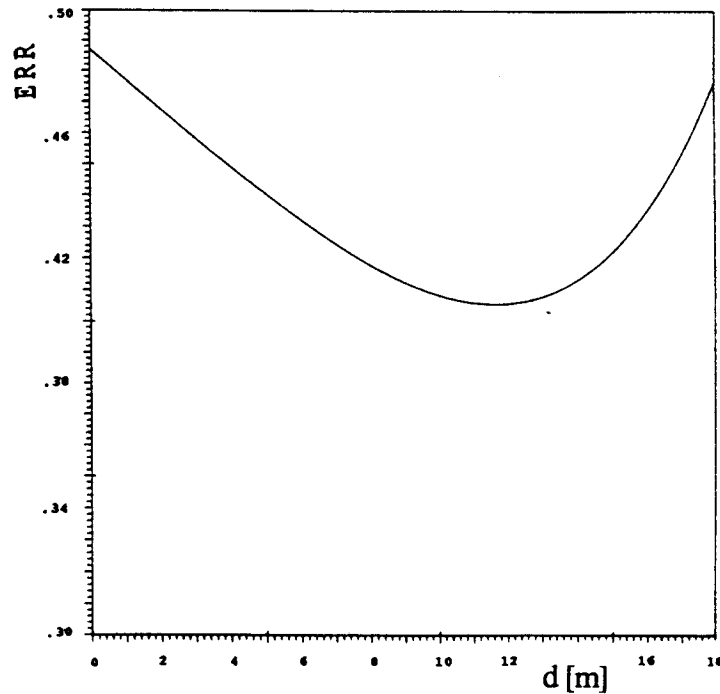- if no buildings are present: code for land use category (cf. Table 6.2)

Figure 6.2   Example for the variation of the error (err) for various estimates of the zeroplane displacement height d. Example for the wind direction sector 0-45°.

The procedure used to calculate the required parameters for the models of Counihan (1971) and Kutzbach (1961) respectively can easily be described with reference to Fig. 6.4. The cartesian grid of surface data is converted into polar coordinates with the point A ("Anwand") at its center and a resolution of $\Delta r = 15$ m and $\Delta\Theta = 2.5°$. This is done by sweeping the cartesian grid with a radial comb and using a distance weighing scheme to reassign the polar grid values from the respective four nearest cartesian grid points. This "radial data set" is then used to determine an estimated value for d according to Counihan (1971) and Kutzbach (1961). For every event (a 15 minutes averaging period, for compatibility with the TVM) the wind direction is determined first and it is attributed to one of the eight wind direction sectors. Then, the source area for this event is determined with the so called mini-SAM (a statistical version of the source area Model, SAM, as described by Schmid and Oke, 1990). Number of buildings, average heights etc. of the "radial data set" for those rays (and those radii) that fall within the 0.9 effect level (see Fig. 6.4) are averaged subsequently. The weights for this averaging procedure are given by Schmid and Oke (1990) and correspond to the relative importance of the different effect levels. Fig. 6.4 also illustrates this averaging procedure. Since the mini-SAM model requires a measuring height as input (and hence a value for d), the zeroplane displacement has been prescribed as calculated from the TVM (a value of 0.75h, however, would not yield significantly different results).
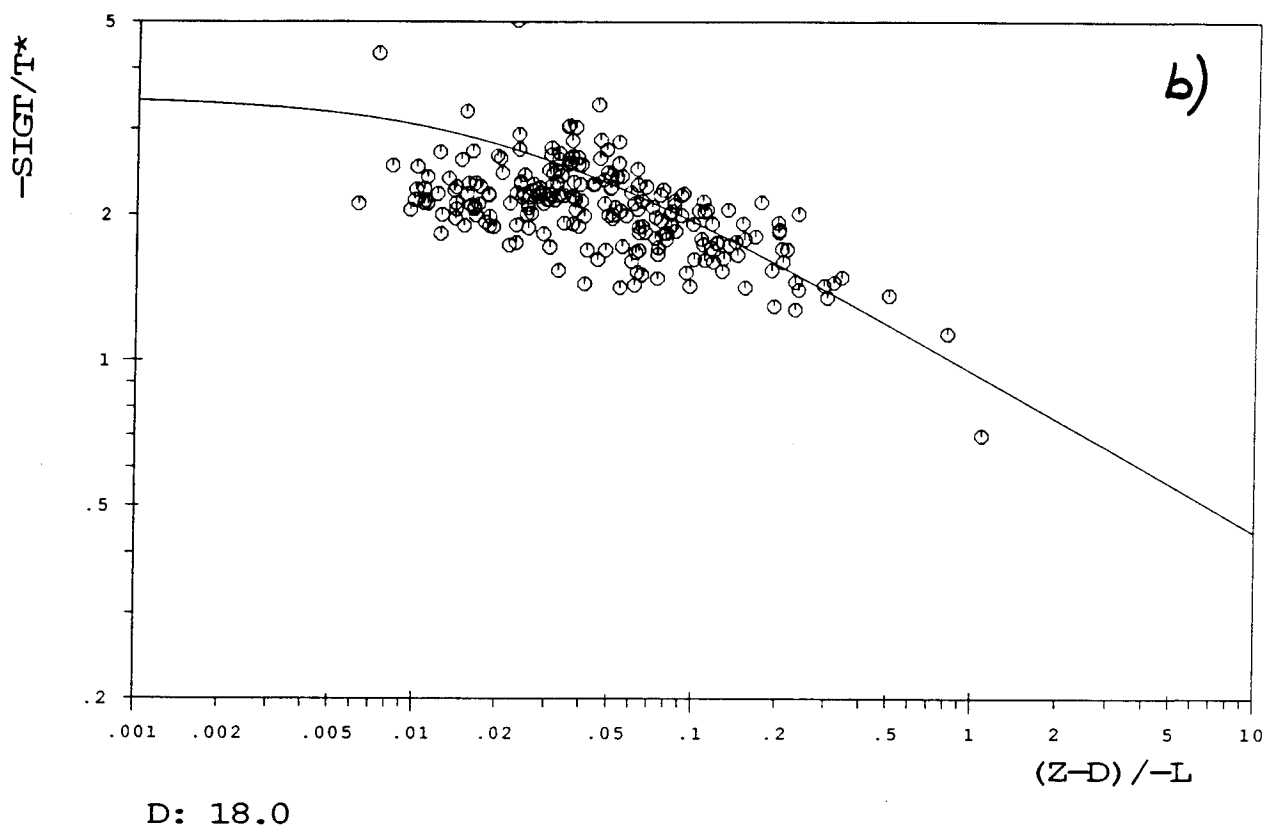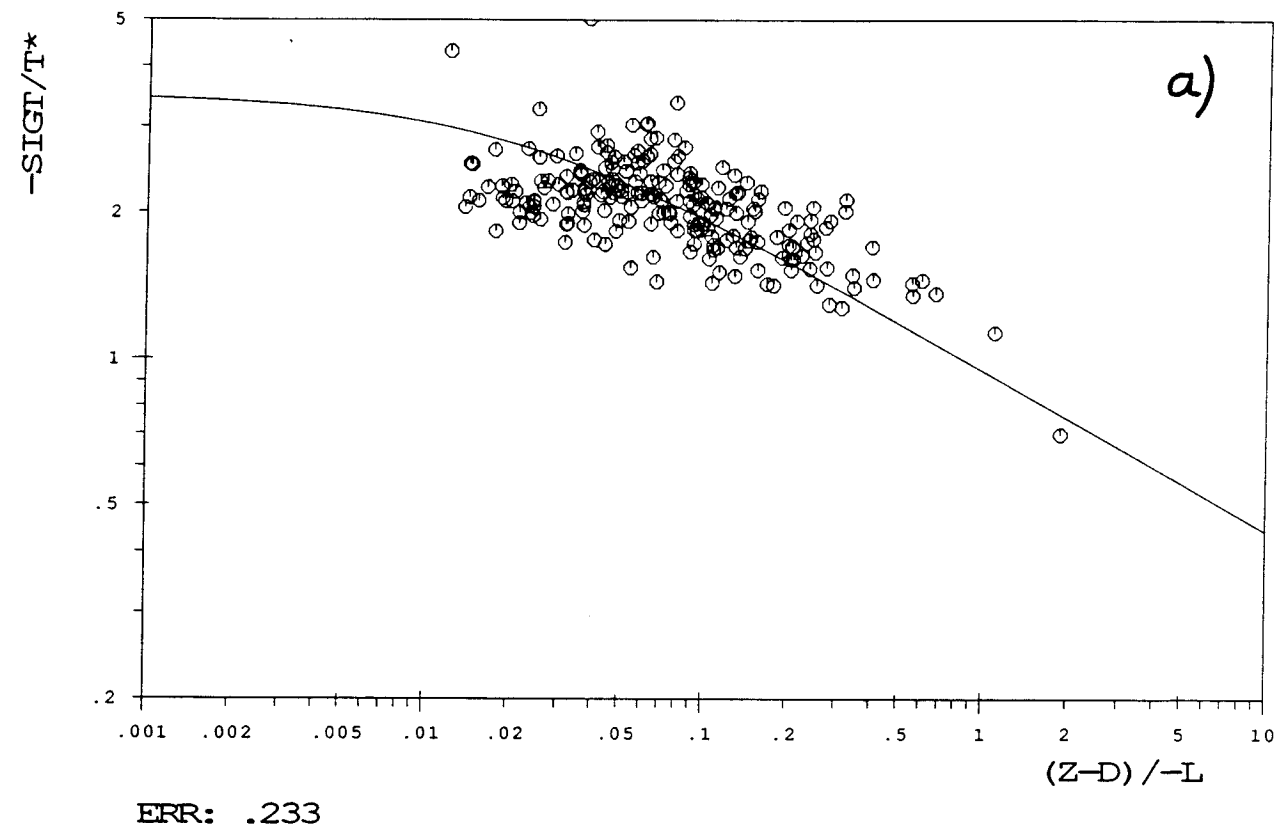
ERR: .233

D: 18.0

Figure 6.3 σ_θ/θ_* (z/L) as calculated a) with the optimal d from the respective wind
direction sector and b) with d= 18m for all sectors.

Table 6.2   Land use categories and the respective heights and area fractions that were attributed to them. h_b and A_b indicates that these values are available from the land use inventory.

Land use category	Average height	Fraction covered by roughness elements
Buildings	h_b*)	A_b
Gardens,Courts	2 m	0.1
Streets, Corners	2 m	0.1
Playgrounds, Parks Sport-areas	7 m	0.3
Agricultural ground, grass land	2m	0.2
Forest	15 m	≈ 1
Railway area	2 m	0.2
Miscellaneous	2 m	0.2
Open water	0 m	0

*) If there are houses on the square considered, it is assumed (from visual inspection of the situation) that half of the area not covered by buildings is covered by trees of mean height $h_t = 10$ m. The mean height for that square is then calculated according to $\overline{h} = h_b A_b + h_t(1 - A_b)\,0.5$

A comparison of the Temperature Variance Method results with the estimates from the geometrical approaches is given in Fig. 6.5. Already from Fig 6.1 it is clear that the formula of Counihan (1971) will always yield smaller values of d than Kutzbach's (1961). The Kutzbach-formula estimates lie quite close to the values of the TVM for most of the wind direction sectors. Also, the shape of the two curves is very similar apart from the sector 181 - 225°. On the other hand, sector 7 (271 - 315°) shows quite a low d as determined by TVM, and also Kutzbach's geometrical approach yields at least a somewhat smaller value than the two adjacent sectors. Only in sector 5 (181 - 225°) not only the numerical values of the two methods are quite different but also the the position relative to the two neighbouring sectors. This might be mainly due to the very small number of observations falling into this range of wind direction. In general, the TVM shows a larger variation of d with wind direction than either of the geometrical approaches. This is believed to be mainly due to the relatively rough resolution of the original data base on land use distribution. Also, it reflects the crude formulation in terms of the distribution of the roughness elements of the two geometrical methods.

It is concluded that TVM provides a simple tool for the determination of the zeroplane displacement that

- is related directly to the surface features of the measuring site (in the sense that d is obtained from what the measurements "see" of the temperature field)

- does not require an extra data base on the distribution of the roughness elements

- is not restricted to uniformly distributed roughness elements

- is not dependent on the "behaviour" of the wind speed profile.

The restrictions to the application of TVM were given at the beginning of this section. They require that the sources and sinks for sensible heat are equally distributed as the roughness elements. Especially, for lower densities of roughness elements the geometric approaches of Counihan (1971) and Kutzbach (1961) yield quite different results. A comparison with the TVM indicates that for an urban environment the formulation of Kutzbach (1961) is more appropriate than the one of Counihan (1971).
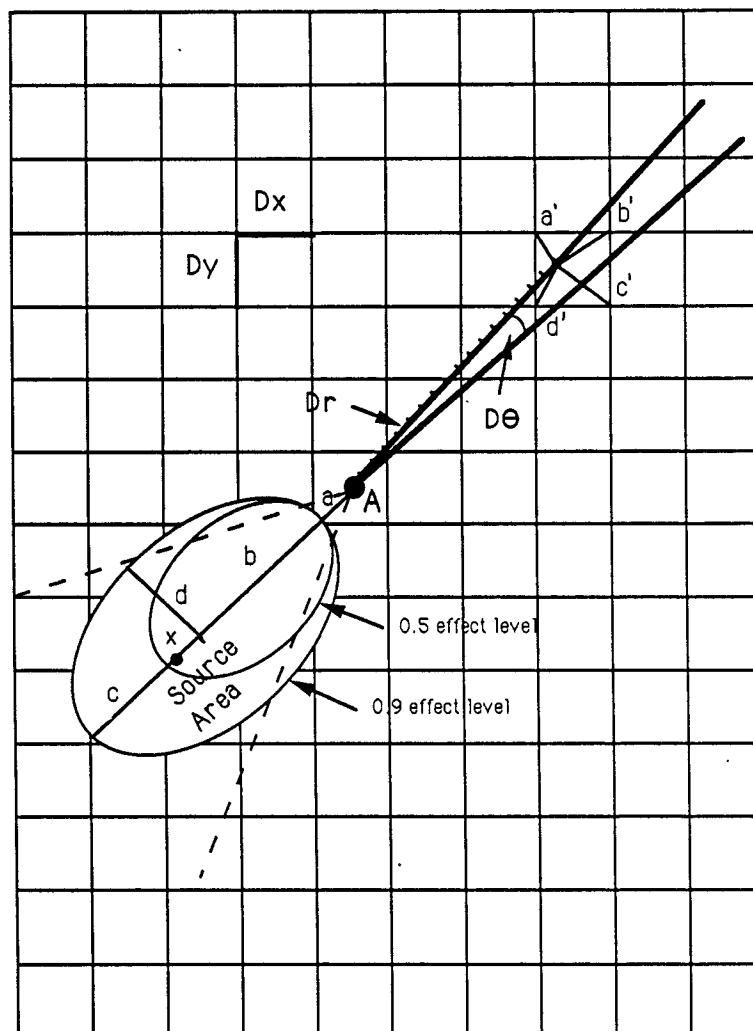
Figure 6.4   Definitions for the transformation of surface characteristics data in a cartesian grid into polar coordinates. a,b,c denote characteristic distances for the source area (Schmid and Oke, 1990), and a',b',c',d' are the distances to the nearest cartesian grid points. Dr and DΘ denote Δr and ΔΘ, respectively as described in the text.

ZEROPLANE DISPLACEMENT

WIND DIRECTION [DEG]

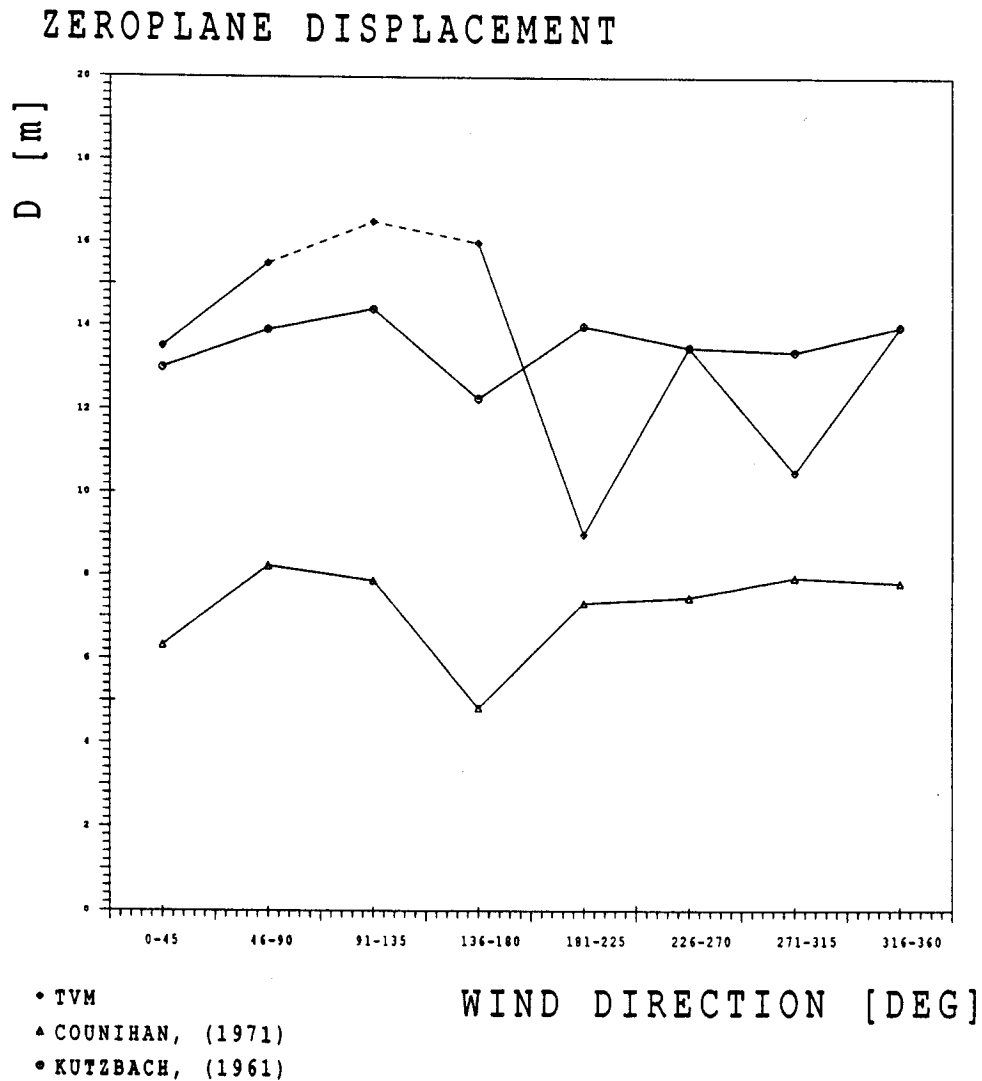- TVM
- COUNIHAN, (1971)
- KUTZBACH, (1961)

Figure 6.5   Comparison of estimated zeroplane displacement d for the different
wind direction sectors.

6.2 The Roughness Length

The roughness length z_0 is an important length scale for the description of the mean
wind profile in the *inertial sublayer*. It is, however, also *defined* by the latter and can
therefore not be deduced from measurements taken entirely within the roughness
sublayer. Clarke et al. (1982) have suggested to calculate z_0 as

$$z_0 = \frac{z'}{\exp(\overline{u}/u_*k)}$$
(6.6)

in near-neutral stability and in an urban environment, where they used the wind speed
and friction velocity measured at the same height. (6.6) corresponds to the assumption
that surface layer scaling holds at the height of observation (or, in other words, that this

height does not belong to the roughness sublayer). As will be shown in the following chapters, this condition is not fulfilled for the present measurements. Especially the height dependence of Reynolds stress (and therefore the *local* u*, see Chapter 7) makes z_0 height-dependent itself. If z_0 is calculated at the four levels above the roof by (6.6), using a local u* determined also from the profile for near-neutral stability (equation (2.26)), z_0 is found to vary by about one order of magnitude (typically between $z_0 \approx$ 0.2 m at the 3 m level and $z_0 \approx$ 2 m at the 20 m level). Also, the z_0 -value obtained for the 10 m and 20 m level, respectively may differ by more than one meter.

Although this brief analysis has shown that z_0 is not a useful length scale within the RS, a determination of the roughness length can be of importance e.g. for modelling applications. The "geometric approach" considering size and distribution of the roughness elements in the upwind fetch (source area) has therefore also been used to determine z_0. The same land use inventory and procedure as described in the previous section was utilized. In addition to the two parameterisations proposed by Kutzbach (1961) and Counihan (1971), two others were included for comparison. Lettau (1969) suggested

$$z_0 = 0.5 \ h \frac{s}{S} \tag{6.7}$$

where S is the so-called lot area (measured in the horizontal plane), and s is the silhouette area of the roughness elements and h is their height. Kondo and Yamazawa (1986) proposed a model for z_0 based on the relation between the roughness length and the geostrophic drag coefficient using Rossby number similarity (see Kondo and Yamazawa (1986) for details). An average "height" h_k is defined after

$$h_k = \frac{1}{A}\Sigma_i H_i S_i \tag{6.8}$$

through which z_0 can be related to the upwind geometry by

$$z_0 = 0.25 \ h_k. \tag{6.9}$$

Here, h_k is the geometrical roughness, S_i the area occupied by elements of height H_i and A the total area under consideration.

Fig. 6.6 shows a comparison between the four z_0-models and the variation of the roughness length with the wind direction. The estimates from the different approaches are distinctly different in magnitude and variation over the wind direction sectors. Largest variations are obtained by the method of Lettau (1969) with z_0 ranging from

1.8m to 5.4m. Not surprisingly, the method of Kutzbach (1961) yields very similar results, since Lettau's formulation is based on Kutzbach's experiments. On the other hand, the approach of Counihan (1971) results in rather small z_0 with no variation between the different wind direction sectors. Equations (6.8) and (6.9) (Kondo and Yamazawa, 1986) yield z_0-estimates that are intermediate in magnitude and show a similar variation between the wind direction sectors as the two methods discussed first. Since the approach of Kondo and Yamazawa (1986) has been established using data from various field studies in large and small cities (and does not rely on experiments using artificial roughness elements), this method is considered to be most useful for a site similar to the present.
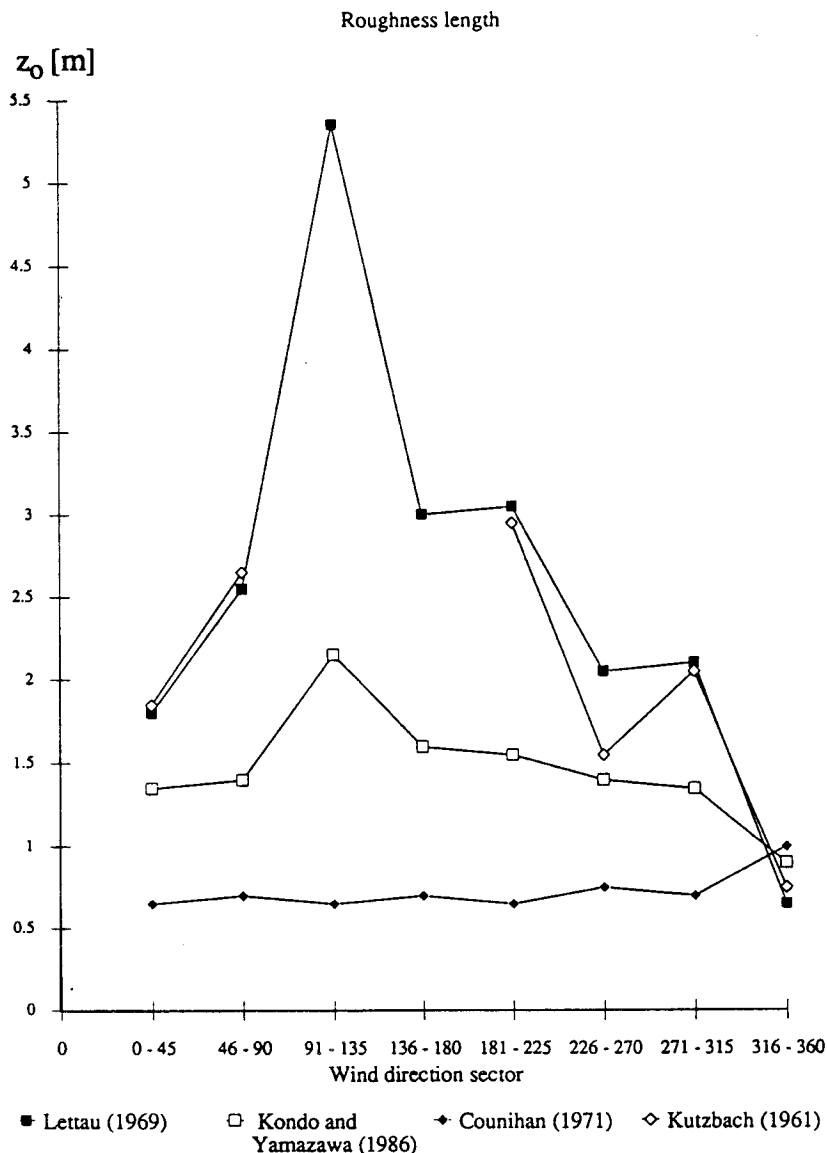
Roughness length

Figure 6.6 As Fig. 6.5, but for roughness length.

7. Reynolds Stress

The total turbulent transport of horizontal momentum in the vertical direction is given by

$$\tau = \bar{\rho} \left(\overline{u'w'}^2 + \overline{v'w'}^2 \right)^{1/2} \tag{7.1}$$

in the inertial sublayer and referred to as Reynolds Stress. From this quantity the friction velocity u_* is derived as an important scaling variable in the inertial sublayer

$$u_* = \left(\frac{\tau}{\bar{\rho}} \right)^{1/2} . \tag{7.2}$$

Under ideal conditions and if the coordinate system is defined such that the x - axis points in the direction of the mean wind, the second term on the right hand side of (7.1), $\overline{v'w'}$, vanishes (Busch, 1973) so that the fluctuating components of longitudinal and vertical wind suffice to determine u_*. The measurements of the fluctuating wind components at the present site show that even if the coordinate system is aligned with the mean wind direction for each run, the vertical flux of lateral momentum ($\sim\overline{v'w'}$) does not vanish completely for all runs. This indicates that the direction of the action of friction forces is not exactly aligned with the mean wind direction. The more general definition of u_* (as in (7.2)) has therefore been adopted for the calculation of the Reynolds stress. However, the results presented in the following chapters, are not sensitive on this definition of u_* (i.e. the non-alignment of the stress-tensor with the wind direction does not seem to have an influence on the derived relations). At the lower levels of observation (within the canyon), where the total vertical transport of momentum is small in general, $\overline{v'w'}$ is sometimes positive and for some runs even larger than $\overline{u'w'}$. Physically, this means that the net turbulent flux of momentum is directed upwards (though very small). In order not to hide this behaviour through the definition of the local u_* (7.1 and 7.2), the following sign convention has been applied

$$u_*(z) > 0 \text{ if } \overline{u'w'} + \overline{v'w'} < 0$$
$$u_*(z) < 0 \text{ if } \overline{u'w'} + \overline{v'w'} > 0 .$$

If variables such as Reynolds stress are considered as spatially averages in a roughness sublayer, (7.1) is modified according to equation (3.3). It will be shown, however, that the additional term, the dispersive covariance, is generally small in the

present observations and therefore will be neglected. In addition, Reynolds stress in the URS turns out to be not constant with height (see below). Thus, the "friction velocity" as in (7.2) is not a characteristic velocity for the whole layer anymore and is thus meaningless as a scaling variable. A possible choice for u_* could therefore be the value derived from the inertial sublayer above. However, with the present experimental configuration, it was not possible to measure Reynolds Stress (via eddy correlation) high enough above the surface to prove that

i) there is an inertial sublayer at all above an rough urban surface and

ii) to obtain valuable data at z_* or higher.

To derive a scaling velocity for the URS, *local* values of Reynolds Stress have been used as suggested by Högström et al. (1982) and the local friction velocity derived from this quantity will be denoted as u_*. Note that through this choice also θ_*, the characteristic temperature scale and the Obukhov length L are essentially local and height dependent. To derive profiles of Reynolds stress, however, the *assumption* that the uppermost of the profile levels (z = 38.3m) lies close to the height of the roughness sublayer (z_*) has been adopted in order to obtain an overall scaling variable for the whole RS and canopy layer. In the following, results are therefore presented either locally scaled (the notation $u_*(z)$ refers to $(\overline{u'w'}^2(z) + \overline{v'w'}^2(z))^{1/4}$) or through "inertial sublayer" variables (the notation $u_{*c}(38m)$ refers to a value calculated ("c") from the profile of mean wind speed at z =38.3m).

In Sections 7.1 and 7.2 the vertical and horizontal characteristics of the Reynolds stress field is discussed and analyzed, whereas in Section 7.3 and 7.4 some additional information is presented in order to get some deeper insight into the processes that are possibly responsible for the observed characteristics.

7.1 Height Dependence of Reynolds stress

A comparison of Reynolds stress as measured simultaneously at two heights above the roof level is shown in Fig. 7.1 (expressed as local friction velocity). " Level 1" is located at 5m above the roof (position 10) and "level 2" at 10m above the roof (triangles, position 11) or also at 5m (diamonds). These latter runs have been included to make sure that the observed increase of Reynolds stress with height is not due to systematic instrument differences (at the two levels, two different sonic systems have been used, cf. Appendix A2). If a gradient for u_* is calculated between the two levels, it is found to be almost constant for the near-neutral runs (z'/L > - 0.05, L determined at the 10m level), with an average value of 0.064 ± 0.009 s^{-1} (Fig. 7.2). Beyond
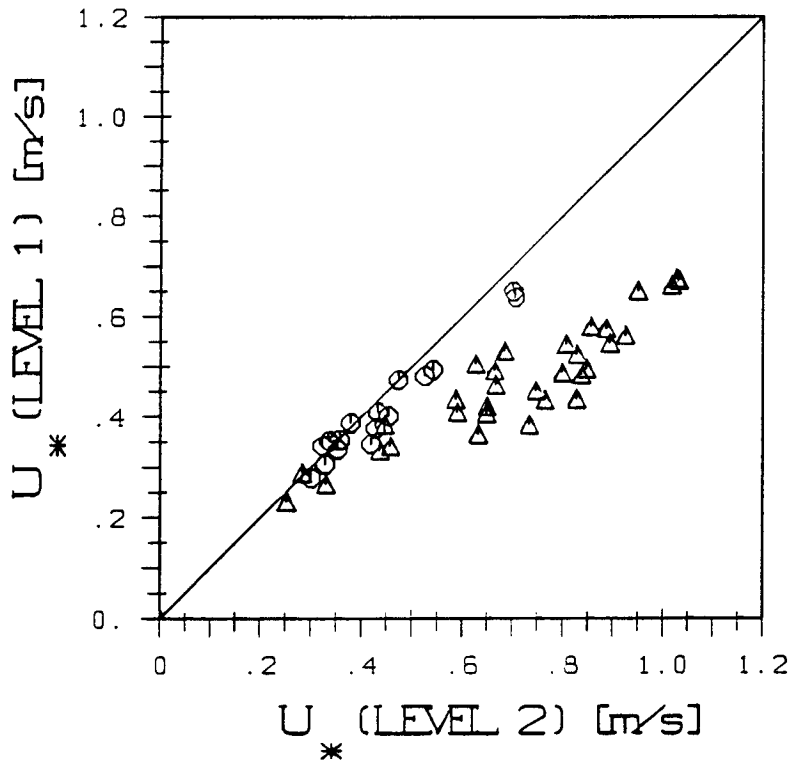
Figure 7.1   Comparison of simultaneous u∗ at different levels. (△): level 1 = position 10 and level 2 = position 11. (⊘): level 1 = level 2 = position 10).

z'/L = -0.05 the gradients of u∗ sharply decrease to much smaller values. Not so much the numerical value of the *near-neutral* gradient of u∗ , which is certainly specific for the present site (height above d, roughness and structure of the underlying surface) is an interesting feature of RS flow, but rather the relatively small scatter. In many wind tunnel experiments, where flow over rough surfaces was studied, a similar increase of Reynolds stress with height was observed (Antonia and Luxton, 1971; Mulhearn and Finnigan, 1978; Raupach et al. 1980) but usually attributed to measurement difficulties close to the surface. In the present case, there is no reason to believe that the two sonics differ systematically (Fig. 7.1) or that the measurements at the lower level were biased for some reason. If the observed gradient of Reynolds stress (or equivalently of the derived local u∗) is extrapolated downwards to the zeroplane displacement height d of the respective wind direction sector, a mean value $\overline{u_*^{2\,\text{ext}}}(z{=}d)$ = - 0.03 ± 0.05ms^{-1} is found for the near neutral runs (the superscript "ext" referring to "extrapolated"). For the unstable runs, $u_*^{2\,\text{ext}}$ (z = d) tends to increase to slightly positive values (Fig. 7.3).

Högström et al. (1982) recommend for the urban RS to use the logarithmic wind profile to calculate u∗. It is clear from the dependence of Reynolds stress found in the present observations that this method cannot yield proper estimates at any height. Fig. 7.4 shows the profile of the local u∗ as derived from (neutral) wind speed profiles

(assuming the logarithmic profile to hold) and as measured directly by eddy correlation. It is evident from Fig. 7.4 that this approach might lead to erroneously large estimates of u* close to the roof level.
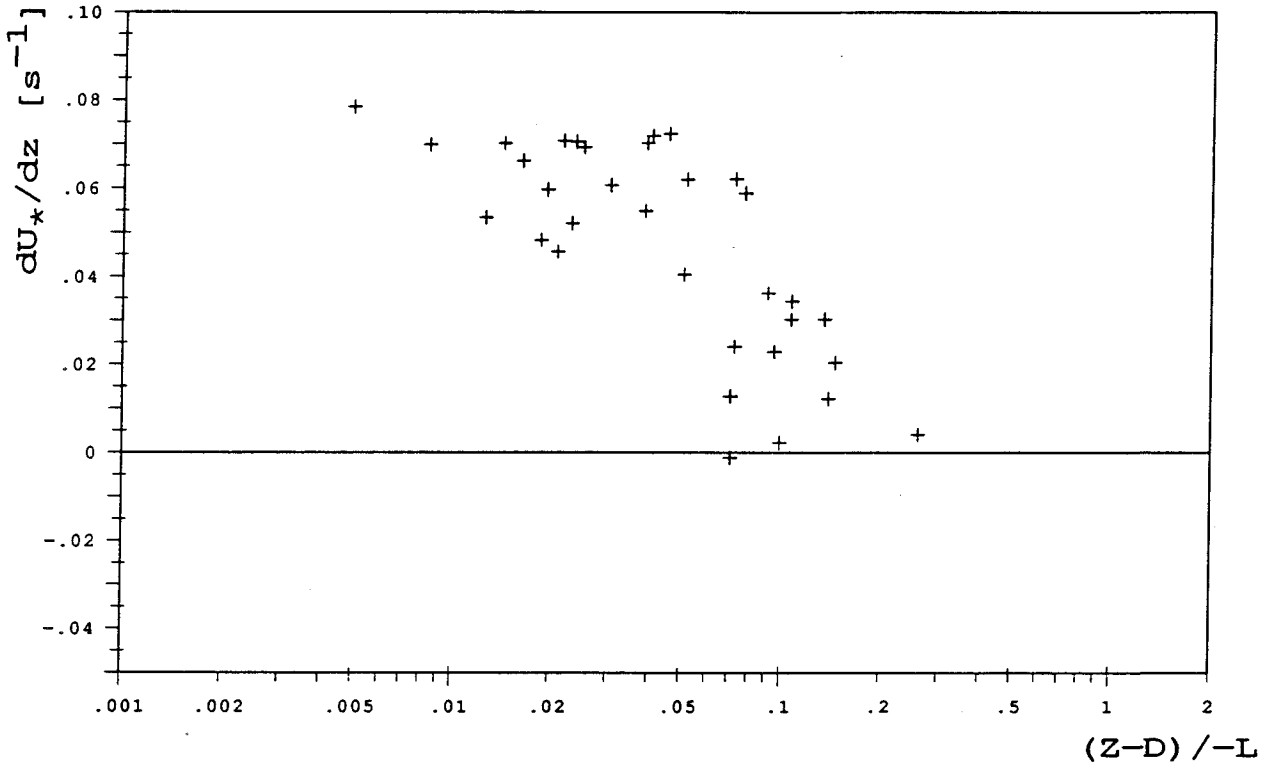

Figure 7.2 Gradient of u*(z) between positions 10 and 11 (simultaneous observations) for different stabilities.
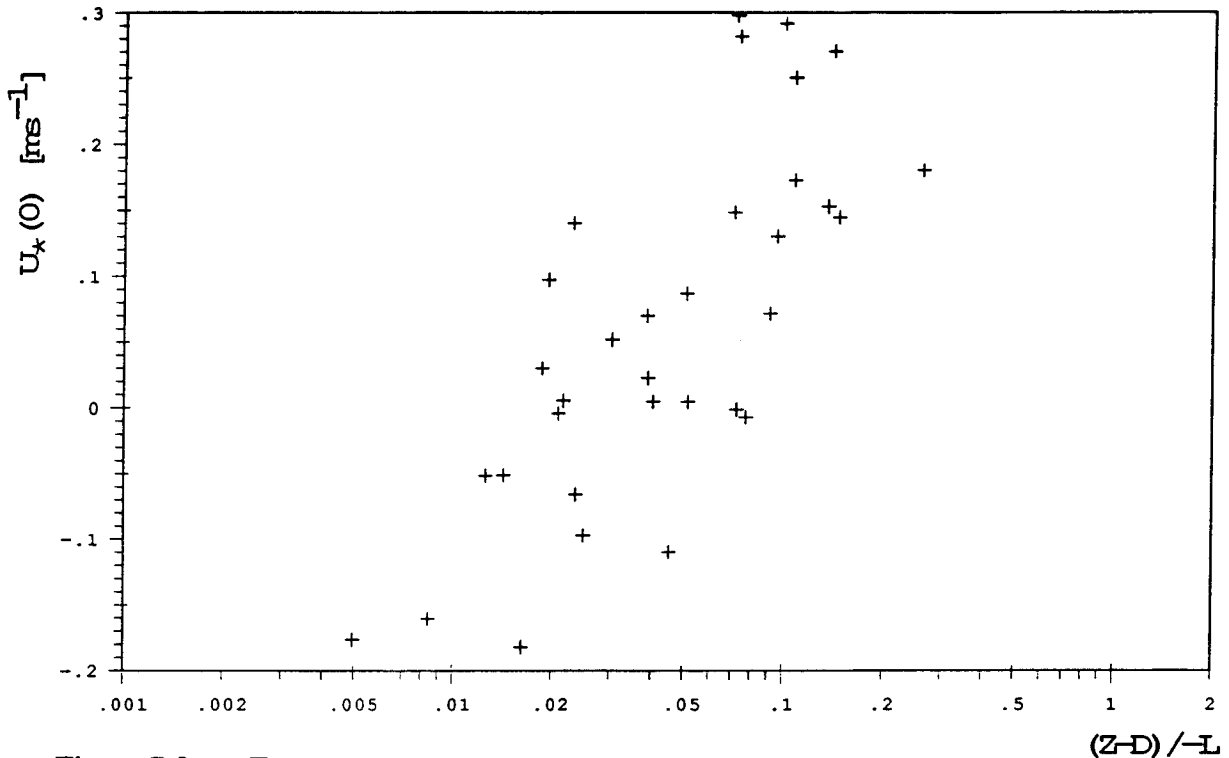

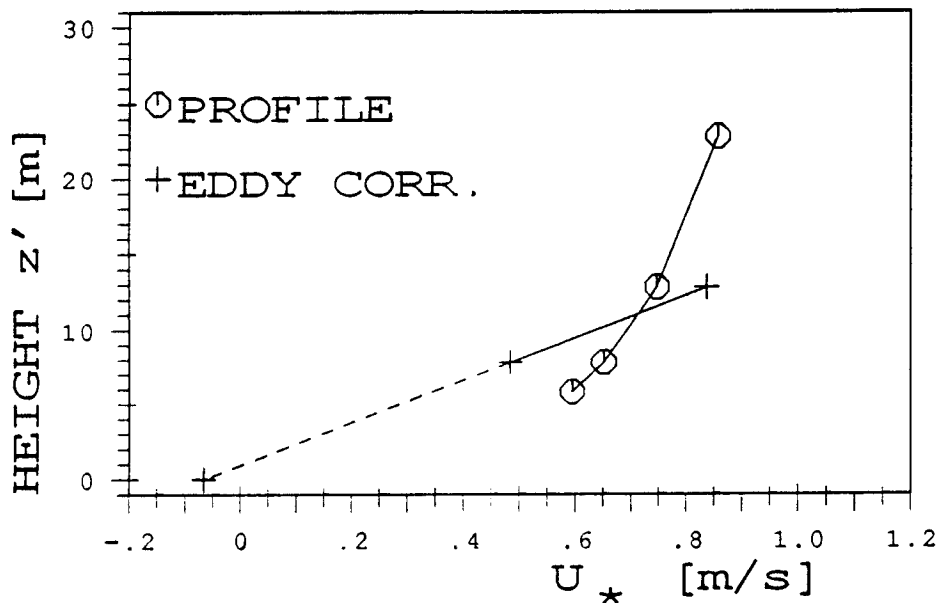**Figure 7.3** Extrapolated value of u* at z'=0 (z=d) as calculated from simultaneous measurements at positions 10 and 11 for various stabilities.

Figure 7.4   u* as measured by eddy correlation and calculated with equation (2.26).
Example for neutral stability. The dashed line refers to an extrapolation
from the eddy correlation measurements to z=d.

Unfortunately, it was not possible with the available instrumentation to determine the
Reynolds stress at more than two levels simultaneously. To make the results from the
different runs comparable, the measured Reynolds stress is scaled with the Reynolds
stress at 20m above roof level (z=38.3 m), calculated from the gradient of the mean
wind speed by equation (2.26) and assuming inertial sublayer scaling to hold
approximately at this height. This has the advantage that the profile data are available
for all turbulence runs. The assumption concerning the inertial sublayer scaling at
38.3m will be justified through the results. Fig. 7.5a shows the overall decrease of
Reynolds stress when approaching the surface. However, there is considerable scatter
which shows that there is another important quantity influencing the stress at a given
height. In Fig. 7.5b only those runs are shown, for which both wind directions, at
10m above level and within the canyon read within ±30° from an axis orthogonal to the
canyon (wind direction = 30°± 30°). Here, the scatter is clearly reduced, especially at
13m and at 23.3m above ground. The Reynolds stress is essentially zero at the lower
level within the canyon for both positions, at the canyon center (triangle) and closer to
the (upwind) wall (+ sign). For this wind direction, for which one would expect a
vortex to develop (see Section 3.1), the Reynolds stress is different at 23.3m above the

(downwind) roof and over the canyon (closer to the upwind wall). Fig. A2.7 shows that for this situation the wind shear at the top of the canyon (especially on the windward side) is very large and thus shear production must be responsible for the large and distinct difference in Reynolds stress over the canyon and over the roof. At the highest level, the scatter is not reduced to the same extent as for the other levels, but is still considerably smaller. For the other three well defined wind directions (parallel to the canyon from either side, or at a right angle but from the opposite direction), only one or two runs at each level are available, so that no meaningful statistics can be obtained. It is interesting to note, however, that for flow parallel to the canyon , the Reynolds stress at the mid canyon level (16.7m) is very small (or even positive), while at the other levels its value is similar to that shown in Fig. 7.5a.

The shape of the scaled u_*-profile changes considerably when looking at different ranges of stability. Due to the height dependence of Reynolds stress and thus stability, the latter was calculated from the Richardson Number Ri at the uppermost level (z = 38.3m), using the relation between z'/L and Ri (equation 2.24a; see also Section 11.3) iteratively. Fig. 7.6 shows the scaled profiles of local u_* for near neutral (z'/L > -0.05), weakly unstable (-0.05 > z'/L > -0.5) and strongly unstable (z'/L < -0.5) situations. Again, the scatter at the different levels is considerably reduced, indicating the influence of stability upon the vertical profile of Reynolds stress. It is interesting to note that the observed gradient of Reynolds stress from *simultaneous* measurements at 23.3m and 28.3m (Fig. 7.2), is much less pronounced in scaled profiles (Fig. 7.6a) and, surprisingly, decreases towards greater instability. This is opposite to the stability behaviour of the scaled profiles (Fig. 7.6a-c). However, these two contradictory findings, are difficult to compare, since "stability" appears to be height dependent (through the height dependence of Reynolds stress): For Figures. 7.1 - 7.3 the local Reynolds stress and turbulent heat flux at z = 28.3m was used to determine z'/L, whereas z'/L at 38.3m were used to determine the stability class of the scaled profiles. This again points out the difficulties of the stability concept as long as the turbulent fluxes of momentum and heat are not constant with height. Since the second approach, using $u_{*c}(38m)$ as a scaling variable, i) covers more cases and ii) is a more general approach because it uses the most undisturbed (since most distant from the surface) variables, it is concluded that the behaviour shown in Fig. 7.6 provides a more general picture of the stability dependence of the Reynolds stress profile. It can be summarized as follows:

- Reynolds stress decreases when approaching the (rough) surface for all stabilities (of the inertial sublayer).
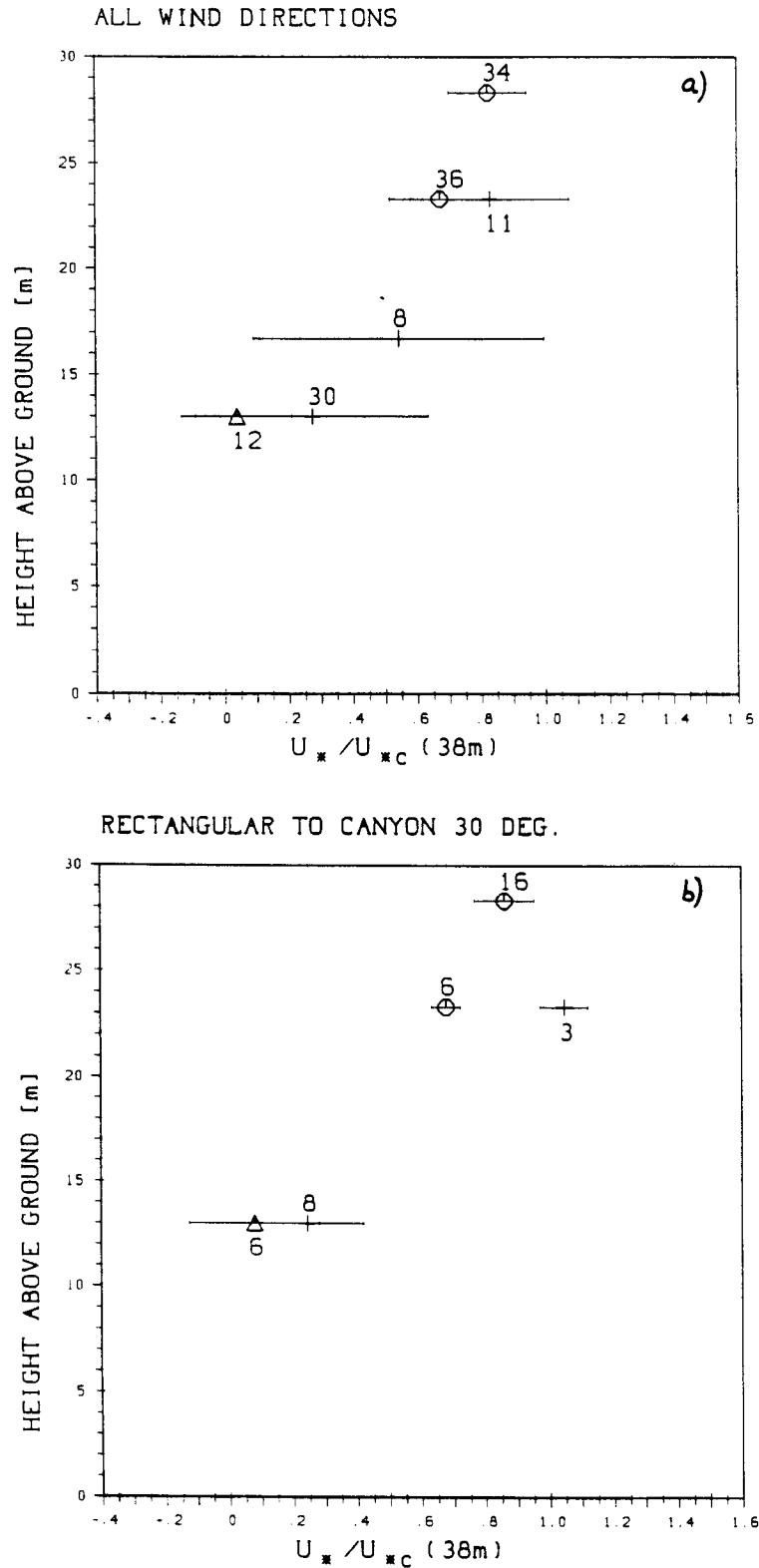
ALL WIND DIRECTIONS

RECTANGULAR TO CANYON 30 DEG.

Figure 7.5   Scaled profile of u*(z) for a) all wind directions and b) for approaching
flow (above roof) within a sector of ±30° from north east (orthogonal to
the canyon). u*c(38m) is calculated from the profile data at position 12
(see text). Error bars refer to the run-to-run variability (standard
deviation) and the numbers next to each symbol indicate the number of
observations available to calculate average values (and variances). (O):
positions 10 and 11; (+): positions 2, 3 and 4[+]; (▲): position 6.

- while $u_*(z)/u_{*c}(38m)$ is approximately 0.8 at $z = 28.3m$ for all stabilities, the decrease with decreasing height is least pronounced for near neutral situations and stronger with increasing instability.

- at the lowest level ($z = 13m$, within the canyon) momentum transport is clearly downwards in near neutral situations, but much smaller and sometimes even upwards in strongly unstable situations.

The present data show that the Reynolds stress field is strongly influenced by the local geometry (and therefore flow direction) as well as by the stability in the close vicinity of the roughness elements. The largest horizontal differences (see Section 7.2) we find close to the roof level h, especially for the flow orthogonal to the canyon.
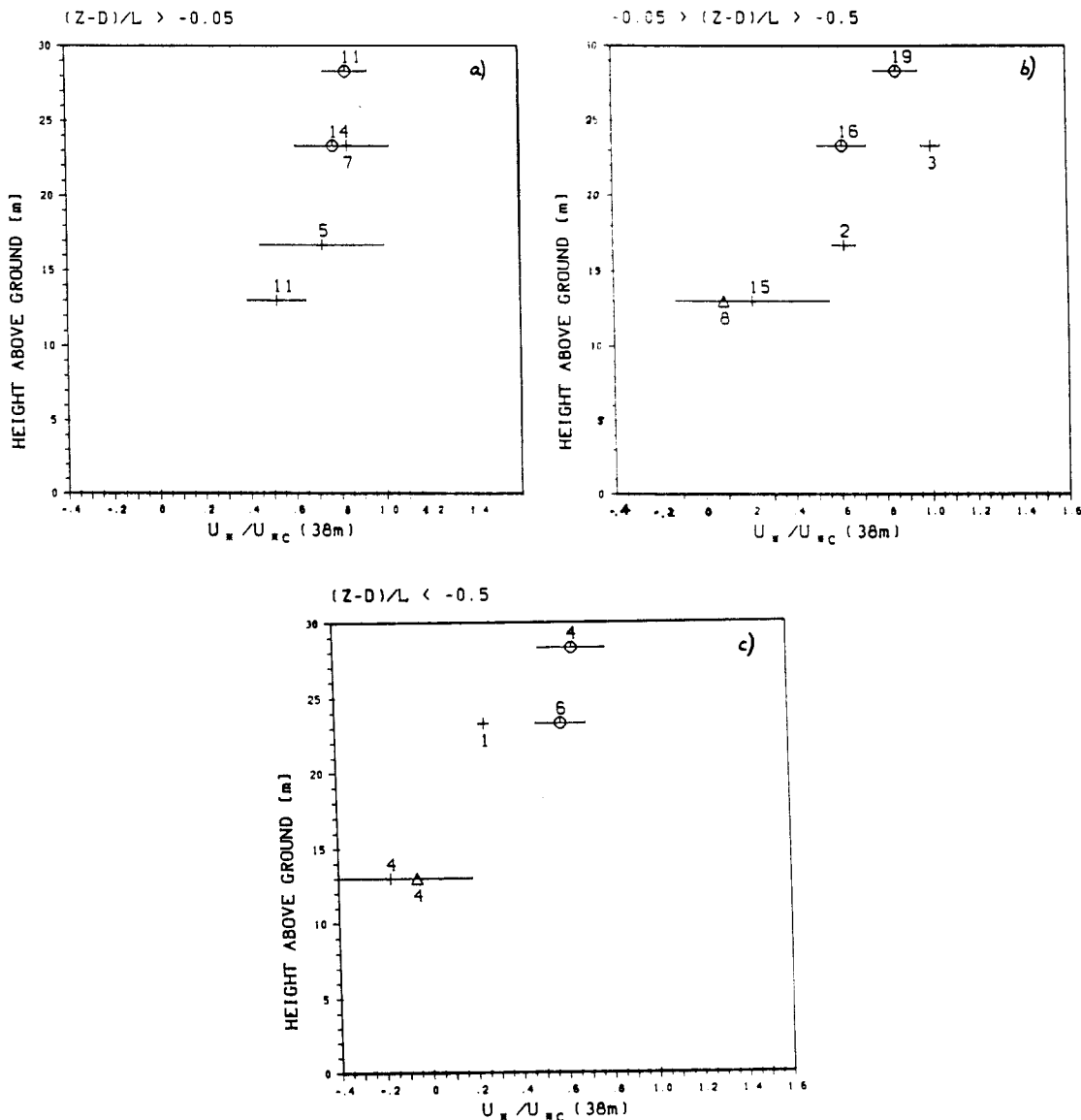

Figure 7.6   As Fig. 7.5, bur for a) near neutral, b) weakly unstable and c) strongly unstable runs.

7.2 Horizontal Inhomogeneity

The present data certainly do not allow the calculation of true horizontal averages as it would be required in a roughness sublayer (see Section 3.2). For an urban structure, as in the vicinity of the Anwand site, the location of the measurements at 23.3m can be considered "extreme" in the sense that there is no possible position for which it must be assumed that Reynolds stress could take values that are much smaller or much larger than those given e.g. in Fig. 7.5b. The same can be said for the two positions at the 13m level, within the canyon. Taking into consideration that the averaging over all runs (and thus over different wind directions) combines a variety of different positions relative to the upwind geometry at each level, it is concluded that the present data yield useful estimates of horizontally averaged momentum fluxes.

Both, the variance of the observed values $u*(z)/u*_c(38m)$ at a particular position (shown as error bars in Figures 7.5 and 7.6) and the differences of the average values between the two horizontal positions at 23.3m and 13m provide a measure for the horizontal variation of the Reynolds stress field. In addition, the variances indicate whether the chosen scaling variable (i.e. $u*_c(38m)$) and the chosen stratification scheme of the data (according to the wind direction and the stability) reflect important influences upon the stress field. In general, horizontal variability increases when approaching the surface. At 23.3m, the Reynolds stress appears to be quite well defined at each position for a given wind direction and/or stability. Close to the roof level ($z = 16.7m$), the run-to-run variability increases considerably (Fig. 7.5a), but at this level too few data are available to study the influence of wind direction and stability. The relatively large scatter at the lowest level ($z = 13m$, within the canyon) indicates that the flow at this level is very much influenced by the local (geometrical) configuration. Nevertheless, a comparison of the mean values for the different inertial sublayer stabilities (Fig. 7.6) shows that the influence of the above-canyon flow upon the Reynolds stress field within the canyon may not be neglected.

Assuming that an average of the scaled Reynolds stress over all wind directions and (where available) horizontal positions provides a reasonable measure for the horizontally averaged stress field, the following statistical model for the height dependence of $u*$ has been evaluated

$$\frac{u*(z)}{u*_c(38m)} = a \left(\ln \frac{z}{z_r} \right)^b \tag{7.3}$$

Here, a and b are numerical coefficients and z_r is some reference height, where the vertical transport of (horizontal) momentum vanishes. The mathematical form of (7.3)

and the measured value of $u*/u*_c(38m)$ at $z=13m$ (0.206) require that either $z_r < 13m$ or that b be an integer. A parameter fit for the whole data set (Table 7.1) yields $a = 0.92$, $b = 0.48$ and $z_r = 12.4m$. Note that the uppermost level, from which $u*_c(38m)$ was calculated, is included in the data set (anticipating a result of Chapter 11, where it will be shown that Reynolds stress is in local equilibrium with the gradient of mean wind speed).

Table 7.1: Measured and calculated (7.3) values of $u*/u*_c(38m)$

z	measured	calculated after (7.3)
38.3	1.0	0.975
28.3	0.823	0.839
23.3	0.710	0.737
16.7	0.543	0.514
13.0	0.206	0.213

The value of the reference height z_r is of particular interest. If the formulation (7.3) is of any general significance (and not only a best-fit model), z_r must be related to a more fundamental length scale of the problem under consideration. The most obvious choice in this case is certainly the zeroplane displacement height d, the level of mean momentum absorption (Thom, 1971). The average $\bar{d}$ (over all wind direction sectors) at the present site is 13.6m, indeed not significantly different from what has been found for z_r. Unfortunately, not enough data for all wind direction sectors (and all heights) are available to determine, whether the analogy between $\bar{d}$ and z_r holds for all wind directions, at least qualitatively. Furthermore, Figs. 7.6a - 7.6c indicate that z_r might be stability dependent: in strongly unstable situations z_r seems to lie somewhere close to roof level h, whereas for more neutral situations z_r is situated deeper within the canyon. Again, the limited amount of u*-profiles for different stability ranges prohibits one to establish a functional relation between z_r and z'/L.

From the present data set it is (in principle) not possible to decide whether or not the chosen scaling variable $u*_c(38m)$ is identical with $u*^{IS}$, the inertial sublayer friction velocity. From the fact that measured Reynolds stress is in (local) equilibrium with the gradient of mean wind speed (see Chapter 11) at even lower levels than 38.3m, the most obvious assumption is that this is also the case at the uppermost level. Thus, the "true" $u*^{IS}$ may be somewhat larger than $u*_c(38m)$. Nevertheless, the shape of the u*-profile (e.g. Fig. 7.5) indicates that Reynolds stress tends towards a constant value above the RS. In addition, the relatively small scatter in the u*-profile suggests that

$u*_c(38m)$ is a valid and useful (though somewhat small) scaling variable for the present data.

The rate of change with respect to height of the function $u*(z)/u*_c(38m)$ (equation (7.3)) may provide an estimate for $z*$, the height of the roughness sublayer. Above $z=42m$, the derivative of (7.3) yields a less than 1% change per meter. It is therefore concluded that the interface between the roughness sublayer and the inertial sublayer at the present site is located at $z \approx 2.5h$ - $3h$ (h being the roof level at the present site). This compares best to the formula given by Garratt (1980), $z* \approx 3D$ (D being the spacing of the roughness elements) if D is set equal to the canyon width (D $\approx$ 15m) at the present site. However, it is very difficult for an urban-like distribution of buildings, blocks, etc. to define a quantity such as D (see Fig. 4.2 and also the discussion in Section 11.1.3). It is impossible to conclude from the present case study, whether or not this relation is of general applicability for urban rough surfaces.

The above considerations lead to the following description of the height dependence of Reynolds stress (expressed as local friction velocity):

$$u*(z) = u*^{IS} \cdot a \ln \left(\tfrac{z}{d}\right)^{1/2} \tag{7.4}$$

where a is a coefficient of the order of 0.9. It remains to be shown whether (7.4) is of general validity for a typical European city structure within the height range between the mean zeroplane displacement $\bar{d}$ and the roughness sublayer height $z* \approx 3h$.

7.3 The Dispersive Covariance

If the horizontal averaging operator is applied as described in Chapter 3, the streamwise Navier-Stokes equation for stationary and horizontally homogeneous conditions with negligible mean horizontal pressure gradient and neutral flow (no buoyancy forces) within and above a canopy can be written as (Raupach and Shaw, 1982)

$$\frac{\partial}{\partial z} \langle \overline{u''w''} \rangle = \frac{1}{\rho} \left\langle \frac{\partial p''}{\partial x} \right\rangle + \nu \left\langle \nabla^2 u'' \right\rangle \tag{7.5}$$
$$= f_D + f_V$$

where f_D and f_V are the forces per unit mass of air exerted by form and viscous drag, respectively. The term on the left hand side describes the total flux of momentum (if molecular stress is neglected) as noted in equation (3.3). However, the measured gradient of Reynolds stress does not include the dispersive covariance $\langle \overline{u''}\overline{w''} \rangle$. Although

it has been shown for wind tunnel flows over highly rough surfaces (Mulhearn, 1978; Raupach et al., 1986) that the dispersive covariance is much smaller than the Reynolds stress, it might be instructive to justify this finding for the present situation. Since no horizontal flow field was measured from which $\langle \overline{u''w''} \rangle$ could be calculated, an *upper limit* for the dispersive flux at the 23.3m level is estimated as follows: Assume that $\overline{u''}$ is of the order of $L_m(d\overline{u}/dx)$ between the roof top and the canyon towers, where L_m is a length scale for dimensional consistency. If a very simple mixing length concept is introduced, L_m may be written as $L_m = k \cdot D_{9,8}/2$, where $D_{9,8}$ is the horizontal distance between positions 9 and 8 ($D_{9,8} \approx 20m$). The difference between the mean wind speed at these two positions is smaller than approximately $1/4\ \overline{u}_{p9}$ (position 9, roof top) as can be found from Fig. A3.9 or A3.10. Thus $\overline{u''}$ is of the order of (or smaller than) $1/20\ \overline{u}_{p9}$. If we further assume that $\overline{w''}$ is not larger than $\overline{u''}$ (De Paul, 1984) for a street canyon, it follows that an estimate for the upper limit of $\overline{u''w''}$ is given by

$$\overline{u''w''} \leq 2.5 \cdot 10^{-3}\ \overline{u}_{p9}^2 \qquad (7.6)$$

which is an estimate for the *upper limit* of $\langle u''w'' \rangle$ if $\overline{u''}$ and $\overline{w''}$ are not perfectly correlated in the horizontal plane. If the dispersive covariance vanishes at only 5 meters above the level considered (28.3m) which is probably a conservative assumption, its derivative with respect to z becomes smaller than $4.5 \cdot 10^{-3}\ ms^{-2}$ ($\overline{u}_{p9} = 3ms^{-1}$). This compares to the measured gradient of Reynolds stress under neutral conditions of about $0.065\ ms^{-2}$ ($\overline{\rho}$ set to unity, dimensionless) Thus, it is concluded that closely above the roof level of an urban street canyon, the dispersive covariance can be neglected. Penetrating deeper into the canyon, the gradient of Reynolds stress increases (Fig. 7.5a) while $\overline{u''}$ diminishes. For a doubled $\overline{w''}$, (7.6) can still be assumed to hold approximately and thus, the dispersive covariance is still much smaller than the rate of change of the Reynolds stress.

For an urban street canyon, viscous drag (equation 7.5) can be neglected, so that the vertical gradient of Reynolds stress must be caused essentially by form drag. Inserting the numerical values ($du*/dz \approx 0.065ms^{-2}$, $\overline{\rho} = 1.3\ kgm^{-3}$, $\Delta x = 20m$) into equation (7.5) we find the horizontally averaged streamwise gradient of pressure perturbations to be approximately $0.085\ Pam^{-1}$ (Note that $\langle \partial p''/\partial x \rangle \neq \partial \langle p'' \rangle/\partial x$, since the latter is identically zero by definition, cf. Raupach and Shaw, 1982). This value, calculated for the layer between positions 10 and 11, shows that experimental determination of horizontal pressure perturbations close to roof level would require very accurate measurements.

7.4 Conditional Sampling for Reynolds Stress

The Reynolds stress field within and above the street canyon was examined using the technique of conditional sampling (see Section 3.3) in order to illustrate the effect of forces exerted on the flow by form drag at different heights. Since in the present study Reynolds stress is defined according to (7.1) and thus includes vertical transport of *lateral* momentum, this latter contribution would have to be analyzed separately using the conditional sampling technique. For most of the runs, however, $\overline{v'w'}$ turns out to be much smaller than $\overline{u'w'}$. In addition, the different stress fractions (of $\overline{v'w'}$) do not show any typical or characteristic behaviour at the different heights. For this reason, the analysis will be constrained to the main contribution of momentum transport. i.e. $\overline{u'w'}$.

Fig. 7.7 shows the vertical distribution of the averaged stress fractions $S_{i,o}$, i.e. at hole size zero. At the upper most level outward and inward interactions are small and of the same order of magnitude while sweeps (i =4) slightly dominate the ejections (i=2) (see Table 7.2). At the 23.3m level, the dominance of sweeps is much more pronounced, mainly due to the "above canyon" runs (position 4), whereas the ratio between $S_{2,o}$ and $S_{4,o}$ above the roof remains unchanged as compared to 28.3m. Below roof level the contribution of sweeps further increases and thus ΔS_o, the difference between $S_{4,o}$ and $S_{2,o}$, becomes larger ($S_{2,o}/S_{4,o}$ smaller). The large contributions of the stress fractions $S_{i,o}$ at the lowest level arise from averaging over a number of runs with small, sometimes positive momentum transport. At this height, the total turbulent flux of momentum is often found to be the small sum of large contributions of the individual sectors. Note that for the averaging as shown in Fig. 7.7, those runs with total Reynolds stress smaller than $0.05 \text{m}^2\text{s}^{-2}$ were excluded to avoid the results to be dominated by single runs (this, essentially only affects the contributions at the lowest levels and in particular the mid-canyon position at 13m. For this position none of the runs passed the threshold given above).
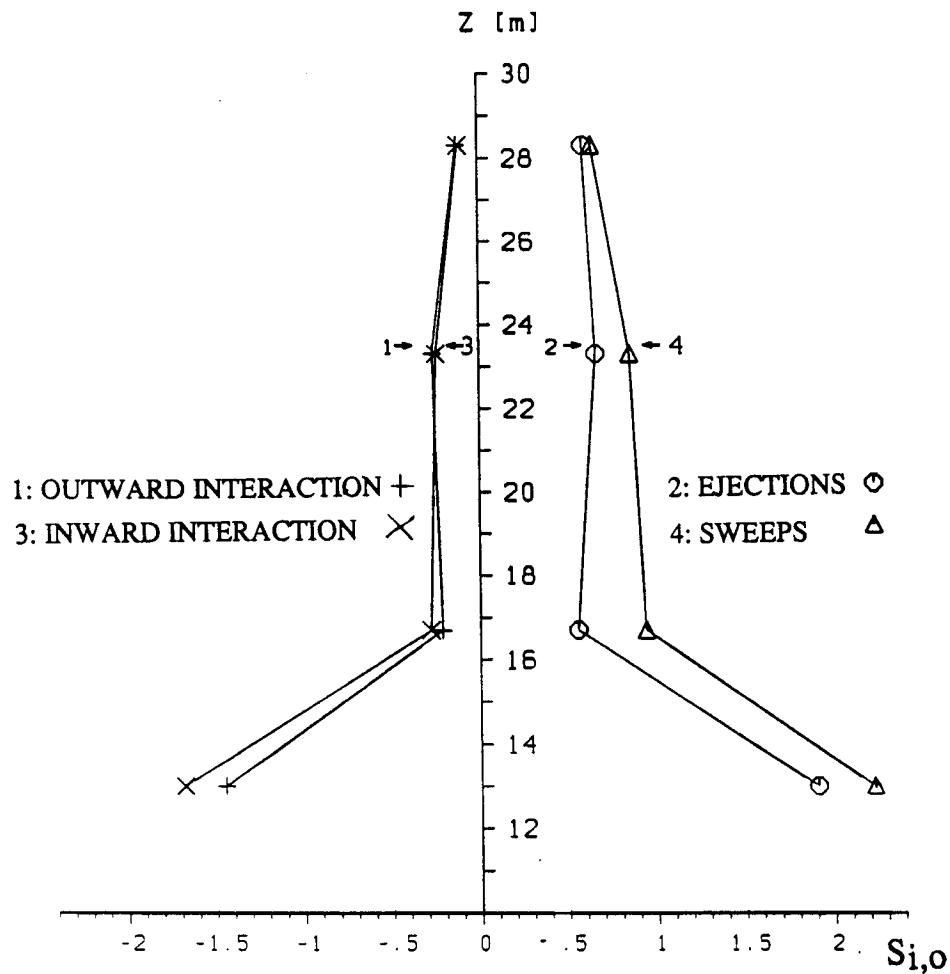
Figure 7.7   Averaged vertical profiles of the four contributions to Reynolds stress $S_{i,o}$, i= 1, 2, 3, 4.

A comparison of the exuberances (i.e. the ratio of upward to downward transport of momentum, equation (3.12)) at the two levels above the roof (Table 7.2) shows the increasing importance of inward and outward interactions at 23.3m as compared to the upper level. These arise from the disturbance of the more or less organized shear flow at a, presumably, small length scale. Fig. 7.8 illustrates this in an example. While the fluctuations of the longitudinal component are often similar at both heights, the low-frequency variations of w' are broken up at the lower level into fluctuations of higher frequency that are less correlated to the u'-component. This leads to the larger contributions of interactions at the expense of sweeps and ejections close to the surface. Furthermore, from Fig. 7.9 it is evident that for the lower level over the roof the larger contribution of the sectors 1 and 3 is due to *small* scale turbulent motion. For example, the contribution of inward interactions, $S_{3,o}$, is approximately -0.34 while at position 11 $S_{3,o} \approx$ -0.11. For hole size 5, on the other hand, the contribution of inward interactions is already smaller than -0.05 at both heights.
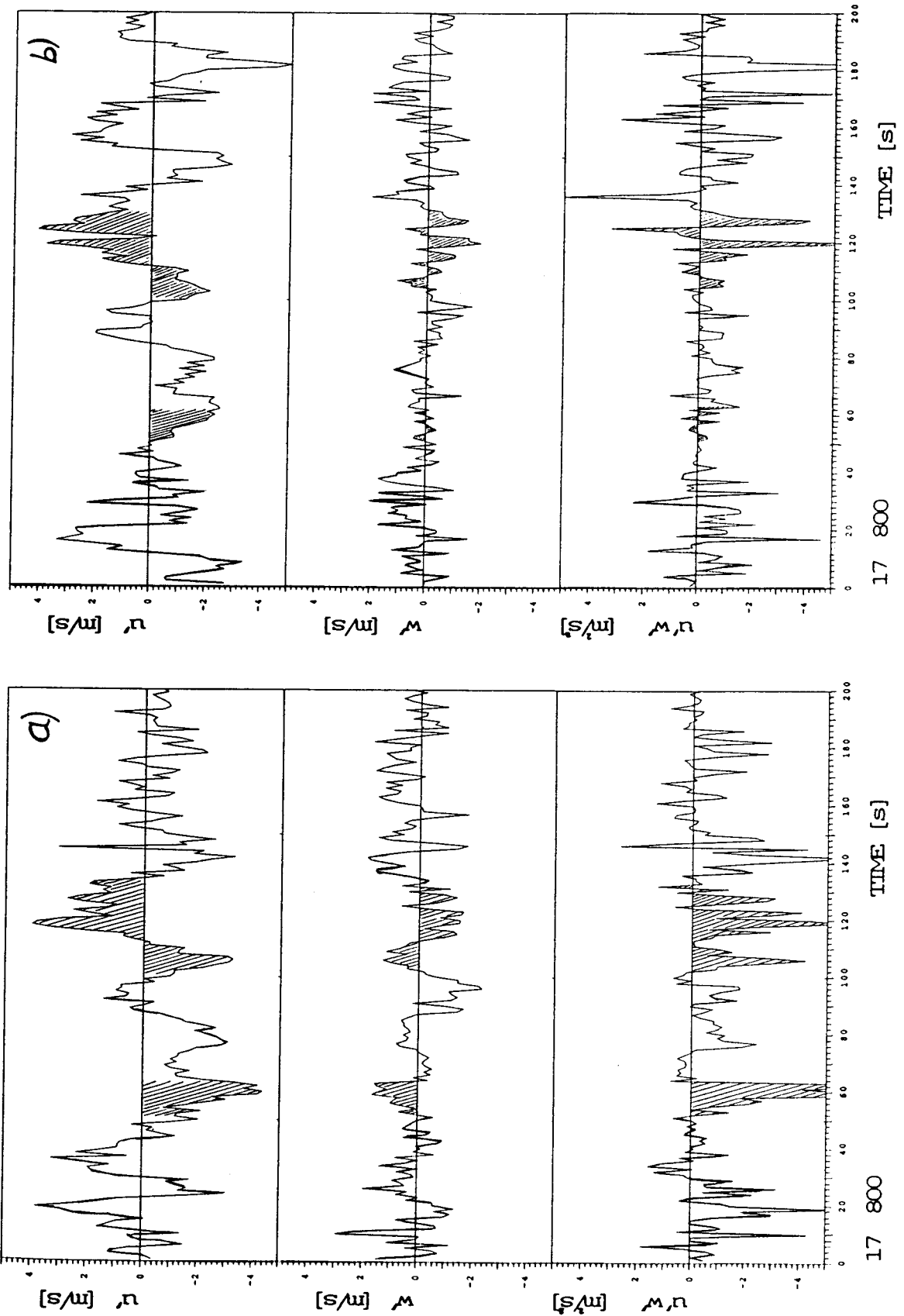
Figure 7.8   Time series of u', w' and u'w' for an arbitrarily chosen interval of 200
              seconds. a) position 11 and b) position 10. Shaded areas emphasize
              time intervals during which sweeps and ejections observed at the upper
              level appear as outward or inward interactions 5m closer to the surface.

Table 7.2   Parameters related to quadrant analysis.See definitions in Section 3.3

Position	z [m]	z/h	$S_{2,o}/S_{4,o}$	ΔS_o	E [*]
11	28.3	1.55	0.921	0.051	-0.190
10	23.3	1.27	0.887	0.107	-0.415
4+	23.3	1.27	0.655	0.273	-0.237
3	16.7	0.91	0.592	0.383	-0.331
2	13	0.71	0.856	0.321	-0.758

[*] Exuberance as defined in equation (3.12)

The contributions of the four quadrants at varying hole sizes and for the different heights (Fig. 7.9) indicate that sweeps are associated with processes of much larger scale than ejections. Particularly at positions 3 and 4, closely above and below roof level, respectively, significant contributions to momentum transport due to sweeps occur at hole sizes up to 30. This is, to a somewhat lesser extent, also observed at position 10 but not at the uppermost level. This behaviour indicates that momentum is transported into the street canyon by sporadically (see below) penetrating eddies from aloft. From Fig. 7.9, a tendency for increasing, partly offsetting contributions from the four quadrants can be observed with decreasing height at both positions in the horizontal plane (i.e. "above roof" and "above and within the canyon"). This is a further indication for the "disorganisation" of the flow or, in other words, the reduced correlation between the u'- and the w'-fluctuations when approaching the surface.

Fig. 7.10 gives a comparison between the summed stress and time fractions (equation (3.9)) at hole size zero and at different heights as a measure for intermittency. The most intermittent turbulence is observed at the 16.7m level. Here, about 70% of the total momentum transfer at hole size 5 occurs during less than 10% of the time and the ratio between total time fractions and total stress fractions is only 0.129 (cf. Table 7.3). At the other extreme, the level near the zeroplane displacement height within the canyon (position 2), large fractions of total stress occur up to hole size 30 during at an almost comparable fraction of time (note, that total stress is very close to zero at this height). There are no significant differences in intermittency between the three positions above roof level (Table 7.3) Thus, from Fig. 7.9 (and Fig. 7.7) the transport of momentum at the different heights can be characterized as follows:

z/h = 1.55: About 30% of total stress contributions occur at hole sizes smaller than 5.
              Sweeps slightly dominate ejections. Small interactions.

z/h = 1.27:

"roof"   Enhanced contributions from the interactions (as compared to z/h =
              1.55). Tendency to smaller scale transport of momentum (40% of total
              stress contribution at hole size smaller than 5). Sweeps slightly dominate
              over ejections. All $S_{i,o}$ larger than at z/h = 1.55.

"canyon"   Sweeps clearly dominate ejections at all hole sizes, while the interactions
              are much smaller than at the same height over the roof. No enhanced
              intermittency as compared to positions 10 and 11.

z/h = 0.91: Transport of momentum occurs at large hole sizes (more than 70% of
              total stress at hole sizes larger than 5) and strongly intermittent.
              Downward transport is partially offset by upward transport
              (interactions). Sweeps clearly dominate.

z/h = 0.71: Almost no net transport of momentum with large contributions $S_{i,o}$ (>1)
              from all sectors. Large stress fractions at hole sizes up to 30 with also
              considerable time fractions at this hole size.

Table 7.3   The ratio of summed time fractions to summed stress fractions
             $\Sigma\vartheta_{i,H}/\Sigma S_{i,H}$.(i=1 to 4) at hole sizes 5 and 10

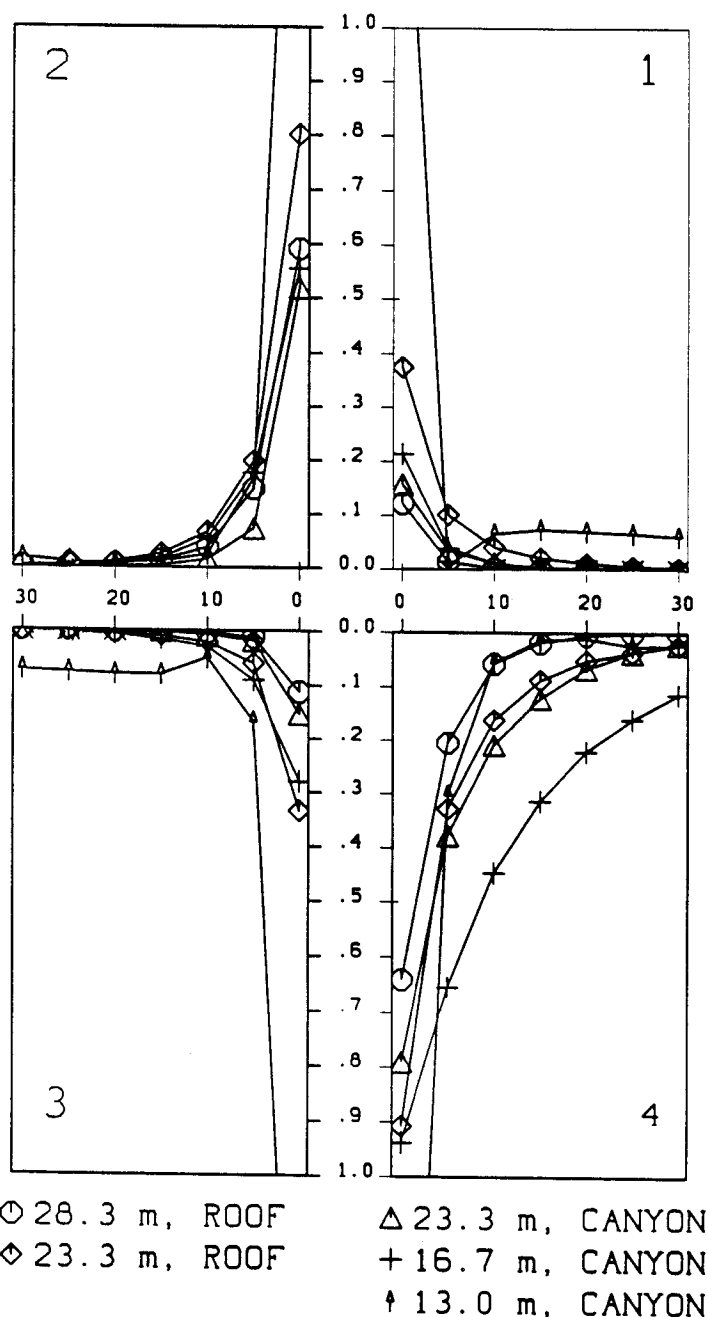| Height	Hole size	
z [m]	5	10
28.3	0.166	0.081
23.3 (roof)	0.199	0.111
23.3 (canyon)	0.171	0.092
16.7	0.129	0.065
13	0.633	0.571

Figure 7.9 $|S_{i,H}|$ (i= 1, 2, 3, 4) (vertical axis) for hole sizes zero to 30 (horizontal axis) and at different heights. Large numbers in the corner of each box denote the quadrant number i.

The present results are in very good agreement with what was reported by Raupach (1981) from artificial rough and smooth surfaces in a wind tunnel study. The inertial sublayer is identified in these wind tunnel experiments as a layer with $S_{2,0} \approx S_{4,0} \approx$ 0.6, both having significant contributions at $H \geq 10$, whereas $S_{1,0} \approx S_{3,0} \approx -0.1$ with vanishing contributions for $H \geq 5$. Within the roughness sublayer over the roughest surface, sweeps are dominating turbulent transport of momentum and have

contributions to total stress up to $H \geq 20$, whereas ejections cease to contribute at $H \geq 3$. The main differences to the present observations are:

- Raupach (1981) observes clear roughness sublayer behaviour at $z/h = 1.46$, whereas at $z/h = 1.55$ over the urban surface (which seems to be a comparable height), the distribution of the 4 quadrants tends towards inertial sublayer behaviour.

- The fast decrease of contributions from ejections as hole size increases, is not so pronounced in the URS as observed in the wind tunnel.However, he points out that the ratio of sweeps to ejections (or the difference between them) is strongly dependent on the density of roughness elements.

- The behaviour of his "within Canopy" level ($z/h = 0.53$) rather compares to the present position 3 ($z/h = 0.91$) than to position 2 ($z/h = 0.71$). However, this is associated with considerably larger total downward transport of momentum at the mid-canopy height in the wind tunnel experiment than at the present position 2 (see the results of Raupach et al.1980). It seems, that for "d-type" roughness (in the notation of Perry et al., 1969, see also Section 9.4 for a detailed discussion of "d-type" and "k-type" roughness') where recirculating vortices can be formed behind roughness elements (as can be anticipated for the present case), not ejections dominate the momentum transfer (Townsend, 1976), but rather momentum transfer is stopped at a certain level (identified to be the mean zeroplane displacement in the present study).
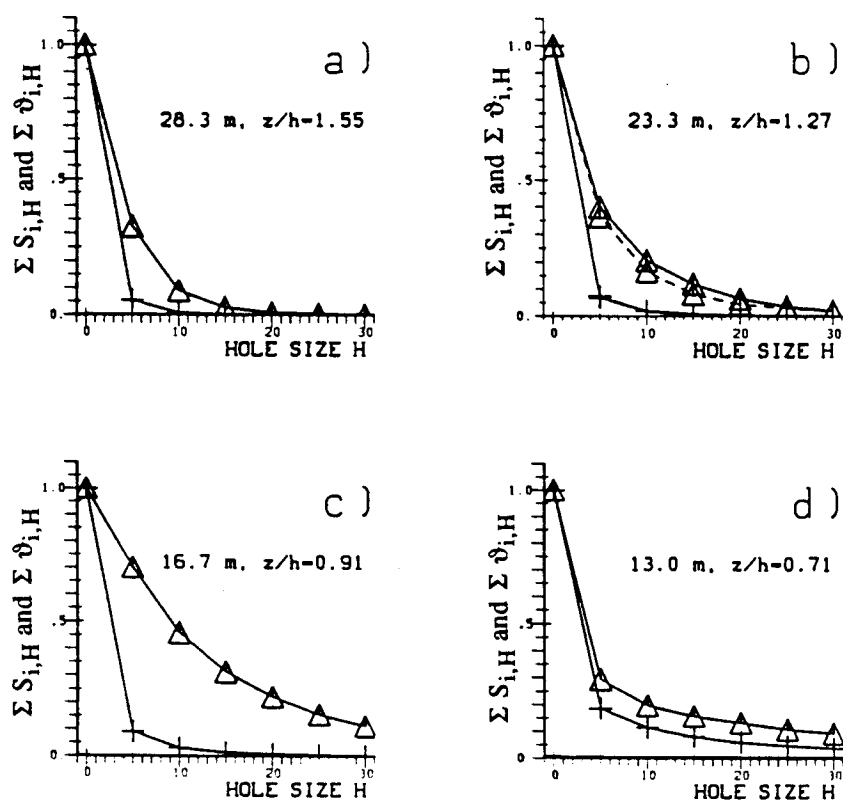

Figure 7.10   Comparison of the summed stress fractions $\Sigma S_{i,H}$.(i=1 to 4) and the summed time fractions $\Sigma \vartheta_{i,H}$ (i=1 to 4) for different hole sizes H. a) position 11, b) position 10 (—) and position 4[+] (---, above canyon), c) position 3 and d) position 2.

This last point is also the main discrepancy when comparing the present results to a corn canopy flow (Shaw et al., 1983). For this type of canopy, no decrease of the exuberance (to larger negative values) with decreasing height was observed but rather a relatively constant value of -0.2. It arose from approximately constant contributions (within the canopy) from the interactions while the contribution of sweeps increases with decreasing height (in the upper half of the canopy) and the one of ejections decreases. Within and above a deciduous forest (Baldocchi and Meyers, 1988), the vertical structure of the stress field is also somewhat similar to the present results. At a level (within the crown area), where the total momentum transfer is already small with respect to above canopy values the contributions to total stress from the four quadrants become very large (> 1.5) and are partially offsetting each other. Furthermore, the exuberance within a deciduous forest canopy ranges between -0.3 and -0.8 (associated with small total momentum transport) comparable to the values found for the UCL. Baldocchi and Meyers (1988) argue that large (negative) exuberance values may be associated with wake turbulence and secondary circulations. The present urban canopy, for which the importance of wake effects has been shown earlier and the presence of vortices (at least in some cases with appropriate wind direction) can be assumed, strongly supports this hypothesis.

7.5 Resulting Profile of Mean Wind Speed

If the observed profile of Reynolds stress is the dominant momentum source close to the surface (in stationary flow and non-advective conditions) and thus counteracts the momentum loss due to frictional forces, this has some important consequences for the profile of mean wind speed. Starting with a qualitative argument, one may consider a thin layer of height δz within the roughness sublayer. Turbulent transport of momentum supplies this layer with a certain "amount" of momentum from above and, due to the decrease of Reynolds stress in the profile near the surface, the turbulent transport through the bottom of this layer is somewhat smaller. Thus, the resulting profile of mean wind speed can be expected to have a smaller gradient than the well-known semi-logarithmic profile (equation (2.30)) and, close to the surface, the wind speed must be larger than predicted by equation (2.30). This qualitative behaviour has been reported by Raupach et al. (1980) for the flow close to various types of rough surfaces in a wind tunnel experiment.

Assuming that local scaling holds for the non-dimensional gradient of mean wind speed, i.e.

$$\frac{d\bar{u}}{dz'}\frac{kz'}{u_*(z')} = \phi_m(z'/L(z'))$$

(7.7)

where u*(z') refers to equation (7.3), it is possible to calculate a profile for mean wind speed. The assumption concerning local scaling will be justified in Chapter 11. For every single turbulence run, equation (7.7) has been integrated numerically starting at the uppermost level and propagating downward. The turbulent flux of sensible heat (for the calculation of the local Obukhov length L(z')) has been parameterised using Fig. 8.3 (see Chapter 8). To make different runs comparable to each other, these calculated wind speeds have been scaled with u*c(38m) and then averaged over all runs. In Fig. 7.11, this average "calculated" profile (evaluated at the heights of actual measurements) is compared to the measured profile, which has been averaged in the same manner. Note that the lowest two levels within the canyon have not been included since they are located below the mean zeroplane displacement height and thus, equation (7.3) may not be applied. It can be seen that the correspondence between calculated and measured average profiles is excellent. For comparison, a "constant flux" profile has been calculated in the same manner but with assumed constant turbulent fluxes of momentum and sensible heat. Fig. 7.11 shows that the observed profile of turbulent transport of momentum is indeed sufficient to explain the measured profile of mean wind speed, i.e. there is no other relevant transport of momentum in the roughness sublayer.
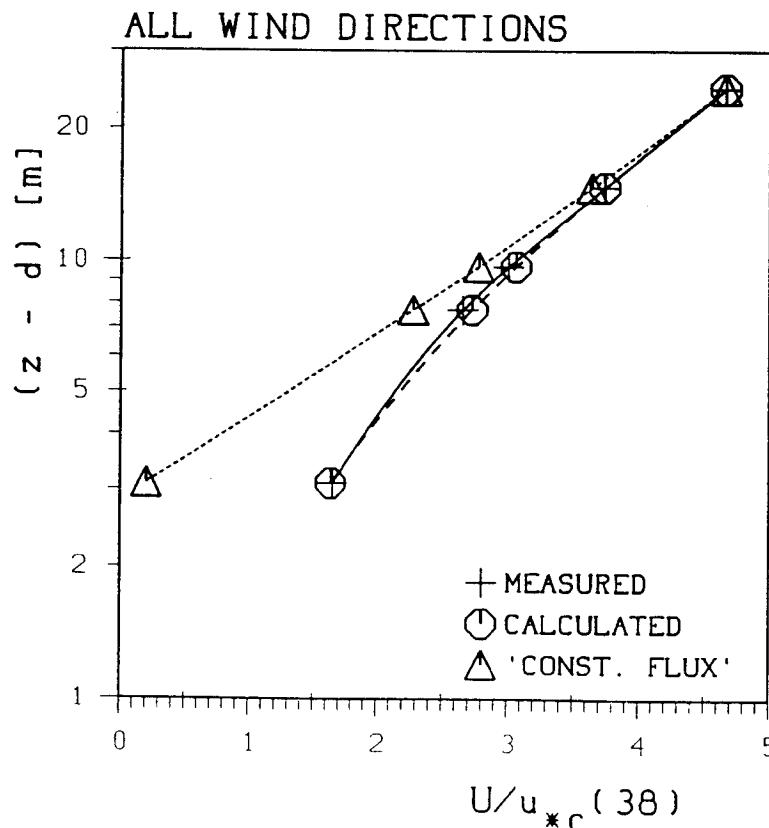
ALL WIND DIRECTIONS

Fig. 7.11   Average profiles of scaled wind speed. "Calculated" refers to equation (7.7). "Constant flux" has been calculated with u*(z) = const.= u*c(38m) and θ*(z) = const. = θ*c(38m) (see Chapter 8).

The above considerations are valid for *average* profiles, reflecting the requirement for horizontal averages. Corresponding to the differing shapes of the Reynolds stress profiles for different ranges of stability (Fig. 7.6), the calculated and measured profiles of wind speed may differ when restricting the data to one of the respective stability classes (not shown). A comparison of calculated and measured profiles of wind speed for individual runs shows that their difference is usually smaller than about 20% apart from the lowest considered level. The scatter decreases with height and reflects the larger horizontal inhomogeneity near the surface (see also Mulhearn and Finnigan, 1978).

7.6 Summary

The findings of the foregoing sections are summarized as follows:

- the horizontal inhomogeneity of the Reynolds stress field is quite large and increasing when approaching the "surface". In a field study, an average over all runs (with different wind directions) may yield an estimate of a horizontal average.

- Reynolds stress increases with height, from very small values at the zeroplane displacement height d to an inertial sublayer value at z_*. The height dependence as found in the present study can be expressed by equation (7.4).

- an estimate of the dispersive covariance contribution to total momentum transport shows, that the dispersive covariance cannot be the main reason for the height dependence (decrease) of Reynolds stress in the roughness sublayer. Pressure effects (form drag) must therefore be responsible for the observed height dependence of Reynolds stress.

- As a result of form drag acting upon the flow (the more effective the closer to the roughness elements), its "organized" structure is broken up by small scale disturbances, resulting in larger ("random") upward contributions to total momentum transfer and smaller ("organized") downward contributions.

- Using the height dependence of Reynolds stress, the profile of mean wind speed can be calculated under the assumption of local scaling (equation (7.7)). On average, difference between the observed and calculated profiles of wind speed are very small, thus indicating that turbulent transport of momentum is the dominant process for the description of the momentum balance within the roughness sublayer.

8. Turbulent Flux of Sensible Heat

With the equipment available, it was not possible to measure the turbulent heat flux ($\sim \overline{w'\theta'}$) simultaneously at more than one height (the 2x2D sonic did not yield a temperature measurement). Since the findings concerning the vertical structure of Reynolds stress made any constant flux assumption for turbulent heat flux in the urban roughness sublayer questionable, it was desirable to define a temperature scale in order to make the different runs comparable and evaluate the vertical structure of turbulent heat flux in the URS. As a scaling temperature, $\theta_{*c}(38m)$ was therefore calculated from the gradient of potential temperature evaluated at the uppermost (profile) level. This means, similar to the calculation of $u_{*c}(38m)$, that it was *assumed* that inertial sublayer scaling is valid at this level (equation 2.32). For the dimensionless temperature gradient Φ_h, the formulation of Businger et al. (1971) (modified after Högström, 1988) was chosen:

$$\phi_h = 0.95(1-19.3\tfrac{z'}{L})^{-1/2} \qquad \text{unstable}$$

$$\phi_h = 0.95 + 7.8\tfrac{z'}{L} \qquad \text{stable} \qquad\qquad (8.1)$$

Stability was determined at z=38.3m using the Gradient Richardson number R_i and equation (2.24).

Two problems concerning the calculation of $\theta_{*c}(38m)$ had to be taken into account in the near neutral range:

- very small temperature gradients: the accuracy of the temperature measurements does not allow to distinguish between e.g. $d\overline{\theta}/dz = 5\times10^{-5}$ Km^{-1} a n d $d\overline{\theta}/dz = 5\times10^{-3}$ Km^{-1} although $\theta_{*c}(38m)$ changes by two orders of magnitude. Runs with a gradient of potential temperature smaller than the *resolution* of the gradient (i.e. $d\overline{\theta}/dz \leq 2\times10^{-3}$ Km^{-1} were excluded from the analysis.

- Although during all runs (and at all heights) a positive turbulent heat flux ($\overline{w'\theta'} \geq 0$) was measured, indicating an unstable stratification, a few cases with (valuable, see above) positive Richardson numbers at z=38.3m occured. These runs, were also excluded from the analysis due to their "chaotic" behaviour.

The scaled turbulent flux of sensible heat $\overline{w'\theta'}$ (z) / $u_{*c}(38m)\cdot\theta_{*c}(38m)$, averaged over all wind directions, is shown in Fig. 8.1. The variance of the individual runs at a particular position (expressed as error bars in Fig. 8.1) is considerably larger than for

the scaled Reynolds stress. It amounts to roughly 50% of the mean value at most positions. This may have three reasons:

- the horizontal variability is considerably larger for turbulent heat flux than for Reynolds stress (see 7.2). However, this is not supported by the difference of the mean values at the 23.3m level.

- $\theta_{*c}(38m)$ is less useful as a scaling variable than $u_{*c}(38m)$, in other words, while the results presented in Chapter 7 support the use of $u_{*c}(38m)$, the temperature field is such that the calculation of $\theta_{*c}(38m)$ may not be justified.

- the fact that $u_{*c}(38m)$ and $\theta_{*c}(38m)$ are both necessary in order to scale $\overline{w'\theta'}$ (z), introduces the uncertainty concerning the assumption of inertial sublayer scaling at 38.3m twice into the analysis.

ALL WIND DIRECTIONS
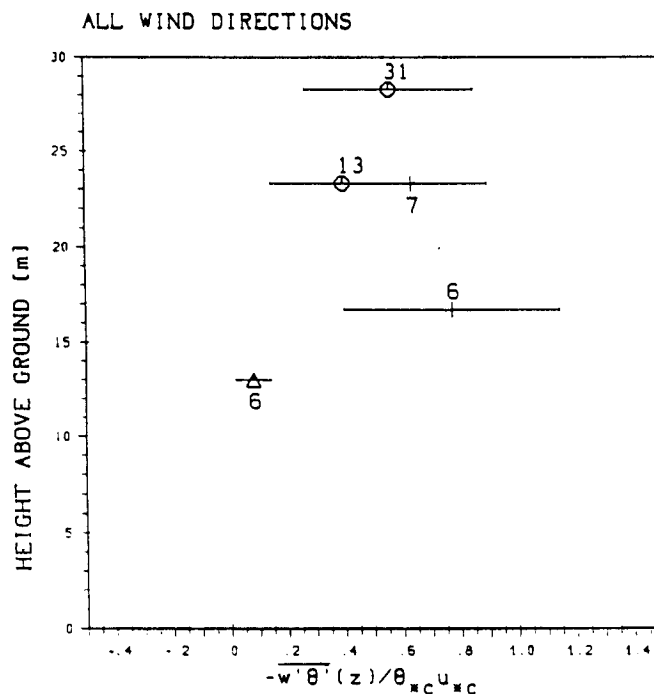
Figure 8.1   As Fig. 7.5 but for $\overline{w'\theta'}$. θ_{*c} and u_{*c} are calculated from the profile data at position 12.

A detailed inspection of the limited number of cases where two or more subsequent runs are available for analysis shows indeed that a change in turbulent heat flux (as measured by eddy correlation) is not necessarily accompanied by a corresponding change in the gradient of mean potential temperature (or, sometimes vice versa). While the mean gradient is strongly influenced by the proximity of the surface (see Appendix A3.3), it must be assumed that processes of larger scales (such as large eddy motions) may influence the characteristics of the observed turbulent heat fluxes. The few runs where "counter-gradient turbulent heat fluxes" were measured (positive $\overline{w'\theta'}$, while the local gradient of potential temperature indicates a stable stratification) point to a possible

importance of large eddy influences (see also Chapter 11). These latter runs, however, have been excluded from the present analysis, since even one single "counter-gradient run" at a particular position introduces a very large variance in the average scaled turbulent heat flux $\overline{w'\theta'}$ (z) / u_{*c}(38m)$\cdot\theta_{*c}$(38m) through the change of sign. Even if taken together into a separate group, no characteristic behaviour can be observed, indicating that in these cases θ_{*c}(38m) fails completely as a scaling variable.
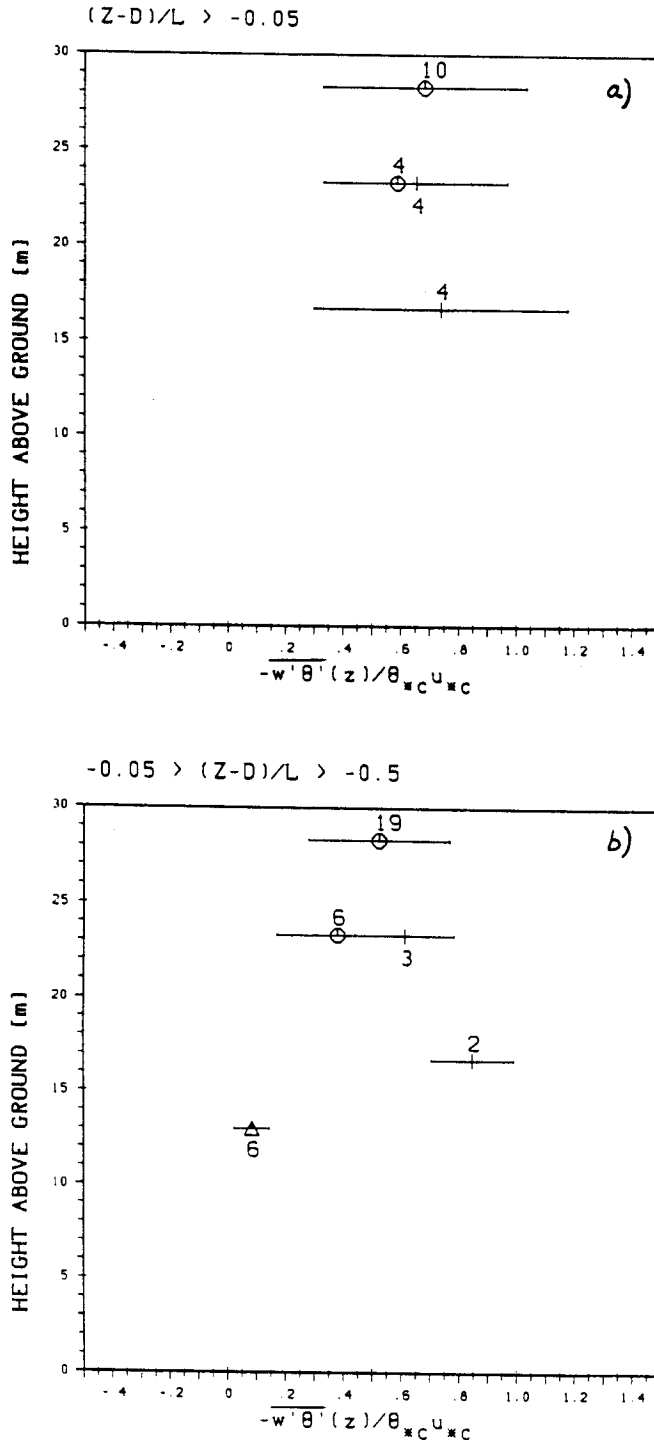
Figure 8.2   As Fig. 8.1, but for a) near neutral stability and b) weakly unstable stratification.

Even though it was shown that $\theta_{*c}(38m)$ is less suitable as a scaling variable than $u_{*c}(38m)$, it might be instructive to look at the mean values of the scaled turbulent heat flux in Fig. 8.1. Vertical turbulent transport of sensible heat appears to be very small (but still positive) within the street canyon. On average, the maximum is observed close to roof level h, while the horizontally averaged turbulent heat flux first decreases and then tends to increase again with increasing height.

The heat source (or sink) is located near the roof level, at the level which has been termed "active surface". Both, the heated roof surface (during the day) and the canyon, acting as a "heat trap", contribute to the source. Since the horizontal differences of potential temperature at 21.3m between the roof and the canyon are usually very small (cf. Appendix A3.3), the local maximum of turbulent heat flux close to the top of the canyon can be understood considering the distorted flow structure (Fig. 7.5): below the active surface vertical turbulent transport of sensible heat is quickly suppressed by the increasing disorganisation of the flow, as it was observed for turbulent transport of momentum. The close presence of the heat source counteracts the general decrease of the "transport capacity" of the flow (Chapter 7) near the roof level. Thus, the scaled turbulent heat flux some meters above roof level is smaller than at the active surface. In this same height range, we often observe perturbed profiles of potential temperature (Fig. A3.18). The numerical values of $\overline{w'\theta'}$ (z) / $u_{*c}(38m)\cdot\theta_{*c}(38m)$ *above* roof level that are always less than unity and the fact that the turbulent flux of sensible heat is in reasonable equilibrium with the gradient of potential temperature at 28.3 m (see Section 11.2), indicate that

- the kinematic turbulent heat flux at 38.3m, $\overline{w'\theta'}$ (38m) , should also be in local equilibrium with the temperature gradient at this level, and therefore

- the turbulent flux of sensible heat is likely to further increase at heights larger than the uppermost position of the present measurements.

In other words, there is some evidence that the tendency for increasing values of $\overline{w'\theta'}$ (z) / $u_{*c}(38m)\cdot\theta_{*c}(38m)$ between positions 10 and 11 reflects such an increase of the turbulent heat flux in the upper part of the roughness sublayer.

In spite of all shortcomings mentioned above, concerning the validity of $\theta_{*c}(38m)$ as a scaling variable in the present case, a conceptual sketch of the vertical structure of turbulent heat flux is given in Fig. 8.3. Due to the large run-to-run variability it cannot be definitely concluded from the present data whether the turbulent flux of sensible heat has a vertical structure as depicted in Fig. 8.3 or whether it is simply increasing with height. Nevertheless, it seems clear that this vertical structure is more complex than that observed for Reynolds stress.

The question arises, to what extent the observed turbulent flux of sensible heat is responsible for the heat exchange in the roughness sublayer between the "surface" (i.e. the roof region) and the layers lying above. A similar analysis as for the profile of mean wind speed (where it has been shown that the profile of Reynolds stress is sufficient to explain the momentum budget) has therefore been carried out for the potential temperature. Starting at the uppermost level, equation (2.32) has been integrated downward numerically using a interpolated profile of the observed average turbulent flux of sensible heat instead of θ_*^{IS}. The average measured and calculated profiles of potential temperature are clearly different (not shown), thus indicating that processes other than turbulent transport significantly contribute to the vertical heat exchange.

The first law of thermodynamics for a stationary flow (for which molecular dissipation and radiation divergence can be neglected) can be written

$$\overline{u}\frac{\partial \overline{\theta}}{\partial x} + \overline{w}\frac{\partial \overline{\theta}}{\partial z} = -\frac{\partial}{\partial x}\overline{u'\theta'} - \frac{\partial}{\partial y}\overline{v'\theta'} - \frac{\partial}{\partial z}\overline{w'\theta'} \qquad (8.2)$$

$$\quad \text{I} \qquad \text{II} \qquad\quad \text{III} \qquad\quad \text{IV} \qquad\quad \text{V}$$

where the advection term associated with the lateral wind component vanishes due to the choice of the coordinate system. From the present measurements, only terms II and V can be estimated at more than one height. In addition, $\overline{v'\theta'}$ is usually very small (due to the choice of the coordinate system) so that term IV becomes much smaller than the others. There is some indication from the present data that terms I and III are somewhat smaller than the remaining two and may vanish if true horizontal averages are considered. It therefore seems that, apart from the turbulent flux of sensible heat, the vertical advection term may significantly contribute to vertical heat exchange. This is supported to a certain extent by the present measurements of term III. However, the spatial resolution of mean vertical wind in the present data is much too small to allow definite conclusions concerning the contributions to the heat budget at different heights of the various terms in equation (8.2).

In future work, the spatial distribution of the vertical advection term and the vertical flux divergence will have to be evaluated in much more detail in order to explain the heat exchange within the roughness sublayer and in particular at its bottom, i.e. close to roof level. In addition, it will be necessary to perform simultaneous measurements of turbulent heat flux at sufficiently large heights to check whether i) there exists an inertial sublayer with respect to turbulent heat transfer and ii) at which height range (if not the same as for Reynolds stress).
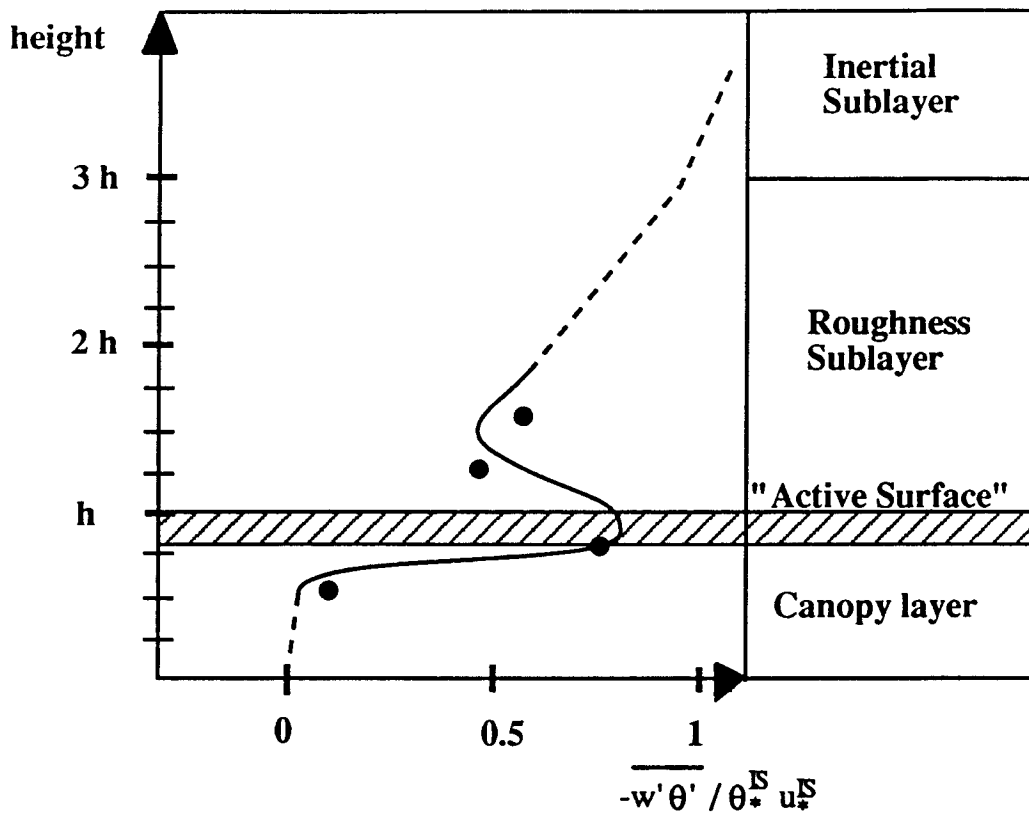
Figure 8.3   Conceptual sketch of the vertical variability of the turbulent flux of sensible heat. Vertical axis in units of h, the building height.

9. Velocity Variances

9.1 Horizontal Velocity Components within the Roughness Sublayer

For purely mechanical turbulence over ideal terrain the horizontal velocity variances can be expected to obey the simple relations

$$\sigma_{u,v} = A_{u,v} \cdot u_*$$ (9.1)

where $A_{u,v}$ are constants to be determined in neutral stability. Values for $A_{u,v}$ are in very good agreement for different sites (as long as only homogeneous fetch conditions are considered) and can be given as 2.4 and 1.9 respectively (e.g. Panofsky and Dutton, 1984). In complex (or rolling) terrain, however, they can be considerably larger (up to 4.5 and 3.8, respectively) or smaller due to the fact that horizontal velocity variance is mainly produced by large quasihorizontal eddies that are modified only slowly and "remember" rougher conditions of the upwind fetch (Panofsky and Dutton, 1984). For non neutral (convective) conditions low-frequency variations of large amplitude are superposed to horizontal velocity records. These variations are independent of height so that Monin - Obukhov scaling is not likely to apply. Therefore Panofsky et al. (1977) suggested a dependence on mixed layer height z_i

$$\frac{\sigma_{u,v}}{u_*} = \Phi_{u,v}\left(\frac{z_i}{L}\right)$$ (9.2)

Nevertheless, some authors report a certain dependence of $\sigma_{u,v} / u_*$ on stability, too (e.g. Steyn, 1982; Clarke et al., 1982; Ramsdell, 1975). In general, also the scatter of $\sigma_{u,v} / u_*$ increases considerably with larger - z_i/L.

For various urban environments neutral values for $\sigma_{u,v} / u_*$ have been reported (see Table 9.1). While σ_u / u_* show little differences to results from homogeneous terrain (2.2 - 2.8), values for σ_v/u_* vary between 1.5 (Bowne and Ball, 1970) and 2.8 (Högström et al. 1982). No dependence on surface characteristics can be found for these large departures to "ideal fetch"-values (Table 9.1). This might be partly due to the fact that not all authors provide the same information on geometry of the urban surface (height of roughness elements at the experimental site and - more important - z_0 and / or zero plane displacement in the upwind fetch or source area) or use different methods to determine those numbers.
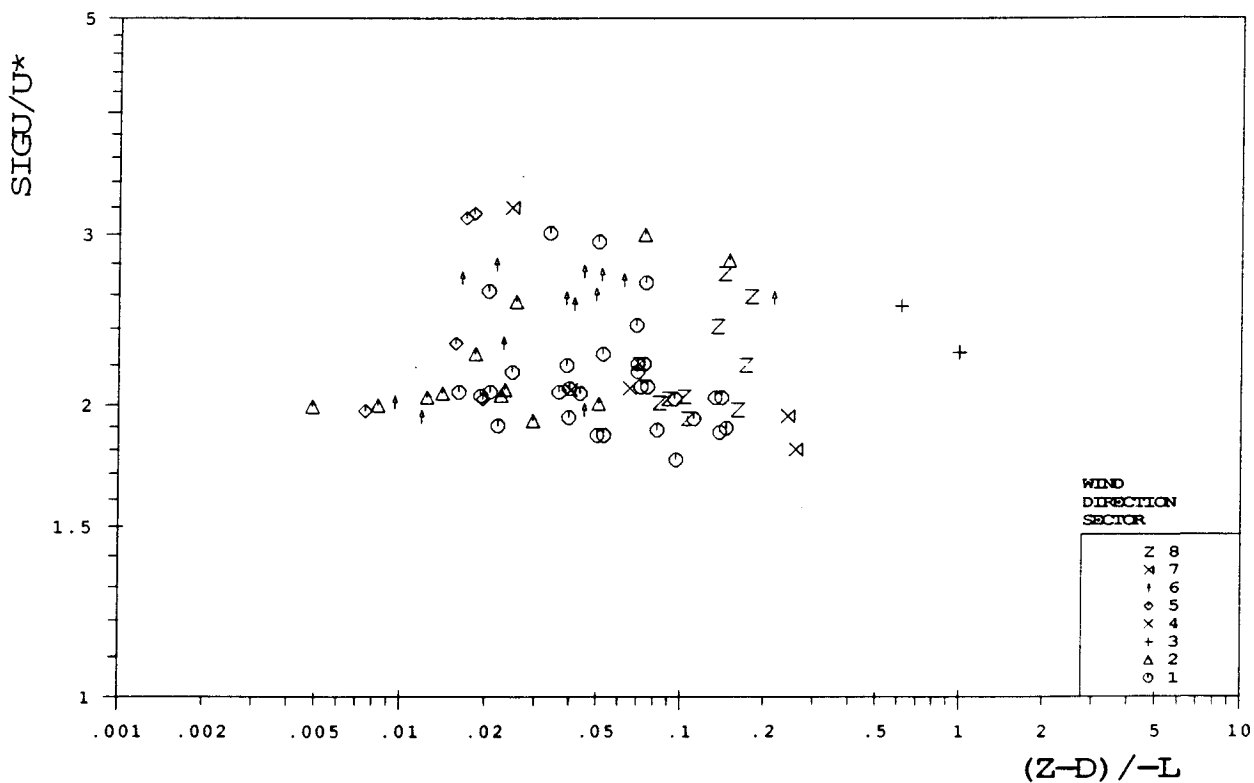
Figure 9.1   σᵤ/u* for different stabilities and wind direction sectors (as indicated by the different symbols). Measurements from positions 10 and 11.
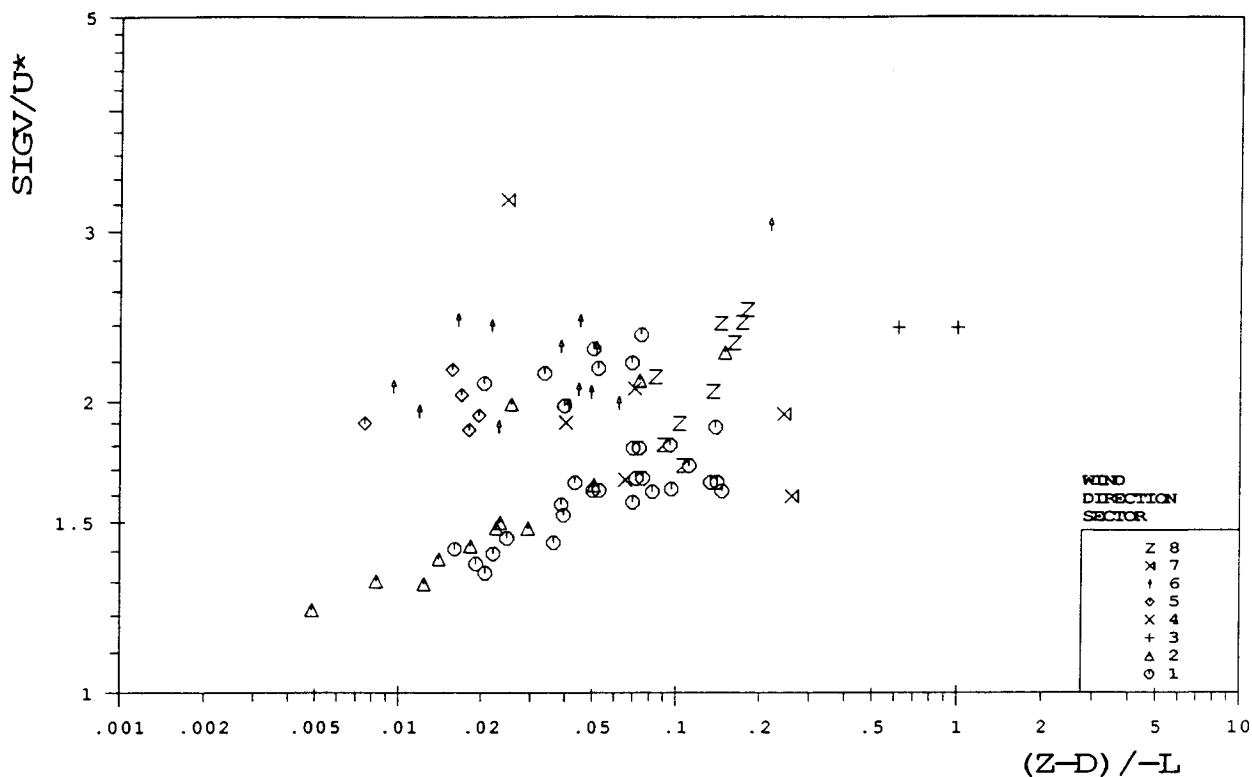

Figure 9.2   As Fig. 9.1 but for σ_v/u* .

Table 9.1:   Comparison of horizontal velocity variances as measured at different urban sites.

site, author	neutral limit σ_v/u_*	neutral limit σ_u/u_*	characteristic dependence on stability	height z above street level	height of buildings [m]	z'/z_0	alternative scaling
St.Louis, Clarke et al. (1982)	2.4	1.8	large scatter	30m	5.5 / 7.5 / 7.5	40 / 18 / 15	$w^* = \left(\frac{g}{T}\overline{w'T'}\cdot L_m(u)\right)^{1/3}$, $z/L < -1$, z_i: weak dependence
Vancouver, Steyn (1982, suburban)	2.2	1.7	scatter:larger for larger $\|z/L\|$, $\sigma_v/u_* = (a + b\frac{z}{L})^c$	20m	8.5	33	z_i/L or z/L: no preference
Uppsala, Högström et al.(1982)	2.5 / 2.8	2.2 / 2.8	no dependence on z'/L	50m / 27m / 8m	? / 15	?	
Fort Wayne, Bowne and Ball (1970)	~2.5	1.5	-	53.5m (?)		~ 8 $\left(=\left[\frac{z-z_0}{z_0}\right]\right)$, $z_0 = 6m$ (!)	
Adelaide, Coppin (1979)	2.5		weak trend	33.8m	~10	~200 [d = 0.75h, z_0 =0.12]	
Seattle, Ramsdell (1975)	2.5	2.0	weak dependence	0.6 - 48.2 m	9 - 15	11.25 - 18.75 [assumption: d = 0.75h]	
Zurich, present study	2.2	1.5	none	28.3m / 23.3m	9.3 - 16.1	3.2 - 21.6	

Table 9.2:   As Table 9.1, but for vertical velocity variances.

site, author	neutral limit	characteristic dependance on stability	height z above street level[m]	height of buildings [m]	z'/z_0	alternative scaling
St.Luis, Clarke et al. (1982)	1.3	yes (see text)	30	5.5 / 7.5 / 7.5	40 / 18 / 15	"mixed velocity scale" works best: $(u_*^3 + 0.4u_*)^{1/3}$ stable: u_*
Vancouver, Steyn (1982, suburban)	1.4	yes	20	8.5	33	z_i or z: no preference
Uppsala, Högström (1982)	1.4 - 1.5	none	50 / 27	? / 15	?	-
Adelaide, Coppin (1979)	1.1	yes	33.8	~10	~200 [d = 0.75h, z_0 =0.12]	-
Fort Wayne, Bowne and Ball (1970)	1.3	?	53.5	-	~8	?
Seattle, Ramsdell (1975)	1.5	weak	0.6 - 48.2	9 - 15	11 -.19 cf. Table 12.1	?
Zurich, present study	~1.0	see text	28.3 / 23.3	9.3 - 16.1	3.2 - 21.6	cf. Clarke et al.

Results from the present study are presented in the following. In Figs. 9.1 and 9.2 $\sigma_u/u*$ and $\sigma_v/u*$ respectively are plotted vs. the local value of stability (note that all turbulence characteristics including u* and L are taken as local values throughout the following). Different symbols indicate the 8 wind direction sectors. For the along-wind component a lower boundary of approximately 1.8 can be observed but no variation over the (relatively small) range of stability. An average value for all data from runs with stabilities (z'/L) larger than - 0.05 is determined as 2.2. For $\sigma_v/u*$ (Fig. 9.2) the same overall feature is observed and the mean value in the near neutral range is 1.5. Two very distinct groups of data, however, are found for small negative values of z'/L producing a larger scatter than for $\sigma_u/u*$ (these distinct groups are even maintained if all unstationary or otherwise rejected data - cf. Section 5.3 - are included in the analysis). Small values of $\sigma_v/u*$ are found only for situations with flow from wind direction sectors 1 and 2 (0 - 90°). These wind direction sectors have no predominant characteristics, neither close to the site (in a distance of the order of the surface areas for the various measurements, or approximately 1km) nor on a regional scale: the distance from the Anwand site to the surrounding hills - and their height - is not very different for the various sectors, apart from sector 3 where the lake provides a further opening. A reduced ratio of σ_v to u* might be an indication for a flow over rough ground, downstream of a smoother terrain (Panofsky an Dutton, 1984). However, an inspection of the z_0 values for the wind directions sectors (see Section 6.2) and of the city map does not provide further evidence that this could be the reason for the reduced $\sigma_v/u*$ when the flow approaches from sectors 1 or 2. Recalling equation (9.2), it has to be assumed that large-scale processes are responsible for the differences in $\sigma_v/u*$ between the wind direction sectors.

9.2 Vertical Velocity Component within the Roughness Sublayer

As the horizontal velocity components, σ_w is in non-buoyant situations over homogeneous terrain expected to obey the simple relation

$$\sigma_w = A_w \cdot u*$$ (9.3)

where A_w is a constant found to be approximately 1.3 over wide range of different sites. For non-neutral (convective) conditions, σ_w scales - other than the horizontal velocity variances - with the height of observation and is expected to follow Monin - Obukhov scaling.

$$\frac{\sigma_w}{u*} = \Phi_w \left(\frac{z'}{L}\right)$$ (9.4)

Panofsky et al. (1977) suggest for Φ_w

$$\frac{\sigma_w}{u_*} = 1.3 \left(1 - 3 \cdot \left(\frac{z'}{L}\right)\right)^{1/3} \tag{9.5}$$

while other authors find slightly different formulations (e.g. Businger, 1959; Wyngaard et al., 1971; cf. Fig. 9.3). In the limit of free convection, the vertical velocity variance becomes independent of friction velocity and can be described in terms of the convective velocity scale u_f

$$\sigma_w = 1.3\, u_f = \left(\frac{g\, \overline{w'T'}\, z'}{T}\right)^{1/3}. \tag{9.6}$$

In various studies, vertical velocity variances have been determined in urban environments. The values given in Table 9.2 for the neutral limit indicate a good general correspondence to ideal terrain values. Clarke et al. (1982), who provide the most extensive results on urban turbulence statistics in the literature, observed σ_w/u_* to be smaller in magnitude than predicted by (9.5) especially for weakly unstable runs (small negative values of z'/L) at their urban sites.

In Fig. 9.3 the stability dependence of σ_w/u_* at the Anwand site is depicted together with two examples of (9.4). A neutral value is determined from all measurements with $|z'/L| \leq 0.05$ as 1.0. In general, vertical velocity variances are smaller than predicted by e.g. (9.5) but the relatively small amount of data does not allow strong conclusions. Due to small range of stabilities observed, results are not conclusive in terms of the -1/3 power for strong convection. There is, however, no contradiction, either.

Using a simplified TKE budget equation (Clarke et al., 1982)

$$\varepsilon = \frac{u_*^3}{l} + \frac{g}{T}\overline{w'T'} + \frac{1}{2}\frac{d}{dz}\left(\overline{w'e^2}\right) + \frac{1}{\rho}\frac{d}{dz}\left(\overline{p'w'}\right) \tag{9.7}$$

and an expression for the dissipation rate of TKE (Tennekes and Lumley, 1972)

$$\varepsilon = \frac{\sigma_w^{\,3}}{L_\varepsilon(w)}, \tag{9.8}$$

equation (9.4) can be rearranged: if the last two terms on the right hand side of (9.7) are neglected (results of Wyngaard and Coté (1971) indicated the net effect of these terms to be small) and $l = kz'$, Clarke et al. (1982) find

$$\sigma_w = C \left(u_*^3 + k u_f^3 \right)^{1/3} \qquad\qquad (9.9)$$

with $C \sim (L_\epsilon(w)/l)^{1/3}$. To determine the relative importance of the thermal and shear induced vertical motions, a similar form as (9.9) but consistent with (9.5) can be obtained through a least square fit of the form

$$\sigma_w^3 = C_1 u_*^3 + C_2 u_f^3 \qquad\qquad (9.10)$$

as done by Clarke et al. (1982). In this notation, (9.5) by Panofsky et al. (1977) corresponds to $C_1 \approx 2.2$ and $C_2 \approx 2.6$.
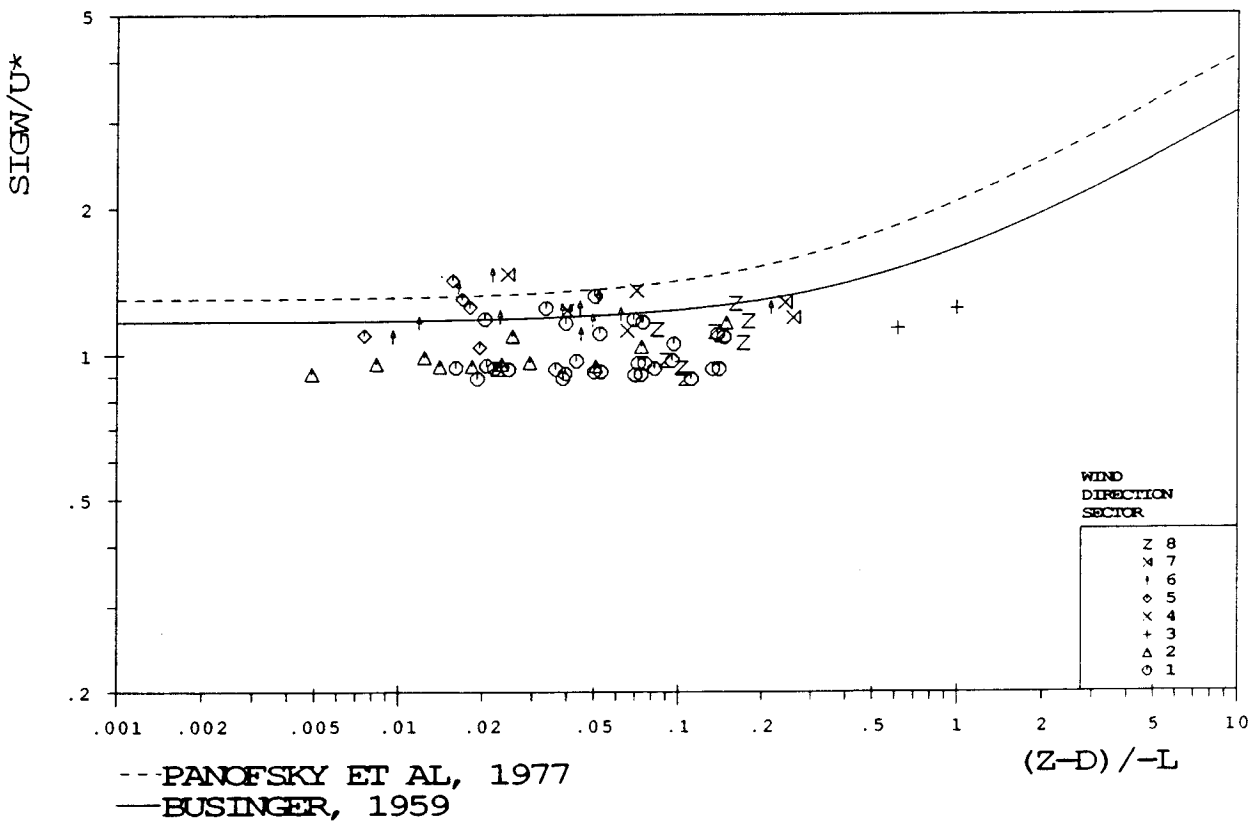
Figure 9.3   As Fig. 9.1 but for σ_w/u_*. Solid and dashed lines are predictions by Businger (1959) and Panofsky et al. (1977), respectively.

In Fig. 9.4, the right hand side of (9.9) is shown vs. σ_w. The factor of proportionality, C, is slightly larger than unity (C $\approx$ 1.12) but smaller than reported by Clarke et al. (1982) (1.18 for their urban sites, 1.27 for the rural site and the same stability range). These differences might be due to different measurement heights z' or boundary layer states (see definition of C after equation (9.9)), since $L_e(w)$ can be expressed in terms of λ_m, the peak wave length of e.g. the w-energy spectrum, Clarke et al., 1982). It is also not far from experimental uncertainty. Table 9.3 lists the values for C_1 and C_2 (9.10) for the Anwand data and St. Louis data (Clarke et al., 1982).

Table 9.3 also lists the Parameters C_1' and C_2' determined after (9.10) in a form consistent with (9.5). In this notation we have

$$C_1' = C_1^{1/3} \text{ and } C_2' = \frac{C_2}{0.4 \cdot C_1}.$$

For comparison, results from an ideal site (Panofsky et al., 1977) and from the St.Louis study (Clarke et al, 1982) are given. As compared to ideal sites (or at least rural sites), the urban measurements show a less pronounced dependence on stability, indicated by considerably smaller values for C_2'. The parameters C_1 and C_2 are smaller in urban areas indicating that both friction velocity and u_f are larger while the ratio σ_w/u_* remains relatively unchanged (or slightly smaller). The relative importance of the two processes that are involved in generating vertical fluctuations, mechanical and thermal effects, is quite different for urban and non-urban sites. In the former, mechanical production clearly dominates (see Table 9.3, C_1/C_2) whereas for rural sites thermally induced vertical fluctuations seem to be more important than those that are mechanically induced. In the case of the present data one might argue that due to the small stability range (0>z'/L> -1) this result could have been anticipated. The fact that almost the same ratio C_1/C_2 was found in St.Louis for a stability range of 0 >z'/L> -5, however, indicates that the dominance of mechanical over thermal production can be viewed as a general feature of vertical fluctuations over urban surfaces.

Table 9.3: Parameters for the determination of $\sigma_w/u_* = C_1'(1 - C_2'z'/L)$ and

$\sigma_w^3 = C_1 u_*^3 + C_2 u_f^3$, respectively from various sites.

study	C_1'	C_2'	C_1	C_2	C_1/C_2	site
Panofsky et al. (1977)	1.3	3	2.20	2.64	0.83	"ideal"
Clarke et al.(1982)	1.16	2.95	1.56	1.84	0.85	rural reference site*), z'/L > -5
Clarke et al. (1982)	1.13	1.56	1.44	0.90	1.60	four urban sites, average values *
present study	0.94	1.29	0.83	0.48	1.73	urban site, 0 > z'/L > -1

*) averaged over a value for the summer and fall data set, evaluated separately.
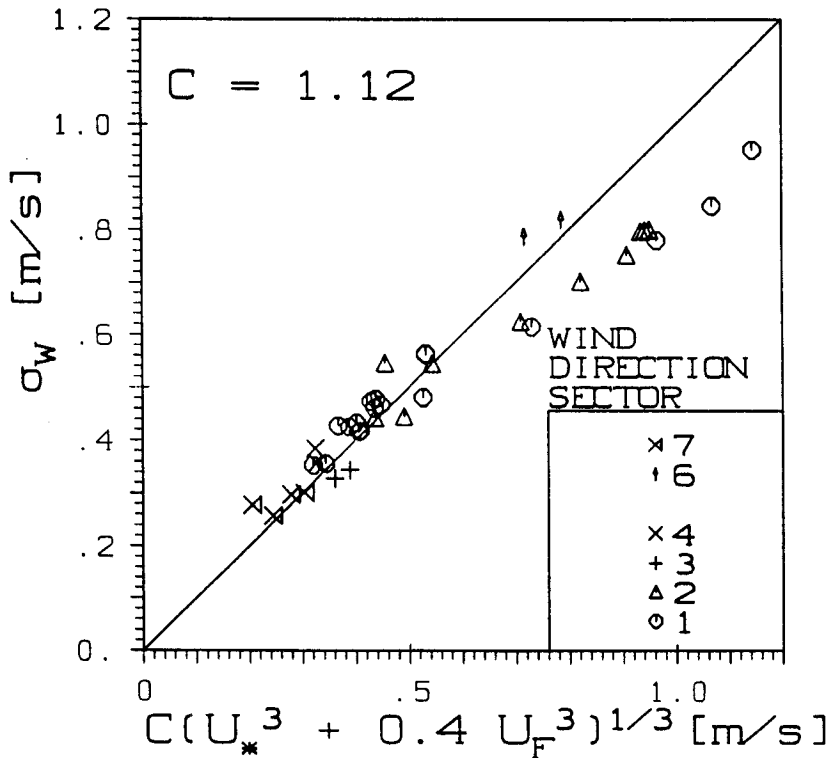
Figure 9.4 σ_w/u_* vs. the right hand side of equation (9.9). Different symbols for wind direction sectors as indicated.

9.3 Temperature Variance

The non-dimensionalized variance of temperature was used to determine the zeroplane displacement height (see Chapter 6.1). Thus, using the optimal d for the various wind direction sectors, σ_θ/θ_* is in fact forced to follow the inertial sublayer prediction (equation 6.2) as closely as possible. It was one of the prerequisites of the TVM (temperature variance method to calculate d) that the temperature variance obeys inertial sublayer scaling (even within the roughness sublayer over a certain type of surface) and *small* systematic departures may occur through an erroneous estimate of d. Nevertheless, this "forcing" of σ_θ/θ_* towards its inertial sublayer prediction does not change the fact that there are no large deviations from the inertial sublayer prediction for the present data (Fig.6.3a). If d would have been determined by e.g. a geometric method, this would not alter this result drastically. Fig 6.3b shows that even an extreme value of d (d $\approx$ h) has no severe effect on the general agreement of the present data with the inertial sublayer prediction. Note, however, that the temperature variance in Fig. 6.3 is scaled with the *local* θ_* and also stability is calculated from local values. Clarke et al. (1982) report a similar accordance of σ_θ/θ_* over an urban surface (St. Louis). Their temperature variances were also locally scaled (since only one measurement level was available). It appears therefore to be a general result that rough (urban) surfaces do not change the behavior of the non-dimensionalized temperature variance as long as they can be considered thermally homogeneous (see 6.1).

9.4 Scaled Profiles of Velocity variances

The same scaling variable as for Reynolds stress, $u_{*c}(38m)$, was used to obtain vertical profiles of the velocity variances and $\theta_{*c}(38m)$ for the profiles of σ_θ. See Chapters 7 and 8, respectively, for the definition and limitations in the use of these variables. Note especially that stability ranges given in the following refer to stability as determined at z = 38.3m.

a) longitudinal velocity variance

The averaged profile of $\sigma_u/u_{*c}(38m)$ over all wind directions and therefore corresponding to a horizontal average is presented in Fig. 9.5. Note that this type of scaling (i.e. non local), results in "too small" values as compared to ideal sites. This simply reflects the height dependence of the local u_*. The scaled σ_u increases with height throughout the canyon and remains more or less constant within the RS. At the lowest level within the canyon, we find a very large variability at both horizontal

positions and a clear difference in the averages among them. The two positions at z=23.3m still show considerable scatter but no systematic difference.

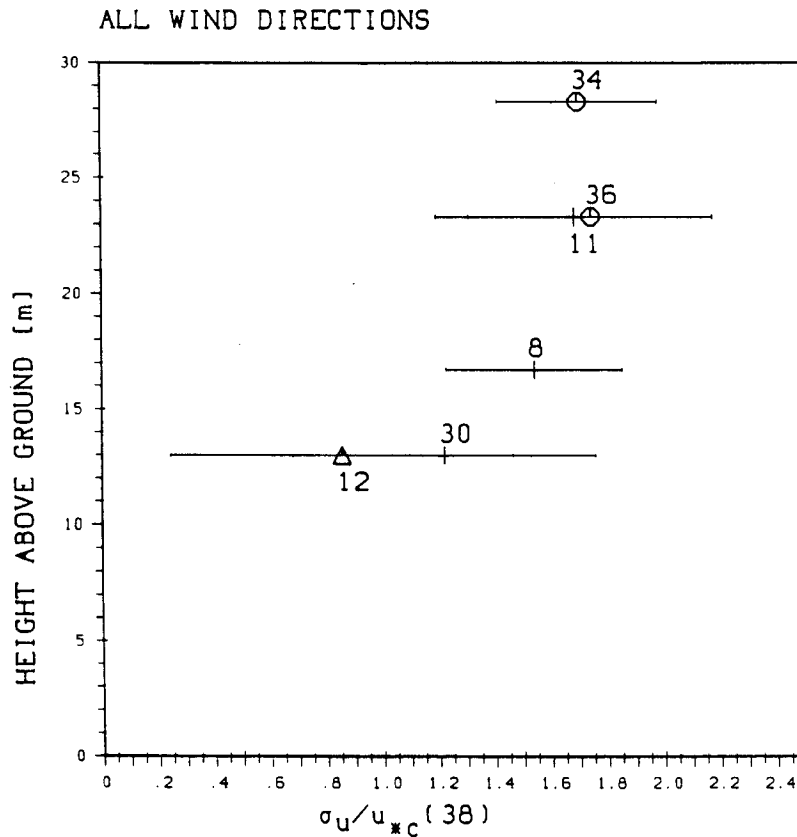ALL WIND DIRECTIONS

Figure 9.5   Scaled profiles of $\sigma_u/u*_c$(38m). $u*_c$ calculated from the profile data at position 12. Error bars indicate the run-to-run variability at any one level. (☉): positions 10 and 11, (+): positions 2, 3 and 4[+], (△): position 6. All available data included. The number close to each symbol refers to the number of runs for which averages (and variances) are shown.

a) longitudinal velocity variance

The averaged profile of $\sigma_u/u*_c$(38m) over all wind directions and therefore corresponding to a horizontal average is presented in Fig. 9.5. Note that this type of scaling (i.e. non local), results in "too small" values as compared to ideal sites. This simply reflects the height dependence of the local u*. The scaled σ_u increases with height throughout the canyon and remains more or less constant within the RS. At the lowest level within the canyon, we find a very large variability at both horizontal

positions and a clear difference in the averages among them. The two positions at z=23.3m still show considerable scatter but no systematic difference.

The profile does not show any well defined dependence on wind direction. For the *near neutral* runs, the vertical dependence within the canyon almost completely vanishes and a constant value of 1.75 throughout the whole height range under consideration is observed (not shown). While the profile of $\sigma_u/u_{*c}(38m)$ for the weakly unstable runs is quite similar as Fig. 9.5, no clear vertical structure can be observed if $z'/L < -0.5$. These latter runs, however, largely contribute to the large scatter at all levels in Fig. 9.5. It seems that the longitudinal velocity variance within the street canyon is only weakly influenced by the above-canyon flow in these cases.

ALL WIND DIRECTIONS
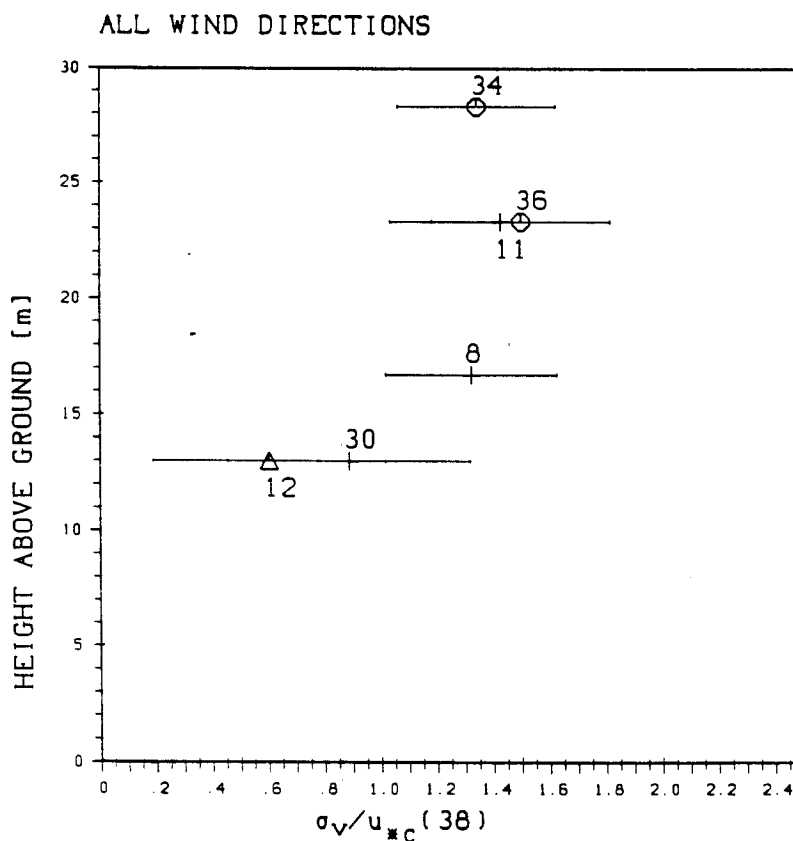
Figure 9.6   As Fig. 9.5, but for $\sigma_v/u_{*c}(38m)$

b) lateral velocity variance

$\sigma_v/u_{*c}(38m)$ behaves very similar on average as σ_u (Fig.9.6). There is, however, a slight tendency within the RS to decrease with height. This tendency originates from the near neutral runs (Fig. 9.7). For $z'/L < -0.5$, we observe again a completely different picture, contributing to the scatter in Fig. 9.6. No characteristic behaviour for different wind directions could be observed.

(Z-D)/L > -0.05
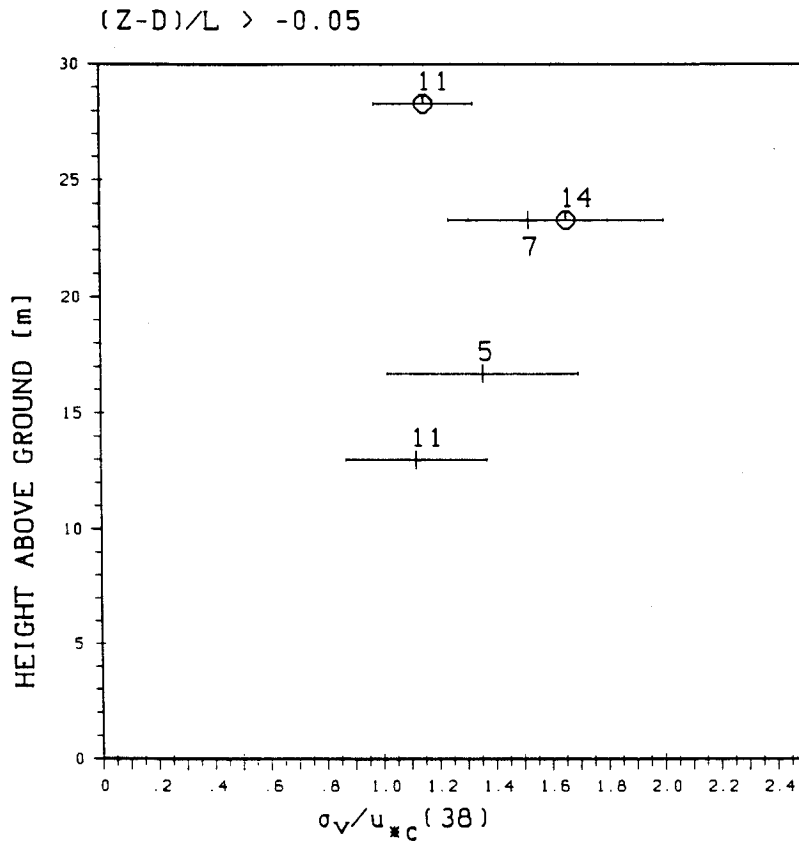
Figure 9.7   As Fig. 9.6, but for near neutral runs.

c) vertical velocity variances

The vertical velocity variance has the most complex structure. While showing little vertical variability in the overall average (all wind directions) but a large "scatter" at the lowest level (Fig. 9.8), the situation changes drastically for the three stability ranges (Fig. 9.9). In the near neutral runs, $\sigma_w/u*_c(38m)$ decreases with height over the whole height range (Fig. 9.9a), under weakly unstable conditions it does not change very much with height (Fig. 9.9b), and it increases with height if $z'/L < -0.5$. At $z=28.3m$ and also at $z=16.7m$ (!) we find rather little variation of $\sigma_w/u*_c(38m)$ with stability. At $z= 23.3m$ (especially the "above canyon" position) on the other hand, and clearly at $z=13m$ within the street canyon, σ_w seems to be strongly influenced by the stability of the overlying flow.

ALL WIND DIRECTIONS
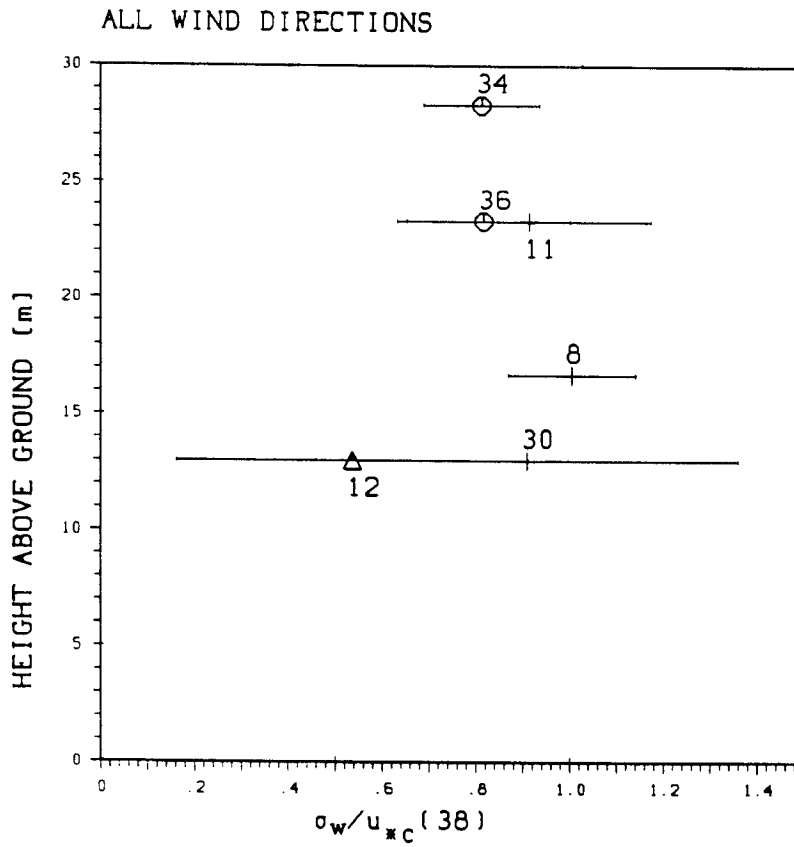
Figure 9.8   As Fig. 9.5, but for $\sigma_w/u*_c(38m)$

$(Z-D)/L > -0.05$
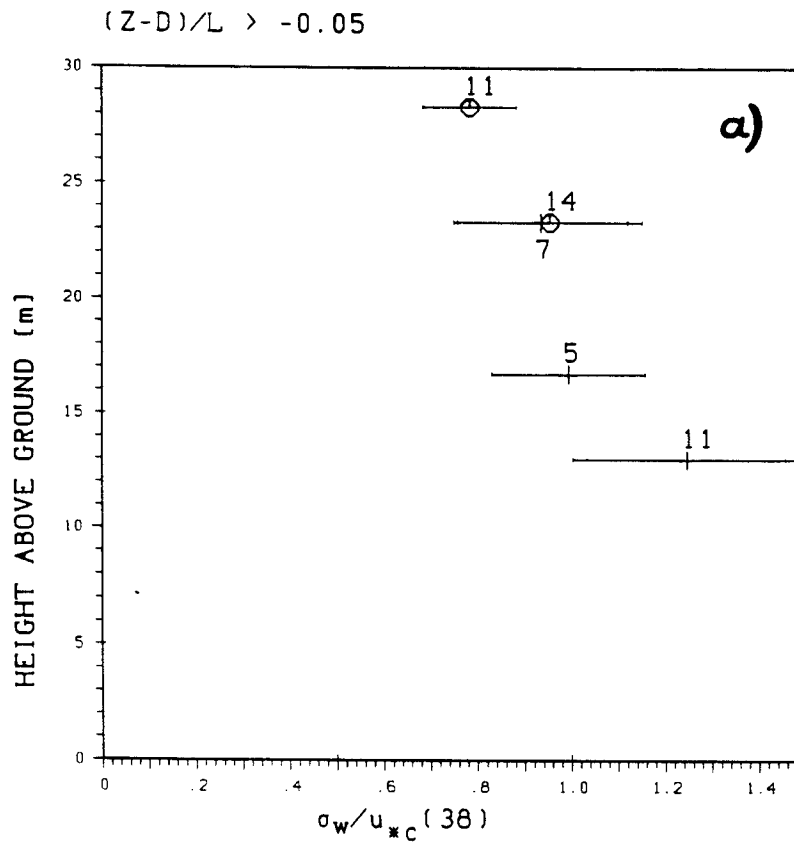
Figure 9.9a   As Fig. 9.8, but for near neutral stability.

-0.05 > (Z-D)/L > -0.5

(Z-D)/L < -0.5
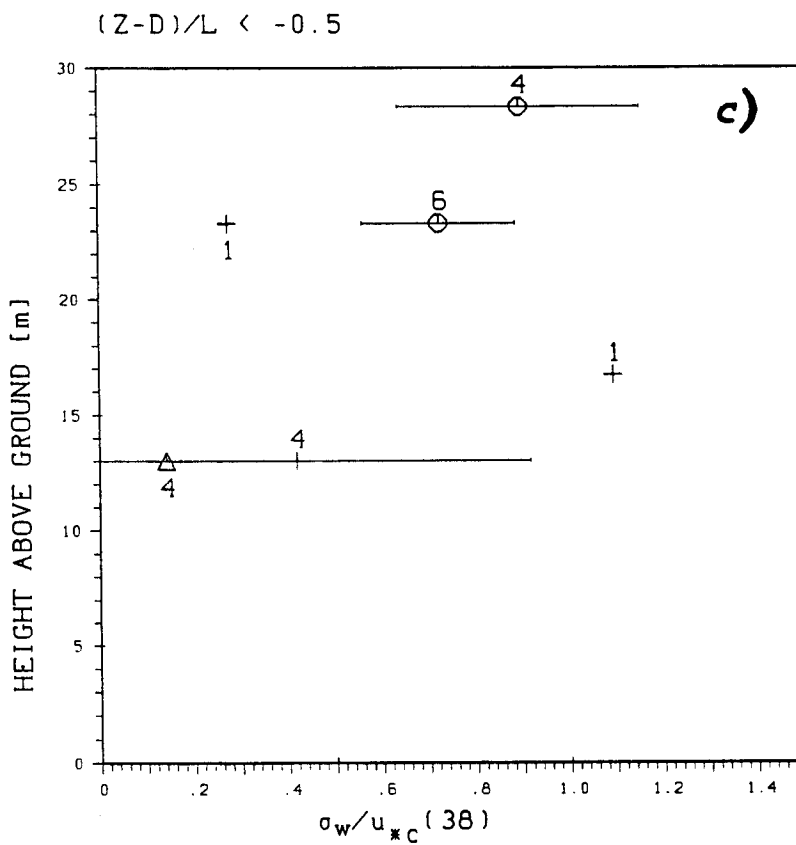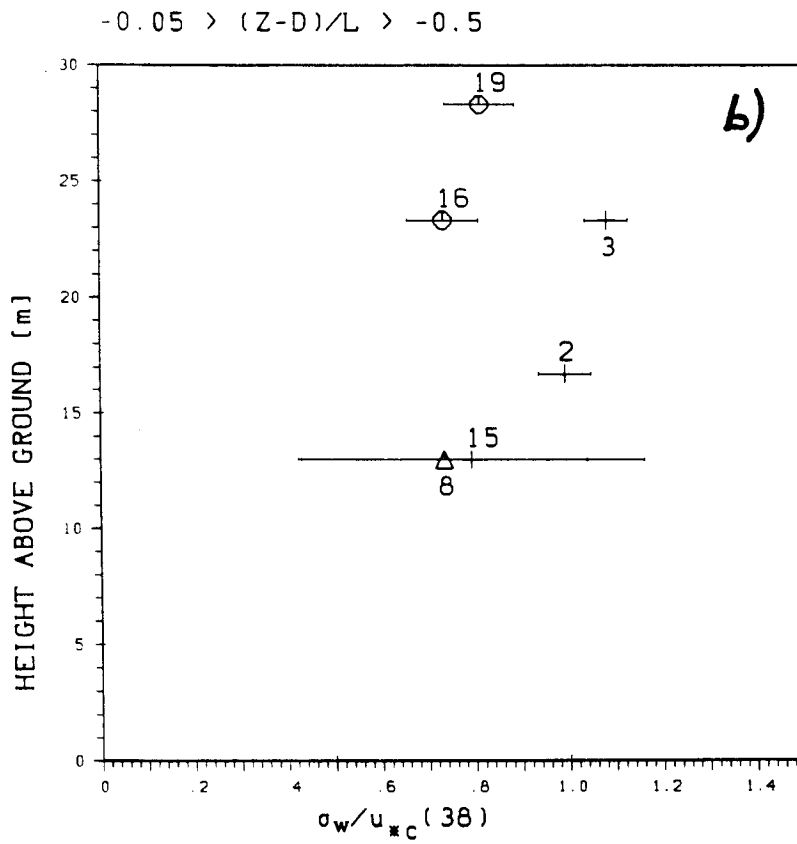
Figure 9.9b,c As Fig. 9.8, b) weakly unstable and c) strongly unstable situations.
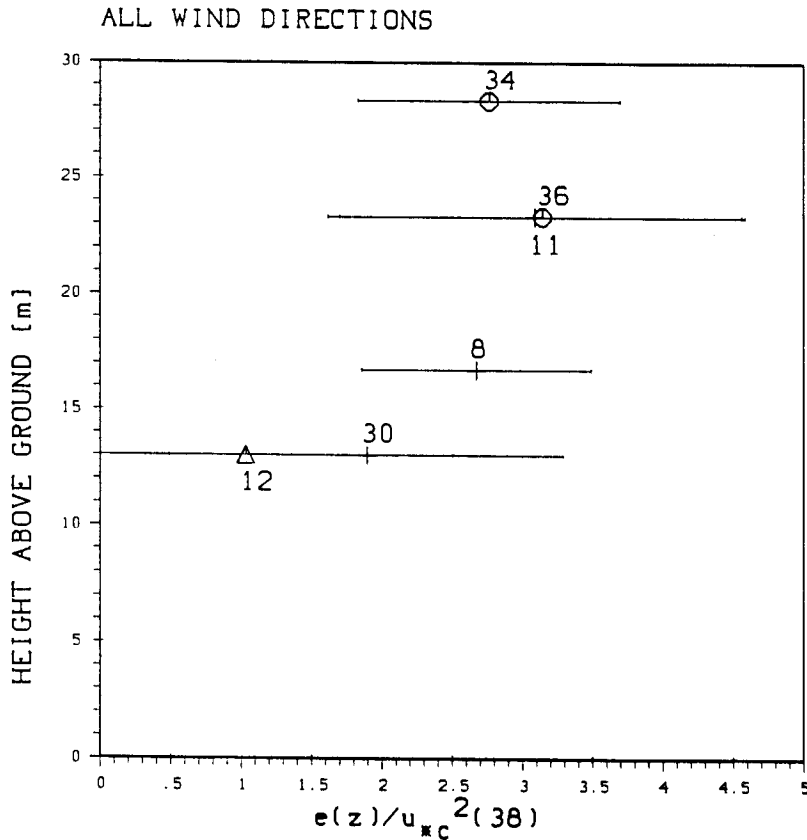
ALL WIND DIRECTIONS

Figure 9.10   As Fig. 9.5, but for turbulent kinetic energy.

d) Turbulent kinetic energy

Taking all three velocity components into consideration, it might be instructive to look at the turbulent kinetic energy e, i.e.

$$\frac{e}{u_{*c}^2(38 \text{ m})} = \frac{1}{2\,u_{*c}^2(38 \text{ m})}(\sigma_u^2 + \sigma_v^2 + \sigma_w^2).\qquad(9.11)$$

An average over all wind directions (Fig. 9.10) shows e to increase within the canopy up to a height close to (and presumably above) h. In the RS, the turbulent kinetic energy decreases again with height. The variability around the average at each position is again (and particularly at the lowest position within the canyon) considerable, and at least partly due to the different behaviour for the stability ranges (Fig. 9.11).

It has been stated in Section 7.2 that the layer close to roof level h is characterized through the break-up of the organized flow due to wake effects resulting in a reduced transport capacity (turbulent fluxes of sensible heat and momentum). The same processes are probably responsible for the local maximum of turbulent kinetic energy at the interface between UCL and URS.
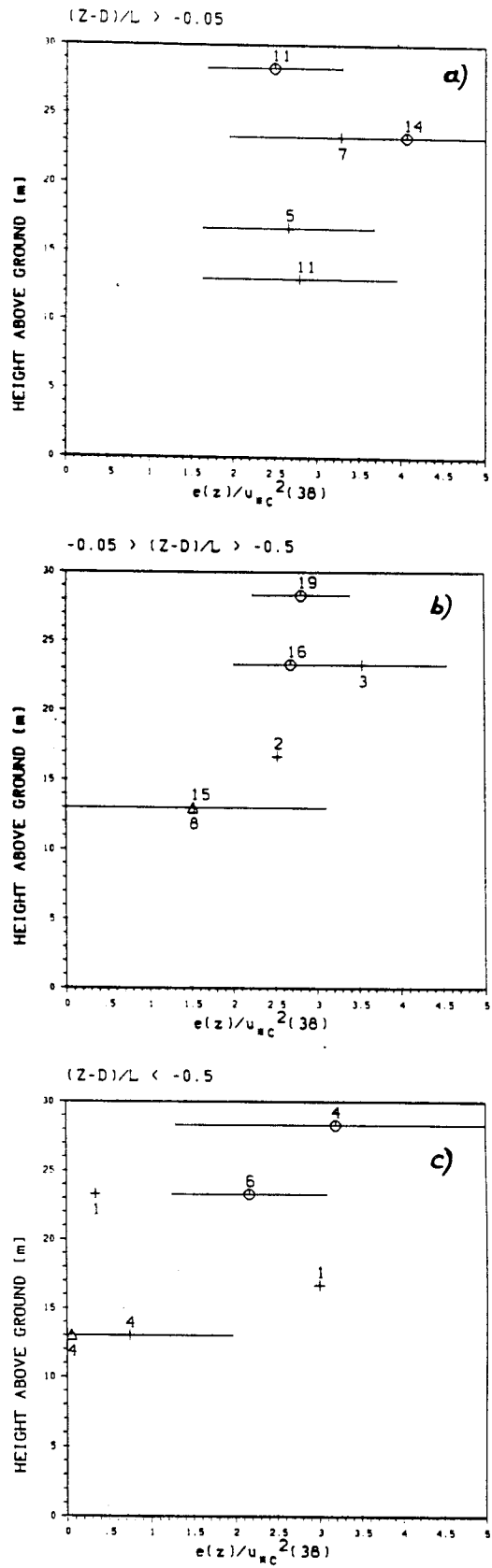
Figure 9.11   As Fig. 9.10, but for a) near neutral stability, b) weakly unstable and c) strongly unstable situations.

In order to interpret the stability dependence of the e - profiles (or that of the velocity variances) it may be appropriate to recall the conceptual picture of Perry et al. (1969) concerning different types of rough surfaces. Their most important findings (for the present purpose) are the following:

- there are two types of rough surfaces: above "k-type" surfaces, velocity profiles are predominantly determined by the roughness scale k (corresponding to the roughness element height h in the present notation). Above "d-type" surfaces, the important scale determining the velocity profile is an outer flow scale d (the pipe diameter in their experiments). See Fig. 9.12 for a conceptual sketch of the flow over both surfaces.

- d-type roughness is associated with a much shallower roughness sublayer.

- for roughness elements of equal height, the transition between k-type and d-type roughness depends on the ratio between the width of the roughness elements and the inter-element spacing.

- the pressure distribution within the canopy is for d-type surfaces very sensitive to "vertical misalignment" of the roughness elements. This means that e.g. a five percent change in height of the cavity under investigation resulted in a ~ 35% change of the surface drag coefficient (proportional to the wall shear stress).

- the results of pipe flow experiments might be applied to real boundary layers in the case of zero (mean) pressure gradient. Then, the pipe diameter d might correspond to the mixing height z_i
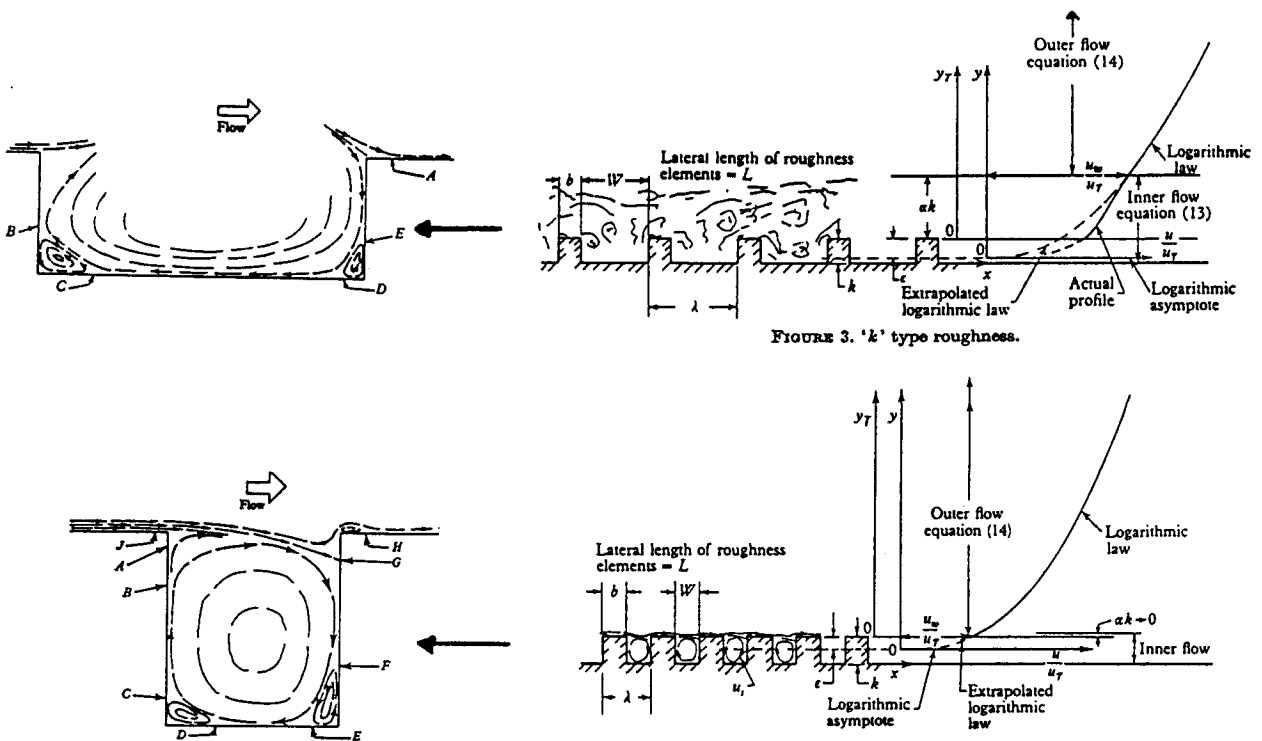

Figure 9.12   Flow over a) k-type and b) d-type surfaces. Modified after Perry et al. (1969).

Especially the second last point shows that d-type roughness is an idealized concept for roughness elements of exactly the same height. Thus, real rough surfaces can hardly be expected to behave according to d-type roughness. Although Perry et al. (1969) treat the "misalignment" of the roughness elements as an error in the determination of surface shear stress and therefore keep the element's heights within a small tolerance, it must be assumed that the observed pressure differences in the case of roughness elements of not exactly the same height are real and will lead even for d-type distribution of roughness elements to a k-type behaviour.

Clearly, the observed profiles of turbulent kinetic energy and the velocity variances indicate a k-type surface in the case of neutral stability or weakly unstable stratification, where the turbulent state within the UCL seems to be related to a certain extent to the RS turbulent structure (Fig. 9,12a). In the case of stronger instability, the flow within the canyon appears to be decoupled from the flow above (e.g. Fig. 9.11) and thus, it seems possible that, despite the irregularities in surface geometry, the flow behaves like over a d-type surface. In particular, the following characteristics may support this hypothesis:

- the very small turbulent kinetic energy within the canyon indicates a certain decoupling of the canyon flow.

- the large run-to-run variability of all velocity variances points to highly intermittent turbulence dominated by (rare) large scale events.

- the general increase of e with height and in particular the lacking maximum close to the roof level indicate that large scale processes dominate the distribution of turbulent kinetic energy.

Although this hypothesis is highly speculative and cannot be proved with the present data, a conceptual sketch of the flow over an urban surface is given in Fig. 9.13 for near neutral and strongly unstable situations.
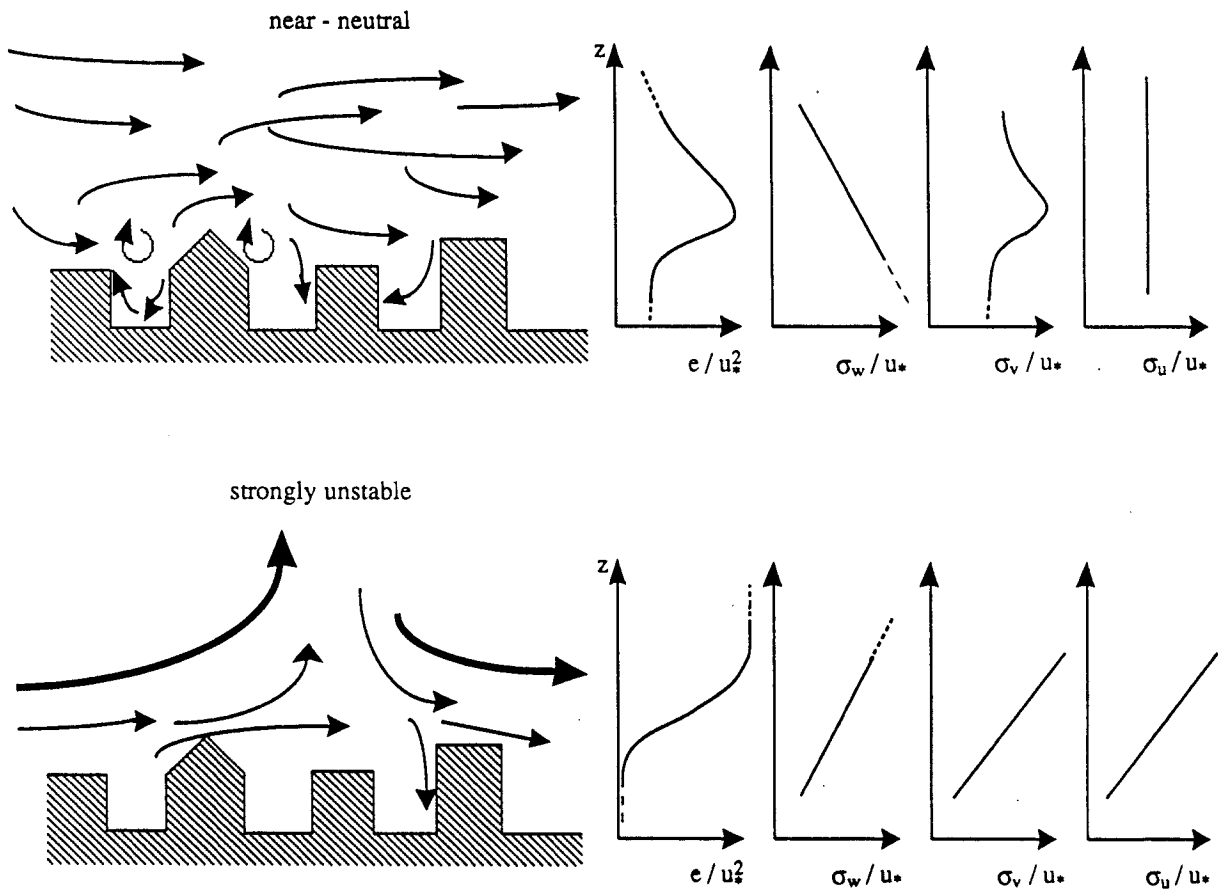
near - neutral

strongly unstable

Figure 9.13   Conceptual sketch of the flow close to an urban surface together with schematic profiles of turbulence variables. (u* denotes the *inertial sublayer value*). a) near-neutral and b) strongly unstable situations

e) Comparison to other rough surfaces

Profiles of velocity variances have been reported from several wind tunnel studies. Results of Raupach (1981) indicate that close to the rough surface (z < 2h) σ_i - profiles are highly dependent on the surface geometry. While the profiles of the horizontal velocity components are comparable to the present results, $\sigma_w/u*$ increases with height in the lower roughness sublayer (or even canopy) in contrast to the present (near neutral) observations. A clear decrease of both σ_u and σ_w within the canopy is also reported by Raupach et al. (1986). These differences in σ_w profiles between wind tunnel and the present results must probably be explained by the completely different geometry and distribution of the roughness elements (even in "rough surface" experiments in the wind tunnel, the roughness elements are distributed with much less density and are of different shape than urban buildings).

9.5 Scaled Profile of Temperature Variance

In order to obtain a profile of the temperature variance, the measurements of the various runs were scaled with $\theta_{*c}(38m)$. Fig. 9.14 shows that, on average, σ_θ is approximately constant with height above the canyon. Within the canyon, the temperature variance is remarkably reduced (-50%) apart from its uppermost part. The variability is, especially at the uppermost level, very large mainly for reasons concerning $\theta_{*c}(38m)$ as a scaling variable as discussed in Chapter 8.

Unfortunately, not enough measurements are available (in particular within the canyon) to present a σ_θ profile for strongly unstable stratification. This would be very interesting in the context of the flow behaviour as hypothesized in the previous section.
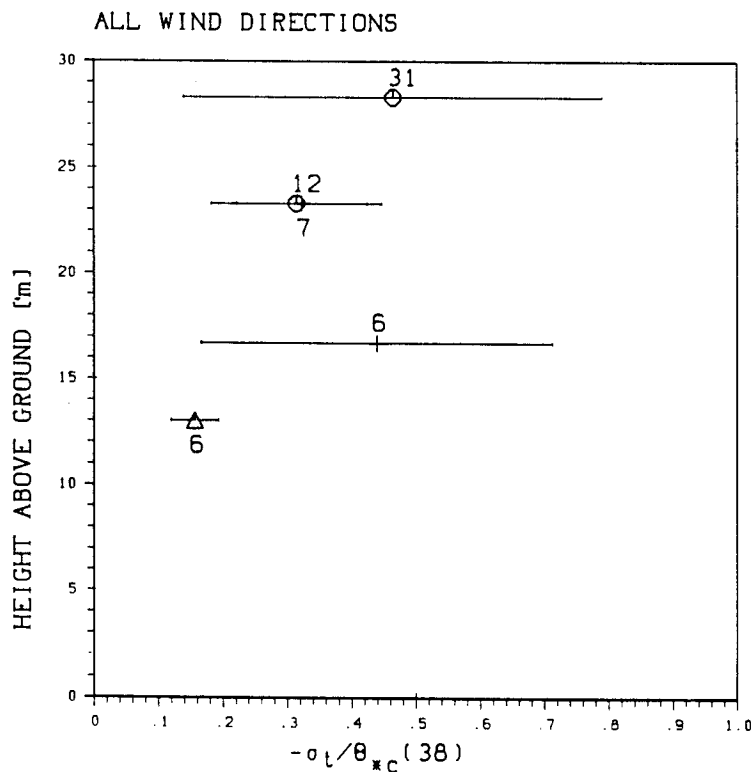
Figure 9.14   As Fig. 9.5, but for $-\sigma_\theta/\theta_{*c}(38m)$.

Seite Leer /
Blank leaf

10. Turbulence Intensity

Turbulence intensity is defined as the ratio of the standard deviation of the respective wind component to the mean wind speed

$$I_i = \sigma_i / \overline{u} \, , \, i = u,v,w \qquad\qquad (10.1)$$

For ideal fetch conditions, one can use the equation for the mean wind speed $\overline{u}$ (2.28) and (9.2) to derive a relation between I_v and z_i/L, z'/L and z'/z_0. This is desirable since I_v is an important variable for diffusion modelling. However, Panofsky and Dutton (1984) point out that through a tendency to a strong (negative) correlation between z_i and $-L$, I_v is predominantly dependent on stability. For observations within the roughness sublayer, a general relation for I_i using the non-dimensional wind shear (for a description of $\overline{u}$) seems unlikely. Results are more likely in terms of the departure of the non-dimensional wind shear from ideal formulation (see Chapter 11) than for I_i. Fig. 10.1 shows I_v vs. stability for the Anwand site, I_u being very similar to I_v. There is no strong variation with stability to be observed since the amount of data is rather small. Nevertheless, a regression has been performed to indicate a tendency in stability. I_v (and I_u, too) is always larger than about 0.25 and $I_w \geq 0.15$. These "lower limits" are considerably higher than what is observed over ideal terrain (e.g. Panofsky et al., 1977) but also somewhat higher than what can be deduced from average I_i (and its standard deviation) reported for various urban sites (e.g. Brook, 1972; Högström et al., 1982; Clarke et al. 1982). Very large turbulence intensities ($I_{u,v} \approx 0.8$, $I_w \geq 0.3$) can be observed for very light wind conditions ($u < 1ms^{-1}$). Although many authors report a dependence of I_i on wind direction in urban areas (Brook, 1972; Ramsdell, 1975; Clarke et al., 1982) indicating that turbulence intensity is dependant on the roughness characteristic in the upwind source area of the measurement, no such variability can be observed for the present data (Fig 10.1). This is probably due to the relatively small difference in urban structure for all wind directions at the Anwand site. Clarke et al. (1982) report a dependence of I_v and I_w on z'/z_0 using the logarithmic wind profile to calculate z_0. From what has been stated in Section 6.2 concerning this approach for z_0, it seems that the given relation might be rather a hidden dependence on $u* / \overline{u}$ than on z_0. If z_0 is calculated from land use characteristics (see Section 6.2) as in the present study, no such characteristic can be found. Table 10.1 lists the overall averages (and standard deviations) of I_i for the Anwand data set together with the linear regression coefficients for the (very weak) stability dependence.
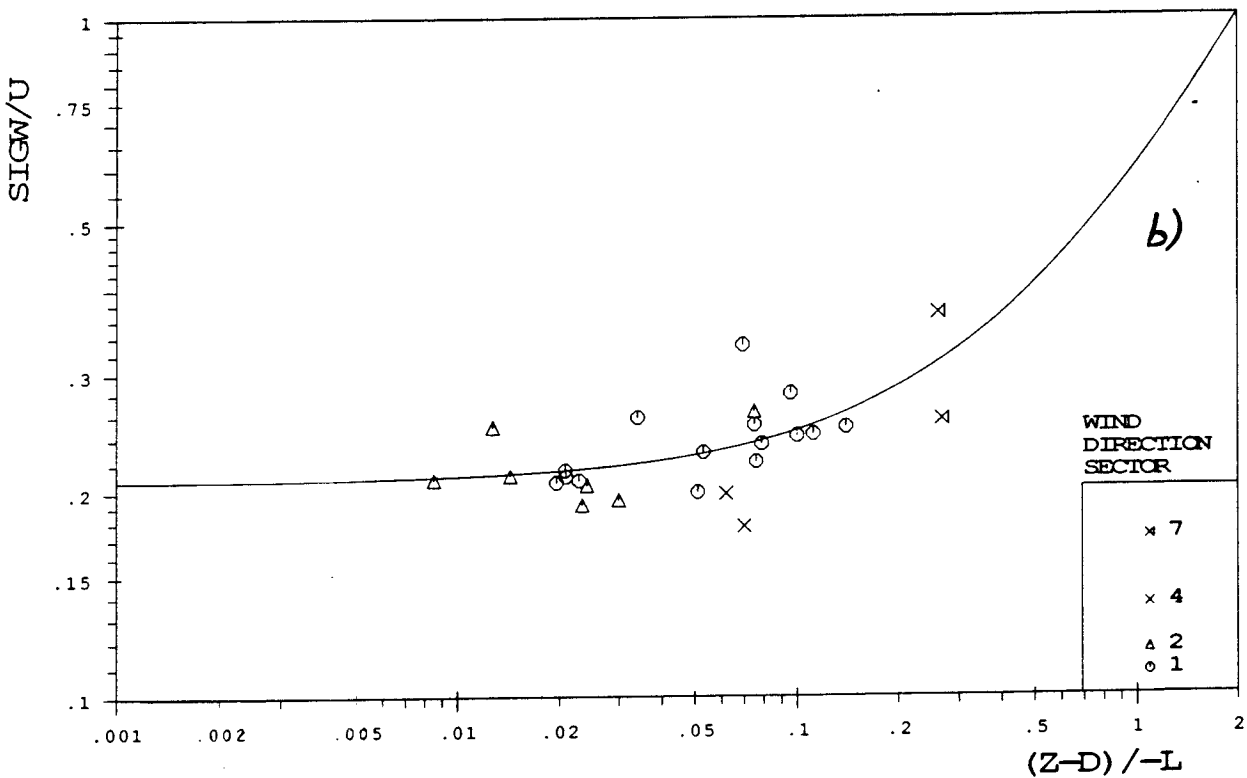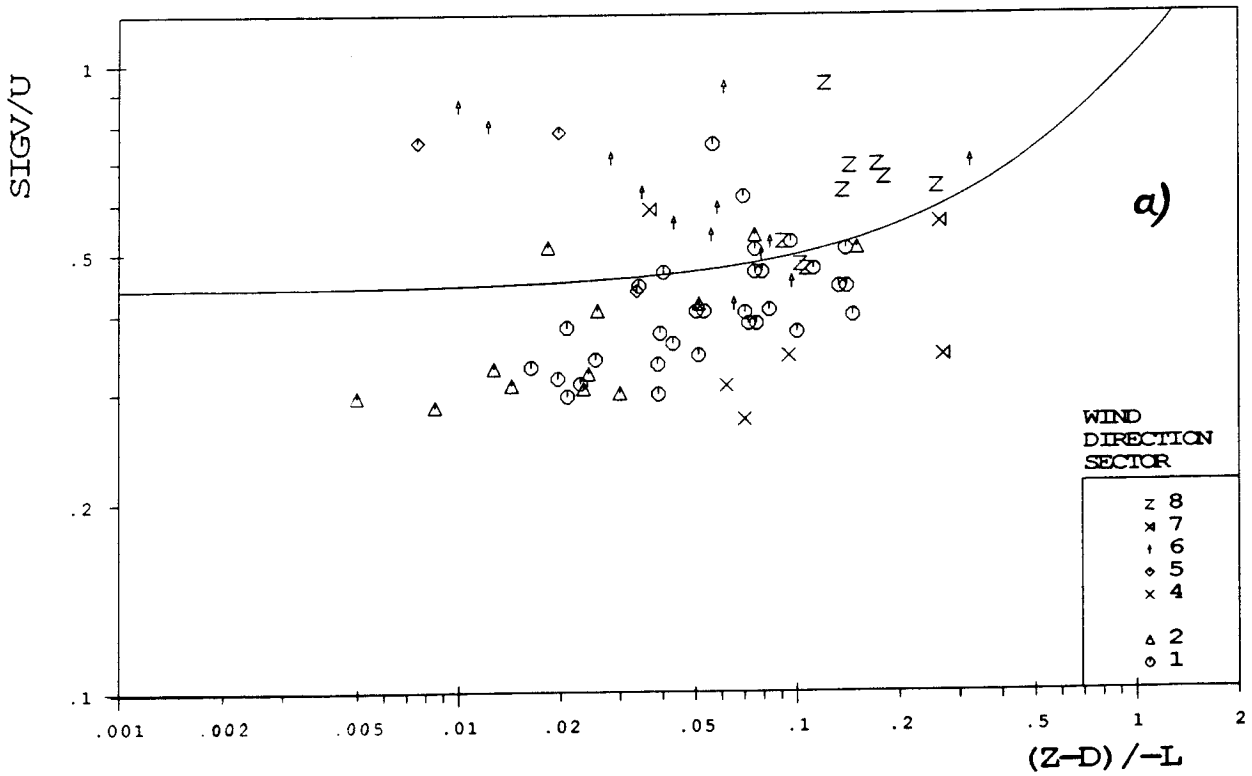
Figure 10.1   Turbulence intensity a) I_v and b) I_w for different stabilities and wind directions (symbols as indicated). SIGV denotes σ_v and SIGW denotes σ_w. Measurements from positions 10 and 11. The solid lines represent the linear regression line according to Table 10.1 (note the semi-logarithmic representation)

Turbulence intensities can vary significantly with height of observation, z', as pointed out e.g. by Bowne and Ball (1970), Brook (1972), Ramsdell (1975) and Högström et al. (1982). All authors agree that turbulence intensities decrease with increasing height. This observation is confirmed by the present data (Fig. 10.2) between positions 10 and 11. Differences in I_i can amount to more than 50% of the upper value but show no distinct dependence on I_i itself. Note that *all* data are shown in Fig.10.2, even if they are considered unstationary or rejected for other reasons (see Section 5.3). The only exception is the locally disturbed w component by the sonic itself (Appendix A2) for certain wind directions. In general, the observed characteristics do not change if the "rejected" data are included. Even for a small increase in the height of observation (5m), turbulence intensities decrease remarkably. This tendency is less prominent for large u*. For small u* a considerable scatter in $I_i(z_2)$ - $I_i(z_1)$ is found, whereas for u* $\geq 0.8\text{ms}^{-1}$ the difference in I_v (and also I_u, not shown) is of the order of -0.05 and the difference in I_w disappears for the given interval in measurement height. The measurements for which $z_1 = z_2$ = position 10 are shown in Fig. 10.2 for comparison. The results from these few runs indicate that the scatter between the two instruments amounts to approximately 0.05 ($I_{u,v}$) and 0.02 (I_w), but is considerably smaller than the observed differences if the instruments were mounted at different heights. As the mean wind speed increases with height, height-constant velocity variances would result in decreasing I_i. A direct comparison of σ_i simultaneously measured at heights z_1 and z_2 shows that, in addition to the increase of wind speed with height, a more or less continuous decrease of σ_i with height can be observed.

Table 10.1   Parameters of regression analysis for the stability dependence of turbulence intensities $I_i=a(z'/L)+b$. The third column is calculated including the *rejected* data in the case of w (disturbed vertical component by the sonic itself, see Appendix A2).

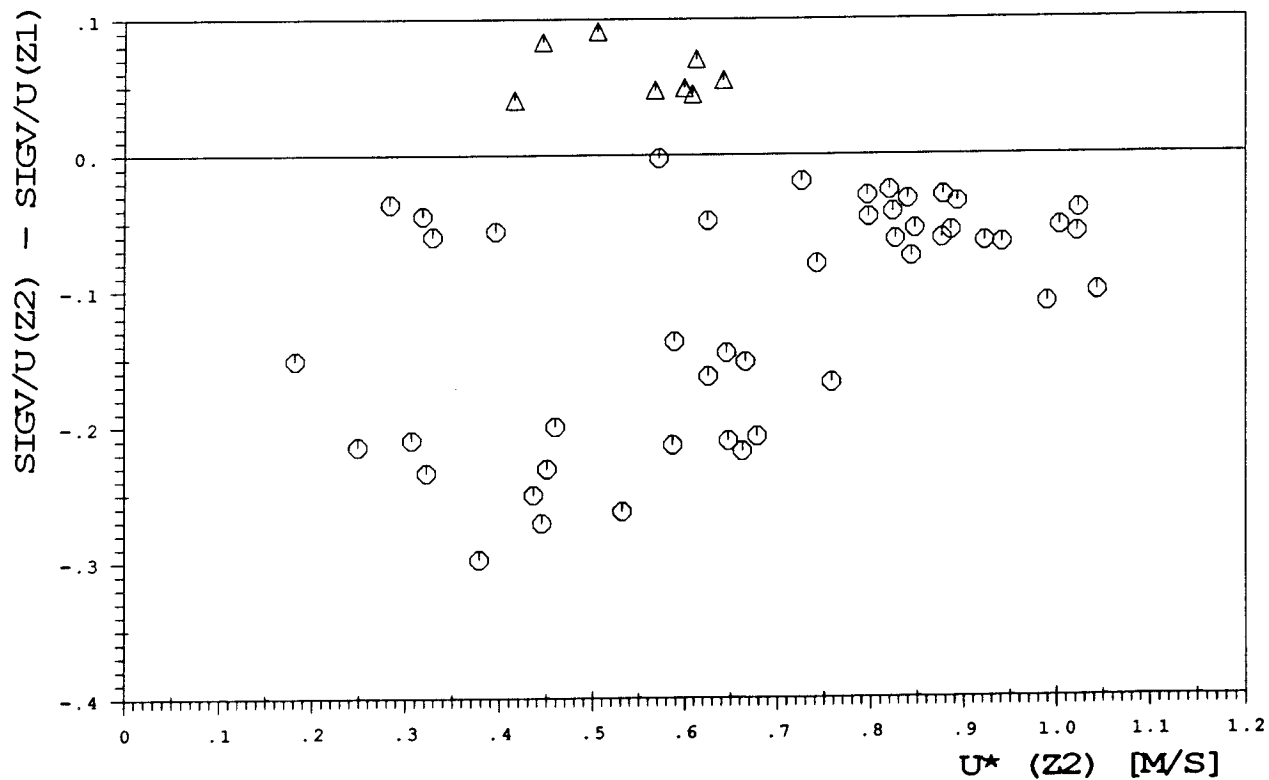|	$\sigma_u/\bar{u}$	$\sigma_v/\bar{u}$	$\sigma_w/\bar{u}$	$\sigma_w/\bar{u}$
A	0.0114	0.592	0.145	0.392
B	0.566	0.438	0.263	0.207
R^2	0.0056	0.239	0.129	0.623
Mean	0.567	0.482	0.274	0.235
sd.-dev.	0.131	0.109	0.072	0.042
number of observations	74	74	74	26

Figure 10.2a   (○): Difference of turbulence intensity between positions 10 (z_1) and 11 (z_2) for I_v. (△): $z_1=z_2$=position 10.
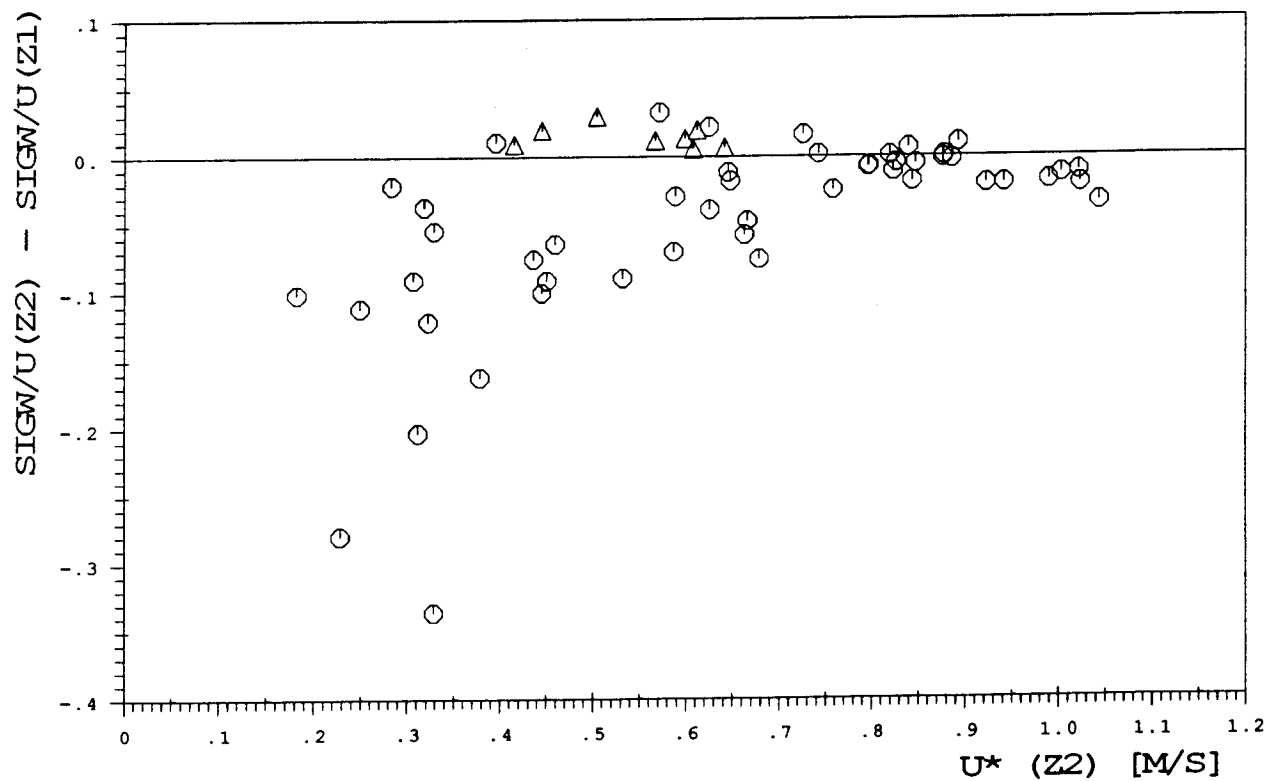

Figure 10.2b   (○): Difference of turbulence intensity between positions 10 (z_1) and 11 (z_2) for I_w. (△): $z_1=z_2$=position 10.

11. The Dimensionless Gradients of Wind Speed and Potential Temperature

In order to study the behaviour of the dimensionless gradients of wind speed and temperature (equations (2.26) and (2.32) respectively) in the urban roughness sublayer, all turbulence runs with at least one sonic anemometer above canyon height h were analyzed and compared to the well known semi-empirical relationships Φ_m^{IS} for the inertial sublayer (often referred to as surface layer). Since the turbulent moisture fluxes ($\sim\overline{q'w'}$) were not directly measured, it was not possible to calculate the dimensionless gradient of specific humidity. With the 2 x 2D Sonic system no direct measurements of the fluctuating temperature were available. The average vertical variation of u_* and $\overline{w'\theta'}$ between the heights of interest (23.3m and 28.3m, respectively), in particular the relatively small change with height of $\overline{w'\theta'}$ (see Chapter 8), led to the following assumption: the local θ_* at the height of the 2 x 2D sonic was calculated using Reynolds stress as measured by the 2 x 2D sonic and $\overline{w'\theta'}$ from the 3D sonic (i.e. 5m higher up in most of the runs). Results will be shown to be not affected by this assumption (concerning essentially the dimensionless temperature gradient and, less important, the local stability z'/L). Gradients of mean wind speed were calculated by fitting a second order polynomial in ln z' to the four measured wind speeds and taking the derivative with respect to z' at the height of interest. In the case of the gradients for potential temperature, the same procedure was applied in principle. For some turbulence runs, however, only two temperature levels were available (at 3 and 20m above roof level, respectively) and thus, for these runs the differential was replaced by the differences of potential temperature and height.

11.1 The Dimensionless Wind Shear

The calculated values of dimensionless wind shear Φ_m are shown in Fig. 11.1 in comparison with a semi-empirical formulation of Businger et al. (1971) modified after Högström (1988). Two features are apparent at a first glance:
- At the higher level (10m above roof level, position 11), the correspondence to the inertial sublayer prediction is fairly good. Φ_m at this level seems to be rather small and there is considerable scatter (not dependent on stability).
- At the lower level on the other hand (position 10), large deviations from the Businger et al. (1971) formulation are observed over whole (small though) stability range.
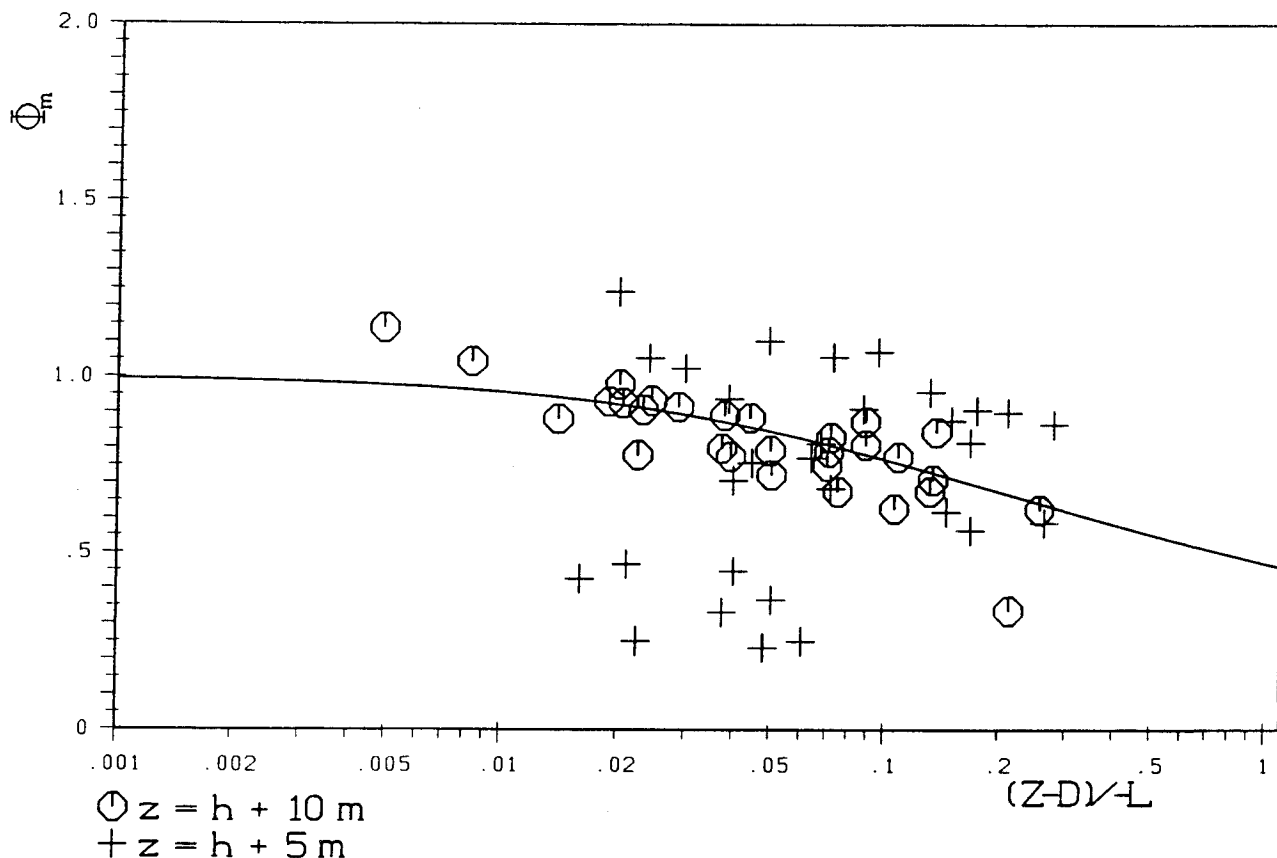
Figure 11.1 Φ_m for different stabilities at positions 10 (+) and 11 (⊙). The solid line
represents equation (2.29), Businger et al. (1971).

From the first point, it can be concluded that the gradient of wind speed is in
equilibrium with the *local* turbulent flux of momentum at the height distinctly above the
mean roof level but well within the roughness sublayer. If scaled with the proper u*
from the inertial sublayer (see Chapter 7), Φ_m can be expected to be biased by some
15% below its IS value (for that particular height). At only 5m (or ~0.25h) closer to
roof level, this equilibrium between local flux of momentum and gradient of mean wind
speed is completely absent. Φ_m is either much larger or much smaller than Φ_m^{IS}.
Although during most of the time, the 2 x 2D Sonic was used at this level (and the 3D
System at the upper level, cf. Table 4.2) this discrepancy cannot be attributed to
systematic measurement errors, since the 3D Sonic, mounted for short time at position
10, too, does not yield different results (under- and over-estimating drastically). This
finding also justifies the use of $\overline{w'\theta'}$ as measured by the 3D sonic for the calculation of
the local stability z'/L at the position of the 2 x 2D sonic (see above). These runs are
also included in Fig. 11.1. When classifying the runs at the 5m level according to wind
direction, it is found that in general, Φ_m is underestimated if the above roof wind
direction lies between 46° and 270° and overestimated else. There are, however, two or

three exceptions from this "rule" that may well be attributed to the fact that wind direction was measured instantaneously with a 10 minute interval between the measurements.

11.1.1 Possible Reasons for the Observed Φ_m Departures

a) distant urban structure

An inspection of a city map (Fig. 11.2) shows that for the wind direction sector where Φ_m is overestimated, we find the building structure to be quite different in the upwind (source) area, i.e. loosely arrayed large industrial complexes, as compared to the other wind direction sector with its more regular urban structure. This region of industrial complexes is located some 500 - 2000m from the Anwand site, whereas in the closer environment , the urban structure is quite similar for all wind directions. The question arises whether this difference in building geometry in a (distant) upwind area can be the reason for the observed difference in Φ_m. To find a conclusive answer, the following has to be taken into consideration:

- wind direction sector 1 (see Fig. 11.2) certainly represents the rougher upwind fetch. Raupach et al. (1980) show that the eddy diffusivity K_m (proportional to $\Phi_m^{-1} \cdot u_*$) is not dependent on the surface roughness and, in general, larger within the RS than over smooth terrain. Thus, from this point of view, air advected from both wind direction sectors would have to show the same characteristics (i.e. Φ_m being smaller than Φ_m^{IS}).

- It is very unlikely that in a layer of high turbulence activity with enhanced eddy diffusivity a disturbance can be advected over several hundreds of meters in a distinct shallow layer (Φ_m at position 10 does not show the same characteristic).

- When calculating the source area (Schmid,1988) for the runs at position 10, its extension is found to be of the order of 50 - 100 m. (Note, however, that the source area model of Schmid (1988) requires as an input a value for z_0, the surface roughness, which is defined in relation to the inertial sublayer profile of mean wind speed; see also Section 6.2)

It is therefore concluded that the differences in the (distant) upwind sectors cannot be the reason for the observed under- and overestimation respectively of Φ_m. Since a closer look at the nearby environment does not show any features being characteristic for either wind direction sector 1 or 2, it has to be assumed that the dependence of Φ_m - Φ_m^{IS} on wind direction only "masks" another factor of influence.

Figure 11.2   City map of Zurich showing the wind direction sectors as discussed in the text.

b) estimation of z'

The only wind direction dependent variable in the calculation of Φ_m is in fact the zeroplane displacement height (see 6.1). At this low level under consideration (z' varying between 6 and 13 m) a change in d (and therefore z') can indeed seriously affect the calculation of Φ_m. For all runs, a quantity d' was calculated through

$$\frac{d\overline{u}}{dz} \cdot \frac{k(z-d')}{u_*} = \Phi_m^{IS} \qquad (11.1)$$

where Φ_m^{IS} is the inertial sublayer prediction given by equation (2.29). Results are averaged over the same wind direction sectors as the zeroplane displacement d and compared to the latter in Table 11.1. Differences between d and d' lie between 1m and 2.5m (or 5 and 25%) in general. For one sector (226° - 270°) all values of d', and for another (316° - 360°) the value of d' for one run, however, are negative! This shows that the possibly wrong zeroplane displacement height cannot be considered the main source of the Φ_m departures at the 5m level. It shows, on the other hand, also drastically how severe the Φ_m departures can be. There is another reason, why a systematically biased zeroplane displacement cannot be the source of the Φ_m departures. If this would be the case, z' would also be biased in the same direction at position 11 (however less pronounced) and correspondingly Φ_m. This is not proved by the data.

c) measurement uncertainty

The *scatter* in Φ_m at the different heights introduced by the uncertainty of the determination of $d\overline{u}/dz$, z' and u_* respectively, can be calculated through

$$\frac{d\Phi_m}{\Phi_m} = \frac{\Delta(d\overline{u}/dz)}{d\overline{u}/dz} + \frac{\Delta z'}{z'} + \frac{\Delta u_*}{u_*} \qquad (11.2)$$

where Δ indicates the uncertainty of the respective variable. Inserting typical values into equation (11.2) for the two levels and estimating the uncertainties (Δ z' = 0.5m - the resolution of d; $\Delta(d\overline{u}/dz)$) from the relative accuracy of the wind speed measurement; Δu_* after equation (5.2)) yields very small differences in $d\Phi_m/\Phi_m$ at 5m and 10m above roof level respectively. Some 30% at the upper and around 35%at the lower level. While this figure corresponds reasonably well to the observed scatter at position 11 (Fig.11.1), the Φ_m departures are much larger than 35% at position 10.

Table 11.1   Comparison of the zeroplane displacement height d and d' (equation (11.2)) for different wind direction sectors at position 10.

wind direction sector	d [m]	d' [m]	number of observations
0° - 45°	14	12.5	3
46° - 90°	15.5	14.5	4
91° - 135°	17	15.9	2
136° - 180°	16	14.9	2
181° - 225°	-	-	
226° - 270°	13.5	-4.2	5
271° - 315°	10.5	13.1	2
316° - 360°	14	12.5	4

d) wake diffusion effect

According to Raupach et al. (1980) a reduced Φ_m (or an enhanced eddy diffusivity K_m) close to a rough surface can be attributed to the so-called "wake diffusion effect". They point out that it may be associated with the "horse-shoe" vortex which develops if an isolated roughness element is exposed to a shear flow (see Fig. 11.3). The shear flow's (transverse) vorticity will be transferred to streamwise directed vorticity concentrated in the two horse-shoe limbs. From the direction of rotation in the two horse-shoe limbs, it follows that high velocity fluid is is transported into the center of the wake. Further downstream of the obstacle, the horse shoe vortex breaks up and thus contributes to the turbulent kinetic energy in the roughness sublayer. Since eddies with a streamwise axis of rotation are very effective in transporting momentum (in the vertical), a region of interacting wakes is likely to be one of enhanced diffusivity (for details see Raupach et al., 1980). Fig. 11.3 shows the complicated turbulence structure around an isolated obstacle leading to the above described effects (adapted from Hosker, 1984)). It is easily seen from this conceptual drawing that horizontal inhomogeneity may "mask" the wake diffusion effect leading to locally large differences in Φ_m.

11.1.2 Qualities of Φ_m in the Roughness Sublayer

To obtain "horizontal averages" (Fig. 11.4), the dimensionless wind shear has been averaged over all wind directions and grouped into classes of stability (note that for the lower level two horizontal positions - "above roof" and "above canyon", respectively - are included, whereas at the upper level but one position is available). If Φ_m i s calculated using local values of u_* (and $\overline{w'\theta'}$ for the determination of L) and

horizontally averaged, it is quite well represented by the inertial sublayer formulation at both heights (Fig.11.4). Closer to the roughness elements, the departures are still somewhat larger. Calculating the run-to-run variance of the values shown in Fig. 11.4, it is found to increase by a factor of 2-5 between the upper and the lower level (Table 11.2).

If the gradient of the mean wind speed would alternatively be scaled with u_*^{IS} (corresponding to the Reynolds stress in the inertial sublayer), Φ_m would be smaller than Φ_m^{IS} at both heights and for all stabilities at the present site (cf. Fig. 7.5). Using this type of scaling, Φ_m was often found to be smaller than Φ_m^{IS} over similarly rough but different types of surfaces such as forests (Garratt, 1978 a,b; Raupach, 1979; Garratt, 1980; Beljaars et al.,1983; Högström et al., 1989). Thus, considering these differences in scaling, the characteristic departures of Φ_m from inertial sublayer behaviour is similar in the roughness sublayer over an urban surface as over various types of rough natural surfaces.
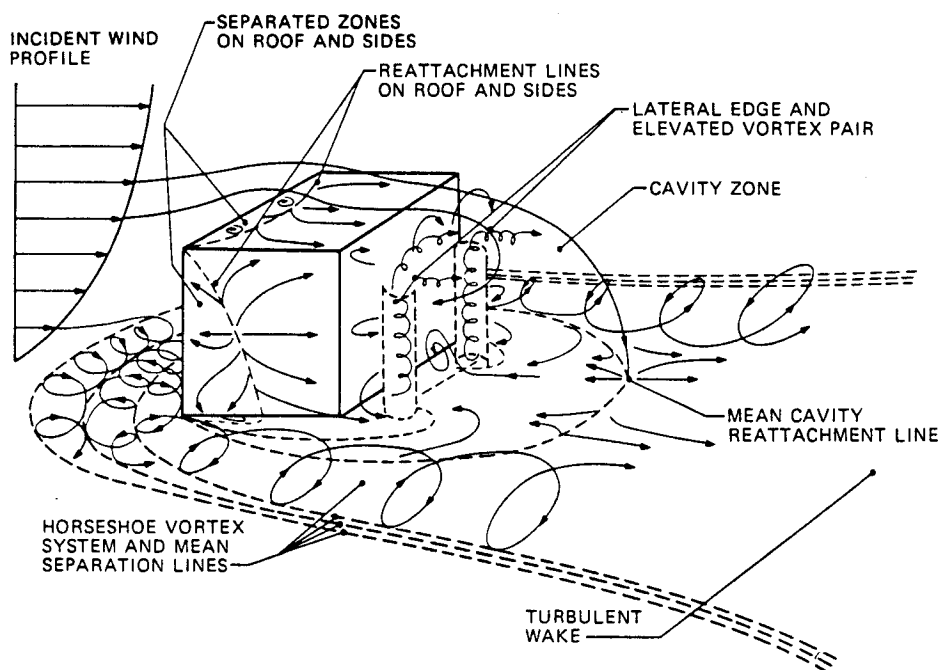
Figure 11.3   Flow near a sharp-edged three-dimensional building in a deep boundary layer. Adapted from Hosker (1984).

Table 11.2:   Variance of the average Φ_m (Fig. 11.4) for the various stability ranges and number of runs,N, contributing to the respective range.

stability range, z'/L	Φ_m			
	10m	number	5m	number
< 0.03	0.091	10	0.374	6
0.03 - 0.05	0.050	5	0.297	7
0.05 - 0.07	-	1	0.244	4
0.07 - 0.09	0.063	6	0.153	3
0.09 - 0.15	0.076	5	0.167	4
> 0.15	0.143	2	0.333	7

The above considerations can therefore be summarized as follows

- Φ_m as measured at a mid-roughness sublayer height over an urban surface is well represented by the inertial sublayer prediction if *local* covariances are used for its calculation.

- If, alternatively, the fluxes from the inertial sublayer are used to scale the gradient of mean wind speed,Φ_m becomes smaller than its inertial sublayer prediction. This is consistent with findings over rough surfaces of different qualities.

- Close to the roof level, the departures of Φ_m from its inertial sublayer prediction are large and, if locally scaled, positive and negative.

- They cannot be explained by differences in urban geometry, possible errors in the determination of the height and the measurement uncertainty. It is very likely that the wake diffusion effect is responsible for the observed Φ_m departures at this level.

- In the horizontal average, the locally scaled Φ_m is still reasonably well represented by the inertial sublayer prediction. The scatter, however, is large.
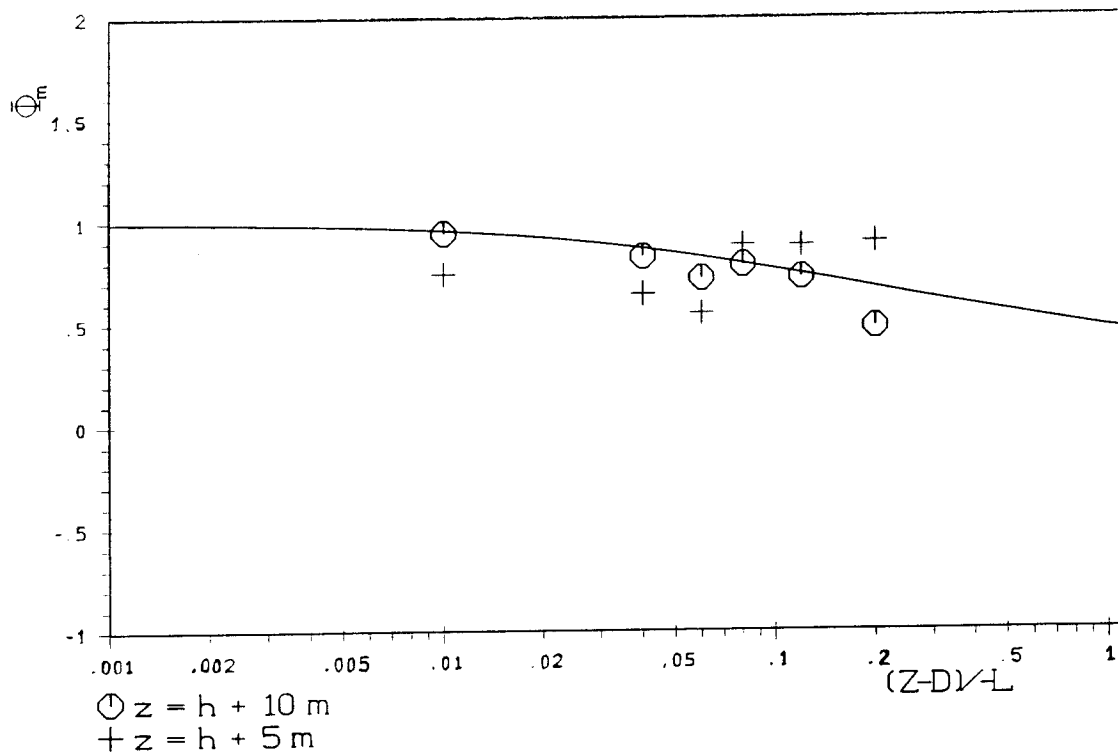
$\bigcirc z = h + 10 m$
$+ z = h + 5 m$

Figure 11.4   As Fig. 11.1, but averaged over stability ranges.

11.1.3 Horizontal Inhomogeneity of Φ_m

It was found that at position 11 the run-to-run variance corresponds roughly to the measurement uncertainty as calculated by equation (11.2). Furthermore, there is no dependence of the Φ_m departures on wind direction to be observed at this level. Thus it is concluded that horizontal inhomogeneity plays a minor role at $z/h = 1.55$. At position 10, on the other hand, horizontal inhomogeneity must be considered important and the run-to-run variance is large as compared to the measurement uncertainty. It can therefore be stated that horizontal inhomogeneity ranges up to a height z_h that lies between 1.27h and 1.55h. Note that z_h is not necessarily equal to the lower boundary of the inertial sublayer, z_*: processes such as the wake diffusion effect may influence the average flow characteristics, but still exhibit the same (within measurement uncertainty) departures from inertial sublayer behaviour at all positions in the horizontal plane.

Raupach et al. (1980) give as a characteristic height z_h, up to which horizontal inhomogeneity is non-negligible, $z_h = h + D$, where D is the inter-element spacing (center to center). Different than for a wind tunnel experiment (Raupach et al., 1980), it is very difficult to define a quantity like the inter-element spacing for an urban configuration of buildings, streets, squares etc. Difficulties arise especially when

considering large combined houses (cf. Fig. 4.1) that may be considered as one "element" or, equivalently, as "many". However, for the particular structure of blocks near the Anwand site, D ranges from 15m to 100m for the different wind direction sectors. Since z_h was found to lie between positions 10 and 11, $z_h = h + D$ is not a useful parameterisation for the present site. The lack of data from other real-scale sites with different building geometries makes it furthermore impossible to give a general description for z_h from the present observations. It is clear that more experiments are necessary at different sites in order to establish such a general relationship between z_h and the building geometry over an urban surface.

$\bigcirc z = h + 10\ m$

$+\ z = h + 5\ m$
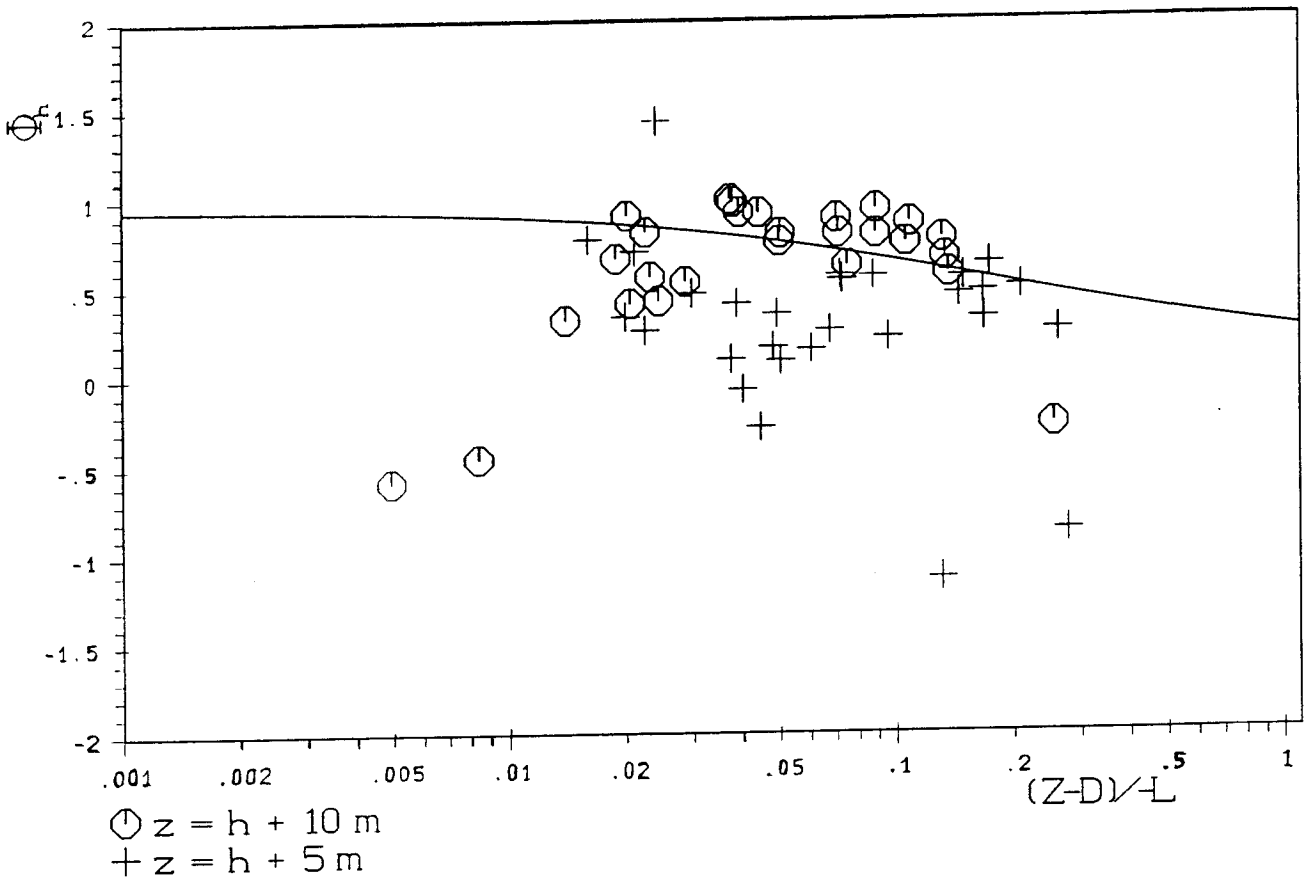
Figure 11.5   As Fig. 11.1, but for Φ_h.

11.2 The Dimensionless Temperature Gradient

The dimensionless gradient for potential temperature Φ_h (equation 2.32) is shown in Fig. 11.5 as compared to the inertial sublayer prediction Φ_h^{IS} (Businger et al. 1971; modified after Högström 1988). At the upper level, it is found that Φ_h is strongly underestimated for the near neutral runs and slightly overestimated for weakly unstable stratification. Closer to the roof, deviations from Φ_h^{IS} are again much larger and negative for most of the runs. Φ_h can also take much smaller, even negative, values. It is again important to notice, that the erratic behavior of the dimensionless temperature gradient at position 10 is not due to the use of the 2 x 2D Sonic for most of the time at this height: the (few) runs with the 3D Sonic at the 5m level cover almost the whole range of Φ_h shown in Fig. 11.5 (where they are included as crosses). In contrast to the Φ_m departures, over and underestimation, respectively, of Φ_h is not characteristic of any wind direction sector. Thus, the departure from the respective inertial sublayer prediction of the locally scaled Φ_m and Φ_h may have a different sign.

The thermal properties of the roof have a large influence on the calculated value of Φ_h. In the average profiles for the potential temperature (see Fig. A3.18) it can be seen that cooling and heating starts at roof level propagating upwards and strongly influences the temperature profile. The resulting "wave like" structure in the temperature profile can be much more pronounced for individual averaging periods (i.e. 50 minutes) than for the average profiles shown in Fig.A3.18. The differences between two neighbouring levels are typically distinctly larger than the relative accuracy of the measurements. (Fig. 11.6). These "wave like" temperature profiles (it might be inadequate to speak of inversions) lead to even negative values of Φ_h at both levels. These cases of "counter-gradient-flux" indicate (as speculated in Chapter 8) that processes of different scales may determine the local flux of sensible heat and the gradient of potential temperature. Not even a "local similarity" as for momentum can therefore be observed in general in the case of the turbulent flux of sensible heat.
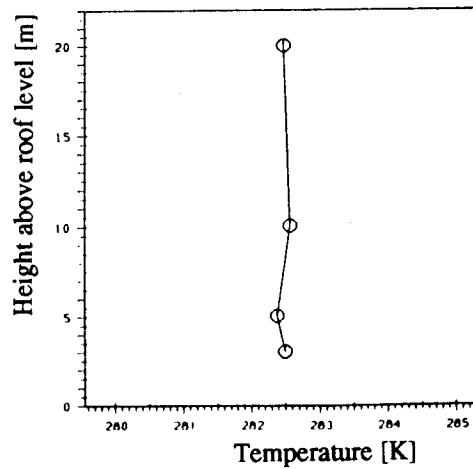
Figure 11.6   Arbitrarily chosen profile of potential temperature above roof level for one 50 minute averaging period

Looking at Fig. 11.5 in detail, we find that the above statement may not hold for weakly unstable runs. At least at some distance from the "active surface" (i.e. at position 11), the scatter of Φ_h around Φ_h^{IS} is relatively small. Although runs with very small gradients of potential temperature were excluded from the analysis (see Chapter 8), the near neutral stability range is one of very large run-to-run variability. The two negative Φ_h at the upper level arise from runs where very small (positive) values of $\overline{w'\theta'}$ were observed in conjunction with a positive gradient of positive temperature. The fact that also negative Φ_h are observed even for strongly unstable stratification, supports the hypothesis of large scale motions (large eddies) influencing the turbulent sensible heat fluxes, while the gradients of potential temperature remain determined by the close (active) surface.

At the lower level (position 10), local similarity between turbulent fluxes of sensible heat and temperature gradients seems to be completely absent. Especially for weakly unstable runs Φ_h is usually very small. This is, at least partly, due to the decreasing u_* when approaching the surface (increasing θ_* and therefore decreasing Φ_h). When grouping the data into stability ranges (Fig. 11.7), the large departures from Φ_h^{IS} close to the active surface are obvious. In contrast to the dimensionless wind shear, the variance of Φ_h within each stability range is not systematically reduced at the higher level (Table 11.3).

It has to be noted that it is not even possible to speak of horizontal inhomogeneity when considering Φ_h departures in the RS. If looking at the temperature profiles (see Fig. 11.6 as an example), it becomes clear that large changes in $d\overline{\theta}/dz$ (and even a change of sign) can occur over very small vertical distances . It is, however, very likely to find a similar temperature gradient at a different horizontal position over the roof (not over the canyon). Thus, Φ_h is influenced by both, horizontal inhomogeneity (through

θ_*, i.e u_*) and a temporal variability due to the extraordinary heating or cooling of the close roof surface. Although the roughness sublayer is in a region of enhanced turbulence and therefore mixing, the "distorted" temperature gradients persist as long as the heating or cooling persists. It was shown in Section 7.4 that the exuberance (the ratio between upward and downward flux of momentum, respectively) increases considerably when approaching the roof level. At this height of distinct wake influences, the shear flow is distorted and large eddies are broken up to smaller irregular eddies,which are no longer governed solely by the mean properties of the flow field.

○ z = h + 10 m
+ z = h + 5 m
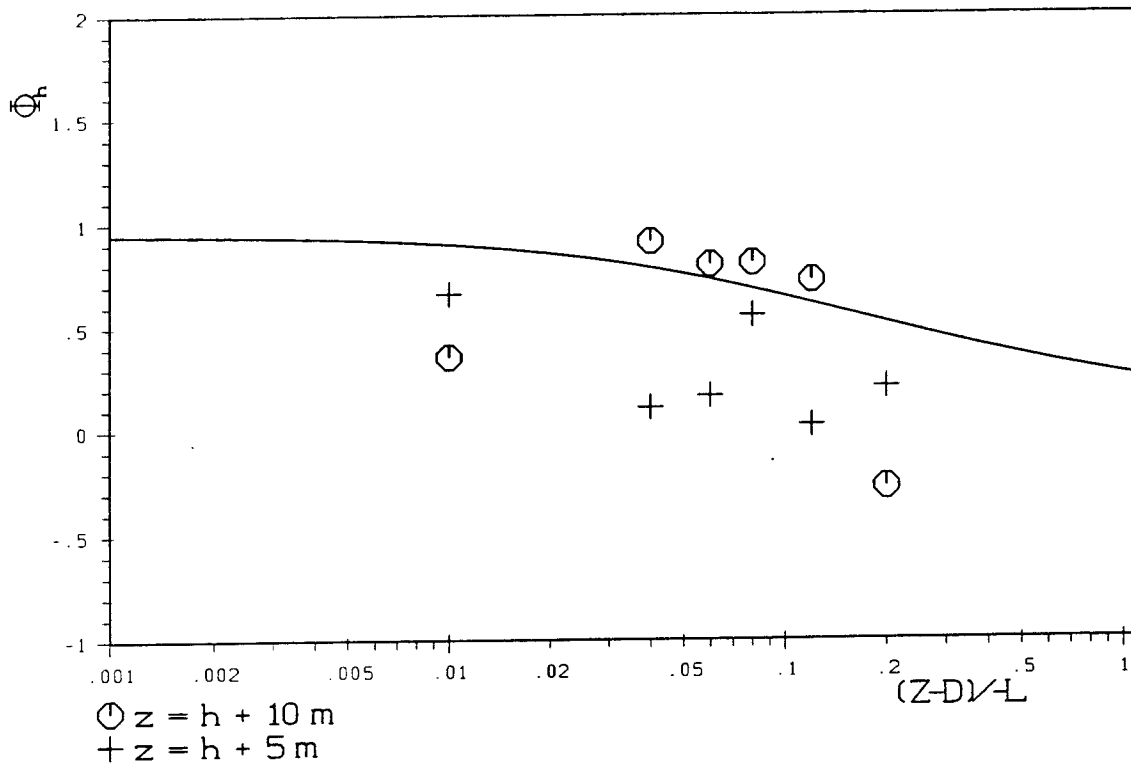
Figure 11.7   As Fig. 11.5, but averaged over stability ranges.

When scaling the dimensionless gradient of potential temperature with the local θ_*, the observations can be summarized as follows:

- close to the active surface, the measured Φ_h are very small as compared to Φ_h^{IS}. There is a tendency for Φ_h to decrease with increasing instability.

- At a mid-roughness sublayer level, Φ_h, when locally scaled, is well represented by Φ_h^{IS} for weakly unstable stability (-0.05 > z'/L > -0.15). Beyond this stability range, Φ_h departures are very large and counter gradient flux can occur.

- Processes of different scales seem to determine turbulent fluxes of sensible heat and gradients of potential temperature, respectively.

Table 11.2:   As Table 11.1, but for Φ_h.

Φ_h				
stability range,z'/L	10m	number	5m	number
< 0.03	0.473	(10)	0.389	(6)
0.03 - 0.05	0.084	(5)	0.238	(6)
0.05 - 0.07	-	(1)	0.070	(3)
0.07 - 0.09	0.107	(5)	0.010	(3)
0.09 - 0.15	0.096	(5)	0.681	(4)
> 0.15	-	-	0.466	(7)

11.3 The Richardson Number

According to Monin-Obukhov similarity theory, the gradient Richardson number R_i can be expressed through

$$R_i = (z/L) \cdot \left(\Phi_h / \Phi_m^2\right) \tag{11.3}$$

which leads to the explicit semi-empirical expression (2.24a) for unstable stratification

$$R_i = \frac{0.95 \, z/L \, (1-19.3 \, z/L)^{1/2}}{(1-11.6 \, z/L)^{1/2}} \text{ (unstable)} \tag{2.24a}$$

If R_i is calculated from the gradients at position 11, its dependence on stability is (with some exceptions) very well represented by (2.24a). This leads to the interesting observation, that - although flux-gradient-relations may not be preserved in the roughness sublayer over the whole stability range - a "gradient - gradient" relation still holds. This can be seen best in the near neutral range (Fig. 11.8), where Φ_m and Φ_h behave distinctly different. It has, however, to be noted that z'/L in Fig. 11.8 refers to local stability (i.e. calculated from u_* and $\overline{w'\theta'}$ at position 11).
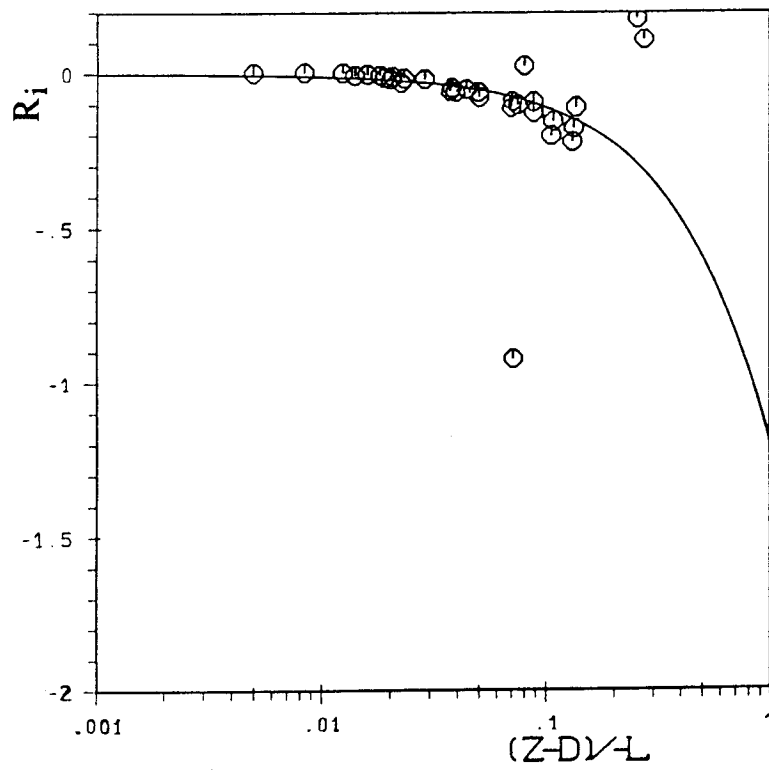
Figure 11.8   The gradient Richardson number R_i as calculated from equation (2.25)
for different stabilities. The solid line corresponds to equation (2.24a).

Seite Leer /
Blank leaf

12. Spectra

12.1 Scaling

It is traditional in atmospheric work to plot spectral densities not against the natural frequency n (as measured in s^{-1} or Hz) but rather against a non-dimensional frequency $f=nz/\bar{u}$ (Kaimal et al., 1972). Nevertheless, Raupach et al. (1986) have reported for their spectra obtained within an (artificial) roughness sublayer that they collapse in the inertial subrange when plotting against n. If plotted against the inertial sublayer frequency f on the other hand, they appeared much more scattered. The effect of using the non-dimensional frequency has therefore been established for all of the present spectra and will be outlined using those for the longitudinal velocity component as an example.

Fig. 12.1 compares the spectral representation of u as plotted against n and f, respectively, at the uppermost height of turbulence measurements (position 11). Firstly, the increase of spectral densities at the high frequency end has to be recognized (Fig. 12.1a). It is most likely that this has to be attributed to aliasing due to the relatively low sampling rate of 1 s^{-1}. Apart from this, the scatter in the high frequency range is considerably reduced when plotting the spectra with the inertial sublayer scaling f (Fig. 12.1b). Looking at the spectra within the street canyon (Fig. 12.2), there is no difference in high frequency scatter between plotting against n or f, respectively. Inspecting the whole range of non-dimensional heights z/h, it is found that the positive effect of using f instead of n decreases with decreasing z/h. Close to roof level or within the canyon it is clear that one cannot expect f to be a useful dimensionless frequency. However, no other dimensionless frequency f', using another length scale, could be found for the spectra at z/h $\leq$ 1, for which the data collapse at the high frequency end. The same behaviour was reported by Raupach et al. (1986) for their measurements within an artificial plant canopy. They conclude that this may have to be explained through the fact that in this particular height range at least two length scales are significant in the spectra: one associated with larger-scale coherent eddies above the canopy (possibly proportional to z) and another referring to the element-wake scale. For different heights the relative importance of the two length scales changes, so that no single scale can be deduced for the spectra within the canopy.

Since f is preferable to n at z/h > 1 and equally bad as the latter within the canyon, the composite spectra presented in the following sections will be plotted against the

non-dimensional frequency f. Note, that through this choice, $f=nz/\bar{u}$ has to be used rather than $f^*=n(z-d)/\bar{u}$, in order to avoid negative frequencies at the lowest level $z=13m$ (d being larger than 13m for certain wind direction sectors). Fig. 12.3 shows the spectra at $z/h = 1.55$ when plotted against f^*. A comparison with Fig. 12.1b indicates that z and z' (=z-d) are equally suited for the calculation of the non-dimensional frequency.

12.2 Composite Spectra

Composite spectra have been calculated at all non-dimensional heights separately. In order to reduce the influence of aliasing, the four highest frequencies were not included into the analysis. Due to the averaging of the original spectral estimates into frequency bands of approximately equal width in the log space (see Section 5.5) the run-to-run scatter is much larger at the low frequency end of the spectra. At their high frequency end, the scatter among the spectra at the uppermost level is considerably larger than what can be expected over ideal terrain (e.g. Kaimal et al., 1972). Nevertheless, individual spectra appear to be characteristic for that particular non-dimensional height, so that the construction of a composite spectrum is certainly justified. When penetrating deeper into the street canyon, the scatter among individual spectra increases (see above). Thus, composite spectra within the canyon are less representative for single runs, but may nevertheless be informative to show the overall shape of energy distribution.

In Fig. 12.1, different symbols have been used for runs with average wind direction rectangular or parallel to the canyon (see caption Fig. 12.1). Since at neither height a characteristic according to wind direction could be established, composite spectra were constructed from all available runs, regardless of wind direction. Also the stability range covered by the present runs is too small with respect to typical variations in spectra obtained over ideal surfaces (Kaimal et al., 1972) to allow a distinction into different categories of stability.
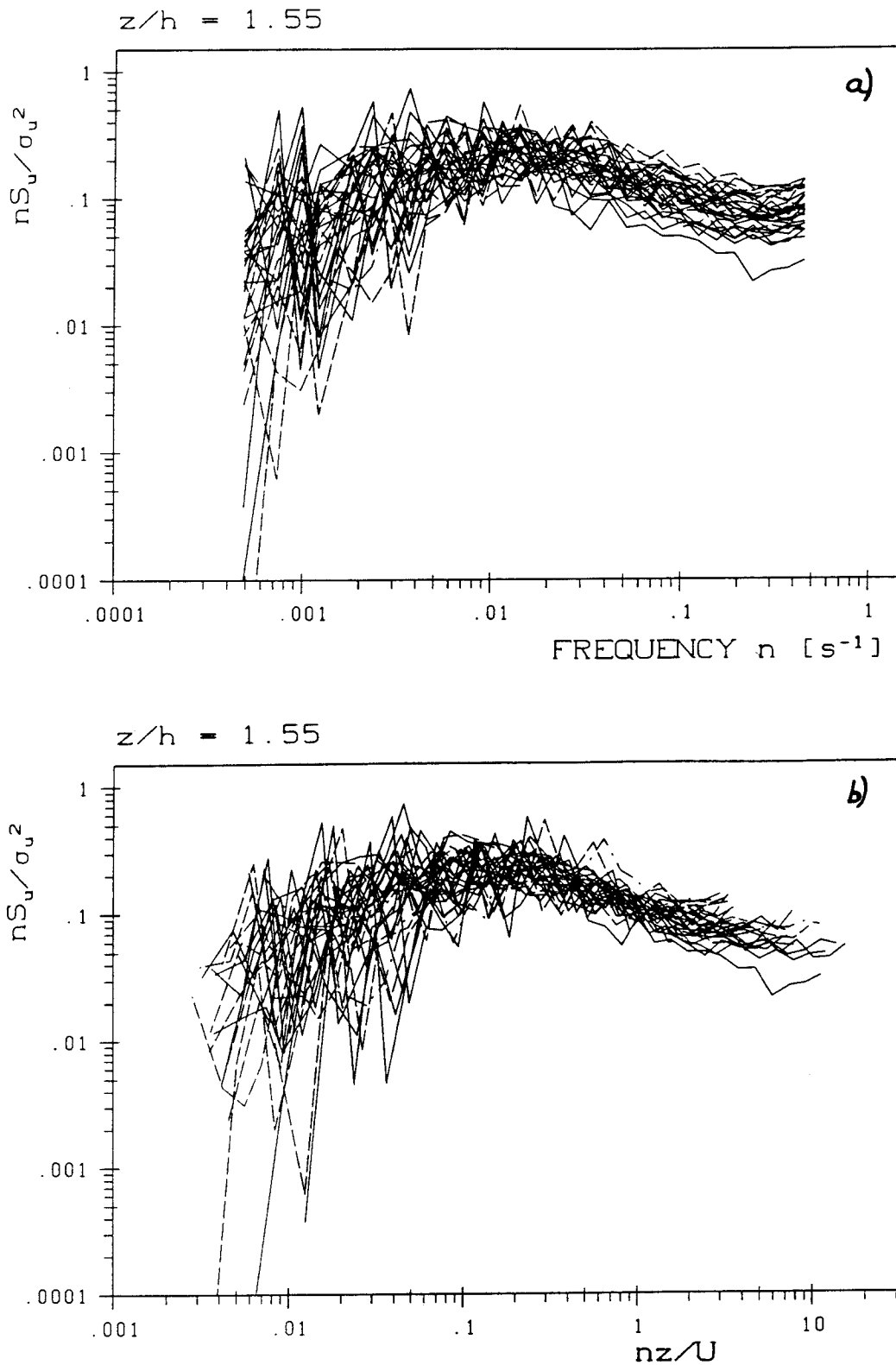
Figure 12.1   Spectra of longitudinal velocity component at position 11 plotted against
a) the natural frequency n and b) against the non-dimensional frequency
f. (— →): flow rectangular to the canyon, 0° - 60°, (—·—): parallel to the
canyon 90° - 150°, (········): rectangular to the canyon, 180° - 240°; (----)
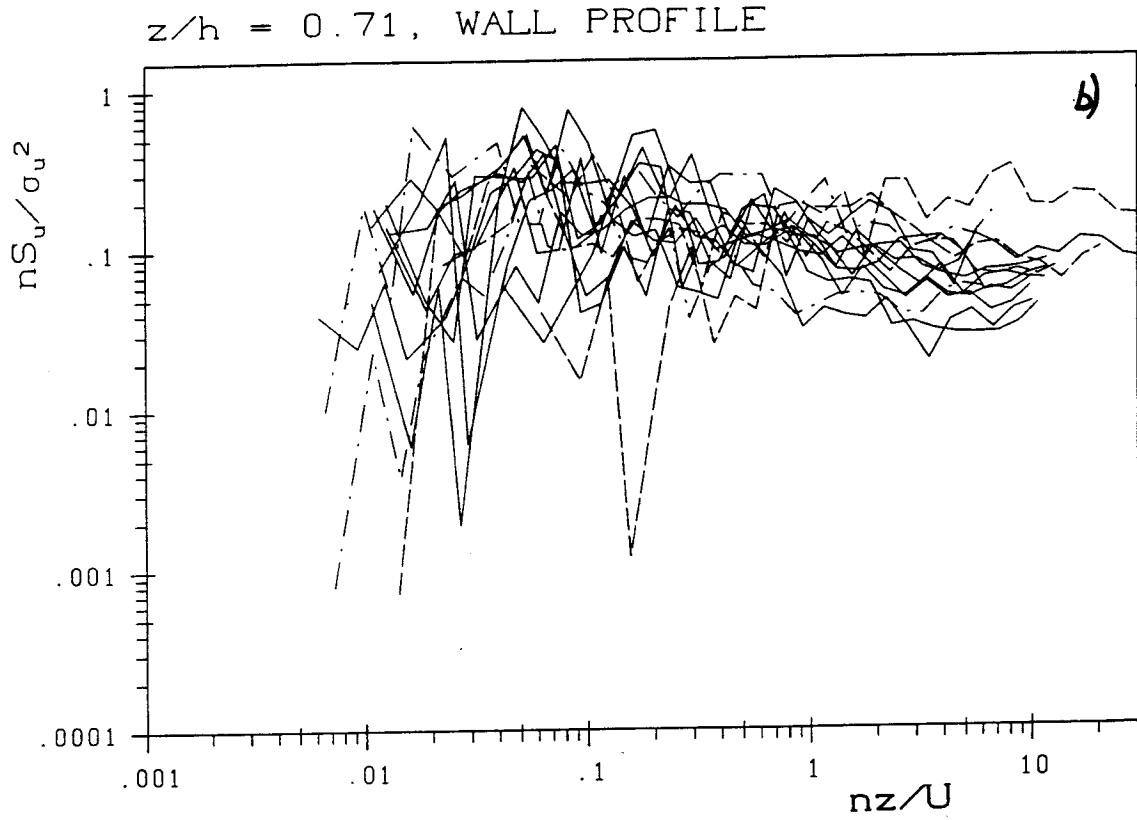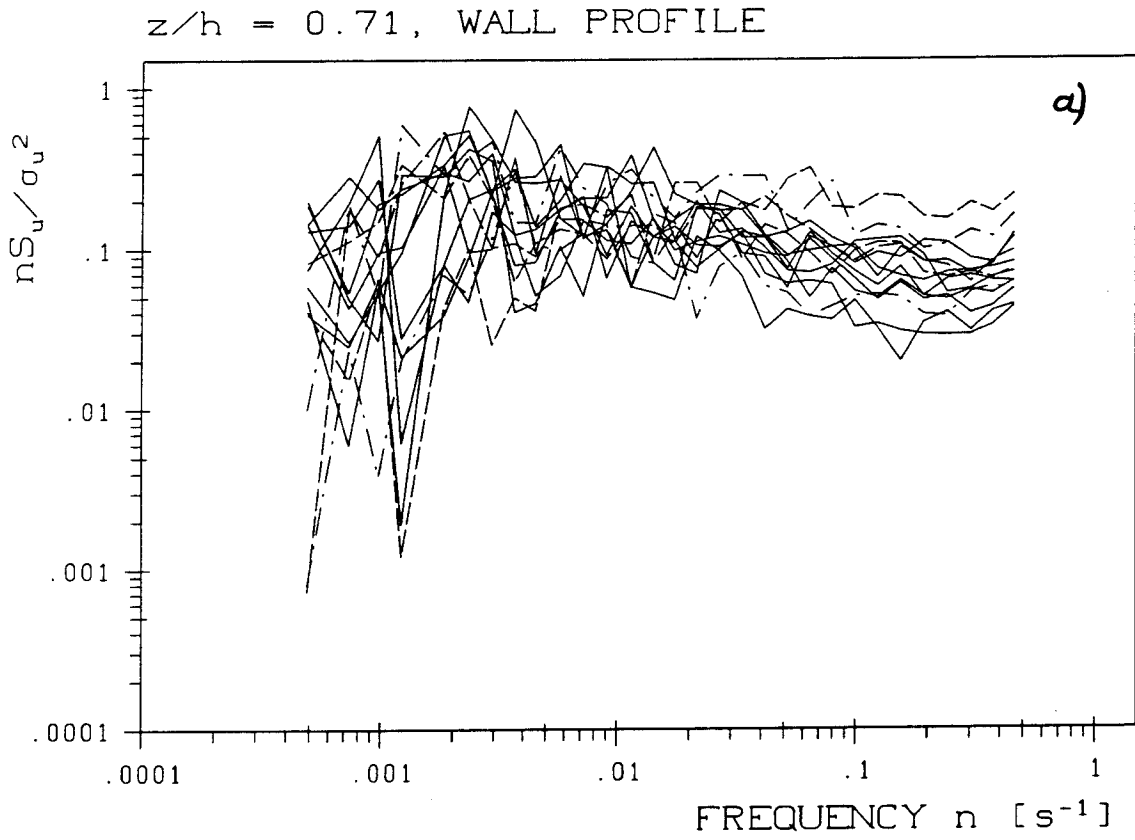parallel to the canyon, 270° - 330; (——): all other wind directions.
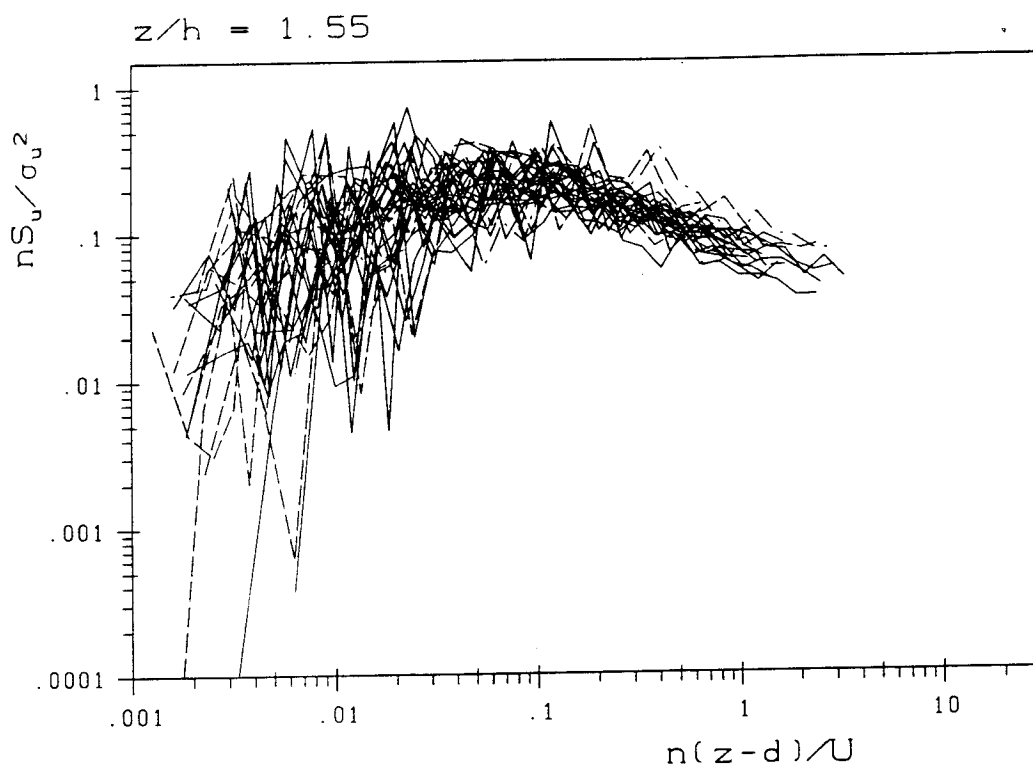
Figure 12.2   As Fig. 12.1, but for position 2.

z/h = 1.55

Figure 12.3   As Fig. 12.1, but using the non-dimensional frequency $f^* = n(z-d)/\bar{u}$

12.3 Spectra of Horizontal Velocity Components

Composite spectra at all non-dimensional heights (and horizontal positions, respectively) of the longitudinal velocity component are shown in Fig. 12.4. At the uppermost height ($z/h = 1.55$), the characteristic shape of surface layer (inertial sublayer) spectra is generally observed. The -2/3 slope in the inertial subrange predicted by Kolmogorovs hypothesis (cf. equation (2.19)) is almost met apart from a slightly slower roll-off, probably due to aliasing (for a detailed discussion of inertial subrange behaviour see next section). The peak frequency f_m lies in the range $0.1 < f_m$ < 0.2 (interpreting the irregularities in exactly this frequency range as scatter rather than as a characteristic feature). Since $f_m = z/\lambda_m$ by virtue of Taylor's hypothesis, it follows that λ_m, the peak wave length, ranges from 150 to 300 m. The wave length of the spectral peak of horizontal velocity spectra has been shown to be related to the mixed layer height z_i through (Kaimal, 1978)

$$\lambda_m = 1.5 z_i \qquad\qquad (12.1)$$

Although z_i has not been measured in the present case, the obtained value for λ_m is certainly too small to satisfy (12.1). For spectra of undisturbed flow, the peak frequency f_m is usually found at frequencies of the order of 0.01 in a comparable stability range (Kaimal et al., 1972; also Roth et al., 1988). If z' would have been used

instead of z for the calculation of f, the peak frequency f_m would be reduced by approximately a factor of two (z' ≈ 0.5z, typically at z/h = 1.55). Thus spectra obtained within a roughness sublayer exhibit their peak at a frequency that is 5-10 times larger than spectra from the inertial sublayer. Reduced mean wind speed (see the definition of f) may partly contribute to this behaviour but cannot explain the observed difference. It can therefore be stated that the scale of the eddies containing the maximum of the energy is considerably reduced within the roughness sublayer as compared to the inertial sublayer. At the low frequency end, two dips at f = 0.01 and f = 0.025 are observed. Interesting enough, Roth et al. (1988) have reported of dips at similar frequencies in the u-spectrum obtained at a site in sub-urban Vancouver.

At z/h = 1.27, above roof, a range of enhanced spectral density is observed between 0.05 < f < 0.5, corresponding to λ = 47 m to λ = 470 m. Outside this range the spectrum looks somehow "filtered". While the high frequency shape of the spectrum is retained to some extent at the above roof position (position 9), it appears to be lost completely at position 4 (above canyon). Here, the spectral characteristics of the roughness sublayer flow (low frequency end) and those observed within the street canyon (high frequency end) seem to be merged together resulting in a pronounced dip at f = 0.04. There is a clear shift of energy into the high frequency range, leaving a very broad and almost indiscernible maximum between $0.1 < f_m < 0.5$.

Within the canyon, at z/h = 0.91, the spectral densities are almost uniformly distributed over the whole (covered) frequency range with a steep roll-off at frequencies smaller than 0.015. At the lowest level of measurements, z/h = 0.71, two features are apparent: a further redistribution of low frequency energy into the mid-frequency range resulting in a more distinctly shaped spectrum. In particular the "middle profile" spectrum seems to be partly adapted to a new scaling regime. Secondly, spectral densities increase again at the high frequency end for f > 0.5. Although these estimates are certainly severely "polluted" by aliasing, it is reasonable that energy at small length scales that correspond to the size of balconies or other elements of building surfaces, appear in the spectrum. However, it is clear that Taylor's hypothesis does not apply within a street canyon in general. Not only that often $\sigma_h/\bar{u}$ is much larger than 0.5 (see Section 2.1.5) due to small wind speeds in this layer. The idea of "advected frozen turbulence" can certainly not be retained. At high frequencies, it might be assumed that turbulence characteristics are "transported" over distances much smaller than the characteristic length scales of the canyon (its height or width) with wind speeds corresponding to the within-canyon observation. But this is certainly not the case for low frequency contributions. No attempt can therefore be made to "translate" frequency scales into spatial scales at this height. Thus it can simply be stated that fluctuations at (natural) frequencies of the order of 0.1 s^{-1} or larger

significantly contribute to the total variance of the longitudinal velocity component. Comparing e.g. the two spectra at z/h = 0.91 and z/h = 0,71 (wall profile) it is most likely that energy from the range 0.2 < f < 5 is very efficiently shifted towards high frequencies. It is not possible to decide from the present data, to what extent the various production terms in the budget equation for velocity variances (e.g. Stull, 1988; cf. also equation (2.11)) contribute to the enhanced spectral densities observed at the high frequency end of the spectra within the canyon.

The spectra of the lateral velocity component (Fig. 12.5) are in many aspects similar to those of the longitudinal one. There are, however, some important differences. The v-spectrum at z/h = 1.55 is less "well behaved" (i.e. corresponding to the well known inertial sublayer spectral shapes) than it was the case for the u-spectrum. There is a very broad and flat maximum to be observed and an unusual behaviour in the high frequency range. It cannot be decided from the present data, however, whether the unexpectedly high spectral density at f = 3.5 or, equivalently, λ = 8m, reflects a physical process or must be attributed to aliasing.

Whereas the spectral curves at intermediate heights are very similar to those discussed above, a comparison of Figures. 12.4 and 12.5 shows that the adaption to the new environment takes place much more effectively for the lateral turbulence kinetic energy than for the longitudinal within the canyon. The spectrum at z/h = 0.71, mid-canyon position, in particular, exhibits a clear maximum at f_m = 0.65.

Very little can be found in the literature concerning spectra at a comparable height range over rough surfaces. Most measurements over urban areas were carried out at larger non-dimensional heights z/h. Högström et al. (1982), Clarke et al. (1982) and Roth et al. (1988) report small differences to horizontal spectra obtained over ideal surfaces (e.g. the "Kansas spectra", Kaimal et al., 1972). For flow over artificial rough surfaces (wind tunnel experiments), Mulhearn and Finnigan (1978) report similar correspondence to ideal spectra at heights z' > 2h. It has been mentioned in Section 12.1 that Raupach et al. (1986) found spectra within the roughness sublayer to collapse into one curve at the high frequency end when using n instead of the non-dimensional frequency f. This is consistent with the present results when considering the following:
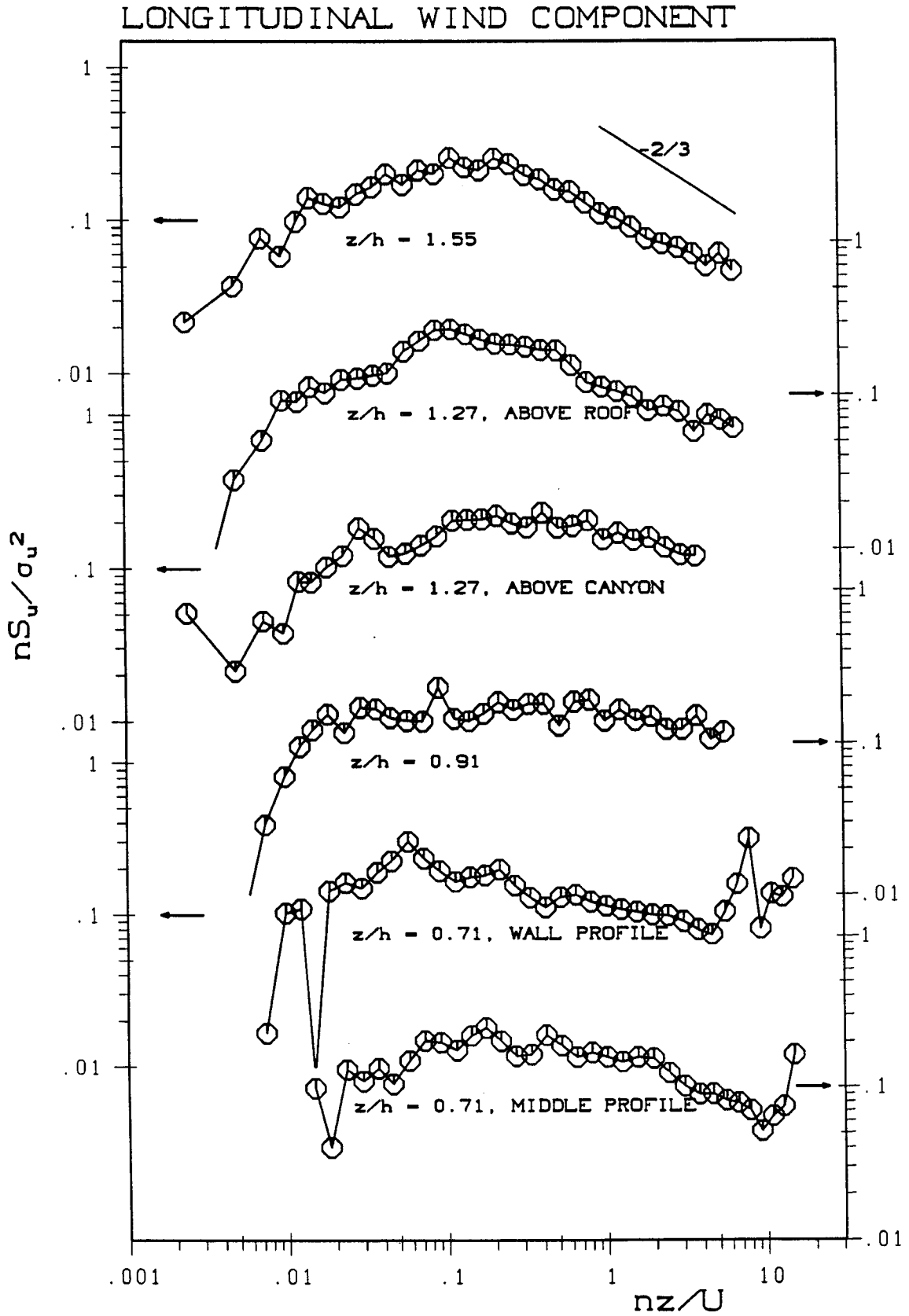
LONGITUDINAL WIND COMPONENT

Figure 12.4   Composite spectra of the longitudinal velocity component at the different non-dimensional heights as indicated.
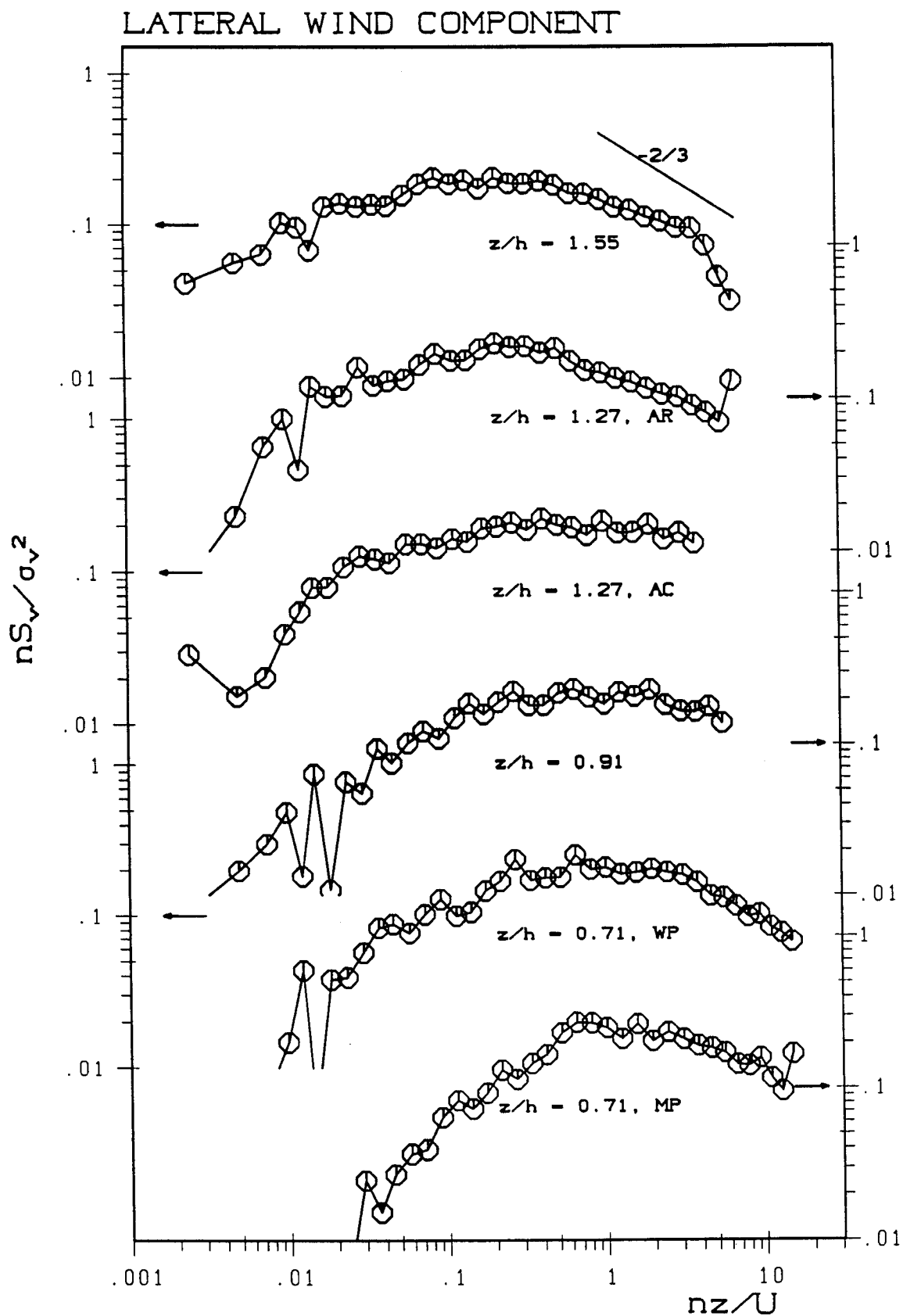
LATERAL WIND COMPONENT

Figure 12.5   As Fig. 12.4, but for the lateral velocity component. AR="above roof",
AC="above canyon", WP="wall profile", MP="middle profile".

- They were working with a constant free stream velocity so that different values of f referred to different measurement heights. The preference of f over n for the present data is only valid for spectra obtained at the same height

- thus spectra within the roughness sublayer are influenced by the measurement height twofold: once through the ratio z/ū (i.e. the turbulence state of the boundary layer) and secondly through the modification of their shapes that seem to be characteristic for a certain height z/h.

Within the canopy, Raupach et al. (1986) find a similar shift of energy towards higher frequencies in conjunction with a broad, not well defined "peak" for decreasing non-dimensional heights. These over-all features are consistent with the present results. The broadening of the spectral peak starts, however, at much lower non-dimensional heights as compared to the present findings. This is probably due to differences in the density of roughness elements.

12.4 Spectra of Vertical Velocity Components

The vertical spectra behave in many respects similar to the above described u- and v-spectra. At the uppermost level (Fig. 12.6), the overall shape of the spectrum is quite well-behaved. The spectral peak occurs at $f_m \approx 0.65$, corresponding to $\lambda_m \approx 45m$. Thus, f_m is somewhat larger than observed over homogeneous surfaces (Kaimal et al., 1972) or higher up over other urban surfaces (Clarke et al., 1982; Högström et al., 1982; Roth et al., 1988). This, however, must probably be attributed to the fact that z has been used for the calculation of f instead of z' (see above). The slope of the spectral curve at its high frequency end corresponds closely to the -2/3 power law for the inertial subrange.

At z/h = 1.27 (above roof position) the spectral maximum appears to be broadened and it is shifted towards higher frequencies ($f_m \approx 1.4$). This corresponds to the observations qualitatively described in Fig. 7.8 and reflects the break-up of eddies in favour of smaller ones due to pressure wake effects. The sampling interval was clearly too slow to resolve the inertial subrange at this height. At the "above canyon" position at the same height, an enhanced high frequency contribution as compared to the "above roof" position is observed and therefore an almost uniform distribution of spectral densities for f > 0.2.
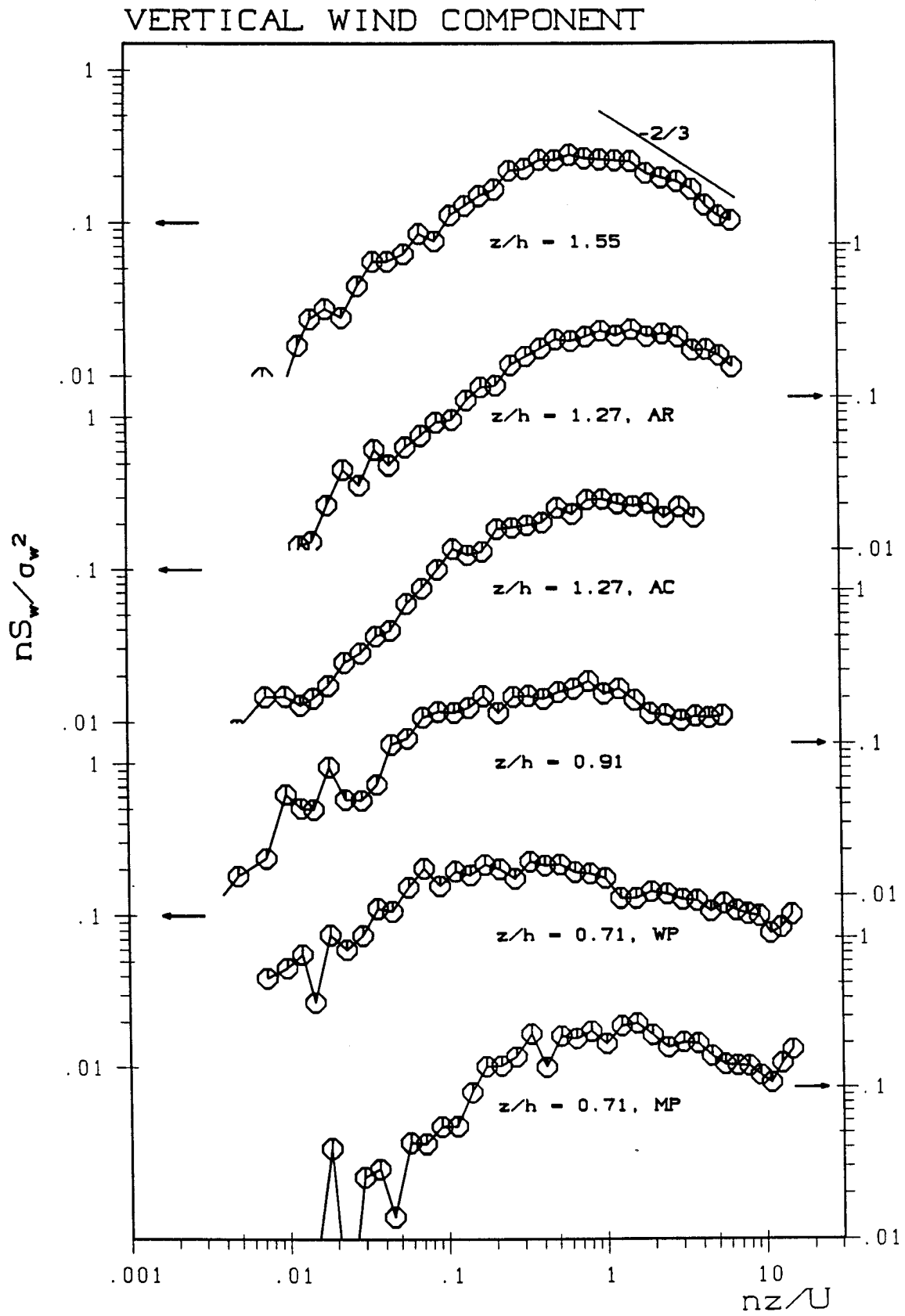
Figure 12.6   As Fig. 12.5, but for the vertical velocity component.

When penetrating into the street canyon the same two tendencies are found as for the u- and v-spectra. The shift of energy towards high frequencies occurs at two spectral scales. The low frequency energy is merged into an intermediate frequency range (especially for the middle profile) resulting in a broad "maximum", whereas the energy from the former maximum-energy-containing range is shifted to high frequencies. These findings complete the picture concerning the canopy - roughness sublayer interactions. From the analysis of Reynolds stress using the conditional sampling technique it was found that momentum transport occurs through intermittent events ("bursts") within the canyon and at its top. It can therefore be concluded that sporadically, eddies (or "fractions" of them) penetrate into the canyon contributing to momentum transport and turbulence kinetic energy. The low frequency contributions in the spectrum, shifted to the mid-frequency range for decreasing height may then be interpreted as a "probability" for these bursts to penetrate into the canyon to the respective depth.

The horizontal and vertical spectra exhibit at their high frequency end the -2/3 slope predicted for the inertial subrange. Nevertheless, the ratio $S_w(f)/S_u(f)$ provides an additional test for the inertial subrange. By means of the Kolmogorov hypothesis concerning local isotropy in this frequency range, this ratio is expected to approach 4/3. Fig. 12.7 shows that this requirement is not fulfilled at either height. $S_w(f)/S_u(f)$ remains smaller than one for almost all frequencies at the various non-dimensional heights. Above roof level, the ratio even decreases again for $f > 3$, reflecting the slower roll-off of the u-spectrum. Similar results have been reported by Mulhearn and Finnigan (1978) and Högström et al. (1982). Anticipating that a true inertial subrange occurs only within an inertial sublayer and recalling the fact that the present measurements were taken within the roughness sublayer, it can be stated that the $S_w(f)/S_u(f)$ ratio provides a much more stringent test for inertial sublayer flow than does the high frequency slope of the spectra.
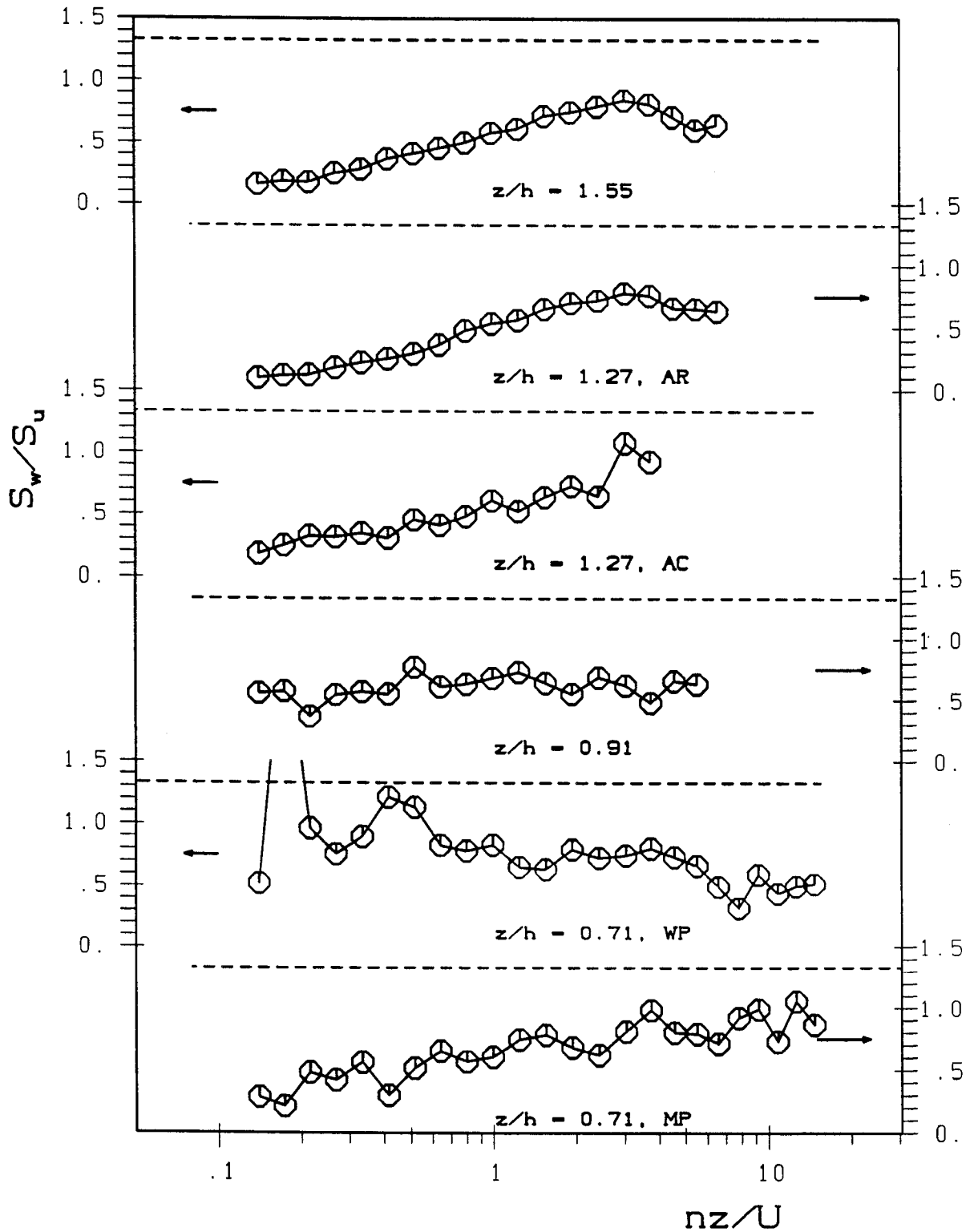
Figure 12.7   The ratio of spectral densities for the vertical to the horizontal velocity
component for various non-dimensional frequencies f. AR, AC, WP
and MP as in Fig. 12.5.

12.5 Temperature Spectra

The temperature spectra at the various non-dimensional heights (Fig.12.8) are most severely distorted. At the uppermost level, a very broad and not well defined maximum is observed. As for horizontal velocity spectra, it occurs at much larger f than observed over smooth surfaces. No -2/3 slope is present at the high frequency end. The most striking feature of the spectral curves at the other heights is the increase of spectral density at the low frequency end. This is consistent with the idea of warm "bubbles" of air, sporadically rising from the canyon. No analogous low frequency contribution is observed in the w-spectra (or, at least much weaker, see Fig. 12.6). Thus these "convective" contributions play a minor role for the vertical velocity variance as compared to the mechanically induced turbulence while being significant for temperature fluctuations.

The almost uniform distribution of spectral densities within the canyon ("white noise") points to a well mixed (with respect to temperature) volume of air. Measurements of Nakamura and Oke (1988) confirm this by stating that within a street canyon most of the thermal effects (of the walls and the floor) are restricted to a thin layer of 1 - 2 m from the respective surface. The same seems to be true for the air above the roof.

Directly above the canyon, the spectral distribution of temperature fluctuations seems to be governed by different processes. Apart from the "bubbles" at the low frequency end a peak at frequencies comparable to that in the w-spectrum indicates that mixing of canyon-air with roughness sublayer-air is also associated with mechanically induced turbulence.
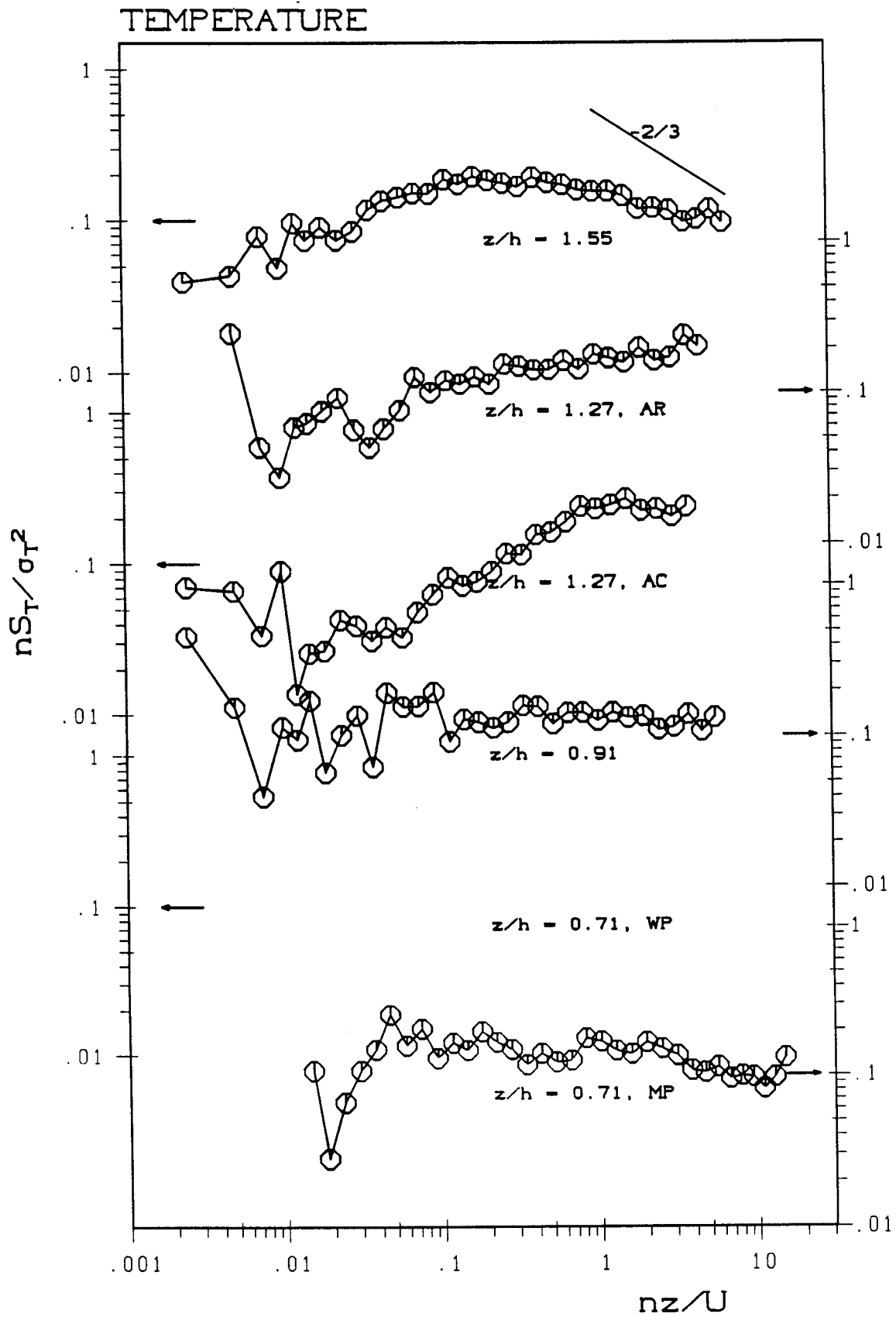
TEMPERATURE

Figure 12.8   As Fig. 12.5, but for temperature.

12.6 Cospectra

Cospectra for Reynolds stress are shown in Fig. 12.9 for the four upper levels. The composite cospectra for momentum flux at $z/h = 1.55$ and $z/h = 1.27$ (both positions) are in reasonable agreement and suggest that there is little variation of the spectral distribution of Reynolds stress over this height interval. They exhibit a spectral peak at $f_m = 0.25$ (somewhat flattened at the lower level). This lies close to the peak of the u-spectrum at the uppermost level and therefore again at a much higher frequency than observed over ideal terrain (Kaimal et al., 1972) or at greater heights over urban terrain (Roth et al, 1989). At the high frequency end, a slope close to -4/3 (as required by theory for the inertial subrange) is observed. Within the canyon, at $z/h = 0.91$, the shape of the cospectrum for Reynolds stress is completely lost. Due to the large run-to-run variability, however, it seems to be very tentative to interpret single "peaks" or "dips". Three examples from the lowest level ($z/h = 0.71$) that all passed the various data validation tests (see Chapter 5) may illustrate this (Fig. 12.10). Since the absolute value of Reynolds stress at this level is very small in general, no attempt has been made to find consistent structures for the Reynolds stress spectra within the canyon.

The cospectrum for the turbulent flux of sensible heat is very similar to that of Reynolds stress at the uppermost level (Fig. 12.11). At $z/h = 1.27$, a large scatter is introduced (particularly above the canyon) preserving the over-all shape of the spectrum more or less. An increase of cospectral density at the low frequency end again emphasizes the possible influence of canyon air "bubbles" as speculated in conjunction with the temperature spectra. At $z/h = 0.91$, finally, the composite cospectrum for heat flux must again be viewed with caution. Some of the "white noise behaviour" observed in the temperature spectrum at this level, however, can be seen in the mid-frequency range.
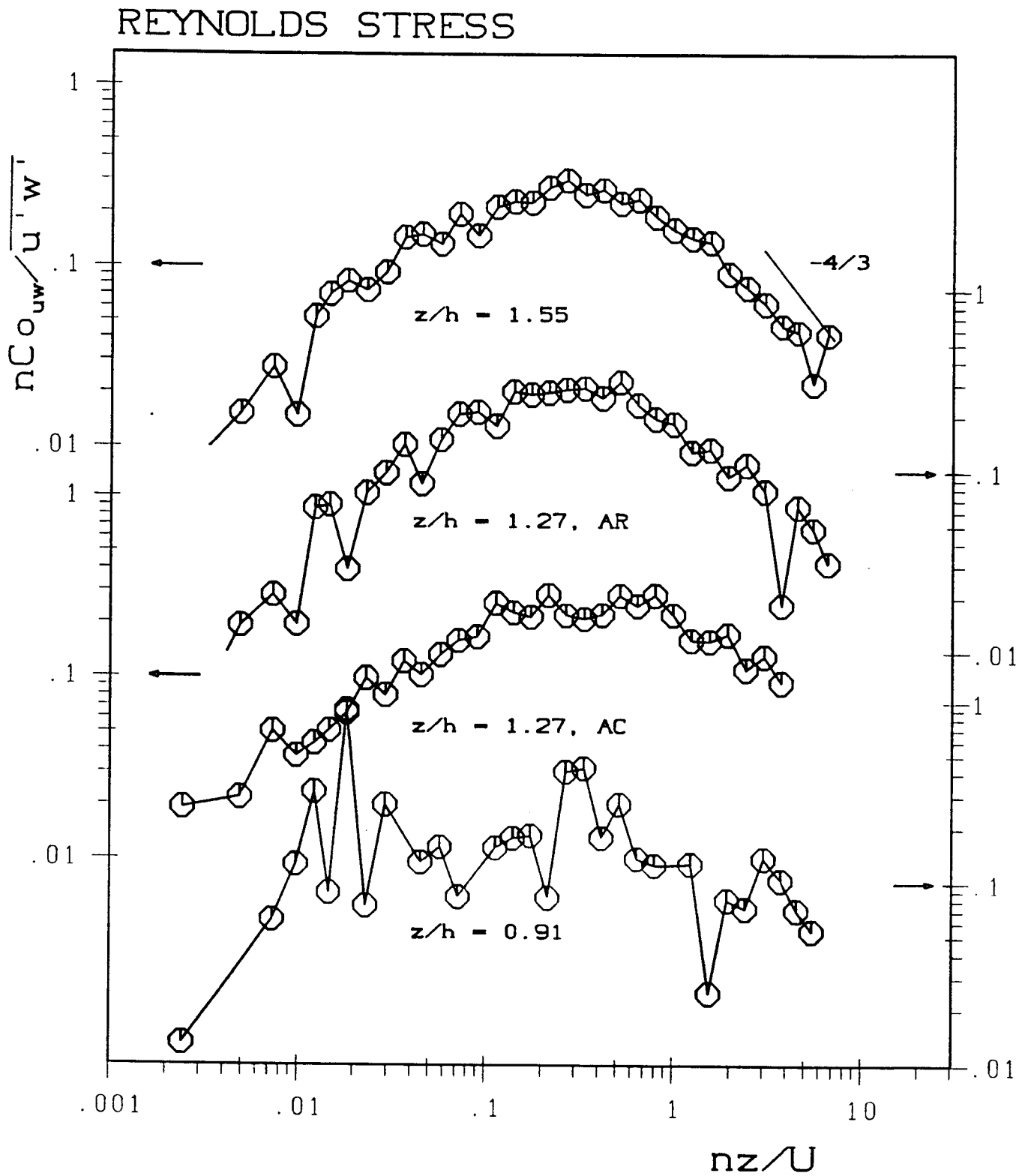
REYNOLDS STRESS

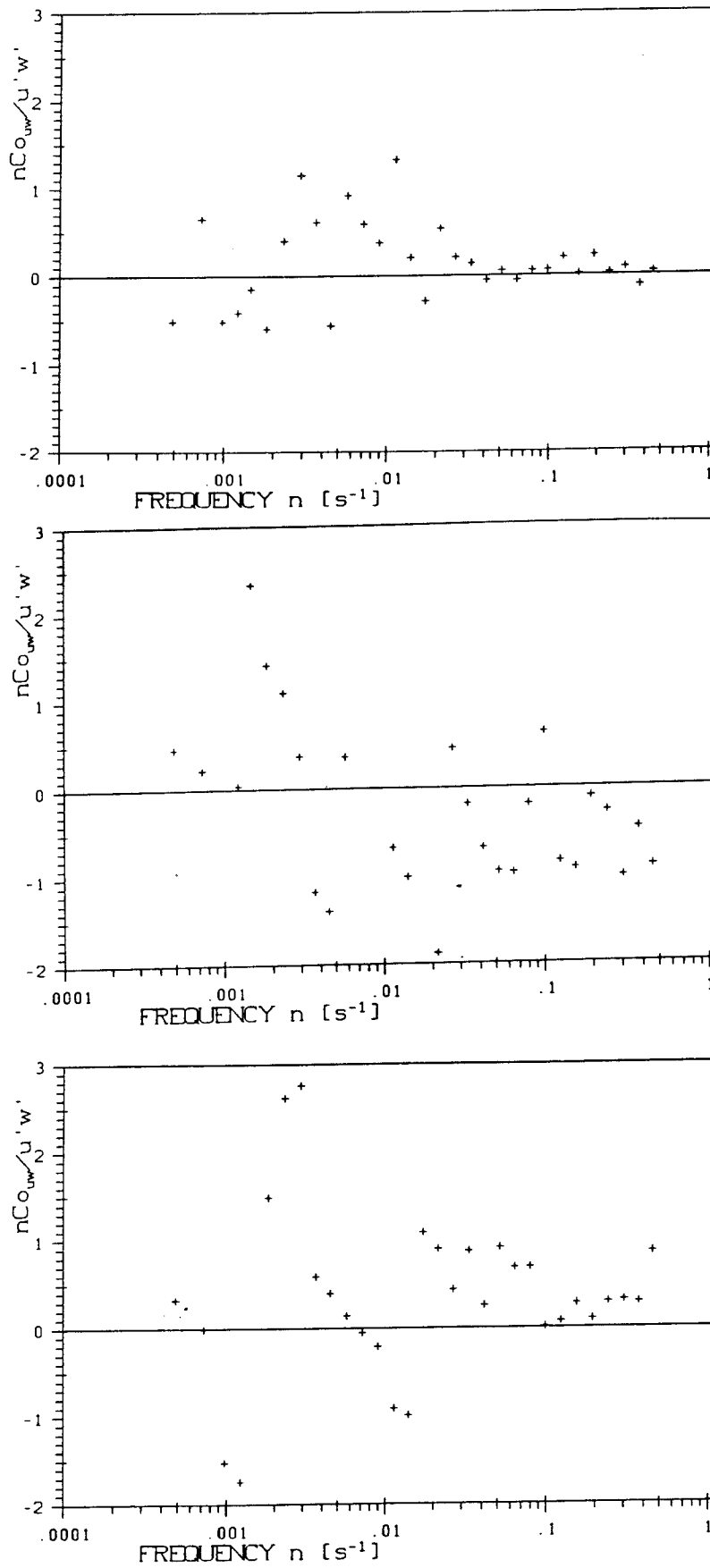Figure 12.9   As Fig. 12.5, but for Reynolds stress.

Figure 12.10   Three different cospectra for Reynolds stress at position 2 showing the very large run-to-run scatter within the canyon. Compare Fig. 12.2 for individual energy spectra at the same height.
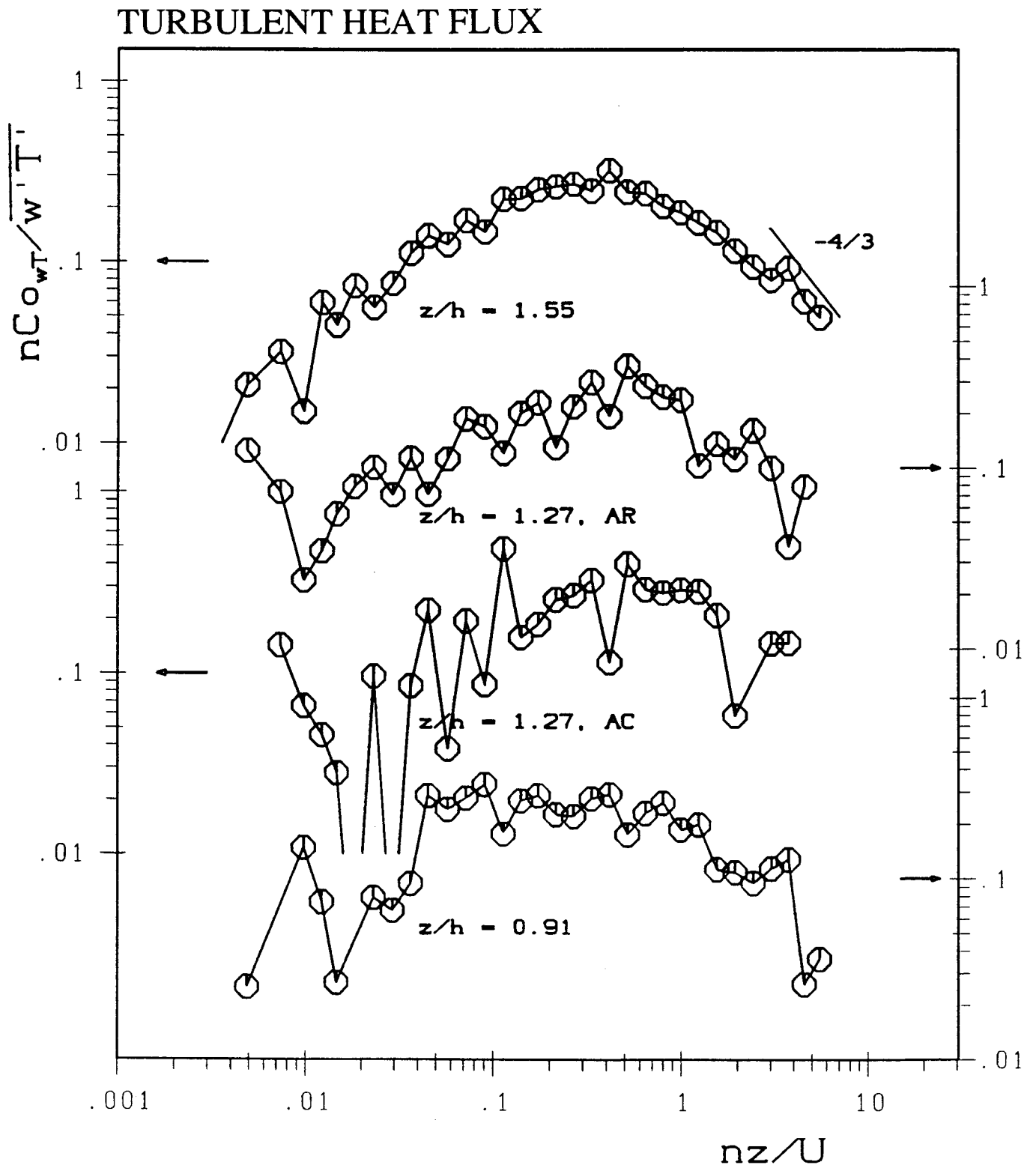
TURBULENT HEAT FLUX

Figure 12.11   As Fig. 12.9, but for turbulent flux of sensible heat.

12.7 Summary

The most important general observations concerning spectra and cospectra in the roughness sublayer and an urban canopy are summarized as follows:

- at a mid-roughness sublayer height (co)spectra *look* very similar to those observed over smooth surfaces or higher up over urban areas. They show a -2/3 (-4/3) slope at their high frequency end but the ratio $S_w(f)/S_u(f)$ does not approach 4/3.

- With the exception of the w-spectrum, spectral peaks occur at this height at frequencies that are 5-10 times higher than over smooth terrain.

- Close to roof level and within the urban canopy, spectral peaks (if any) are shifted towards high frequencies. This results for many variables in a "white noise type" spectrum at intermediate heights. Cospectra within the canyon are essentially unsystematic.

- Cospectra of Reynolds stress scale best with z (above roof level) while temperature spectra exhibit the most prominent difference to inertial sublayer spectra.

- The exchange of air between the canopy and the roughness sublayer occurs through intermittent bursts (i.e. eddies, at least partly penetrating into the canyon). It is suspected that warm bubbles of canyon air also contribute to this exchange. Thus, this exchange is both, partly driven by boundary layer- and partly by canopy layer energetics.

13. Synthesis and Conclusions

A variety of turbulence characteristics close to an urban surface have been presented and discussed in the foregoing chapters. The most important features and consistent findings are summarized in the following, using keywords to characterize turbulence in the urban canopy layer and roughness sublayer. Implications for urban diffusion modelling are given in the following section and finally, some suggestions for future research are listed.

13.1 Turbulence Characteristics of the Urban Canopy - and Roughness Sublayer

reduction of complexity

Although flow- and turbulence characteristics are highly complex if the flow around just one single building is considered, it turns out that a large enough group of buildings can produce regularities in the flow characteristics on a somewhat larger scale. It is therefore meaningful to search for consistent patterns in these characteristics in order to understand and model, for example dispersion of pollutants in this crucial part of the urban atmosphere.

horizontal averages

Due to the three-dimensional nature of the flow close to a rough surface all characteristics outlined in the following are valid only if *horizontal averages* are considered. The averaging of measurements from a single position in the horizontal plane over different wind directions, so that the flow experiences a variety of upwind geometries, provides a useful approach to obtain horizontal averages. In the case of an urban surface in particular, with its characteristic elements such as street canyons and buildings, it is necessary to include all of these elements separately (through measurements, modelling, etc.) since data from one single position (e.g. the roof-top position in the present study) does not cover the whole range of horizontal variability.

non-constant flux layer

Turbulent fluxes of sensible heat and momentum are found to be height dependent. When the urban surface is approached, eddies of the organized shear flow above are broken up into smaller, less correlated flow patterns due to pressure wake effects. This results in an enhanced turbulence kinetic energy close to roof level. Turbulent fluxes vanish at a height that corresponds approximately to the zeroplane displacement height. A parameterisation for the height dependence of Reynolds stress has been proposed.

The vertical variation of turbulent flux of sensible heat is much more complicated to describe than Reynolds stress. Local heating and cooling influences of the roof can lead to counter-gradient heat flux even at mid roughness layer height. The present measurements indicate that the upper boundary of the non-constant flux layer (roughness sublayer) at the Anwand site is at about $z_* = 2.5h$ and that an inertial sublayer is likely to be found aloft.

local scaling

Many of the well-known semi-empirical relationships for the surface layer (strictly speaking for its upper part, the inertial sublayer) are valid within the roughness sublayer (not the canopy layer) when using the local turbulent fluxes and thus stability measures as scaling variables. Turbulence/turbulence relationships (such as σ_i/u_*) are preserved best, but, surprisingly, also those among mean variables (such as the gradient Richardson number). Relationships between mean variables and turbulence measures (flux-gradient relationships) are most complex. Close to the roof level, momentum fluxes are in local equilibrium with the respective gradients (with large horizontal variability, though) while turbulent fluxes of sensible heat are not. At a mid-roughness layer height, inertial sublayer relationships are valid for both fluxes on average when local scaling is applied.

roughness distortions vs. thermal distortions

Local variations in the thermal properties of the roughness elements (e.g. heating or cooling of the roof surface) lead to much stronger deviations from inertial sublayer behaviour (locally scaled) than does the variation in mechanical forcing. Since the above statement holds only for relationships between mean and turbulence variables (and *not* for turbulence/turbulence relationships such as σ_θ/θ_*) it is concluded that the adaptation of mean properties to local changes in roughness occurs much faster and more effectively than the adaption to changing thermal properties of the surface.

length scales

The height above ground (i.e. above the zeroplane displacement height within the roughness sublayer) clearly remains an important length scale for the flow close to an urban surface. However, other length scales, related to roughness element geometry must be considered in order to describe the state of turbulence in this part of the urban boundary layer. Due to the case study approach of this investigation, it was not possible to address the question as to which of the various possible length scales (height of buildings, separation distance between them, zeroplane displacement height, etc.) may be the most important. The zeroplane displacement height which was shown

to be an important length scale in the vertical profile of Reynolds stress, can be calculated using the inertial sublayer prediction for σ_θ/θ_*.

Horizontal velocity fluctuations, found to scale with the mixed layer height z_i over smooth and homogeneous surfaces, exhibit their spectral peak within the roughness sublayer at wavelengths considerably smaller than that.

canopy/roughness sublayer interactions

The exchange between the canopy layer and the roughness sublayer occurs to a rather small extent via small scale turbulent transport. Intermittent bursts penetrating into the canopy are largely responsible for the exchange of energy (and mass) between the two layers. The use of the conditional sampling technique shows that close to roof level large, partially offsetting contributions of upward and downward transport lead to reduced fluxes of momentum. Above the street canyon, and at its upper part, sweeps clearly dominate over ejections. An (at least measurable) contribution to the upward transport of sensible heat appears to be due to (also intermittent) "bubbles" of warmer canyon air rising into the roughness sublayer.

vertical structure

The average vertical profiles of many turbulence variables (additionally to the turbulent fluxes, see above) have been calculated and are shown to be stability dependent.

Due to the local scaling regime found in the urban roughness sublayer, the interpretation of turbulence observations at only one height within the RS may lead to the erroneous conclusion that surface layer similarity applies. The best check for inertial sublayer scaling to hold may be provided by the spectral behaviour of the velocity components: the ratio between spectral densities of vertical and longitudinal velocity approaching 4/3 in the inertial subrange and the peak frequency for horizontal velocity components being proportional to the mixed layer height. Both requirements are found to be clearly violated in the roughness sublayer (and also, of course, within the urban canopy).

13.2 Implications for Urban Turbulence Modelling

Most applied urban pollution models use a surface layer scheme as a turbulence parameterisation for their lowest (few) levels (if not much simpler approaches such as Gaussian models are used). The present results suggest that this could lead to large errors, particularly in the lowest few tens of meters (where concentrations of pollutants are highest and thus turbulence characteristics of great importance). The following

recommendations (not of a modeler, however) may be useful in order to improve such "shortcomings" in micro- or mesoscale models:

- The lowest i levels (up to z_*) should be declared as "roughness sublayer". Level i+1 could then be treated as the first surface layer level.

- If empirical relations based on surface layer characteristics are used in order to calculate certain properties (e.g. a profile for the exchange coefficient K_m), these should be evaluated at level i+1. In this case, the numerical scheme should start at height i+1, "propagating" in both directions upward and downward.

- For the lowest i levels, it seems to be useful to prescribe a profile for Reynolds stress and turbulent heat flux according to the building geometry and calculate the respective local values using u_* and θ_* at level i+1. From the local stability measure it is then possible to calculate whatever turbulence information is necessary for the type of model under consideration.

- The problem of defining the "surface" can be addressed as follows: Due to the exchange characteristics between the canopy layer and the roughness sublayer, it is suggested to define the model surface at the zeroplane displacement height with vanishing turbulent fluxes at this lower boundary. Pollutant sources within the street canyons could then be treated as an area source at z=0 (in model coordinates) with their strength calculated from the actual emissions and the air volume of the canyon.

13.3 Need for Future Research

Since the present results are based on measurements at one single location, it is certainly necessary to assess their general validity for other, similar sites. From comparison with wind tunnel results, it seems that the present findings are indeed characteristic for rough surfaces in general. For phenomena related to sensible heat, on the other hand, the local surface characteristics (e.g. roof materials) might have a considerable influence. It will also be necessary, to assess the horizontal variability of turbulence characteristics in greater detail. The following questions remain unanswered (or arise as questions from this study):

- To what extent is the vertical variation of the turbulent fluxes dependent on building geometry?
- Is the proposed formulation for $u_*(z)$ of general validity for other sites?
- The behaviour of all variables related to sensible heat is very likely to be dependent on building materials. How large is this influence?
- If, for example, Reynolds stress is measured at sufficiently large heights, does it become constant with height over an urban surface, as observed in wind tunnel experiments?

- The present measurements suggest that there is indeed an inertial sublayer above the urban roughness sublayer. How is its lower boundary related to building geometry?

- To what extent may the results for a scalar such as temperature be applied for passive tracers (such as pollutants)?

- When introduced into a numerical model, are the present findings useful to improve their accuracy?

13.4.Epilogue

I hope that the findings and results of the present study can make a contribution to a better understanding of the processes governing turbulence close to a rough urban surface. Since the diffusion of pollutants is inherently related to turbulence, this knowledge of turbulence characteristics will be important for improving urban diffusion modelling. Tasks such as identifying important sources in highly built-up areas indeed require the use of numerical models with reliable parameterisations for turbulence. It should never be forgotten, however, that diffusion does not reduce the total amount of pollutants (nor does diffusion modelling). The important thing and the only solution is therefore to reduce the emissions of pollutants.

Seite Leer /
Blank leaf

REFERENCES

Antonia R.A. and Luxton, R.E.: 1971, 'The Response of a Turbulent Boundary Layer to a Step Change in Surface Roughness, Part I: Smooth to Rough', *J. Fluid Mech.*, **48**, 721-761.

Baker C.B.: 1988, 'Experimental Determination of Transducer Shadow Effects on a Sonic Anemometer', *Preprints 8th symp. turbulence and diffusion*, Apr. 26-29, 1988, San Diego,CA. AMS, Boston, Mass,104-107.

Baldocchi D.D.; and Meyers T.P.: 1988, 'Turbulence Structure in a Decidous Forest', *Boundary-Layer Meteorol.*, **43**, 345-364.

Beljaars, A. C. M.: 1982, 'The Derivation of Fluxes from Profiles in Perturbed Areas', *Boundary-Layer Meteorol.*, **24**, 35-56.

Beljaars, A. C. M.; Schotanus, P. and Nieuwstadt, F. T. M.: 1983, 'Surface Layer Similarity under Nonuniform Fetch Conditions', *J. Clim. Appl. Meteorol.*, **22**, 1800-1810.

Bendat, J. S. and Piersol, A. G.: 1986, *Random Data; Analysis and Measurement Procedures*, J. Wiley, Interscience, New York, 407 p.

Bowne, N. E. and Ball, J. T.: 1970, 'Observational Comparison of Rural and Urban Boundary Layer Turbulence', *J. Appl. Meteorol.*, **18**, 1072-1077.

Brook, R.R.: 1972, 'The Measurement of Turbulence in a City Environment', *J. Appl. Meteorol.*,**11** 443-450.

Busch, N. E.: 1973, 'On the Mechanics of Atmospheric Turbulence', in Haugen, D. A., (Ed.), *Workshop on Micrometeorology*, Amer. Meteorol. Soc., Boston, 1-65.

Busch, N.E. and Kristensen, L.: 1976, 'Cup Anemometer Overspeeding', *J. Appl. Meteorol.*,**15**, 1328 - 1332.

Businger, J. A.: 1959, 'A Generalization of the Mixing-Length Concept', *J. Meteor.*, **16**, 516-523.

Businger, J. A.; Wyngaard, J. C.; Izumi, Y. and Bradley, E. F.: 1971, 'Flux-Profile Relationships in the Atmospheric Surface Layer', *J. Atmos. Sc.*, **28**, 181-189.

Clarke, C.F.; Ching, J.K.S. and Godowich, J.M.: 1982, 'A Study of Turbulence in an Urban Environment', *EPA technical report*, EPA 600-S3-82-062.

Conklin P.S.; Knoerr K.R.; Schneider T.W. and Baker C.B.: 1988, 'A Wind Tunnel Test of Probe Shadow Effects on a Sonic Anemometer in two Orientations', *Preprints 8th symp. turbulence and diffusion*, Apr. 26-29, 1988, San Diego,CA. AMS, Boston, Mass,108-111.

Coppin, P. A.: 1979, 'Turbulent Fluxes over a Uniform Urban Surface', *Ph. D. Thesis*, Flinders University, Inst. Atmos. Marine Science, Adelaide,

Coppin P.A. and Taylor K.J.: 1983, 'A Three-component Sonic Anemometer Thermometer System for General Micrometeorological Research', *Bound.-Layer Meteor.* , **27**, 27-42.

Counihan, J.: 1971, 'Wind Tunnel Determination of the Roughness Length as a Function of the Fetch and density of Three dimensional Roughness Elements', *Atmos. Environ.*, **5**, 637-642.

De Bruin, H.A.R.; Bink, N.J. and Kroon L.J. M.: 1988,'Surface Fluxes under Advective Conditions', *Workshop on "Measurement and parametrization of land-surface evaporation fluxes"*, 10.-21.10. 1988, Banyuls, France.

Denmead, O.T. and Bradley E.F.: 1985,'Flux-gradient Relationships in a Forest Canopy', in Hutchinson, B.A. and Hicks, B.B. (Eds.) *The Forest-Atmosphere Interaction"*, Reidel, 684 pp.

DePaul, F.: 1984, 'A Study of Pollutant Dispersion in an Urban Street Canyon', *Ph. D. Thesis*, Illinois Institute of Technology, UMI, 119 pp.

Dyer, A.J.: 1981,'Flow Distortion by Supporting Structures', *Bound.-Layer Meteor.* , **20**, 243-251.

Dyer, A. J. and Hicks, B. B.: 1970, 'Flux-Gradient Relationship in the Constant Flux Layer', *Quart. J. Roy. Meteorol. Soc.*, **96**, 715-721.

Finnigan , J.J.: 1979a, 'Turbulence in Waving Wheat, I: Mean Statistics and Honami', *Bound.-Layer Meteor.* , **16**, 181-211.

Finnigan , J.J.: 1979b, 'Turbulence in Waving Wheat, II: Structure of Momentum Transfer', *Bound.-Layer Meteor.* , **16**, 213-236.

Gao W.; Shaw R.H. and Paw U K.T.: 1989, 'Observation of Organized Structure in Turbulent Flow within and above a Forest Canopy', *Boundary-Layer Meteorol.*, **47**, 349-377.

Garratt, J. R.: 1978a, 'Flux Profile Relations above Tall Vegetation', *Quart. J. Roy. Meteorol. Soc.*, **104**, 199-211.

___: 1978b, 'Transfer Characteristics for a Heterogeneous Surface of Large Aerodynamic Roughness', *Quart. J. Roy. Meteorol. Soc.*, **104**, 491-502.

___: 1980, 'Surface Influence upon Vertical Profiles in the Atmospheric Near Surface Layer', *Quart. J. Roy. Meteorol. Soc.*, **106**, 803-819.

Georgii, H.W.; Busch, E. and Weber, E.: 1967, 'Investigation of the Temporal and Spatial Distribution of the Emission Concentration of Carbon Monoxide in Frankfurt/Main', *Report No. 11* (of the Institute for Meteorology and and Geophysics, Frankfurt/Main), Translation No 0477, NAPCA.

Goff, J. A. and Gratch S.: 1946, *Trans. Amer. Soc. Heat and Vent. Eng.*, **52**, p.95.

Grant, A.L.M. and R.D.Watkins: 1989, 'Errors in Turbulence Measurements with a Sonic Anemometer', *Bound.-Layer Meteor.* , **46**, 1-2, 181-194.

Hanafusa, T.; T. Fujitani; Kobori,Y. and Mitsuta, Y.: 1982, 'A New Type Sonic Anemometer-Thermometer for Field Operation', *Pap. Meteor. and Geophys.*, **33**, 1, 1-19.

Hicks, B. B.; Hess, G. D. and Wesley, M. L.: 1979, 'Analysis of Flux-Profile Relationships above Tall Vegetation - An Alternative View', *Quart. J. Roy. Meteorol. Soc.*, **105**, 1074-1077.

Högström, U.: 1982, 'A Critical Evaluation of the Aerodynamical Error of a Turbulence Instrument', *J. Appl. Meteor.* , **21**, 1838-1844.

___: 1988, 'Non-dimensional Wind and Temperature Profiles in the Atmospheric Surface Layer', *Bound.-Layer Meteor.* , **42**, pp. 55 - 78.

Högström, U.; Bergström, H. and Alexandersson, H.: 1982, Turbulence Characteristics in a Near-Neutrally Stratified Urban Atmosphere' *Bound.-Layer Meteor.* , **23**, 449-472.

Högström, U.; Bergström, H.; Smedman A.S.; Halldin S. and Lindroth, A.: 1989, Turbulent Exchange above a Pine Forest, I: Fluxes and Gradients'. *Bound.-Layer Meteor.* , **49**, 197-217.

Holtslag, A. A. M. and Nieuwstadt, F. T. M.: 1986, 'Scaling the Atmospheric Boundary Layer', *Boundary-Layer Meteorol.*, **36**, 201-209.

Hosker, R. P.: 1984, 'Flow and Diffusion near Obstacles', in Randerson, D., (Ed.), *Atmospheric Science and Power Production*, US Govt. Publ. DOE/ TIC-27601, 241-326.

Hunt, J.C.R.: 1973, 'A Theory of Turbulent Flow Around Two-dimensional Bluff Bodies', *J. Fluid Mech.*, **61**, 625-706.

Kaimal, J. C.: 1978, 'Horizontal Velocity Spectra in an Unstable Surface Layer', *J. Atmos. Sc.*, **35**, 18-24.

___: 1979, 'Sonic Anemometer Measurement of Atmospheric Turbulence, Proc. Dynamic Flow Conference, Skovlunde, Denmark, DISA Electronic A/S, 551-565

Kaimal, J. C.; Wyngaard, J. C.; Izumi, Y. and Cote, O.R.: 1972, 'Spectral Characteristics of Surface Layer Turbulence', *Quart. J. Roy. Meteorol. Soc.*, **98**, 563-589.

Kaimal, J.C. and Gaynor, J.E.: 1983, 'The Boulder Atmospheric Observatory', *J. Climate Appl. Meteorol.*, **22**, 863-880.

Kondo, J. and Yamazawa, H.: 1986, 'Aerodynamic Roughness over an Inhomogeneous Ground Surface', *Boundary-Layer Meteorol.*, **35**, 331-348.

Kratzer, A.: 1956, *Das Stadtklima*, Die Wissenschaft, Vol. 90, Viehweg & Sohn, Braunschweig, 184 pp.

Kutzbach, J.: 1961, 'Investigations of the Modifications of Wind Profiles by Artificially Controlled Surface Roughness. Studies of the Three-dimensional Structure of the Planetary Boundary Layer', *Annual Report, Dept. of Meteorology, Univ. of Wisconsin,* Madison.

Landsberg, H.E.: *The Urban Climate*, Int. Geophys. Ser., Vol. 28, Academic Press, New York, San Francisco, London.

Lettau,H.: 1957, 'Computations of Richardson Numbers, Classification of Wind Profiles and Determinations of Roughness Parameters', *Exploring the atmosphere's first mile, Vol. 1*, London and NY, Pergamon.

____: 1969, 'Note on Aerodynamic Roughness-Parameter Estimation on the Basis of Roughness Element Description', *J. Appl. Meteorol.*, **8**, 828-832.

Lo, A.K.: 1977, 'An Analytical-Empirical Method for Determining the Roughness Length and Zeroplane Displacement', *Quart. J. Roy. Meteor. Soc.*, **105**, p.1074.

Lumley, J.L. and Panofsky, H.A.: 1964, *The Structure of Atmospheric Turbulence*. New York, Interscience - Wiley, 239 pp.

Mazzoni, R.: 1988, 'Lokalzirkulationen in Zürich', *Diplomarbeit*, Geogr. Inst. der Universität Zürich und Geogr. Inst. E.T.H., Zürich, 62 p.

Monin, A.S. and Obukhov, A.M.: 1958, 'Fundamentale Gesetzmässigkeit der turbulenten Vermischung in der bodennahen Schicht der Atmosphäre', in Goering H. (Ed.): *Statistische Theorie der Turbulenz*, Akademie Verlag, Berlin.

Mortensen N.G.; Larsen, S.E.; Troen, I. and Mikkelsen T.: 1987, 'Two-Years-Worth of Turbulence Data Recorded by a Sonic-Anemometer-Based Data Acquisition System', *Preprints 6th symp. Meteorological Observations and Instrumentation*, Jan. 12-16, 1987, New Orleans,LA. AMS/WMO, Boston, Mass,393-396.

Mulhearn, P. J.: 1978, 'Turbulent Flow over a Periodic Rough Surface', *Phys. Fluids.*, **21**, 1113-1115.

Mulhearn, P. J., and Finnigan, J. J.: 1978, 'Turbulent Flow over a very Rough, Random Surface', *Boundary-Layer Meteorol.*, **15**, 109-132.

Munn, R. E.: 1966, *Descriptive Micrometeorology*, Academic Press, New York and London, 245 pp.

Nakamura, Y. and Oke, T.R.: 1988, 'Wind, Temperature and Stability Conditions in an East-West Oriented Urban Canyon', *Atmos. Environ.*, **22**, 2691-2700.

Nunez, M. and Oke, T. R.: 1977, 'The Energy Balance of an Urban Canyon', *J. Appl. Meteorol.*, **16**, 11-19.

Ohmura, A.: 1982, 'Objective Criteria for Rejecting Data for Bowen-Ratio Calculations', *J. Appl. Meteorol.*, **21**, 595-598.

Ohmura, A. and Rotach, M.W.: 1986, *Mikroklimatologie*, Berichte und Skripten No. 28, Geogr. Inst. ETH, 140 pp.

Oke, T. R.: 1974, *Review of Urban Climatology 1968-1973*, WMO, Geneva, Technical Note, **134**, 132pp.

____: 1979, *Review of Urban Climatology 1973-1976*, WMO, Geneva, Technical Note, **169**, 100 pp.

____: 1987, 'The Surface Energy Budgets of Urban Areas',In: *Modelling the urban boundary layer*, Amer. Meteor. Soc., Boston. pp 1-52.

___: 1988, 'The Urban Energy Balance', *Prog. Phys. Geogr.*, **12**, 471-508.

Panofsky, H. A. and Dutton, J. A.: 1984, *Atmospheric Turbulence, Models and Methods for Engineering Applications*, J. Wiley, New York, 397 p.

Panofsky, H. A.; Tennekes, H.; Lenschow, D. H. and Wyngaard, J. C.: 1977, 'The Characteristics of Turbulent Velocity Components in the Surface Layer under Convective Conditions', *Boundary-Layer Meteorol.*, **11**, 355-361.

Paulson, C. A.: 1970, 'The Mathematical Representation of Wind Speed and Temperature Profiles in the Unstable Atmospheric Surface Layer', *J. Appl. Meteorol.*, **9**, 857-861.

Perry, A.E.; Schofield, W.H. and Joubert, P.N.: 1969, 'Rough Wall Turbulent Boundary Layers', *J. Fluid Mech.*, **37**, 383-413.

Ramsdell, J. V.: 1975, 'Wind and Turbulence Information for Vertical and Short Take-Off and Landing (V/STOL) Operations in Built-up Areas - Results of Meteorological Survey'. Battelle, Pacific Northwest Laboratories, Richland, Washington, *FAA-RD-75-94*, Final Report.

Raupach, M. R.: 1979, 'Anomalies in Flux-Gradient Relationships over Forest', *Boundary-Layer Meteorol.*, **16**, 467-486.

___: 1981, 'Conditional Statistics of Reynolds Stress in Rough-Wall and Smooth-Wall Turbulent Boundary Layers', *J. Fluid Mech.*, **108**, 363-382.

Raupach, M. R., and Shaw, R. H.: 1982, 'Averaging Procedures for Flow within Vegetation Canopies', *Boundary-Layer Meteorol.*, **22**, 79-90.

Raupach, M. R., and Thom, A. S.: 1981, 'Turbulence in and above Plant Canopies', *Ann. Rev. Fluid Mech.*, **13**, 97-129.

Raupach, M. R.; Thom, A. S. and Edwards, I.: 1980, 'A Wind-Tunnel Study of Turbulent Flow close to Regularly Arranged Rough Surfaces', *Boundary-Layer Meteorol.*, **18**, 373-397.

Raupach, M. R.; Coppin, P. A. and Legg, B.J.: 1986, 'Experiments on Scalar Dispersion within a Model Plant Canopy. Part 1: The Turbulence Structure', *Boundary-Layer Meteorol.*, **35**, 21-52.

Roth, M.; Oke, T. R. and Steyn, D.G.: 1988, 'Spectral Analysis of Turbulence in an Unstable Suburban Atmosphere', *Proceedings 8th Symposium on Turbulence and Diffusion*, San Diego, 345-348.

Roth, M.; Oke, T. R. and Steyn, D.G.: 1989, 'Velocity and Temperature Spectra and Cospectra in an Unstable Suburban Atmosphere', *Boundary-Layer Meteorol.*, **47**, 309-320.

Sadeh, W.Z.; Cermak, J.E. and Kawatani, T.: 1971,'Flow over High Roughness Elements', *Bound.-Layer Meteor.*, **1**,321-344.

Schädler, G.: 1988, 'Windprofile über Zürich', *Diplomarbeit*, Geogr. Inst. der Universität Zürich und Geogr. Inst. E.T.H., Zürich,

Schmid, H. P.: 1988, 'Spatial Scales of Sensible Heat Flux Variability: Representativeness of Flux Measurements and Surface Layer Structure over

Suburban Terrain', *Ph. D. Thesis*, The University of British Columbia, Vancouver, Canada, 299 pp.

Schmid, H.P. and Oke, T.R.: 1990, 'A Model to Estimate the Source Area Contributing to Turbulent Exchange in the Surface Layer over Patchy Terrain', *Quart. J. Roy. Meteorol. Soc.*, **116**, 965-988.

Schotanus, P.; Nieuwstadt, F. T. M. and De Bruin, H. A. R.: 1983, 'Temperature Measurement with a Sonic Anemometer and its Application to Heat and Moisture Fluxes', *Boundary-Layer Meteorol.*, **26**, 81-93.

Schuhmacher P.: 1991, 'Messungen und numerische Modellierung zum Windfeld über einer Stadt in komplexer Topographie', *ETH Diss No 9390*, Zürich, Switzerland. 78 pp.

Shaw R.H.; Tavangar J. and Ward D.P.: 1983, 'Structure of Reynolds Stress in a Canopy', *J. Clim. Appl. Meteorol.*, **22**, 1922-1931.

Stearns, C.R.: 1970, 'Determining Surface Roughness and Displacement Height', *Bound.-Layer Meteor.*, **1**, p. 102.

Steyn, D. G.: 1982, 'Turbulence in an Unstable Surface Layer over Suburban Terrain', *Boundary-Layer Meteorol.*, **22**, 183-191.

Stull, R. B.: 1988, *An Introduction to Boundary Layer Meteorology*, Kluwer, Dordrecht, 666 pp.

Tennekes, H.: 1973, 'The Logarithmic Wind-Profile', *J. Atmos. Sc.*, **30**, 234-238.

Tennekes, H. and Lumley, J.L.: 1972, *A First Course in Turbulence*, MIT-Press, Cambridge, Mass., 300 p.

Thom A.S.: 1971, 'Momentum Absorption by Vegetation', *Quart. J. Roy. Meteor. Soc.*, **97**, p. 414-428.

Thom, A. S.: 1975, 'Momentum, Mass and Heat Exchange of Plant Communities', in Monteith, J. L., (Ed.), *Vegetation and the Atmosphere, Vol. 1: Principles*, Academic Press, London, 57-109.

Thom, A. S.; Stewart, J.B.; Oliver, H.R. and Gash, J.H.C.: 1975, 'Comparison of Aerodynamic and Energy Budget Estimates of Fluxes over a Pine Forest', *Quart. J. Roy. Meteorol. Soc.*, **101**, 93-105.

Tillman J.E.: 1972, 'The Indirect Determination of Stability, Heat and Momentum Fluxes in the Atmospheric Boundary Layer from Simple Scalar Variables during dry Unstable Conditions', *J. Appl. Meteorol.*, **11**, p.783.

Townsend, A. A.: 1976, *The Structure of Turbulent Shear Flow*, 2nd Ed., Cambridge University Press, Cambridge,

Willis, G. E. and Deardorff, J.W.: 1976, 'On the Use of Taylor's Translation Hypothesis for Diffusion in the Mixed Layer', *Quart. J. Roy. Meteorol. Soc.*, **102**, 817-822.

Wyngaard, J. C.: 1973, 'On Surface Layer Turbulence', in Haugen, D. A., (Ed.), *Workshop on Micrometeorology*, Amer. Meteorol. Soc., Boston, 101-150.

___: 1981a, 'Cup, Propeller, Vane and Sonic Anemometers in Turbulence Research', *Ann. Rev. Fluid Mech.*, **13**, 399-423.

___: 1981b, 'The Effects of Probe Induced Flow Distortion on Atmospheric Turbulence Measurements', *J. Appl. Meteor.*, **20**, 784-794.

___: 1988, 'Flow Distortion Effects on Scalar Flux Measurements in the Surface Layer: Implications for Sensor Design', *Bound.-Layer Meteor.*, **42**, 19-26.

Wyngaard, J. C. and Coté O.R.: 1971, 'The Budgets of Turbulent Kinetic Energy and Temperature Variance in the Surface Layer', *J. Atmos. Sc.*, **28**, 190-201.

Wyngaard, J. C.; Coté, O. R. and Izumi, Y.: 1971, 'Local Free Convection, Similarity and the Budgets of Shear Stress', *J. Atmos. Sc.*, **28**, 1171-1182.

Wyngaard, J.C. and S.F. Zhang: 1985, 'Transducer Shadow Effects on Turbulence Spectra Measured by Sonic Anemometers', *J. Atmos. Oceanic Technol.*, **2**, 548-558.

Wyngaard, J.C.; L. Rockwell and C.A. Friehe: 1985, 'Errors in the Measurement of Turbulence Upstream of an Axisymmetric Body', *J. Atmos. Oceanic Technol.*, **2**, 605-614.

Yamartino, R. J. and Wiegand, G.: 1986, 'Development and Evaluation of Simple Models for the Flow, Turbulence and Pollutant Concentration Fields within an Urban Street Canyon', *Atmos. Environ.*, **20**, 2137-2156.

Yersel, M. and Goble, R.: 1986,'Roughness Effects on Urban Turbulence Parameters', *Bound.-Layer Meteor.* , **37**, 271-284.

Zhang, S.F.; Wyngaard, J.C.; Businger, J.A. and Oncley, S.P.: 1986, 'Response Characteristics of the U.W. Sonic Anemometer', *J. Atmos. Oceanic Technol.*, **3**, 315-323.

Seite Leer /
Blank leaf

APPENDICES

A1 Data Handling

A1.1 Cup Anemometers

Mean wind speed was determined by Aanderaa Cup anemometers (Type: wind speed sensor 2740S). They have a distance constant of about 11 m and a threshold speed of 0.3 - 0.5 ms^{-1}. The manufacturer gives as accuracy $\pm 2\%$ or ± 0.2 ms^{-1} (whichever is greater). The choice of the instruments is a compromise between accuracy and robustness.

A1.1.1 Calibrations

Three calibrations were performed with the instruments, two of them relative and one absolute (in a wind tunnel). In a field calibration, one Aanderaa Cup was compared with four Thornthwaite cup anemometers which are more sensitive but of much weaker construction and therefore not very appropriate for longtime exposure to "wind and weather". It was found that the Aanderaa instrument underestimates all wind speeds, but a high correlation with $r^2 = 0.999$, approximately) between Thornthwaite and Aanderaa measurements, so that the more robust instruments can be used with an appropriate absolute calibration (the high correlation coefficient should not be overemphasised, since it is clear that a high linear correlation exists between two measurements of the same property with similar measurements; scatter plots, however, showed the good agreement between the two measurements). Four of the Aanderaa cup anemometers were compared in another field calibration. It was found that the individual instruments respond identically (within the instrument uncertainty), i.e. calculated coefficients for a linear regression were almost one and zero, respectively for all combinations (Mazzoni, 1988).

An absolute calibration in a wind tunnel of two Aanderaa cups confirmed the observed underestimation of these instruments. Measurements have therefore to be corrected according to:

$$u^{corr} = (u^{meas} - b) / a. \qquad (A1.1)$$

The coefficients were determined from the wind tunnel experiments as a = 1.011 and b = -0.228. They do not differ significantly for the two instruments (see relative

calibration) so that (A1.1) is used for all sensors. It was found that (A1.1) applies for wind speeds higher than approximately 1 ms^{-1}; for lower wind speeds the measurement of the reference wind speed of the wind tunnel was too inaccurate. The correspondence of different cups however is fair to somewhat lower wind speeds. The sampling interval for the wind speed was 60 sec and 30 of these values were routinely averaged to yield a half-our mean.

A1.1.1 Overspeeding

Cup anemometer measurements are known to be sensitive to fluctuating wind (eg. Wyngaard, 1981a; Busch and Kristensen, 1976). Their response to increasing wind speed is faster than to decreasing wind speed, which results in an overestimation known as "overspeeding". Measurement periods 1 - 4, 11 and 13 (Table 4.2) were used to estimate to what extent this phenomenon occurred in the present study. During all these measurement periods sonic and cup wind speed measurements are available at the same height (see Section 4.3). The relative differences between such pairs (DU = (u^{sonic} - u^{cup}) / u^{cup}) is depicted in Fig. A1.1 (30 minute averages for the sonic data are used for comparison with the cup measurements). A strong dependence on wind speed and u$_*$ (not shown) of DU can be seen (in the case of wind speed this is partly due to the fact that wind speed is both, a dependent and independent variable).
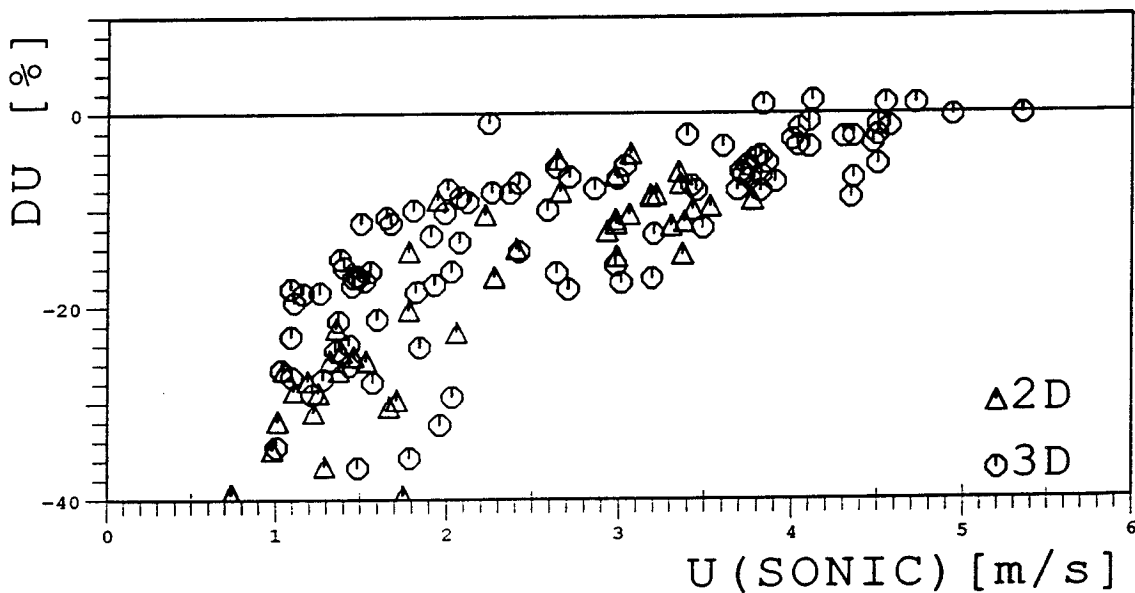
Figure A1.1   Normalized difference between wind speed as measured with the cup anemometers and the sonic. Symbols refer to the two sonic systems used.

Coherence with the standard deviations of the wind components (not shown) is less pronounced but still visible. The same applies for stability (z'/L), whereas no dependence of DU on wind direction can be found. Assuming that the error of the individual measurements is much smaller than the observed relative differences (which is certainly true, see below), two possible mechanisms causing these differences have to be considered. The first is overspeeding of the cups and the second is spatial variability of the flow field or local disturbance of the latter. For most of the measurement periods, denoted as "experiments"[1] in the following, except the 2D measurements in experiments 1- 4, the horizontal distance between the cup and sonic was approximately 2.2m). Because almost all values of DU lie well below zero, it can be concluded that overspeeding is the dominant effect of the two, since spatial variability can be expected to be equally distributed positive and negative.

R= .589   DU (MEAS.)
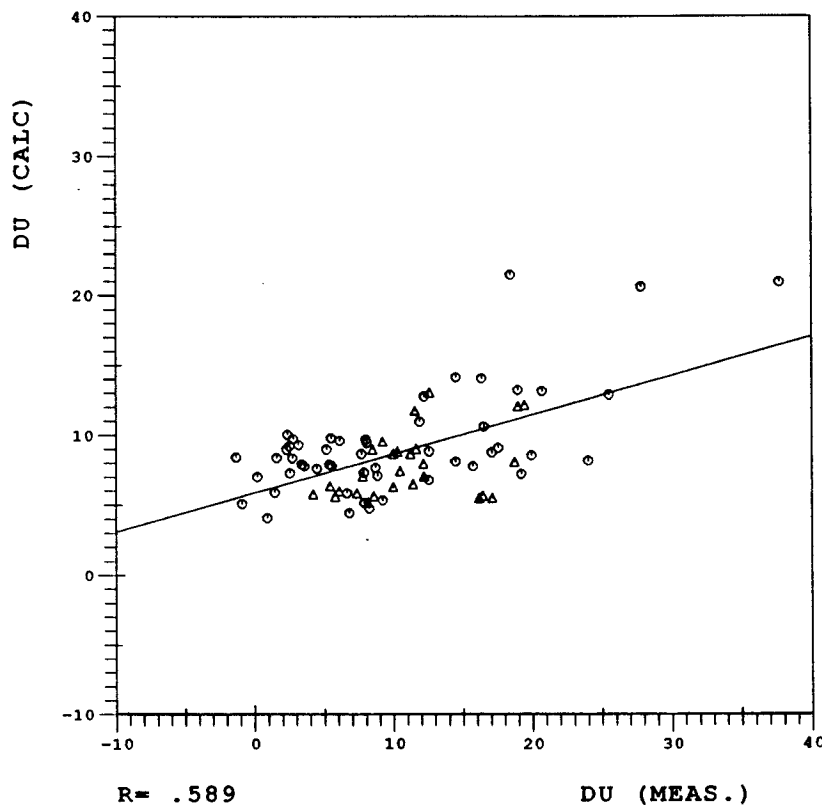
Figure A1.2   Measured overspeeding as compared to the overspeeding calculated with the model of Bush and Kristensen (1976). Values are given in percent. Different symbols refer to the two sonic systems as in Fig. A1.1.

---

[1] Although it is hardly possible to perform experiments in the real atmosphere since it is not possible to control the environmental conditions, this term will be used for a series of turbulence runs obtained on the same day (see Table 4.2).

If the entire difference is attributed to overspeeding and is compared to an estimate according to a model by Busch and Kristensen (1976), the correspondence is quite unsatisfactory (Fig. A1.2). This model of overspeeding is based on cup anemometer dynamics and can be expressed as follows:

$$\frac{\Delta u^{cup}}{u^{cup}} = a\left(\frac{\sigma_h}{u_0}\right)^2 \cdot J_s\left(\frac{l_0}{\Lambda_s}\right) + c\left(\frac{\sigma_w}{u_0}\right)^2 \tag{A1.2}$$

where σ_h^2 is the horizontal variability of the (true) wind u_0, σ_w^2 the vertical variability and J_s is a function that depends on the shape of the spectrum of horizontal turbulent energy, l_0 is the distance constant of the anemometer and Λ_s is a characteristic length scale of the horizontal turbulence. Since Λ_s was not known for the present data, the "calculated" values in Fig.A1.2 were obtained through

$$\frac{\Delta u^{cup}}{u^{cup}} = a'\frac{u_*^2}{u_0^2}\left[\Phi_M\left(\frac{z}{L}\right) - \left(\frac{z}{L}\right)\right]^{\frac{2}{3}}\left(\frac{l_0}{z_0}\right)^{\frac{2}{3}} + c\left(\frac{\sigma_w}{u_0}\right)^2, \tag{A1.3}$$

an approximation which is valid if Monin - Obukhov similarity holds and there is local balance between production and viscous dissipation (Busch and Kristensen, 1976). The discrepancy between measured and calculated overspeeding indicates that these two conditions cannot be assumed to apply under the present conditions. However, Busch and Kristensen (1976) conclude that relative overspeeding of more than 10% is unlikely to occur (only in "extreme cases"), based on their model calculations. This would imply that in the present case a considerable part of the differences DU in Fig. A1.1 would have to be attributed to local variability of the flow field. Runs 1 and 2 can be used to address this question.

In Fig. A1.3 all relevant information on these two experiments is compiled. The general wind direction, however, is not shown for the two experiments: it was around 50° for No. 1 and around 250° for No. 2. The difference between the 3D measurement and the 2x2D measurement is smaller than about 3% for experiment 2, whereas in experiment 1 two "groups" of measurements exist, with about 10% difference and about 20%. Both instruments were mounted at 5m above roof level for these two experiments, horizontal distance about 2m). Firstly, for wind directions, where both sonic anemometers are undistorted by the tower and/or their own mounting structure (experiment 2), the difference between the two measurements is very small and no significant spatial variability is observed. This means that no severe calibration difference exists between the two sonic systems (2x2D and 3D). In this context, 'calibration' is used for the electronic circuit, i.e. the correspondence between actual, local wind speed and sonic's response signal. For calibration in terms of the relation

between actual local wind speed and "true" local wind speed, see Appendix A2). Two mechanisms could be responsible for the observed difference between the two sonic measurements in experiment 1. Either there is a real local difference in wind speed or one of the sonic measurements is off. If the first is the case (i.e. the wind speed at the location of the 2x2D is lower than where the 3D is situated), the overspeeding (difference between 2x2D and cup) of the 2x2D would be small compared to what can be expected from Fig. A1.1. Fig. A1.3 shows that the larger the difference between the two sonics, the larger (negative) the "overspeeding". This indicates that in this particular case, the observed effect is due to overspeeding rather than an actual local variability of the flow field. This deviation of the 2x2D measurement is attributed to the upwind location of the 2x2D sonic array during experiment 2 and this may have distorted the sonic measurements.

exp. 1: ⊕ / +   u(3D) - u(2D)   exp. 2: △   u(3D) - u(2D)

        × / ↑   u(2D) - u(cup)   ◇   u(2D) - u(cup)

                                                  ⋈   modelled overspeeding (2D)
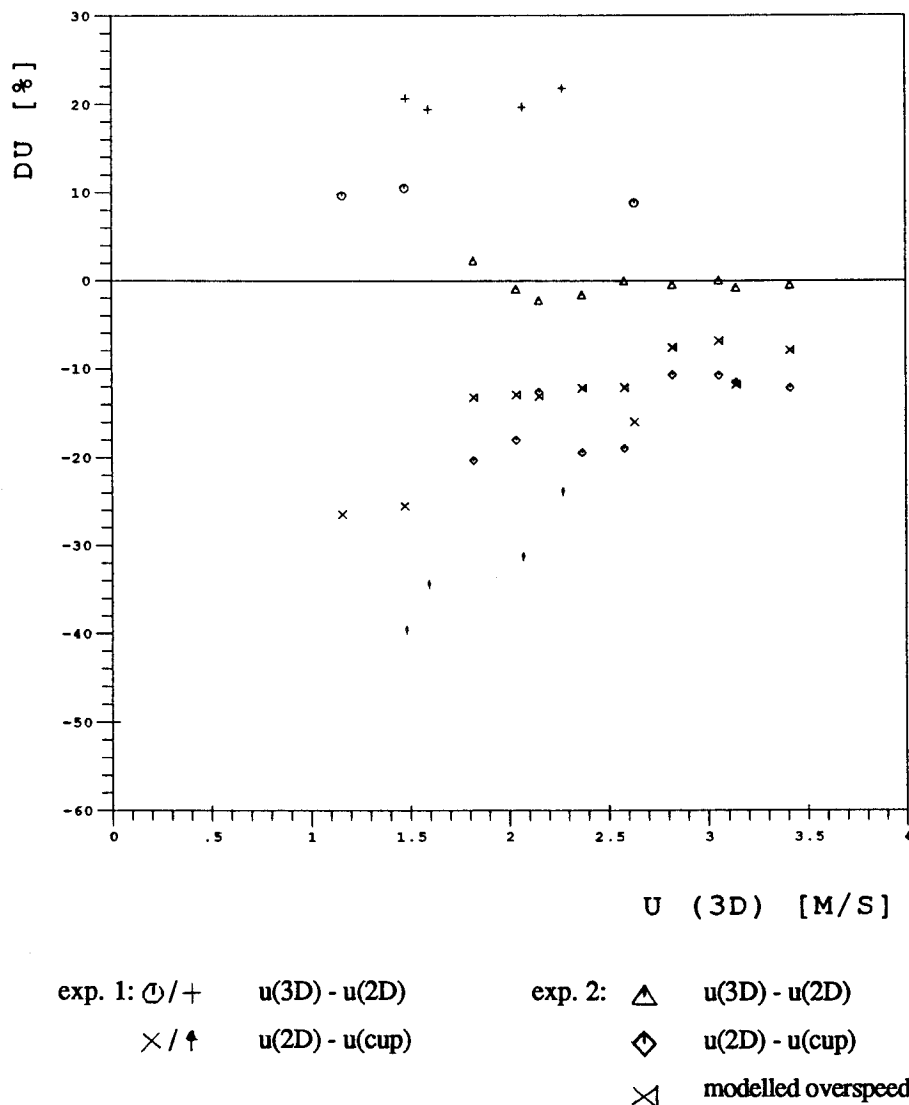
Figure A1.3   Relative overspeeding DU for measurement periods (experiments) 1 and 2 (Table 4.2). Two symbols are used for experiment 1 in order to distinguish between events showing different behaviour (see text).

A second point becomes apparent from Fig. A1.3. For experiment 2 it can be seen that even if spatial variability of the flow field can be excluded directly, the modelled overspeeding according to Busch and Kristensen (1976) yields much lower values than the actually observed differences between cup and sonic. This is probably because restrictions for the parameterisation used are not met (as mentioned before) and due to the extraordinary high level of turbulence intensity. It is concluded that the differences between sonic and cup anemometers are likely to be due to overspeeding, except for the case where the cup is distorting the 2x2D sonic measurement. A best-fit model of observed overspeeding has been constructed using the same independent variables as Busch and Kristensen (1976), and with the dominant powers as in their model:

$$\frac{\Delta u^{cup}}{u^{cup}} = a_1\left(\frac{\sigma_h}{u^{cup}}\right)^2 + a_2\left(\frac{\sigma_w}{u^{cup}}\right)^2 + a_3\left(\frac{l_0}{z'}\right)^{\frac{2}{3}} + a_4\left(\frac{z'}{-L}\right)^{\frac{2}{3}} + a_5\left(\frac{z'}{-L}\right)^{\frac{1}{6}} + a_6 \qquad (A1.4)$$

where a_i are coefficients determined by multiple regression of all available data (with mean wind speed larger than 1.5 ms^{-1}. Fig. A1.4 shows a comparison between measured and calculated overspeeding for this best-fit model. The coefficients are given in Table.A1.1.

Table A1.1   Coefficients a_i for the overspeeding model according to equation (A1.4). With these coefficients an rms difference between observed and calculated overspeeding of 0.039 ms^{-1} is obtained. A regression between observed and calculated overspeeding yields $r^2 = 0.85$ (see Fig. A1.4).

coefficient	a_1	a_2	a_3	a_4	a_5	a_6
value	-0.197	-1.104	-0.056	0.094	0.243	-0.314

When using the model (A1.4) to correct measured wind profiles, a problem arises for a wind speed measurement at a level where no turbulence measurements were taken. Therefore a sensitivity test suitable for the present application has been performed. If turbulence statistics are available at height z_1 and a cup measurement is to be corrected for at height $z_2 > z_1$, a first approximation could be to set $u(z_2)/u_*(z_2) = u(z_1)/u_*(z_1)$ and the same for σ_h/u_* and σ_w/u_*. Thus, a local friction velocity for z_2 can be calculated from the known $u(z_2)$ and similarly a $\sigma_H(z_2)$ and a $\sigma_w(z_2)$. Inspecting the above-roof data, we find that the ratio between $u(z_2)/u_*(z_2)$ and $u(z_1)/u_*(z_1)$ varies between 0.6 and 1.2 for $z_2 = 10$ m above roof level and $z_1 = 5$ m above roof level. The ratios of σ_H/u_* and σ_w/u_* vary in a very similar manner with

height. For some typical cases with $u_*(z_1)$ between 0.29 ms^{-1} and 0.72 ms^{-1} the following calculations were performed: for every case the quantity

$$\frac{u(z_2)}{u_*(z_2)} \Big/ \frac{u(z_1)}{u_*(z_2)} := f_a = \frac{\sigma_H(z_2)}{u_*(z_2)} \Big/ \frac{\sigma_H(z_1)}{u_*(z_1)} = \frac{\sigma_W(z_2)}{u_*(z_2)} \Big/ \frac{\sigma_W(z_1)}{u_*(z_1)} \qquad \text{(A1.5)}$$

was varied between 0.1 and 1.2 and for each of these values a relative overspeeding according to (A1.4) is calculated. In Fig. A1.5 the absolute difference in overspeeding between $f_a = 0.6, 0.65, 0.7,...$ and $f_a = 1$ is plotted for all cases. It can be seen that for the height interval between 5 m and 10 m above roof level this difference is always smaller than 6%, i.e. if overspeeding at level z_2 is calculated with $f_a = 1$, the possible error is not much larger than the uncertainty of the overspeeding model itself (see the caption to Table A1.1). If it can be assumed that these considerations are also valid for the thicker but higher layer between 10 m and 20 m above roof level, the present model (A1.4) can also be used to correct for the highest level of cup measurement.
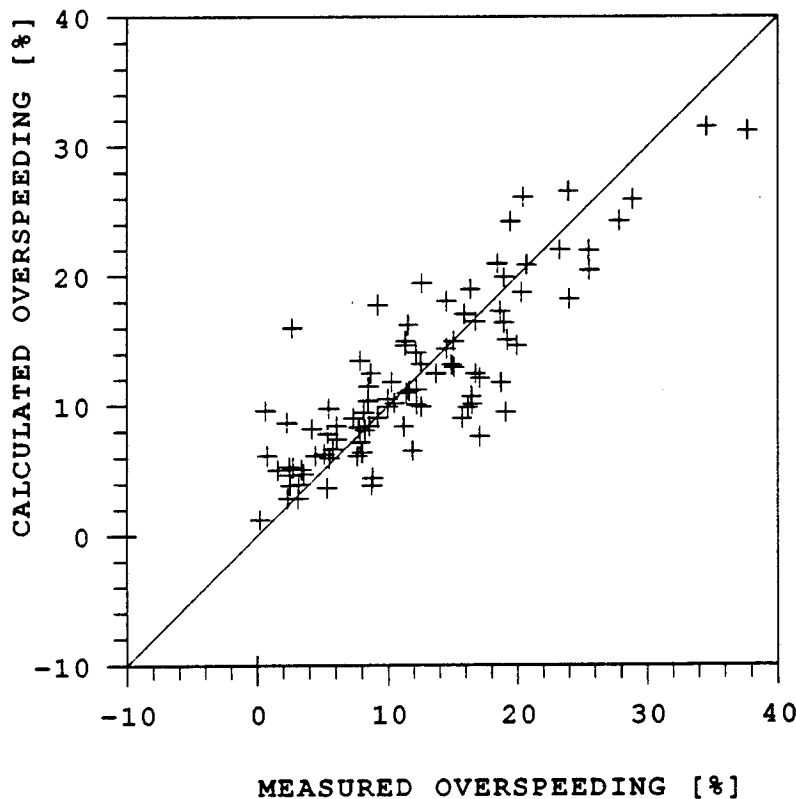
Figure A1.4   As Figure A1.2, but equation (A1.4) used for the calculation of overspeeding.
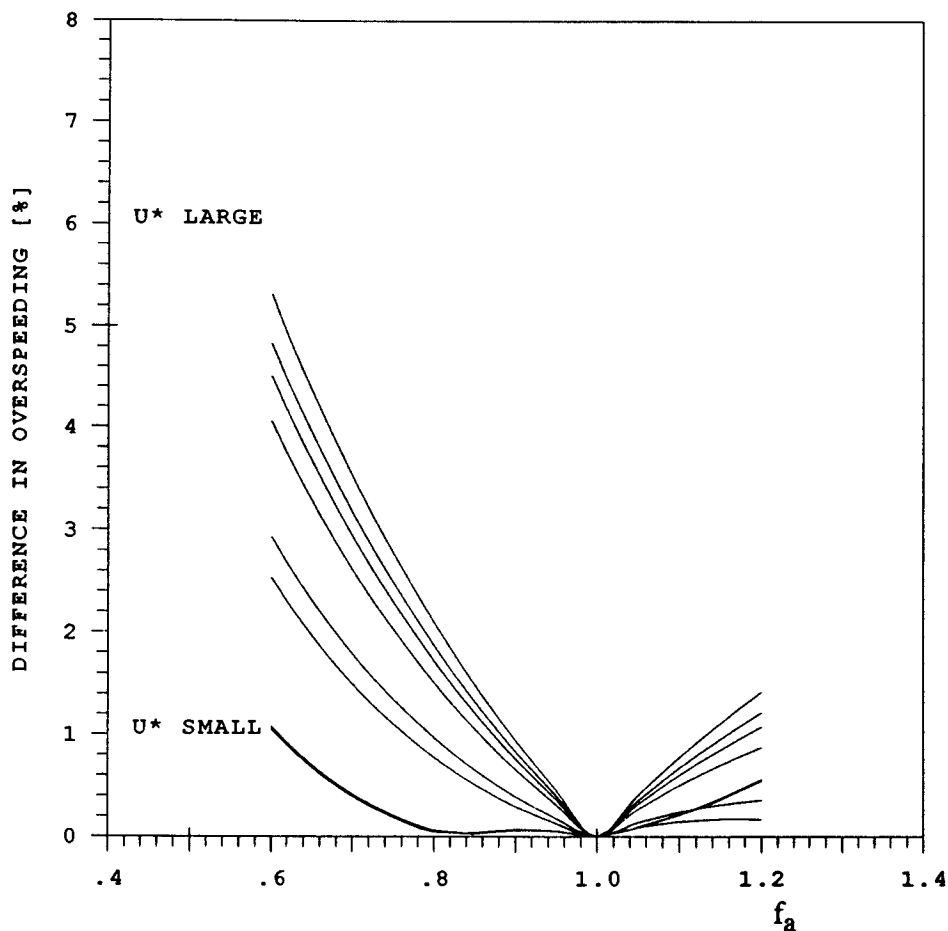
Figure A1.5   Difference in calculated overspeeding (equation A1.4) when using $f_a=1$ instead of a more realistic value in the range 0.6 - 1.2. f_a is defined in equation (A1.5).

A1.2 Temperature and Dew Point

Measurements of temperature and dew point were obtained with a ventilated VT3 probe by Meteolabor. Its accuracy is given by the manufacturer to be ±0.2 K (absolute) for temperature measurements. Dew point accuracy is expected to be slightly worse due to the additional electronic processing required.

Two relative calibrations were performed before the field measurements in July 1986, 458 half-hour measurements, and afterwards: May 1988, 423 half-hour measurements. The probes were mounted such that the distances between the entrances of the suction tubes were 0.10 - 0.15 m. One of the instruments was chosen to be the "reference" and a linear regression was performed between the corresponding data for each pair of probes (Table A1.2). The incidence of high correlation coefficients should not be overemphasized due to inherent correspondence for two measurements of the same quantity. Nevertheless, temperature data were found to be highly comparable. Dew point measurements are slightly less accurate. If the measurements during the relative calibration period are corrected with the regression coefficients given in Table

A1.2, the standard deviation of two temperature measurements is typically smaller than 0.01 K, and the standard deviation between two dew point measurements is about 0.01 K. As can be seen from Table A1.2, the two relative calibrations do not yield the same coefficients for the correction. If the data of calibration period 2 are treated with the coefficients obtained in calibration 1, the standard deviation of two temperatures remains smaller than 0.01 K, the one for two dew points, however, is about 0.03 K. For the correction of the field data the coefficients of the calibration closest to the date of measurement were used.

Temperature and dew point were sampled every 15 seconds and 120 of those averaged to yield a 30 minute mean.

For dew point data the saturation water vapor pressure is calculated according to the formula proposed by Goff and Gratch (1946).

$$\log e_w = -7.9028 \left(T_s/T - 1\right) + 5.02808 \log \left(T_s/T\right) - 1.3811 \cdot 10^7$$
$$\cdot \left(10^{11.334\,(1\,-T/T_s)} - 1\right) + 8.1328 \cdot 10^{-3}\left(10^{-3.49149\,(T_s/T - 1)} - 1\right) \qquad (A1.6)$$
$$+ \log e_{w_s}$$

where

e_w	=	saturation water vapor pressure [hPa]
T	=	Temperature [K]
T_s	=	373.16 K
e_{w_s}	=	$e_w(T_s)$

If in (A1.6) the dew point is used instead of T, the actual water vapor pressure e_a is obtained. From this the specific humidity q is calculated:

$$q = \frac{0.623\,e_a}{p - 0.377\,e_a}, \qquad (A1.7)$$

where p is the atmospheric pressure. An error calculation yields an uncertainty for the specific humidity of about 10^{-5} kg H_2O / kg wet air (for dp = 2 hPa, dTP = 0.02 K, TP = 283 K, p = 960 hPa). This is about 1% or less for usual conditions during the field experiment.

During the field experiment some problems arose with the dew point measurement . The manufacturer recommends that the mirror be cleaned "about once a week". However, it was soon apparent that this was often not enough when used in polluted urban air. Various tests with different time intervals between cleanings showed that the mirrors had to be cleaned at least every second day (for this interval no "step change in dew point" is detected after the cleaning). This was done on all levels during the field

measurements. Due to electrical problems with the dew point measurement data are lacking for a substantial part of the experiment time.

Table A1.2   Correlation coefficients for the relative calibrations between temperature and dew point probes.

| Probe | Position, z | Coefficients a,b relative to Probe # 23 *) | | | | | |
| | | Calibration 1 | | | Calibration 2 | | |
		a	b	r	a	b	r
T # 21	roof, 23.5 m	1.003	-0.714	1.0	1.000	0.070	1.0
T # 23	roof, 38.5 m	1	0	-	1	0	-
T # 24	street, 23.5 m	1.000	0.0210	1.0	1.000	0.023	1.0
T # 25	street, 7.5 m	1.000	-0.101	1.0	1.000	0.036	1.0
T # 5	roof, 5 m	-	-	-	1.009	-1.848	1.0
TP # 21	roof, 23.5 m	0.978	6.132	0.999	1.008	-2.660	0.997
TP # 23	roof, 38.5 m	1	0	-	1	0	-
TP # 24	street, 23.5 m	0.995	1.596	0.999	6.972	7.314	0.993
TP # 25	street, 7.5 m	0.980	5.406	0.999	0.947	16.142	0.989

*):   The correction relative to probe # 23 is performed as follows (example):
T (#21) = a (T#21) + b, where a and b are determined from comparison of T (#23) and T (#21) during the calibration period.

A1.3 Wind Direction

Wind vanes were Aanderaa instruments (model 2750) with an accuracy given by the manufacturer as $\pm 5°$. Since the output signals could not be averaged automatically by the data logger (transition at zero degree), an instantaneous value was read every ten minutes and stored. In the subsequent data analysis, three data points were averaged using a vector decomposition of the mean wind vector to yield a half-hour mean.

A1.4 Pressure

Pressure was measured at the university campus located some 100m higher than the Anwand site, using a "Barograph" (Lambrecht KG, Göttingen). Its resolution is 1 hPa and its accuracy is assumed to be ± 1 hPa. Readings were reduced to the various measurement levels through the barometric formula for the calculation of potential temperature and specific humidity.

A1.5 Correction for Turbulent Flux of Sensible Heat and Temperature Variance

Since the fluctuating temperatures $T' = T - \overline{T}$ of the sonic probe are contaminated by humidity effects (Schotanus et al., 1983), all the sensible heat fluxes have been corrected by the method proposed by these authors using the Bowen ratio. The covariance $\overline{u'_3 T'_m}$, where T_m is the measured deviation from the mean temperature, can be expressed as a function of the true covariance $\overline{u'_3 T'}$ according to:

$$\overline{u'_3 T'_m} = \overline{u'_3 T'} \left(1 + \frac{0.51\, c_p \overline{T}}{L_v\, \beta} \right) - 2\, \frac{\overline{T}\, \overline{u}_1}{c_s^2}\, \overline{u'_1 u'_3} \qquad (A1.8)$$

Here, β is the Bowen ratio, c_p is the specific heat at constant pressure, L_v is the latent heat of condensation and c_s is the speed of sound.

The formula of Schotanus et al. (1983) for the correction of the temperature variance is

$$\sigma_{T_m}^2 = \sigma_T^2 + 1.02\, \overline{T}\, \overline{q'T'} \qquad (A1.9)$$

and thus requires the determination of q', the fluctuating humidity. Since this is not available no correction has therefore been applied to the temperature variance data of the present study. However, the analysis of Schotanus et al. (1983) shows that the present temperature variance data may be slightly overestimated by a few percent (especially if the absolute value is small).

Table A1.3:   Number N of instantaneous or continuous (wind speed) samples taken by the data logger to calculate the stored average.

Variable	N	Averaging time
Wind speed	30	30 min
Temperature	120	30 min
Dew point	120	30 min
Wind direction	3	-
Pressure	1	-

A1.6 Data Logging

All mean variables were stored on a 28 channel data logger (Allgomatic, by A.Ott, Kempten). Through the public telephone line they could be transmitted to a PDP computer, and from there they were transferred to the mainframe computer. Different sampling rates were used for the different variables (Table A1.3).

The turbulence measurements (sonic anemometers) were stored on a Microdata data logger at a sampling rate of 1 s^{-1}. This sampling frequency allowed a continuous time series of 8 channels to be stored on one track of magnetic tape for almost 110 minutes. After this time, the next track had to be prepared by the data logger so that approximately two minutes of data were lost. A sampling rate of $3s^{-1}$ would have been possible (with 8 channels) but then, only about 35 minutes of continuous time series would have been available on each track. The data were subsequently transferred to the mainframe computer for analysis.

A2 The Performance of the Sonic Anemometers

The results presented in this Chapter have been worked out together with Pierluigi Calanca, my fellow doctoral student. Since many mathematical operations will be used to describe the corrections, the tensor notation $u=(u_1,u_2,u_3)$ will be used for convenience rather than $u=(u,v,w)$ as in the rest of this thesis. Due to the large amount of sub- and superscripts necessary to describe the various wind components considered, capital letters are used for averages and $u=(u_1,u_2,u_3)$ for the turbulent fluctuations.

A2.1 Introduction

Turbulence statistics are extremely sensitive to errors that occur in recording each single component. In general, the working principle of sonic anemometers is very simple, since only time measurements are required. These instruments are expected to provide accurate results, but there are at least two serious sources of error: shadowing in the wakes of the transducers and flow distortion by the whole sensor array and mounting structures. The former results in an attenuation of the measured velocity in the case of wind blowing nearly parallel to one of the sonic paths, whereas the latter alters the local flow at the instrument location. The consequences of both sources of error on the derived turbulent statistics have been treated theoretically by Hunt (1973), Wyngaard (1981b), Wyngaard et al. (1985), Wyngaard and Zhang (1985) and Zhang et al. (1986). However, few data have been published to verify these calculations or to estimate the magnitude of the errors. For a laminar flow the underestimation of the mean wind speed due to the transducer shadow effect can reach almost 30% (Hanafusa et al., 1982; Wyngaard and Zhang, 1985; Mortensen et al., 1987; Baker,1988, Conklin et al., 1988), while in the case of turbulent flow Grant and Watkins (1989) report errors of about 10% for mean properties. For an instrument that was developed at the University of Uppsala, Sweden, Högström (1982) found that the flow distortion can affect the turbulent fluxes of momentum, heat and moisture to an extent of about 10%.

The designing of new instruments should certainly take advantage of recent theoretical and experimental work, and an effort should be made to try to minimize the influence of the instrument itself on the measurements (Wyngaard, 1988; Högström, 1982). Unfortunately, this influence can not be completely prevented. In addition, the present types of sonic anemometers will probably continue to be used for some time, due to their cost. Therefore, it is felt that it is still worthwhile to seek good correction

procedures (see also Högström, 1982), which take all kinds of significant errors into account and are not limited to only one possibility.

A2.2 Wind Tunnel Experiments and Data Analysis

A three-dimensional sonic anemometer (Kaijo Denki, Probe: TR-61C) with two orthogonal sensor axes in the horizontal plane and one vertical axis has been used to investigate the response characteristics in a wind tunnel with a cross-section of 1.2 m by 1.4 m. The turbulence intensity in the wind tunnel was less than 0.5%. The relevant characteristics of the instrument are listed in Table A2.1. The probe was mounted on a ground plate that could be rotated around its normal axis with an accuracy for the angle of rotation of ±1°. The plate could be tilted independently at the windward side up to 6° (Fig. A2.1b). A bidirectional inclinometer with a sensitivity of 0.1° was also mounted on this plate. From the two measured tilt angles and the angle of rotation it was possible to calculate the probe orientation relative to the wind vector for every single measurement.

The geometric configuration of the mounting in the wind tunnel cannot be exactly the same as the one used in field studies. However, the experiment was designed to be as similar as possible to the field situation.
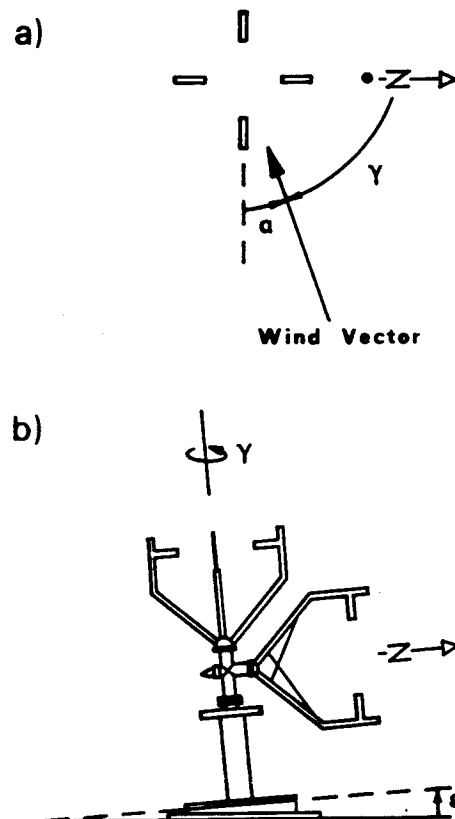
Figure A2.1   Definition of angles in a) the horizontal and b) the vertical plane. ε=elevation angle, γ=azimuth angle, α=deviation angle (from nearest sensor axis)

Several runs were carried out for three different wind speeds (around 10 m s^{-1}, 5 m s^{-1} and 0.5 m s^{-1}), rotating the sonic system around its normal axis with increments of $10°$ or $5°$, and changing the elevation angle of the supporting plate stepwise by $1°$ up to $6°$. At each position the wind velocity was measured at least for 45 s with a sampling frequency of 1 s^{-1} (Table A2.1). Data were stored on magnetic tape and could be analyzed later, either as mean values or as single data points.

Table A2.1   Characteristics of the TR-61C probe

Probe	TR-61C
Dimensions	3, orthogonal array
Diameter of transducers d	15 mm
Path length L	200 mm
d/L	0.075
sampling frequency	1 s^{-1}
No. of samplings for each position	>45
Resolution	$0.005 - 0.01 \text{ ms}^{-1}$ depending on range

The wind speed in the tunnel was measured with a pitot tube. Its accuracy was estimated by means of an error calculation as ± 0.01, ± 0.02 and $\pm 0.2 \text{ m s}^{-1}$ for the three ranges of 10 , 5 and 0.5 ms^{-1} respectively. Considering the uncertainty of the manometer zero point, it is concluded that the error of the pitot tube is less than 1% for high velocities, whereas for wind speed less than 1 m s^{-1} the accuracy is poor. For runs under these latter conditions the reference speed was determined arbitrarily by forcing the ratio of measured and wind tunnel speed to be unity for an angle of attack of $135°$.

The reproducibility of the wind tunnel speed for different experiments was checked by mounting the pitot tube at the position where the sonic anemometer was during the experiments. For that reason, a relationship between the measured speed and the power consumption of the wind tunnel was established. By comparing results with and without the sonic in the wind tunnel, it was found that its presence had no detectable effect on the pitot tube measurement. Since the wind tunnel is rather small for this kind of experiment, one has to be concerned whether the presence of the walls influences the flow pattern in the vicinity of the anemometer under investigation. The flow around the sonic has been visualized with white smoke at a wind tunnel speed of 5 ms^{-1}. Fig. A2.2 shows the streamlines upstream of a circular cylinder of radius 0.1 m calculated after Wyngaard (1981b). The radius of 0.1 m was chosen since it lies between that of the sonic's foot, its "neck" and the sensor array. From photographs of the smoke patterns, the actual flow around the sonic can be determined (e.g. position A in Fig A2.2). A comparison with Wyngaard's results shows, that the used potential flow model can be taken as a rough estimate for the flow around the sonic. For a position near the wall of the tunnel (position B in Fig. A2.2) the model yields a deviation angle of 0.3° from the flow parallel to the wind tunnel and the magnitude of the wind vector is 1.8% higher than the far upstream speed. This indicates that wall effects can not be completely excluded, but are considered small.
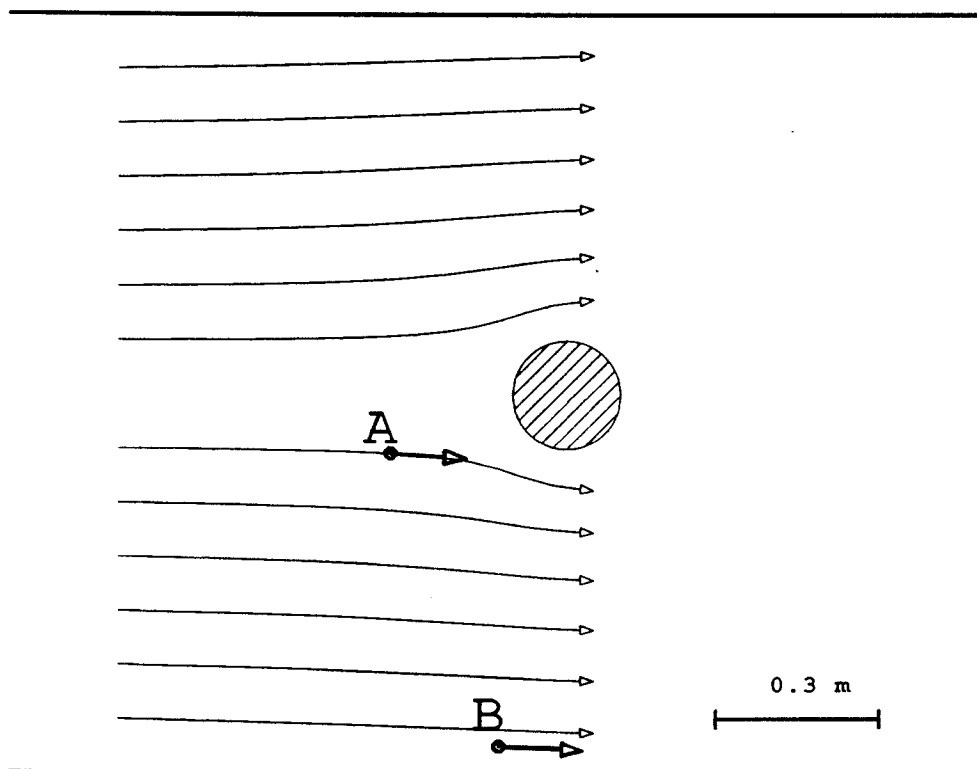
Figure A2.2   Calculated flow pattern around a circular cylinder of radius 0.1 m (after Wyngaard, 1981b). Arrows at A and B are drawn after photographs from flow visualization experiments.

A2.3 Theory of Errors

In a measurement of wind speed with a sonic anemometer, one actually wants to know the three components U_1 U_2 and U_3 of the wind vector *as if* the sonic probe were not at that specific location. Instead, the measurement yields (within the accuracy of the system) the values for a flow which is slightly modified by the probe itself. On a very small scale (of the order of a transducer's diameter) the wind speed is reduced in the wake of the transducer (see e.g. Zhang et al., 1986), resulting in an underestimation of the measured wind component. This phenomenon is commonly called "transducer shadow effect" and its magnitude is dependent on the angle between the sonic path and the wind direction. On a larger scale (of the order of the probe's diameter) the bulk of the sonic array and supporting structure alter the mean flow. This latter phenomenon is usually referred to as "flow distortion". For completeness, misalignment of the transducers as a source of error is also considered here. Even if one works with an "orthogonal" sensor array (as in the present study), deviations from that orthogonal frame of reference of such a probe can be quite substantial. For the probe under investigation, deviation angles amounted up to $1.4°$. For the horizontal components, this effect might be of no great importance, but can be considerable for the vertical sound path: a one degree tilt of the latter and a horizontal wind speed of 10 ms^{-1} result in an additional contribution of about 0.17 ms^{-1} to the vertical component.

In the following, theoretical considerations for these three sources of error for the measurement of mean and turbulent wind speed are summarized. The symbolic notation is as follows: U_i is the undisturbed wind component at the point of the measurement; $\tilde{U}_i$ is the flow with respect to an orthogonal frame of reference, distorted by the presence of the sonic array; $\tilde{U}_i^*$ stands for that same distorted flow, but to the sonic's coordinate system, which is not necessarily orthogonal; and $\tilde{U}_i^{**}$ is the measured wind component, additionally influenced by transducer shadowing. A reasoning for this order of treatment is given in Section A2.5. Equations are written using tensor notation. Free indices ranges from 1 to 3 and the summation convention is applied. Bold characters represent vectors.

The transducer shadow effect has been parameterised by Wyngaard and Zhang (1985) for a transducer produced by Kaijo Denki, on the basis of data presented in Hanafusa et al. (1982). According to Wyngaard and Zhang (1985), the measured wind component $\tilde{U}_i^{**}$ along the i-th path is

$$\tilde{U}_i^{**} = \left[1-(1-C)\exp(-A\,\sin^2\alpha) \right] \tilde{U}_i^* \tag{A2.1}$$

where α is the angle between the wind vector and the corresponding sensor axis, (i.e. the angle of deviation), and A and C are parameters depending on the path length and on the diameter of the transducers.

Correction for misalignment is equivalent to an affine transformation of the coordinate frame. Defining s_i as the i-th axis of the normalized coordinate frame spanned by the misaligned sensors, t_j as the j-th axis of the orthonormal coordinate system of the sonic anemometer and β_{ij} as the angle between s_i and t_j, it follows that

$$\widetilde{U}_i^* = c_{ij}\,\widetilde{U}_j \tag{A2.2}$$

$$c_{ij} = \cos\beta_{ij} = s_i\,t_j. \tag{A2.3}$$

Wyngaard's approach to the problem of flow distortion (Wyngaard, 1981b) is based on the assumption that the integral scale of the turbulence in the undistorted flow is much larger than a characteristic length of the body, which is responsible for the distortion. Under these conditions it is possible to expand the distorted flow $\widetilde{U}_i = \overline{\widetilde{U}}_i + \widetilde{u}_i$ at the location of the measurement x in a Taylor series about the unidirectional undistorted state $\overline{U}_i = U_i - u_i$, neglecting terms of second and higher order

$$\widetilde{U}_i(x,t) \cong \widetilde{U}_i(x,\overline{U}_1,\overline{U}_2,\overline{U}_3) + a_{ij}u_j(t) \tag{A2.4}$$

where

$$a_{ij}(x) = \frac{\partial\widetilde{U}_i}{\partial U_j}\bigg|_0 \tag{A2.5}$$

The matrix a_{ij} contains the flow distortion coefficients, while the subscript "0" indicates that the derivation has to be performed at the basic unidirectional state. Subtracting the mean distorted flow components from (A2.4) yields:

$$\widetilde{u}_i(x,t) = a_{ij}(x)u_j(t) \tag{A2.6}$$

The coefficients a_{ij} can be evaluated using potential flow theory (Wyngaard, 1981b) or estimated from wind tunnel measurements as was partly done by Högström (1982). They must be determined for every angle of attack of the flow. However, it can be assumed that there is only a small difference between these coefficients for angles of

attack relatively close to each other. Thus, for practical purposes they are evaluated separately only for each of the four wind direction sectors given in Table A2.2. The subdivision into the four sectors was chosen so that in each of them, neither U_1 nor U_2 change sign. Furthermore, the following simple linear model is suggested:

$$\overline{\tilde{U}}_i = r_{ij}\,\overline{U}_j, \qquad\qquad\qquad (A2.7)$$

where the occurring coefficients r_{ij} are fitted by linear multiple regression. Using (A2.7) to perform the derivatives according to (A2.5), leads to the approximation of a_{ij} by r_{ij}. The use of temporal averages in (A2.7) arises due to the lack of instantaneous values of the undistorted flow in wind tunnel experiments. Nevertheless, (A2.7) can be applied to instantaneous field data if it can again be assumed that the integral scale of the turbulence is much larger than the dimensional scale of the sonic anemometer. This requirement is met in most of the applications in the atmospheric boundary layer, as has been shown by Wyngaard (1981b).

Table A2.2   Definition of wind direction sectors and corresponding sign of the wind components.

Sector	γ	U_1	U_2	vertical sensor
1	$0°\leq\gamma<90°$	>0	≥ 0	upwind
2	$90°\leq\gamma<180°$	≥ 0	<0	
3	$180°\leq\gamma<270°$	<0	≤ 0	downwind
4	$270°\leq\gamma<360°$	≤ 0	>0	

A2.4 Response Characteristics

Some characteristics of the primary response of the sonic anemometer will first be illustrated. Fig. A2.3 shows that the actual wind speed is severely underestimated if the wind approaches the anemometer from azimuths of 0°, 90°, 180° and 270°, ± 20°, i.e. when the flow is almost parallel to one of the two horizontal sonic paths. The

attenuation reaches a level of 10% to 20%, depending also on the wind speed. The largest underestimation is found at 0°, when the vertical sensor is just upstream of the horizontal ones. The level of attenuation is comparable to results of previous studies (Hanafusa et al., 1982; Mortensen et al. 1987; Baker, 1988; Conklin et. al., 1988) although it is clearly dependent on the geometry of the sensor array. Hanafusa et al. (1982), Mortensen et al. (1987) and Baker (1988) also report a velocity dependence of the sonic's response, whereas the results of Conklin et al. (1988) indicate no such dependence on the absolute wind speed. The behaviour of the U_1 and the U_2 axes are not exactly the same (not shown), resulting in the different levels of attenuation at 0°, 90°, 180° and 270°, respectively. Baker (1988) has already reported an asymmetry in the flow field around the sonic as a function of angle of attack (in that case even for a symmetric geometric design for the U_1 and U_2 axes).
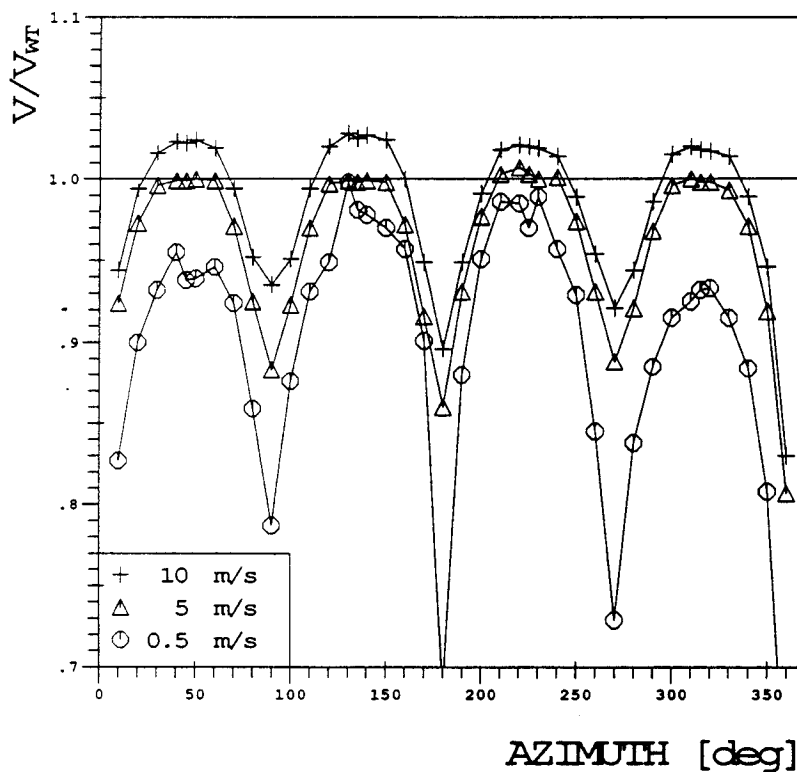
Figure A2.3   Uncorrected response of the sonic anemometer (V) compared to the absolute wind tunnel speed (V_{wT})

For intermediate angles of attack and high wind speeds the actual velocity is slightly overestimated (3%). This behaviour might be attributed to the fact that the wind tunnel is quite small for the probe (see Section A2.2). Similar "overshooting", however, is found in comparable experiments (Mortensen et al., 1987; Baker, 1988) where, at least in the latter case, much larger wind tunnels were used. Another possible explanation is

that for deviation angles of $\alpha \sim 45°$ (Fig. A2.1a) and high wind speeds, a "jetlike" structure develops between the two neighbouring transducers.

As shown in Figs. A2.4a and A2.4b the anemometer and the supporting structure induce an upflow, comparable in magnitude to the average of the values reported during the 1976 International Turbulence Comparison Experiment (Dyer, 1981). Note that Fig. A2.4a and 4b show the difference between the measured and predicted U_3 component, rather than their respective ratio. There is neither a clear dependence of the U_3 response on the elevation of the instrument (Fig. A2.4a) nor on the angle of attack (Fig. A2.4b). The only exception is at $180° \pm 10°$, when the vertical sensor is downwind of the sonic array (negative values in Fig. A2.4a). However, since this situation can easily be avoided in practical field applications, data for an angle of attack of $180° \pm 10°$ are not further considered in the subsequent data analysis .

Every point in Figs. A2.3 and A2.4 is calculated as the average of at least 45 measurements at the respective position (for most of the positions 60 or more measurements are available). Fig. A2.5 shows the standard deviation of the total wind speed σ_v divided by the wind tunnel speed of 5ms^{-1}. Different measurements at the same azimuth result from different elevation angles ($0°$ to $6°$). If one of the two horizontal sensor axes lies parallel to the flow, the total turbulent intensity is clearly increased, this being most pronounced for higher elevations. The effect of the elevation angle alone can be seen at the intermediate positions $45°$, $135°$, $225°$ and $315°$. Here, no increase is found of the turbulent intensity for the horizontal position where the turbulence is increased for elevated positions.

Table A2.4   Evaluated coefficients for equation (A2.1).

A	C1	C2	C3
11.8 0.300	0.937	0.218	
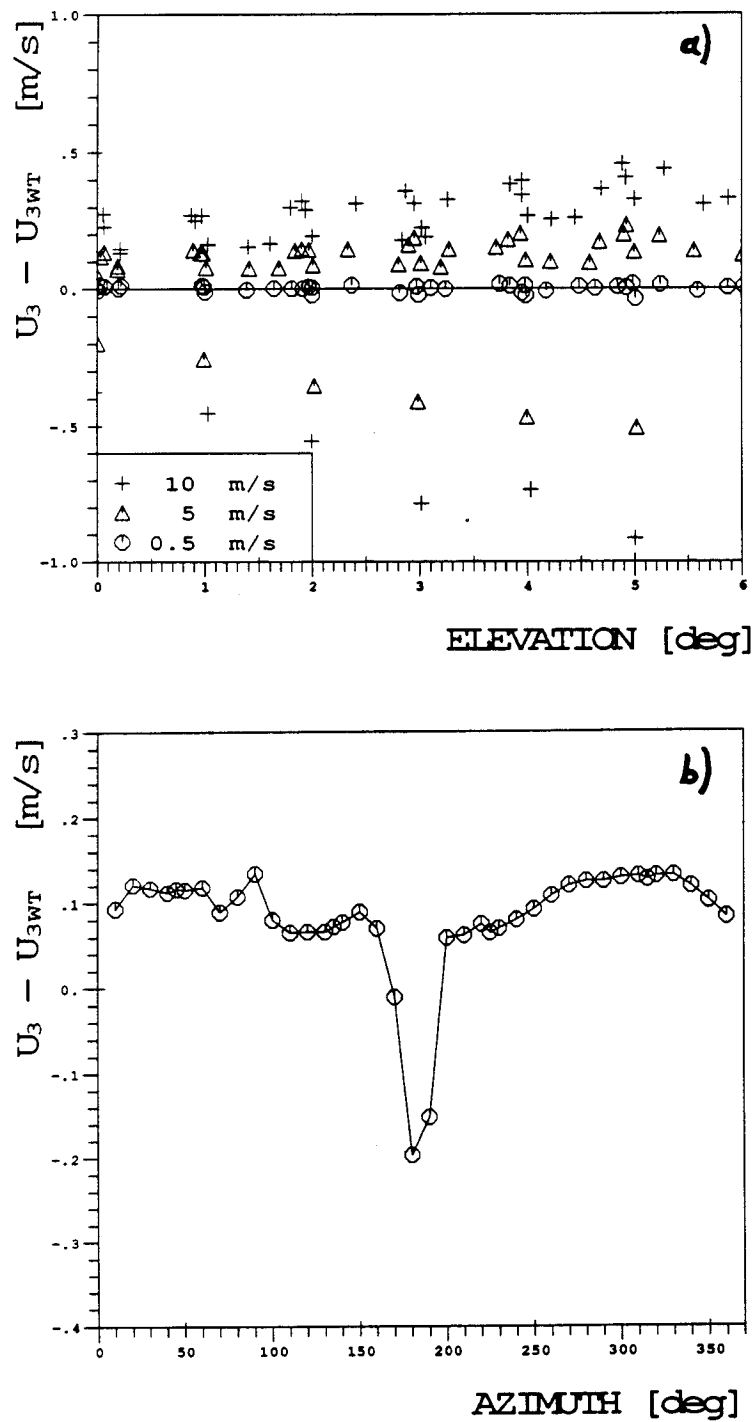
Figure A2.4   Difference between uncorrected and wind tunnel vertical component for
a) different wind speeds and elevations, azimuth angles are at 45°
intervals from 0° to 315°, and b) all azimuth angles in the case of $V_{WT} =$
5 ms^{-1}, elevation = 0°. Negative values in a) are measured at an azimuth
angle of 180°.
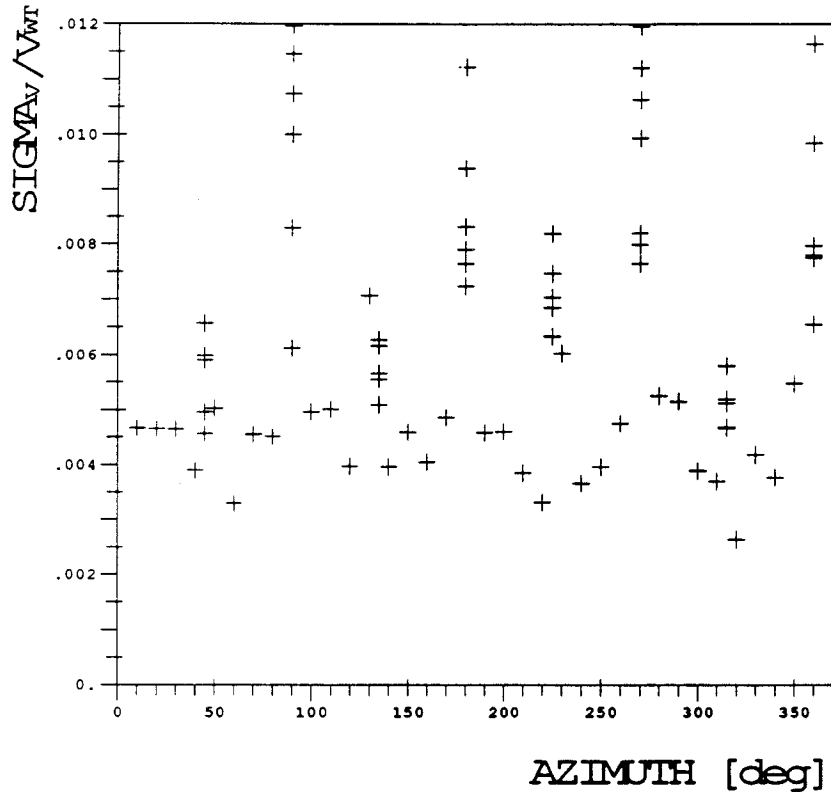
Figure A2.5   Turbulence intensity σ_v/V_{WT} as measured by the sonic anemometer at a
wind speed V_{WT} of 5 ms^{-1}. For azimuth angles at 45° intervals from 0°
to 315° the different values originate from different elevation angles.
The higher the elevation, the greater is σ_v/V_{WT} in these cases.

A2.5 Corrections

When testing a sonic anemometer in a wind tunnel, one can (strictly speaking) only
compare the measured wind speed $\tilde{U}_i^{**}$ with the theoretical (predicted) U_i. There are
two ways to find the "true" wind components from a sonic measurement, when
knowing the response characteristics. The first possibility is to store the corresponding
"true" values U_i for every triplet $\tilde{U}_i^{**}$ and correct as a one to one assignment. The best
way to achieve this, is to find a mathematical function of arbitrary form that represents
the best (statistical) fit between measured and predicted data. The problem with this
procedure is that the relationship between $\tilde{U}_i^{**}$ and U_i is not necessarily unique (see
e.g. the nonlinear shape of the expected transducer shadowing curve, Fig. A2.6). A
second approach to correct sonic data would be to find a transfer function that takes
into account the physical processes that lead to the departure of measured and predicted
wind components. A disadvantage of this latter procedure is that it is experimentally not
yet possible to determine the effects of transducer shadowing and flow distortion

separately (see Wyngaard and Zhang, 1985). Attempts have been made to investigate the transducer shadow effect alone using a single pass sonic system (e.g. Kaimal, 1979; Hanafusa et al., 1982; Coppin and Taylor 1983). This clearly minimizes the flow distortion. However, when using an equally shaped pair of transducers within a three dimensional array, the attenuation for flow parallel to the axis seems to be changed as compared to the single pass (Hanafusa et al., 1982; Baker,1988).
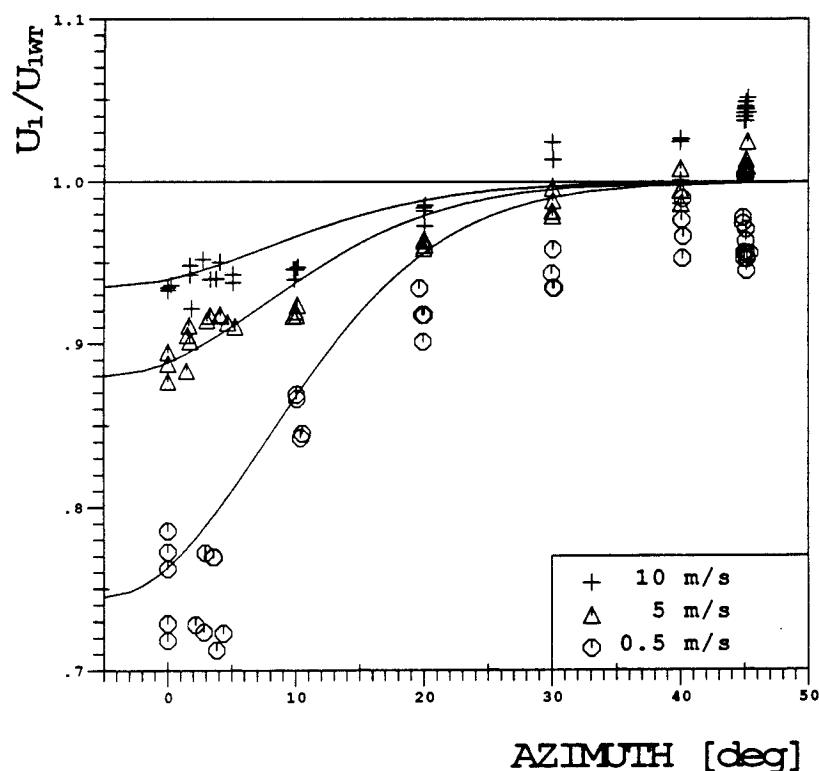
Figure A2.6   Attenuation of measured wind component U_1 as a function of deviation angle from sensor axis α. Solid lines after equation (A2.1) and (A2.8) with parameters listed in Tables A2.2 and A2.3. Note that the solid lines approach 1 as $\alpha \rightarrow 45°$ due to the functional form of (A2.1).

Both correction procedures have been tested with the present data. When applying a linear multiple regression model to the measured data the ability to reproduce the theoretical wind tunnel components is worse than with a physically based correction procedure (see Table A2.5). It is clear, that this performance can be improved by allowing higher order terms as dependent variables. In Table A2.5, the results of a second order model are also shown. Here, the results are better than for the physically based procedure. An almost one-to-one representation of the theoretical wind components could probably be achieved by extending the function to still higher orders. In general, it is preferable to work with a physically based transfer function if one wants to extrapolate its applicability to conditions not covered by the wind tunnel

experiments (e.g. wind speeds higher than 10 ms^{-1} in the present case). For this reason, and since the results of a model with a physically based transfer function gives satisfying results (Table A2.5 and Fig. A2.8, this latter procedure has been chosen and will be outlined in detail in the following.

When looking at the ratio between measured and predicted wind speed (e.g. U_1/U_{1wt}, Fig. A2.6) as a function of deviation angle from the sensor axis, the curve shows a similar shape as the one reported by Hanafusa et al. (1982) for the same type of transducer. It is therefore assumed, that for flow which is near parallel to one of the sensor axes, the difference between measured and predicted wind components is in general mainly due to transducer shadowing. Deviations from this model appear for the various elevation angles (at angles of attack of $0°$ and $45°$). Additionally, the two sensor axes do not respond in exactly symmetric fashion and the attenuation for flow parallel to the axis is lower than in Hanafusa et al. (1982). If the shadow effect is caused by the reduced wind speed in the wake of the transducer, it must be dependent only on the shape of the transducer and the wind speed that determine the extension of the wake, and on the distance between the transducers which determines the partitioning between reduced and undisturbed wind speed. Two equally shaped transducer pairs should therefore provide the same attenuation under the same conditions. For that reason, only one correction function has been evaluated and the remaining differences are attributed to flow distortion. The question remains why attenuation for the flow parallel to the axis in a three dimensional sensor array is smaller than for a single pair of transducers (Hanafusa et al., 1982; Baker, 1988). Taking Fig. A2.5 into account, it is suggested that the increased turbulent intensity for flow parallel to the axis is at least partly responsible for this behaviour. An increase of turbulence intensity means that individual wind vectors have a higher probability for a larger deviation angle from the sensor axis than the experimentally fixed of $0°$ and suffer therefore from a less pronounced shadow effect.

The order of applying the corrections for transducer shadowing and flow distortion (and therefore also the order in which we can determine their functional form from the wind tunnel experiment) is very important. Consider a pair of transducers to measure the wind speed along its axis and a wind vector of strength V^* with a deviation angle from the sensor axis of α^*. The attenuation (for that specific transducer geometry) will be dependent on V^* and α^*, whether this wind vector represents the "true" flow (as if no sensor were present) or a flow modified by flow distortion. The transducer shadow correction should therefore be applied first.

As a result of the present study it is clear that a wind speed dependence has to enter a shadow effect parametrization. Since we have data for only three different wind speeds, the shape of the functional dependence has been determined using data from Hanafusa et al. (1982), and is found to obey

$$C(V) = C_1 - C_2 \exp(-C_3 V) \tag{A2.8}$$

where C is the same as in (A2.1) and V is the absolute velocity. The parameter A in (A2.1) is found to be essentially constant in our experiments. Unfortunately, it is not clear from Hanafusa et al. (1982) at which ratio of transducer diameter to transducer separation distance the data are evaluated. In addition, their results were obtained with a one-dimensional sonic. While the present observations correspond well with those of Hanafusa et al. (1982) at small wind speeds, the parameter C seems to be somewhat larger at 10 ms^{-1} for the present probe (Fig. A2.7). This could be due to larger turbulence intensity in the case of the three-dimensional array. Since the present value for C at 10 ms^{-1} is the result of a number of observations (see Fig. A2.6), a curve with the *same shape* as (A2.8) has been fitted to the present data, although its applicability at wind speeds higher than 10 ms^{-1} may be questionable.

The application of (A2.1) and (A2.8) (with the numerical values given in Table A2.3) to field data has to be done iteratively, if the angle of deviation α in (A2.1) cannot be determined independently. Deriving α from the measured wind components implies indeed that the angle itself is contaminated by the shadow effect.

In a second step, the wind vector is transformed into a truly orthogonal coordinate system, before determining the flow distortion coefficients. In the analysis for flow distortion, multiple regression has been performed using (A2.7). As mentioned, data for angles of attack of 180°±10° were excluded in the evaluation of r_{ij} for sector 3 in Table A2.2. Results are shown in Table A2.4. Deviation from the identity matrix are small, apart from r_{i3}. In the case of r_{13} and r_{23} this fact is not relevant, since U_3 is usually much smaller than U_1 and U_2. Thus, flow distortion affects the horizontal wind components only slightly (Högström, 1982). The coefficient r_{33} represents the amplification of U_3 (which is generally small) by flow blocking, whereas the coefficients r_{31} and r_{32} account for the observed upflow (Figs. A2.4a and A2.4b).

C
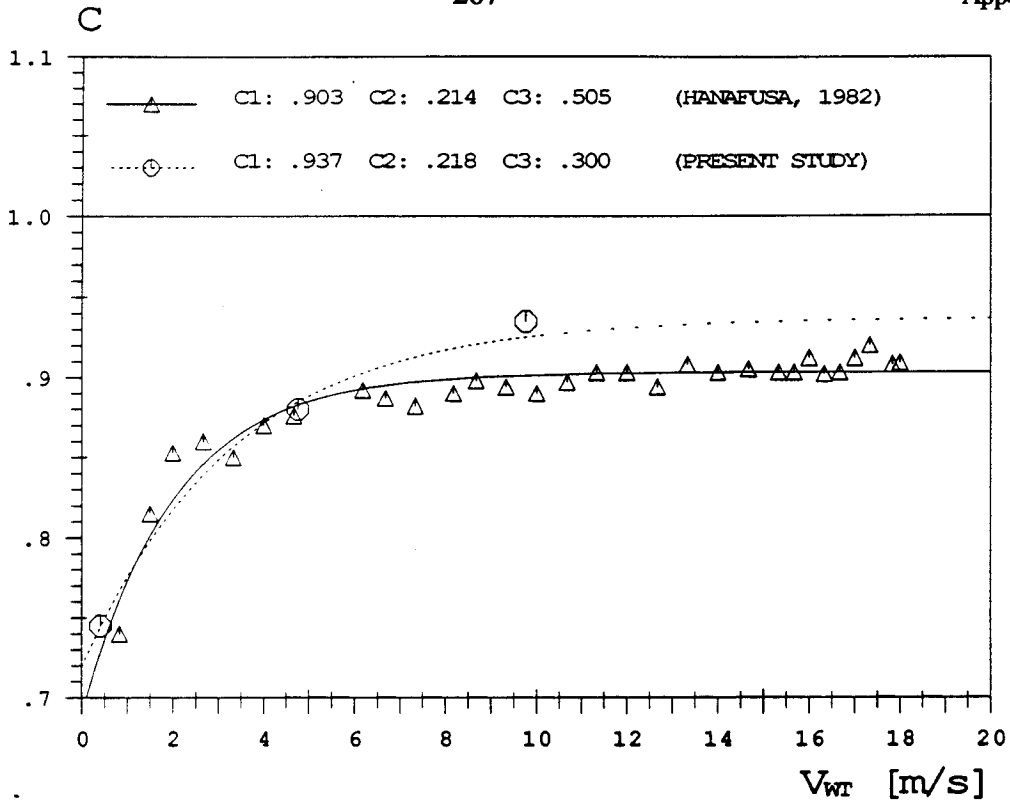
Figure A2.7   Velocity dependence of parameter C in equation (A2.1) derived from data in Hanafusa et al. (1982) and the present study.

A detailed sequence of steps for the correction is summarized as follows:

1. Obtain a first guess for the angle of deviation from the nearest sensor axis from measured $\widetilde{U}_1^{**}$ and $\widetilde{U}_2^{**}$ (or alternately, use an independent instantaneous measurement of wind direction). Correct the component of that nearest sensor pair using equation (A2.1) and (A2.8).

2. Repeat 1) with the improved deviation angle and absolute wind speed until a prescribed accuracy for $\widetilde{U}_i^*$ is reached.

3. Transform $\widetilde{U}_i^*$ into a truly orthogonal coordinate system via (A2.2).

4. Determine the relevant wind direction sector from $\widetilde{U}_i^*$ and Table A2.2.

5. Correct for flow distortion using (A2.7).

A comparison of the fully corrected wind velocities (i.e. after subsequent application of (A2.1), (A2.2) and (A2.7)) with the theoretical values is shown in Fig. A2.8. It illustrates that the ensemble of corrections allows a satisfying representation of the undistorted wind speed, supporting the validity of the parameterisations used.
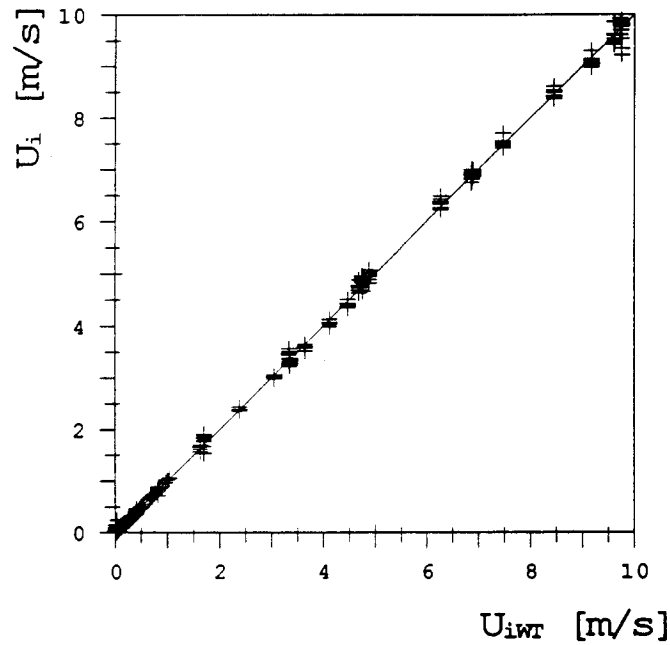
Fig A2.8   Corrected mean values of components U_i as compared to the respective
                wind tunnel components U_{iWT}. Sector 270 - 360°.

Table A2.4   Flow distortion coefficients matrices for the different wind direction
                sectors.

Sector	r_{11}	r_{12}	r_{13}	r_{21}	r_{22}	r_{23}	r_{31}	r_{32}	r_{33}
1	1.005	0.000	0.034	0.063	0.974	0.135	0.020	0.015	1.163
2	0.995	-0.032	0.115	-0.006	1.006	0.145	0.021	0.002	1.195
3	0.986	0.013	0.059	0.038	0.995	-0.055	-0.015	-0.004	1.159
4	0.988	-0.039	-0.146	-0.003	0.990	-0.165	-0.025	0.013	1.211

Table A2.5   Percentage difference between theoretical (U_i^t) and predicted (U_i^p) wind speed $(100*IU_i^t - U_i^pI/U_i^t)$ for different correction models. Theoretical wind components are calculated from the wind tunnel speed and the respective position. The models are: linear multiple regression (LMR): $U_i = a_{ij}U_j$; second order multiple regression (SOMR): $U_i = a_{ij}U_j + b_{ijk}\widetilde{U}_j^{**}\widetilde{U}_k^{**} + c_i$; physically based model (PBM): as described in Section A2.5

Sector	U$_1$			U$_2$			U$_3$		
	LMR SOMR	PBM	SOMR	LMR	PBM	SOMR	LMR	PBM	
1	4.1	3.8	1.3	10.3	6.8	5.5	3.1	3.1	1.5
2	8.4	4.0	3.1	2.2	2.4	1.0	4.5	5.0	1.7
3	4.7	4.0	1.4	3.1	3.1	1.1	4.3	4.2	1.7
4	7.1	4.1	4.6	6.3	5.6	1.7	6.3	6.5	4.3

A2.6 Effect of Corrections to Field Data

One of the crucial questions in the context of wind tunnel calibrations of sonic anemometers is whether results from laminar wind tunnel flow can be applied to turbulent boundary layer flows in field studies. Hanafusa et al. (1982) compared the turbulent statistics of two Kaijo Denki sonic anemometers that were rotated 45° with respect to each other and found no clear differences between the two measurements. They conclude, that the transducer shadow effect produces no significant difference in statistical properties between two sonic anemometers. In contrast, a very recent study by Grant and Watkins (1989), also with two Kaijo Denki type sonics that were rotated with respect to each other, shows a clear dependence of the relative difference between the two measurements on the angle of attack. They report differences in mean wind speed and the longitudinal standard deviation between 10% and 20%. The probes used by Hanafusa et al. (1982) had a rectangular sensor array. For a fluctuation in wind direction of ±20°, which is quite common in surface layer flows, it is very difficult to meet conditions, where one of the sensor axes clearly experiences flow parallel to the axis while the other is distinctly off axis. In Grant and Watkins' (1989) experiment the probes used had an angle of 120° between the horizontal sound paths. This makes it much easier to meet conditions with one probe clearly being influenced by transducer

shadowing and the other not. Model calculations of Grant and Watkins (1989) show that equation (A2.1) is an appropriate description of transducer shadowing even for turbulent real atmosphere flows. It is therefore interesting to evaluate the effect of such corrections to some field data.

Data were processed several times including more and more corrections, indicating therefore the magnitude of the considered source of error. The notation is as follows: "corrected data" indicates that the procedure described in Section A2.5 is applied to every single measurement; "shadow only corrected" means that no flow distortion correction is applied; in the case of "matrix corrected", every single measurement is corrected for transducer shadow effect and flow distortion is accounted for only on the basis of the mean covariances (see Section A2.6.1); "uncorrected" data are only transformed into the orthogonal frame of reference. Due to the lack of other data from the Kaijo Denki instrument (possibly collected at an "ideal site"), the corrections were tested using a number of runs from the experiments at the Anwand site (uppermost level).

A2.6.1 Correction of the Covariance Matrix

If flow distortion coefficients for the instrument used are known but only mean covariances $\overline{u_k u_m}$ are stored, the true covariances can be calculated according to Wyngaard et al. (1985) by

$$\overline{u_i u_j} = a_{ik}^{-1} a_{jm}^{-1} \overline{u_k u_m} \tag{A2.9}$$

where a_{ij}^{-1} is the inverse of the flow distortion coefficients matrix a_{ij}. Unfortunately, a rotation of the coordinate system into the mean wind direction is performed in most works before calculating covariances and this changes the contributions to $\overline{u_i u_j}$ by the different elements of the covariance matrix $\overline{u_k u_m}$. In the present study, application of (A2.9) shows the contribution of flow distortion to the total error. Note that the matrix correction is only useful if transducer shadowing can be neglected. This is assured by rotation of the probe in an appropriate position during measurements or by preliminarily correcting single data for this influence. The friction velocity u_* must then be derived from $\overline{u_1 u_3}$ and $\overline{u_2 u_3}$ assuming that the stress tensor is aligned with the mean wind.

When the covariances $\overline{u_1 T}$ and $\overline{u_2 T}$ are available, the same procedure as for the stresses, using the flow distortion coefficients, can be used to correct the $\overline{u_3 T}$ values. This has been done in the present study ("matrix correction"), whereas "corrected" again refers to covariances derived from individually corrected wind components.

A2.6.2 Results

Figs. A2.9a-c show the percentage difference between corrected and uncorrected data for the friction velocity u_*, the turbulent flux of sensible heat Q_H and the Obukhov length L. The difference between corrected and uncorrected data can reach more than 50% of the corrected value in certain cases. These differences can be either positive or negative, depending on the angle of attack of the mean wind. If the data are "shadow only" corrected, the percentage difference as compared to the corrected values is markedly reduced (Figs. A2.10a-c), indicating that a correction for transducer shadow effect can have a substantial effect on measured turbulence statistics. The same magnitude of shadowing error has been predicted by Zhang et al. (1986) in a theoretical study. If the matrix correction is applied to the mean covariances instead of applying flow distortion correction to every single measurement, the differences become very small (Figs. A2.10a-c). Thus, in general this procedure can be used to save computer time and storage. The only problem with this matrix correction arises from the fact, that different matrices have to be determined for the four sectors of wind direction (see Section A2.3, Table A2.2). If the mean wind direction is e.g. 10° (in anemometer coordinates) we use the matrix r_{ij} for sector 1 (Table A2.3) in the application of (A2.9) even if we have to assume that during the period of averaging the wind direction might have been from sector 4 for a considerable period of time.

Fully Corrected u_* [ms^{-1}]
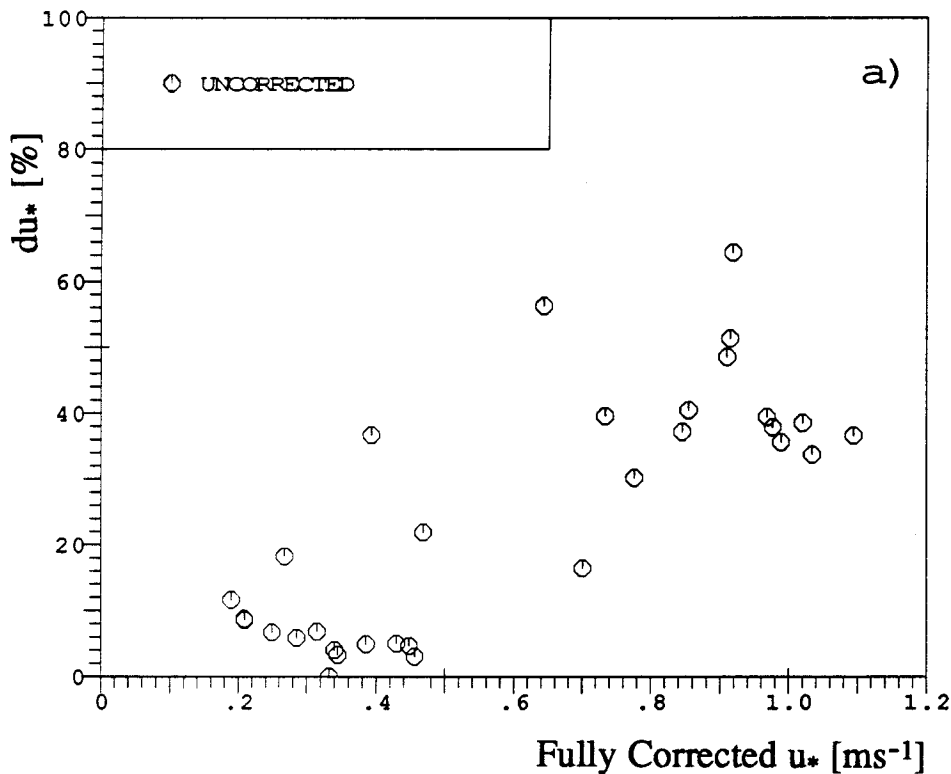
Fig A2.9a   Difference between turbulence properties derived from corrected and uncorrected data normalized by the former value.a) u_*,
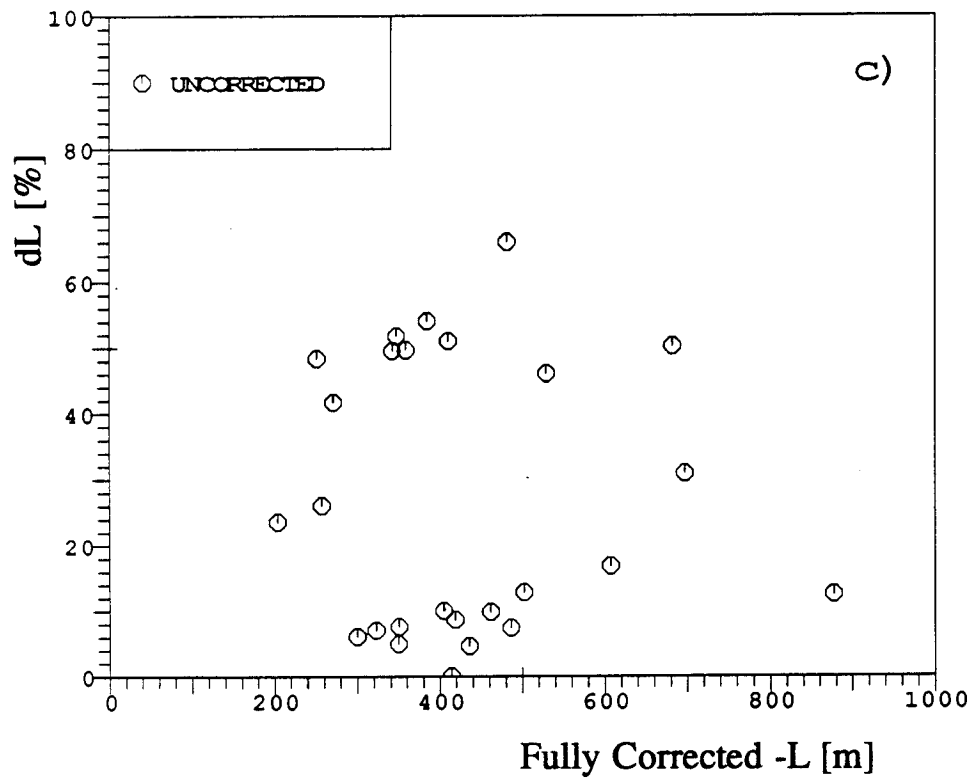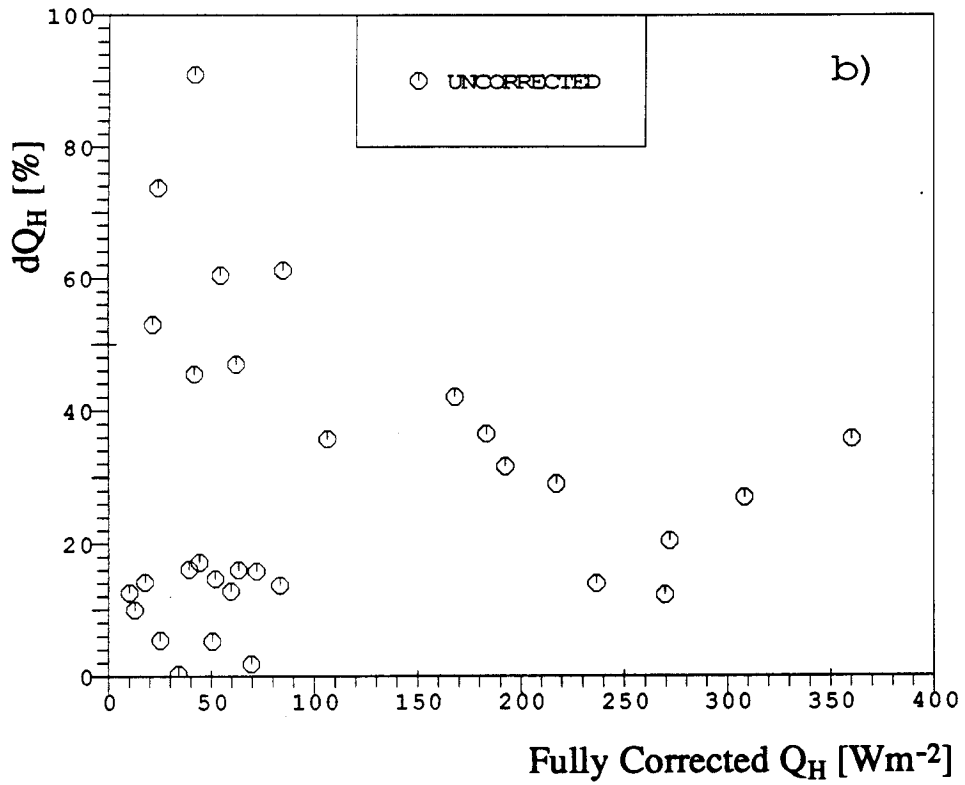
Fig A2.9b,c   As Fig. A2.9a but for b) Q_H and c) -L
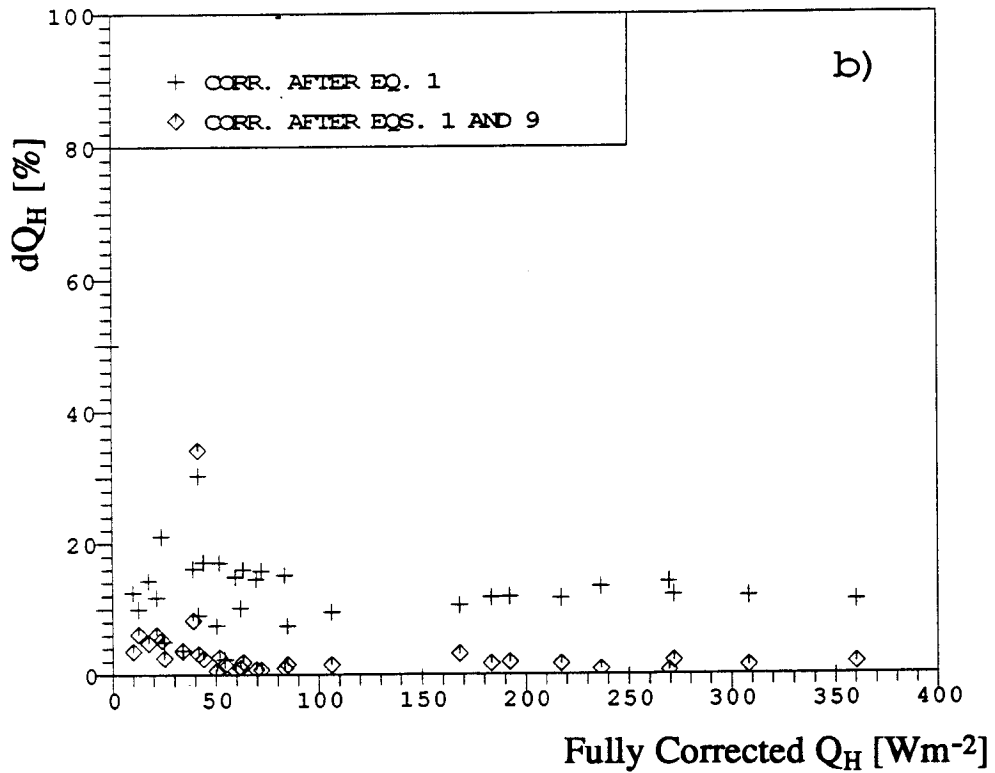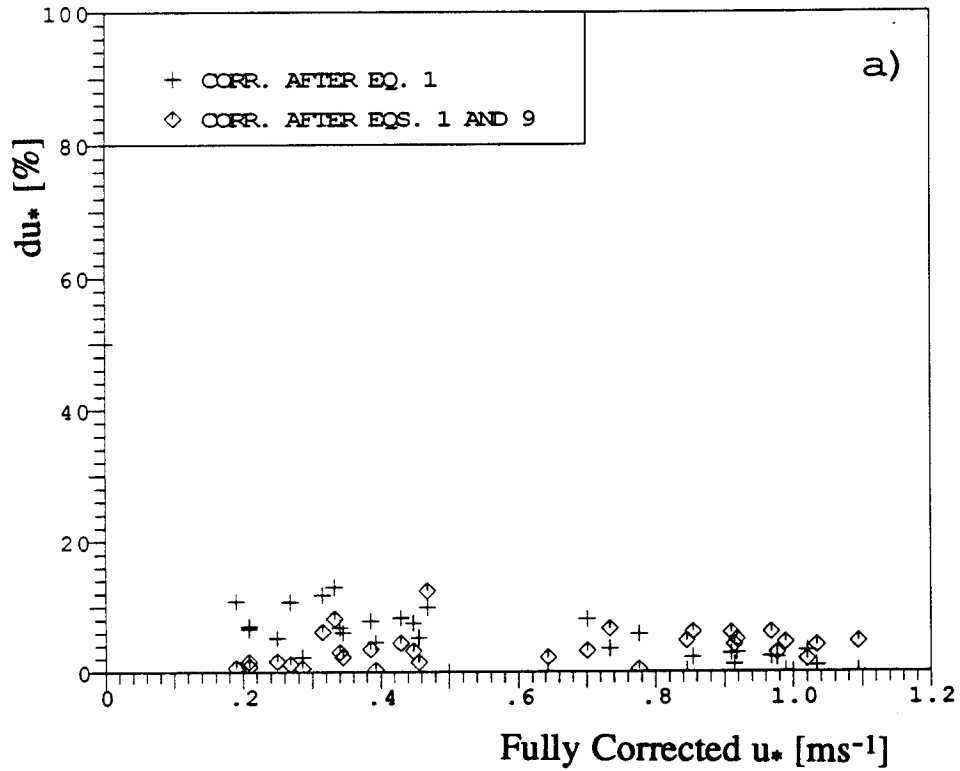
Fig A2.10a,b Same as Fig. A2.9, but for data corrected according to equation (A2.1) or (A2.1) and (A2.9), respectively. a) u* and b) Q_H
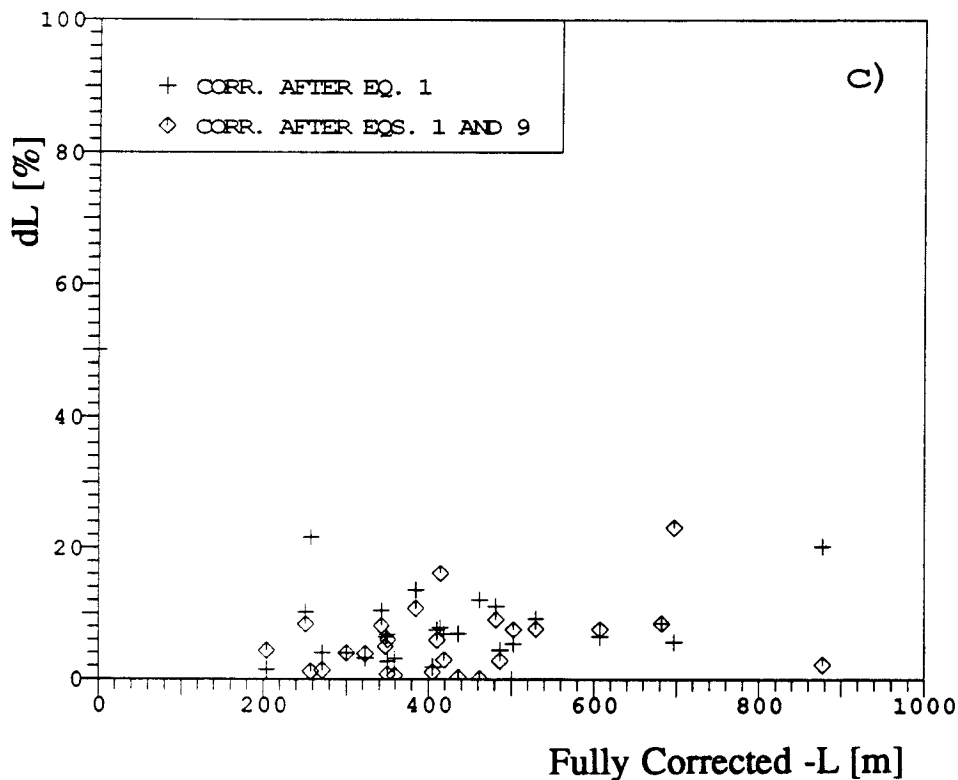
Fig A2.10c   Same as Fig. A2.9, but for data corrected according to equation (A2.1)
or (A2.1) and (A2.9), respectively. c) -L

The data presented may not be typical for micro-meteorological experiments, since
they have been measured at a very inhomogeneous site in (partly) very turbulent
conditions. The errors determined as a result of this study may therefore be considered
as an upper limit rather than as an average.

A2.7 Two Dimensional Sonic Anemometers

Two two-dimensional sonics (Kaijo Denki, probe TJ-51) were combined to yield an
additional three-dimensional unit that is denoted "2x2D". Similar wind tunnel
experiments as with the three-dimensional (3D) probe were performed with the 2D-unit
and the 2x2D configuration. In general, the correction procedure for the two-
dimensional sonics is analogous to the one described in the previous sections for the
3D. However, there are a few points that have to be noted:

- the transducer shadowing effect is accounted for by the same coefficients as
deduced for the 3D. There were not enough wind tunnel data for the 2D (and the
2x2D configuration, respectively) to calculate an extra set of coefficients.

- since the two 2D sonics were used in the 2x2D configuration in the field, which
means that the relative position of the two individual 2D can not be determined to
an accuracy needed to describe the geometric correction angles, the matrix for this

correction is set to the unity matrix. This is not relevant to the horizontal components but for the vertical.

- to determine the flow distortion matrix, the following constraints are relevant: only one run in the wind tunnel was performed with the 2x2D configuration since, in fact, the wind tunnel was too small for this application. Additionally, some runs with only the horizontal 2D sonic (but on the "original" ground plate) were performed. For these runs, no vertical component is therefore available. If one compares run 10 (2x2D, 5ms^{-1}) with run 11 (1x2D, 5ms^{-1}) the results for the measured horizontal components are very similar. The presence of the vertical 2D sonic seems to have no significant influence on the horizontal readings. On the other hand, the vertical component of run 10 can be compared to the vertical component in run 17 (3D, 5ms^{-1}) and is again very similar. For two sectors of azimuth (see A2.1) for which enough data were available, the flow distortion matrix is calculated from the results of run 10 alone and found to be very similar (quantitatively and qualitatively) to the corresponding matrix for the 3D. The two remaining sectors are treated as follows:

i) sector 90° -179°: runs 10 -13 (all available) are used with "estimated" values for the vertical component (if missing). These are adapted from the 3D - runs with the same wind tunnel speed. The resulting flow distortion matrix is comparable to the corresponding 3D matrix.

ii) sectors 0° -90°: the same procedure as in i) (only 0°,10° azimuth had been measured!). For this sector, all matrix elements that are connected to the vertical component (a_{i3}, a_{3i}) are replaced by the respective matrix elements from the 3D flow distortion matrix. This seems reasonable, since for all three other sectors, the two matrices are highly comparable.

An additional problem occurred with the 2D sonics, which was not encountered until the end of the field measurements. For a yet unknown reason, the reading of one of the 2D components could suddenly change to very high or very low values (corresponding to maybe ± 25 ms^{-1} or more). The performance of such an "event" led to the conclusion that the origin of such obviously erroneous readings was possibly an instability in the electric circuit of the 2D sonics. As shown in Fig. A2.11 (as an especially awkward example) such "outbursts" lasted from 1 to a few tens of seconds and happened quite often (sometimes once per run but at other times only every hour). The turbulence statistics of an averaging period have to be excluded in principle if such data falls within this period, since, (even if only one of the three 2D components is affected) through the correction procedure it also significantly affects also the two other components. A high percentage of the 2D data would therefore be subject to rejection which would leave too few events for the direct comparison of turbulence statistics at different heights or horizontal locations. It is therefore desirable to find an appropriate way to i) detect these "outbursts" and ii) estimate the true values for the periods of obviously wrong measurements.
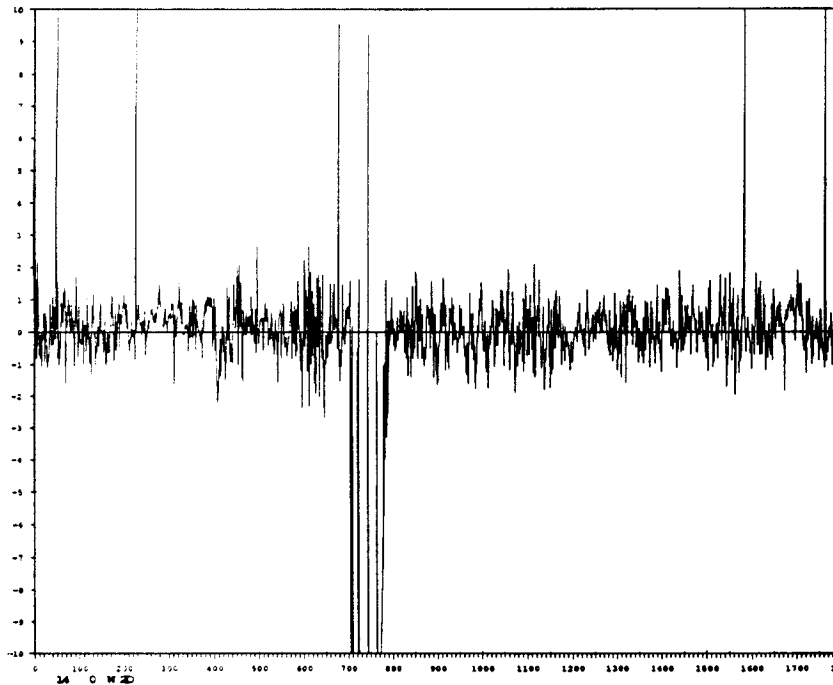
Fig A2.11   Time series (1800 seconds, vertical component) from the 2D sonic showing "outbursts" due to electronic problems.

For the whole averaging period, every measurement was compared with the absolute maximum for the same averaging period of the 3D measurement (either u_1 and u_2 or u_3). If the 2D reading exceeded 1.5 times this maximum, the value was considered wrong and replaced by the arithmetic mean of the foregoing and the following values. With this approach, valuable estimates were obtained if one single measurement was out of the physically meaningful range. If there was a longer period of such data, this estimate is clearly as wrong as the reading itself. To treat this kind of error, the averaging period T_a (e.g. 30 or 50 min) was subdivided into intervals Δt, for which $\Delta t \ll T_a$ and mean and variance of the component was calculated for every interval Δt. An interval was considered not plausible if it had a variance that was more than twice as large than the variance of the foregoing interval and the variance was larger than 5 ms^{-1} in magnitude (2 ms^{-1} for u_3). A second criterion was that the interval's average should not exceed 10 ms^{-1} (2 ms^{-1} for u_3). The first condition recognized a "bad interval" if the foregoing was undisturbed, the second if the foregoing interval was already bad. In this latter case the variance was often not exceptional, but the mean value was much higher than one could expect (see Fig A2.11). Clearly, the threshold value depends on the experimental situation and might be subject to change. All values of such an interval that had been considered not plausible were replaced by random values with the same

mean and variance (gaussian distribution) as a randomly chosen interval of the same averaging period.

The crucial point of this procedure is clearly the choice of the interval Δt. An inspection of the time series by eye shows that there is a characteristic time of "several seconds" (Fig. A2.11). Dutton and Panofsky (1984) give an approximation of the response time for u_3 in complex terrain (the time required for u_3 to adapt to new terrain) as:

$$\delta t = \frac{z}{3\sigma_{u_3}}. \qquad \qquad (A2.11)$$

For $\sigma_{u_3} \approx 0.3$, as in the present experiments, $\delta t \approx z \approx 10$ s. This value has been chosen and was, for convenience, also used for the horizontal components. This is justified "a posteriori" through the results.

To verify the results of the approach to estimate invalid (or missing, in a way) data of the 2D sonic, the estimated time series for the same period as in Fig.A2.11 is presented in Fig.A2.12. The intervals that have been "corrected" can not be identified as being different by eye. To give a more quantitative measure of the possible error introduced by the application of the procedure, the 3D data of measurement period 11a were used (the 3D data did not show those "outbursts"!): mean wind speed, momentum fluxes and variances of the wind components were calculated twice; once as usual and once with 11 arbitrarily selected "bad intervals" (5 of them in a sequence and 6 single intervals). The number of eleven was chosen since it corresponds to the number of bad intervals in the worst averaging period for the 2D. A comparison of the two results shows that mean values are reproduced to an accuracy better than 2% and variances and momentum flux better than 4% (see Table A2.6). If the number of artificial bad intervals is reduced to 7 (3 in a sequence and 4 single) the correspondence is even better. As an example, Fig. A2.13 shows the original and the manipulated results for σ_{u_2}.

If not too many bad intervals occurred within an averaging period, the turbulence statistics of the 2D measurements were used (with caution). In this study, for averaging periods which included any of these bad intervals only mean properties, variances and momentum flux (i.e. the properties for which the above procedure was intended and verified) were included in the data set .

Table A2.6   Mean errors (percent) of the 3D turbulence statistics for measurement period 11a with randomly chosen "bad intervals" (see text) as compared to the true values.

property	11 artificial bad intervals mean difference (%)	7 artificial bad intervals mean difference(%)
$\bar{u}_1$	0.72	
$\bar{u}_3$	1.69	
σ_{u_1}	3.88	3.12
σ_{u_2}	2.19	-
σ_{u_3}	3.83	2.45
$\overline{u_1 u_3}$	2.62	1.82

Figure A2.12   Same time series as in Fig. A2.11, but corrected as described in the text.
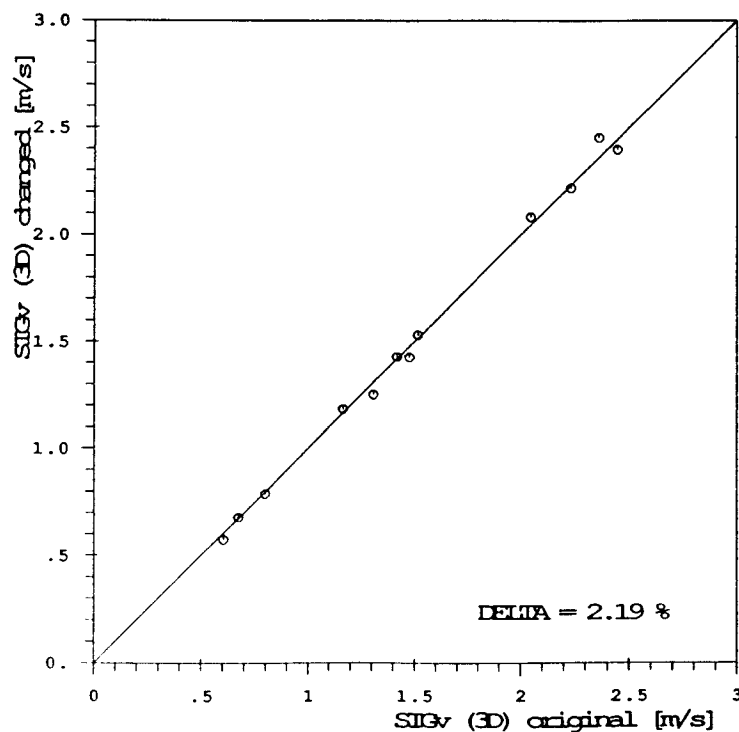
Figure A2.13 Comparison of the original σ_{u_2} (=SIG$_v$) as measured by the 3D sonic to
σ_{u_2} calculated from an artificially distorted "time series" (see text).

A2.7 Conclusions

When analyzing the response characteristics of a sonic anemometer, every departure
of a measured wind component from the respective true one can arise from transducer
shadow effect, flow distortion or from both of these phenomena. Nevertheless, an
attempt has been presented to interpret data from wind tunnel experiments in terms of
these two effects by considering each one separately. This method seems to be
reasonable since the shadowing of the transducers has its most pronounced effect for
along axis flow, whereas flow distortion shows a much more symmetric pattern.
Additionally, the resulting correction formulae become very easy to apply.

The uncorrected mean velocity response of the sonic anemometer in the wind tunnel
experiences a bias of up to 20%. The proposed correction procedure reduces these
systematic errors to less than 5%. Since the correction procedure is based on physical
considerations, it can also be applied in conditions not covered by the experimental set
up in the wind tunnel. The difference between corrected and uncorrected field data
(turbulence statistics) can reach more than 50% in certain cases. Of this difference, a
large portion can be attributed to the transducer shadow effect.

Especially when dealing with along axis flow, but also when the anemometer is
inclined with respect to the wind tunnel flow, a considerable amount of turbulence is
generated by the sensor array. This results in a quite large scatter of data around their
average in these situations. Because of the strong nonlinearity of the correction function

for transducer shadow effect for deviation angles near $0°$, a unique determination of the wind direction from measured data is impossible. It would therefore be desirable to measure this quantity independently in future wind tunnel experiments. It is also suggested that this induced turbulence accounts at least partly for the difference in attenuation observed when comparing the three dimensional sonic anemometer with a one-dimensional instrument.

A3 Long Term Observation of Mean Variables

Profiles of mean wind speed, temperature and specific humidity throughout the street canyon and in the RS were recorded during several months over a period of more than one and a half years (see Section 4.3). The results of these measurements are presented in the following sections in order to give "background" information on the state of the canopy and RS when analyzing the turbulence characteristics.

The measured 30 minute values were averaged to yield hourly means. For the calculation of the mean profiles over a certain time period (e.g. a particular month) or a wind direction sector, data were only included into the analysis if all measurements of the profile under consideration were available at the same time. Otherwise, unrealistic gradients would have been introduced through the day-to-day variation of the variables (if e.g. the wind speed at a higher level was lacking on a stormy day and the value at a lower level was missing at a calm day). For simplicity, the different measurement levels are numbered as depicted in Fig.A3.1.
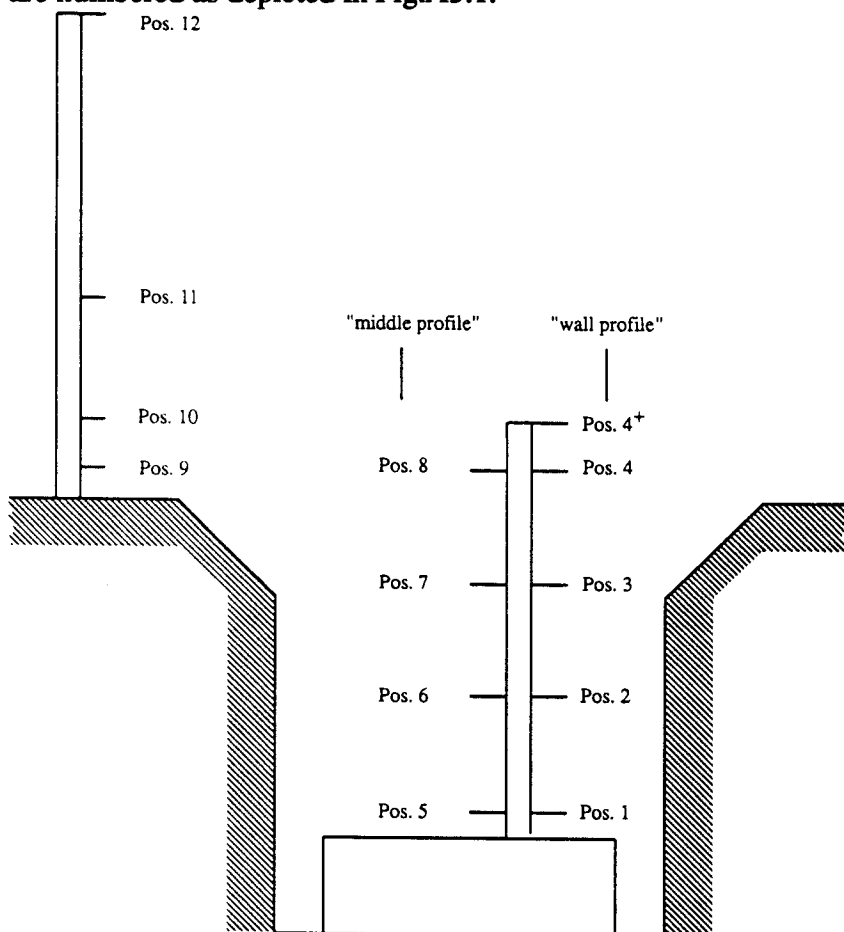
Figure A3.1   Schematic view of the Anwand site showing the definition for the various positions (Pos) of measurement with their respective numbers.

A3.1 Profiles of Mean Wind Speed

An average of all available measurements ("all year") of the mean wind speed profile is shown in Fig. A3.2. Note that no correction for overspeeding was applied (see Appendix A1.1.1) since the required turbulence data were not available for the whole period. Such a correction would tend to increase the gradients (at least above roof level) as the wind speed is overestimated close to roof level by typically 0.3ms^{-1} and somewhat less higher up.

On average, wind speed is quite uniform with height within the street canyon and no large variation with respect to the horizontal positioning can be observed. Above the roof level, the wind speed is considerably reduced over the canyon as compared to the same height on the roof-top tower. There is no difference between positions 4 and 8 (Fig. A3.1) during the day, whereas during the night the wind speed closer to the wall (but still above roof level) at position 4 is somewhat reduced. This is certainly a combined effect of the wind direction and the wind speed characteristics of the profile (see below).

If only hours with light wind speeds are considered ($< 3\ \text{ms}^{-1}$ at position 9), the profiles look very similar to those in Fig. A3.2, since this is simply the most common case. For moderate to high wind speed situations ($3 - 5\ \text{ms}^{-1}$ at position. 9), several features are apparent (Fig. A3.3): gradients above roof level are slightly larger and the variation with height becomes almost linear (especially for certain hours during the night). Within the canyon, uniformity with height is more pronounced for the site closer to the wall (positions 1-4), whereas in the middle of the canyon (positions 5-9) wind speed decreases with height above the second lowest level. The reduction of wind speed over the canyon is more pronounced for higher wind speed at position 8 ("middle of the canyon") but less significant closer to the wall (position 4).

Clearly, the most important influence on the profile of mean wind speed within and just above the street canyon is the local wind direction. The measurements were therefore stratified according to above roof level wind direction (at position 11). Wind directions within $\pm 30°$ of the axis of the canyon are labelled "parallel to the canyon", those within $\pm 30°$ to the cross-canyon direction "rectangular to canyon" (Figs. A3.4 - A3.7). For parallel flow, the profile of mean wind speed looks very much like those observed within and above plant or tree canopies (e.g. Raupach and Thom, 1981). This is especially true for the mid-canyon profile, whereas the profile closer to the wall

is still somewhat reduced with respect to the above roof value at position 9. In bioclimatology, profiles are often described by

$$u(z)/u(h) = \exp\{\alpha_1 (z/h - 1)\}, \qquad\qquad\qquad (A3.1)$$

where α_1 is an empirical parameter that usually lies between 2 and 3 (Raupach and Thom, 1981) and is dependent on the characteristic of the canopy (such as the area density and the effective drag coefficient). However, due to the distinct differences of wind profile for different wind directions it does not seem to be appropriate to fit a function like (A3.1) to the present data.

For cross-canyon flow, it is known from experimental and model results that a vortex within the street canyon can develop (Georgii et al., 1967) as shown schematically in Fig. 3.2. For the present site, flow from SW means that the profile closer to the wall (position 1-4) corresponds to the lee side of the canyon, whereas for flow from NE this profile represents the windward side (Figs. A3.6 - A3.7). Comparing Figs. A3.6 and A3.7, however, it is obvious that the flow pattern is by no means symmetric when considering the profile in the middle of the canyon (positions 5-8). The strong vertical gradient between position 7 (within the canyon) and position 8 (above) for wind from NE is not observed in the case of SW-winds. Considering the various above-roof profiles for the two different wind directions indicates that not only the absolute value of the wind speed above roof level but also the shape of the profile influences the wind speed within the canyon. A building some 50m to the SW of the present site and slightly higher (ca.5m) than those close to the canyon, could be a possible source of the observed differences. The profile in the middle of the canyon is almost uniform with height below roof level and exhibits a strong gradient higher up. The profile on the windward side within the canyon (Fig. A3.7) shows very little variation with height up to the above roof level. This is, however, only true for small wind speeds (Fig. A3.8); the profiles in the middle and on the windward side of the canyon are very similar for higher wind speeds (Fig. A3.9). The lee side profile (Fig. A3.6), on the other hand, shows a larger gradient around the roof level than one in the middle. In Fig. A3.10 these findings are sketched schematically for lighter wind speeds.
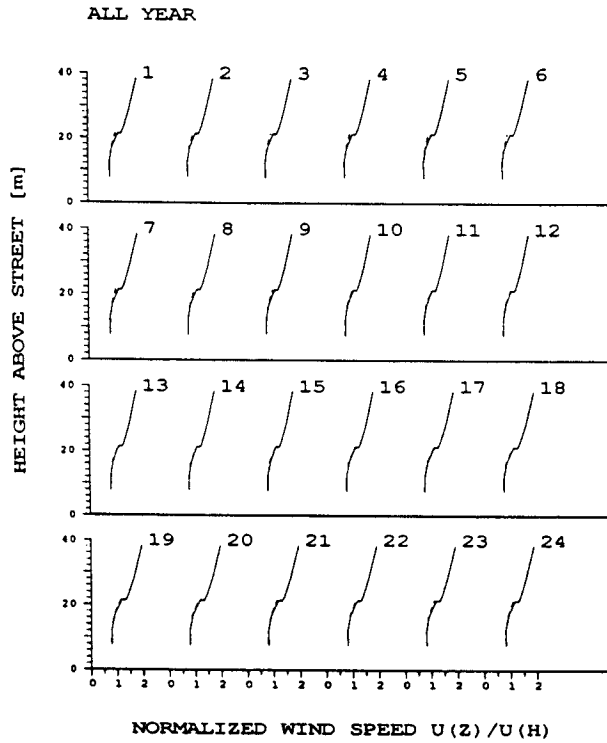
ALL YEAR

Figure A3.2   Averaged profiles of mean wind speed normalized with the respective value at z=h. ū(z=h) is interpolated between positions 7 and 8. The dashed line refers to positions 1-4. Numbers at the top of each profile indicate the hour of the day. Data included: the whole period of measurements.
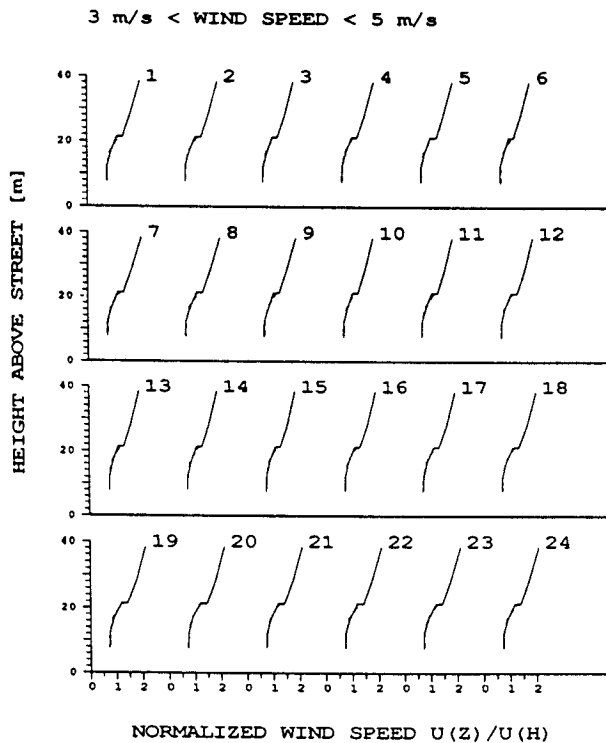
3 m/s < WIND SPEED < 5 m/s

NORMALIZED WIND SPEED U(Z)/U(H)

Figure A3.3   As Fig.A3.2, but only for intermediate wind speeds.

PARALLEL TO CANYON, SE
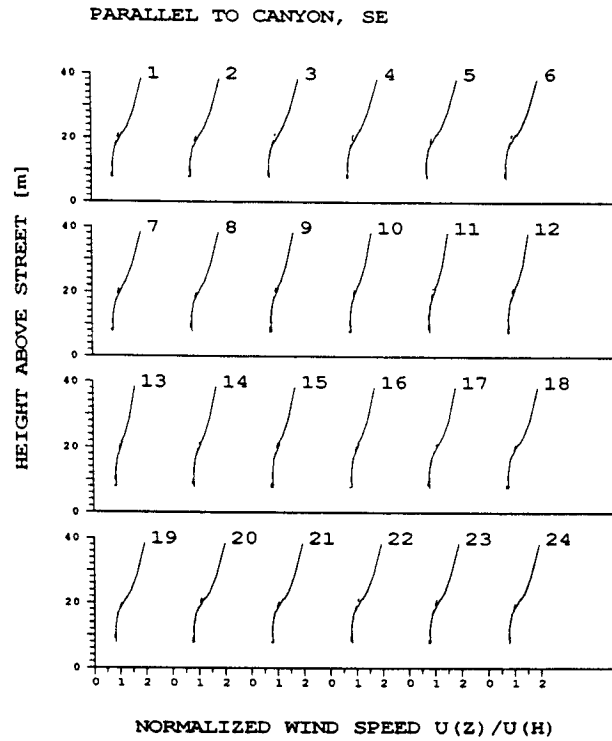
Figure A3.4   As Fig. A3.2, but for flow parallel to the canyon (from south east).

PARALLEL TO CANYON, NW
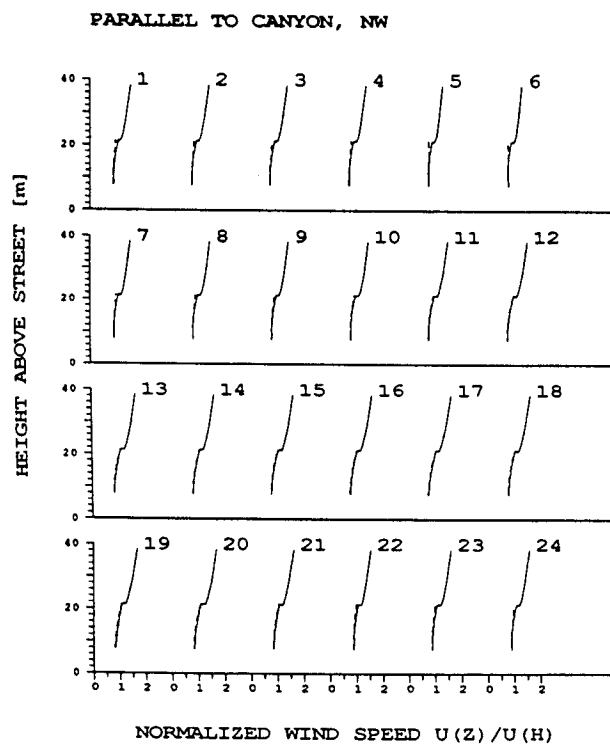
Figure A3.5   As Fig.A3.2, but for flow parallel to the canyon (north west).

RECTANGULAR TO CANYON, SW

NORMALIZED WIND SPEED U(Z)/U(H)
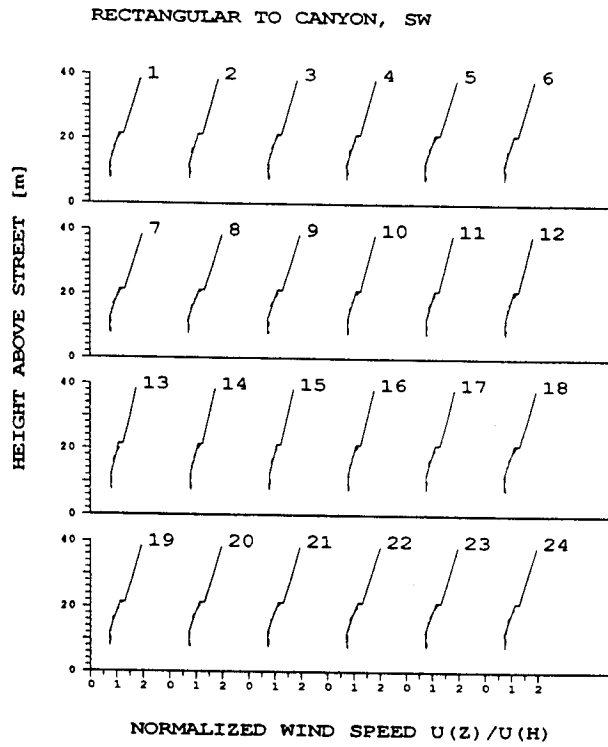
Figure A3.6   As Fig. A3.2, but for flow rectangular to the canyon (from south west).

RECTANGULAR TO CANYON, NE

NORMALIZED WIND SPEED U(Z)/U(H)
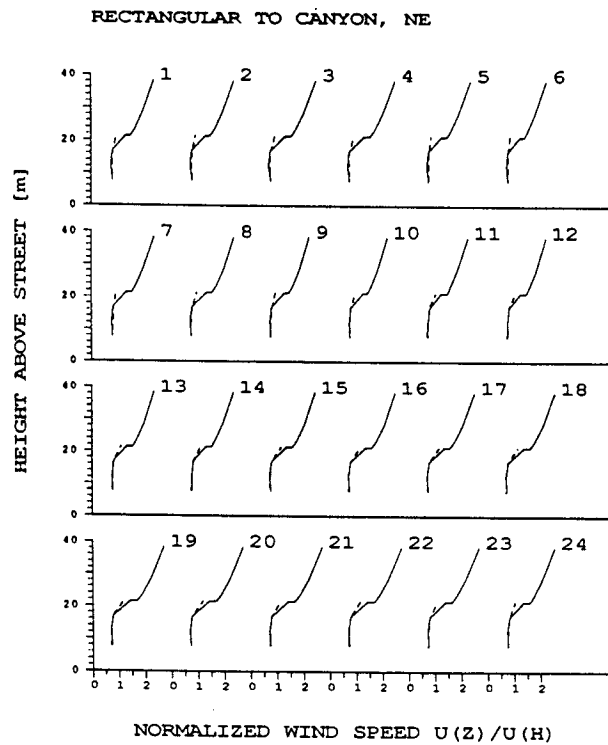
Figure A3.7   As Fig.A3.2, but for flow rectangular to the canyon (north east).

< 3 m/s, NE

NORMALIZED WIND SPEED U(Z)/U(H)
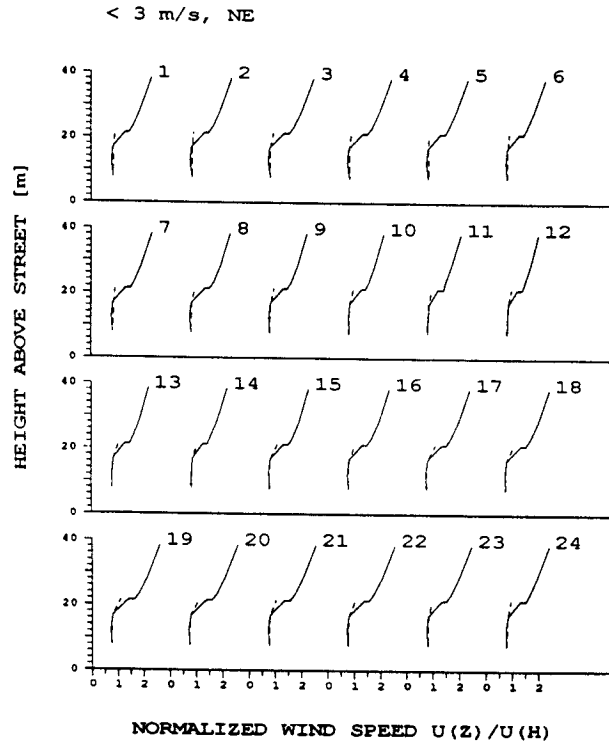
Figure A3.8   As Fig. A3.2, but for flow rectangular to the canyon (from north east).
Low wind speeds.

3 m/s - 5 m/s, NE

NORMALIZED WIND SPEED U(Z)/U(H)
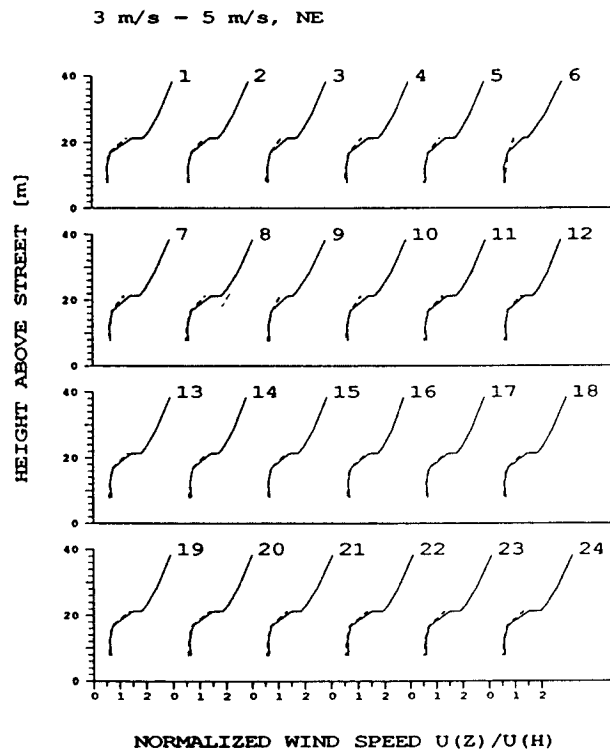
Figure A3.9   As Fig.A3.2, but for flow rectangular to the canyon (north east).
Intermediate wind speeds.
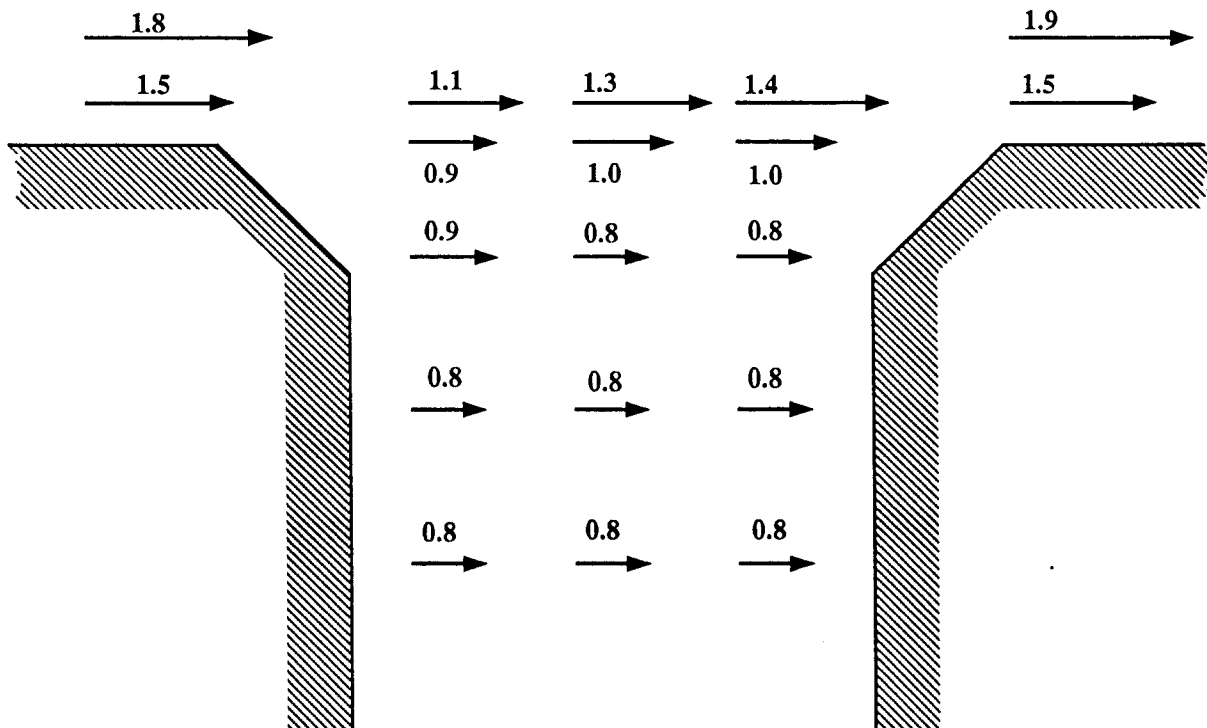
Figure A3.10   Cross section of a street canyon showing the relative magnitude of the wind vector at different positions for light wind conditions. Arbitrary units.

A3.2 Wind Direction

In the last section, it was shown that the flow is systematically slowed down over the canyon, a finding that can be explained by flow divergence. However, this phenomenon is accompanied by a change of wind direction within the canyon as compared to the above roof wind. Comparing the sectors around 30° and and around 210° in Fig. A3.11 (both corresponding to more or less cross canyon flow), it can be seen that this turn of the wind direction is an adaption of the flow to the new physical boundaries (turning towards "more parallel" flow) rather than an effect of changed roughness. If the latter were the case, the larger distance to the "ground" would imply less friction and a positive change in both cases (in the notation of Fig. A3.11). Note, however, that the observed turn is much smaller than the "upper limit" of 90° (from almost rectangular to parallel flow within the canyon) which supports the assumption of Yamartino and Wiegand (1986) that the flow within the canyon can be split into an along canyon and a vortex part. However, Fig. A3.11 shows that the along canyon part is larger as one would infer from the above-roof wind direction.
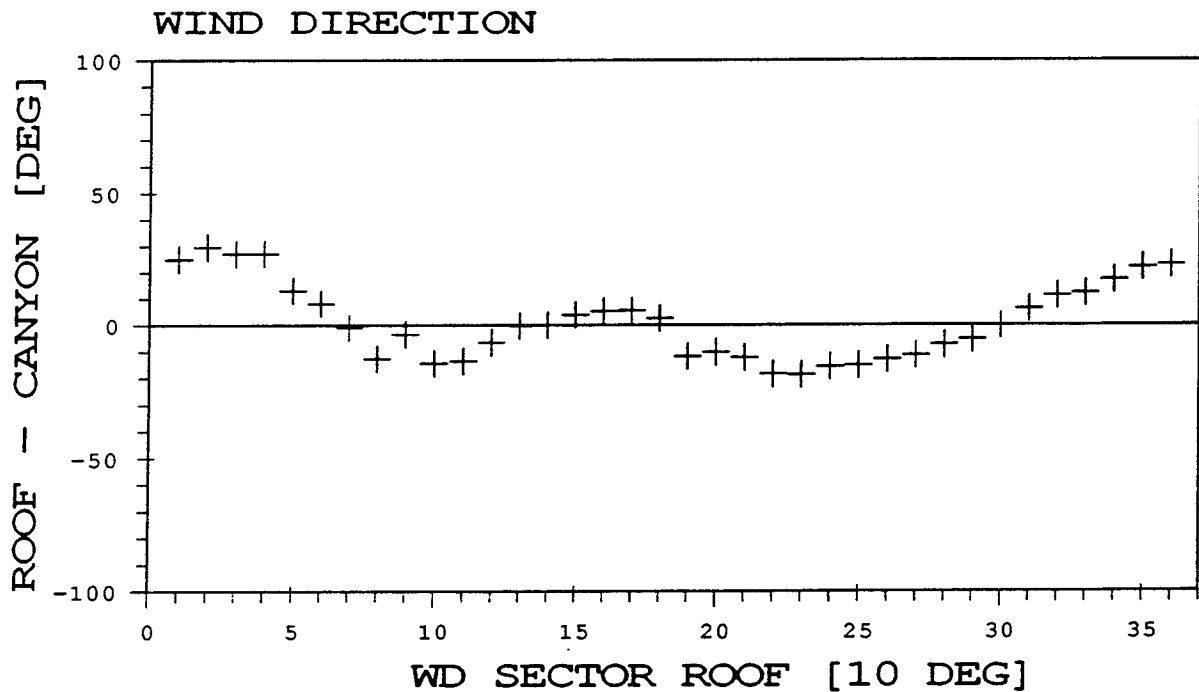
WIND DIRECTION

Figure A3.11 Difference in wind direction between position 11 (roof) and position 7 (canyon).

A3.3 Potential Temperature

Temperature measurements were not performed at the same positions during the whole period of measurements . The following simultaneous recordings will be shown in this section:

- four levels above roof level from April and May 1988 (Positions 9, 10, 11 and 12 respectively)

- three levels above roof level from October and November 1987 (positions 9, 11 and 12, respectively)

- three levels within the street canyon from September 1987 (positions 5, 8 and a level between positions 6 and 7 at 14m above the street, labelled 'position 6').

- four levels within and above the canyon from various times over the whole measurement period between November 1986 to May 1988 (positions 5, 8, 9 and 12, respectively).
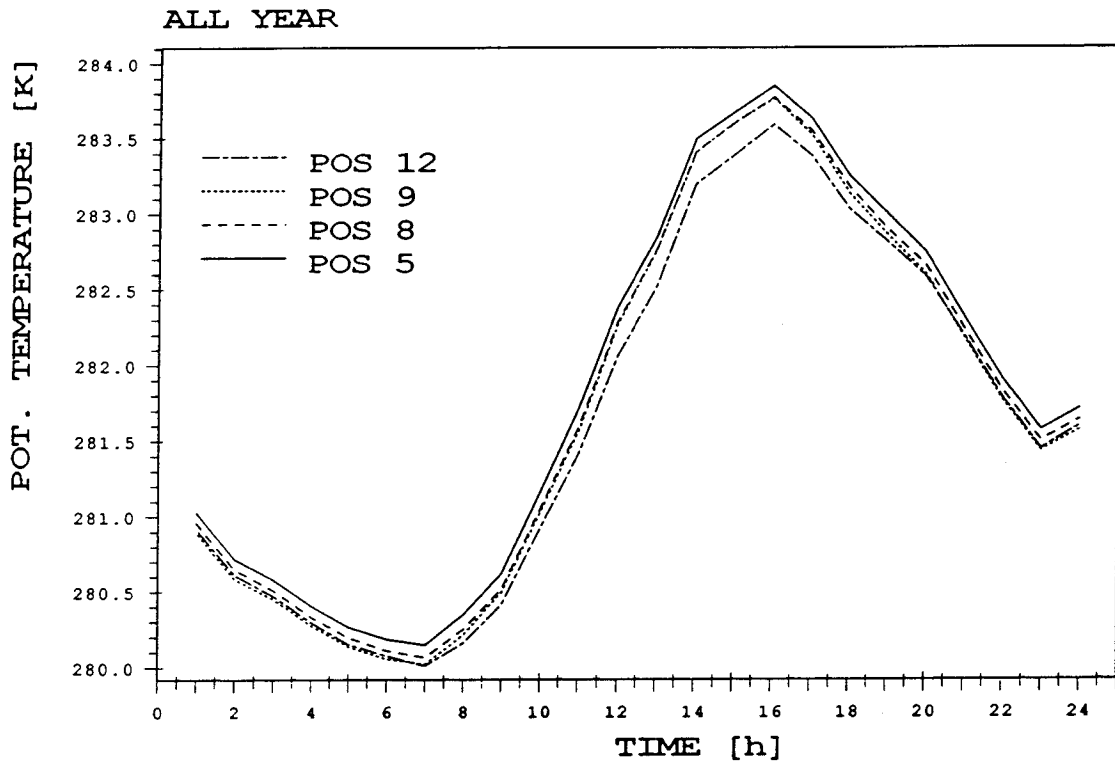
Figure A3.12 Daily course of potential temperature for positions 5,8,9, and 12. Data included: All reliable data from the whole period of measurements.

Fig. A3.12 shows the mean diurnal cycle of the potential temperature over the whole measurement period. The RS above the canyon (positions 9 and 12) is almost neutral during the night and unstably stratified during the day. On the other hand, the potential temperature within the canyon (position 5) is always higher than above (position 8), indicating that the air is unstably stratified within the canyon. On average, the potential temperature above the canyon (position 8) is about 0.1 K higher than over the roof (position 9) during the night, while both were equal during day time. The air is cooling faster over the roof or in other words, heat is trapped by the canyon to a certain extent in the present case. This phenomenon has been observed in other street canyons, where measurements were taken in a much higher spatial resolution (e.g. Nakamura and Oke, 1988). In Figs. A3.13 - A3.15 the profiles for "spring" (MAM), "summer" (JJA) and "winter" (DJF) are shown, respectively. For the autumn month (SON) only about one week of data is available in this configuration, so that the resulting "mean" profiles cannot be considered representative for this time of the year and are not shown. During almost the whole year the urban RS is neutrally stratified during the night, becomes unstable during the day and neutral again in the evening. This is of course more pronounced in summer and spring than in the winter. Potential temperature *within* the canyon is (without a distinct annual or diurnal cycle) on average about 0.1 K higher than above. A more detailed analysis with two measurements within the canyon shows

that on average the temperature distribution is quite uniform with height and a linear interpolation between positions 5 and 8 is justified (Fig. A3.16). Temperature differences between "above roof" (position 9) and "above canyon" (position 8) are apparent in summer and spring during the night when radiative cooling dominates.

The detailed profiles above roof level are not as uniform as those within the canyon (Fig. A3.17 and A3.18). In spring (Fig.A3.17) the air is almost neutral during the early morning hours over the whole height interval, but shows some variation of the potential temperature with height in between. However, they are, rather small and of the order of the uncertainty of the measurements (0.05 K) and will not be considered any longer. During the day, the air closer to the roof is clearly more unstably stratified than higher up so that a linear interpolation between positions 9 and 12 underestimates the potential temperature gradient at heights close to the roof and overestimates it at the upper levels. For the hours before midnight the situation is reversed. The layer close to the roof is near neutral or even slightly stable whereas the layer between 10m and 20m above roof level is essentially neutral. This shape of the profile is similar for the measurements in autumn (Fig. A3.18) where the upper layer is unstable and the one closer to the roof is slightly stable during the day time. For all these autumn measurements, however, the overall stability (i.e. if only measurements at positions 9 and 12 are available) would imply an unstable stratification.
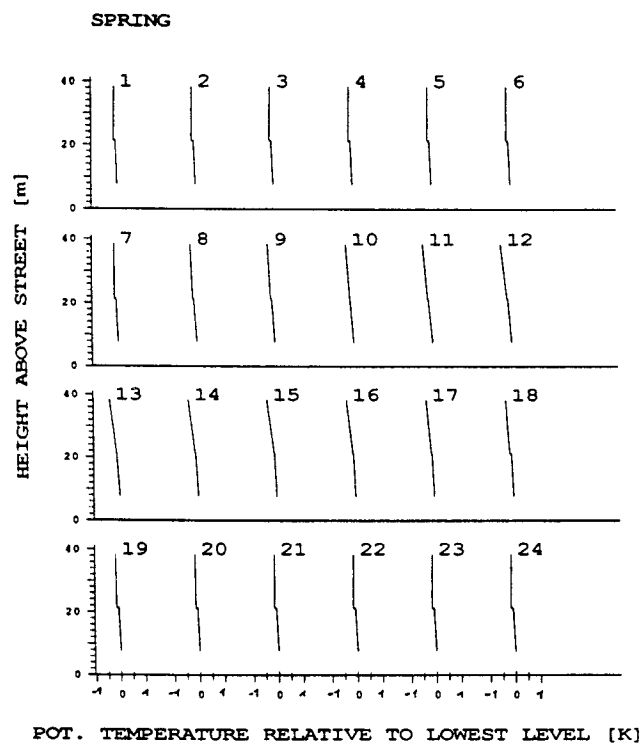

Figure A3.13 Mean profiles for potential temperature. Shown are the differences between the values at heights z and the lowest level (position 5). Numbers at the top of each profile indicate the hour of the day. Data from the months March, April and May.
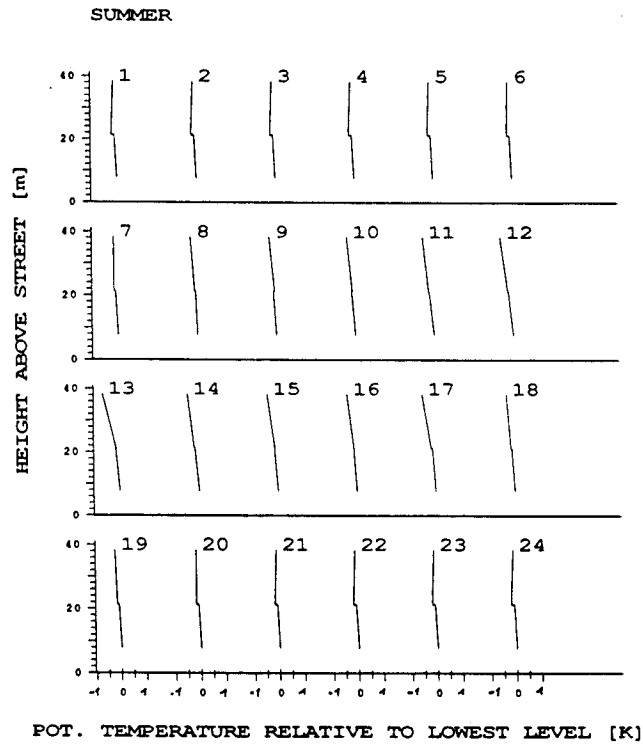
SUMMER

POT. TEMPERATURE RELATIVE TO LOWEST LEVEL [K]

Figure A3.14 As Fig. A3.13, but for the months June, July, and August.

WINTER

POT. TEMPERATURE RELATIVE TO LOWEST LEVEL [K]
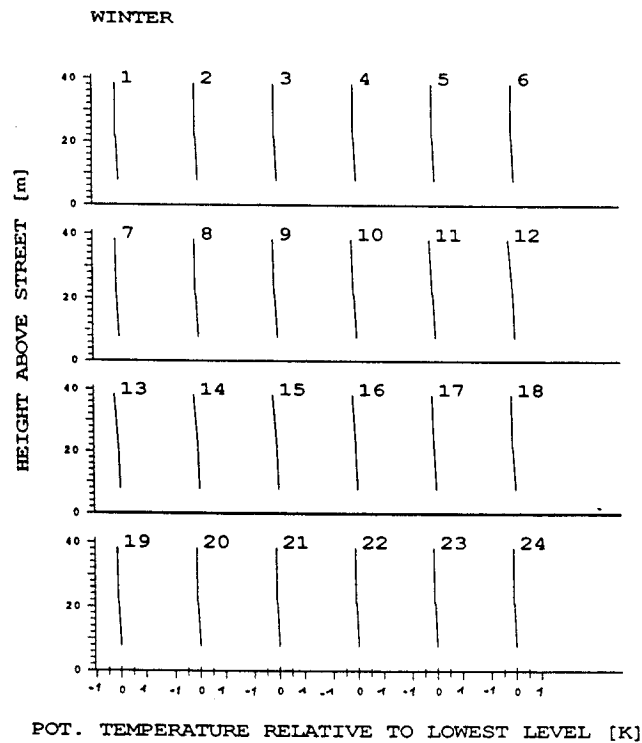
Figure A3.15 As Fig.A3.13, but for the months December, January and February.
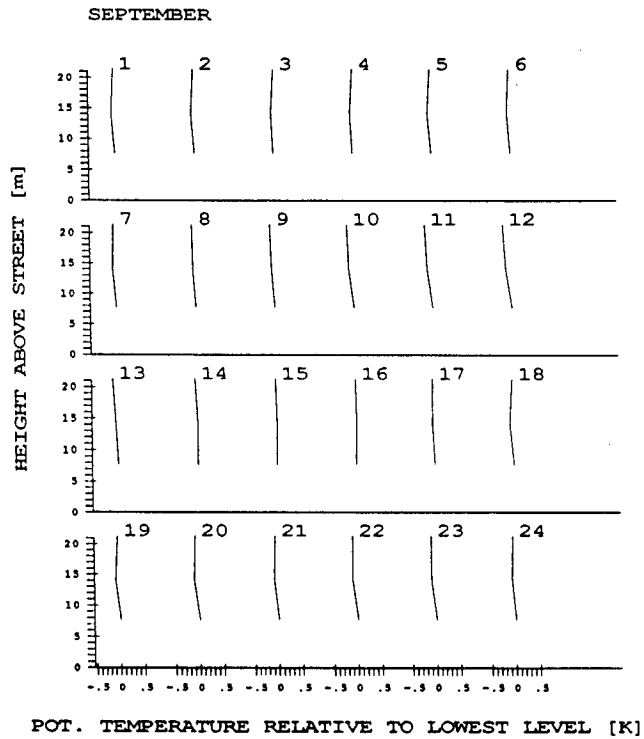
SEPTEMBER

POT. TEMPERATURE RELATIVE TO LOWEST LEVEL [K]

Figure A3.16   As Fig.A3.13, but for September, 1987 and positions 5,7 and 8. Note the different temperature and height scales.
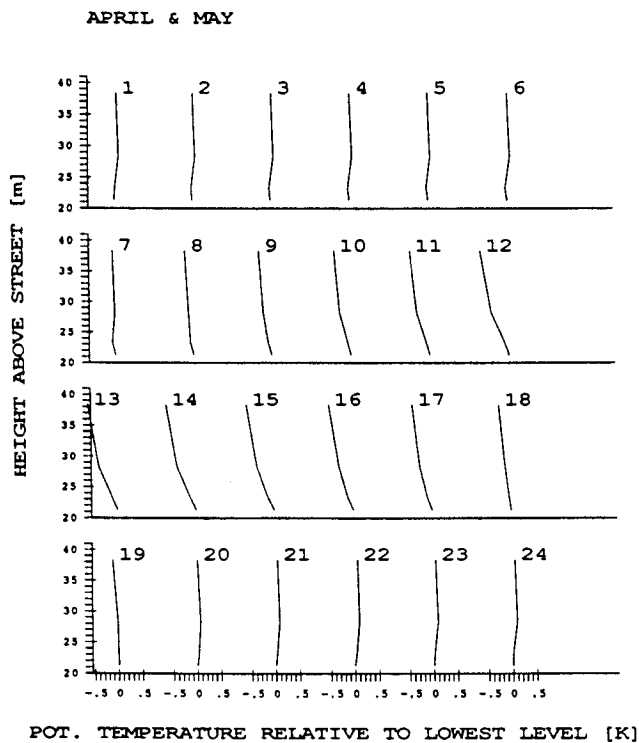
APRIL & MAY

POT. TEMPERATURE RELATIVE TO LOWEST LEVEL [K]

Figure A3.17   As Fig. A3.13, but for month April and May, 1988 and positions 9, 10, 11 and 12. Note the different temperature and height scales.
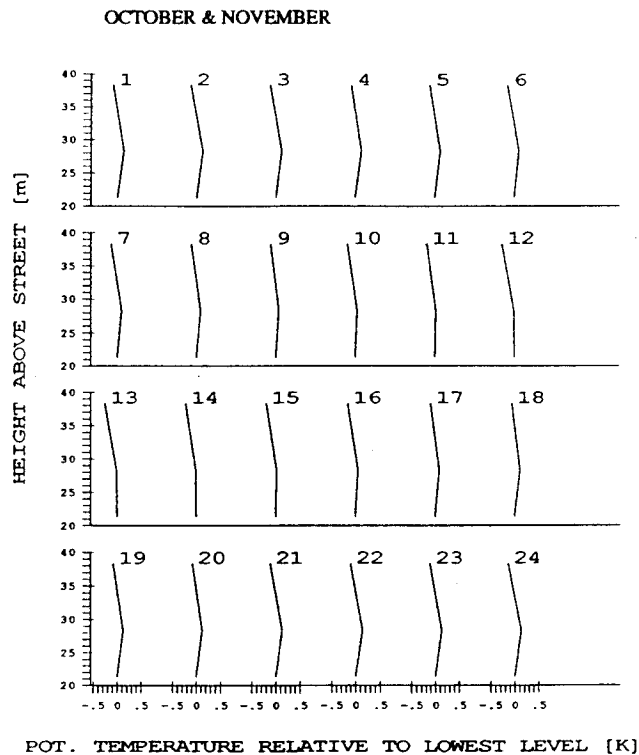
OCTOBER & NOVEMBER

POT. TEMPERATURE RELATIVE TO LOWEST LEVEL [K]

Figure A3.18 As Fig. A3.17, but for October and November, 1987.

A3.3 Specific Humidity

The measurement of the specific humidity is by far the most difficult (and therefore uncertain) among the variables determined in the present study. If the dew point is measured with an accuracy of 0.02 K (see Appendix A1.2) and the pressure with an accuracy of 2 hPa , the uncertainty in the specific humidity under "average conditions" (i.e. p = 960 hPa, dew point = 283 K) becomes roughly 10 ppm (10^{-5} kg H_2O/kg wet air). This has to be kept in mind for the discussion of the profiles of specific humidity. The average profile over the whole period of measurement (Fig. A3.19) shows two outstanding characteristics: the air within the canyon is generally more moist than above roof level (indicated also by the difference between Positions 8 and 9) and there is a slightly positive gradient of specific humidity in the roughness sublayer. The vertical profile of specific humidity does not show a daily cycle. There is considerable variation in the humidity profiles, when looking at shorter time periods. However, the monthly averaged profiles are not so much characteristic of the respective season, but rather they seem to reflect the weather patterns during the previous time of observation. If, for instance, the average profiles for the winter months (DJF) are compared to those of February alone (most observations originating from February 1988), it is possible that

the strong gradient above roof generally observed in winter (Fig. A3.20a) may even be reversed for the average profiles of a whole (winter) month (Fig. A3.20b).

For two periods of roughly 2 months (October/November 1987 and April/May 1988) an additional sensor was mounted at position 11 (10 m above roof). During the two autumn months almost no vertical variation of specific humidity, small gradients in general and no daily cycle was observed (Fig. A3.21a). During the two spring months, on the other hand, the profile within the roughness sublayer shows a distinct daily cycle (Fig. A3.21b). While the gradient over the whole height interval (Positions 9 to 12) is negative for most hours, the profile of specific humidity changes its shape during the day. Dew fall might be responsible for the excess humidity close to the roof in the early morning hours. Around noon, moist air originating from the canyon can be transported upwards through daytime convection, leading to the relative maximum at position 11. A linear interpolation of the humidity profile between Positions 9 and 12 in order to calculate fluxes of latent heat can therefore be misleading.
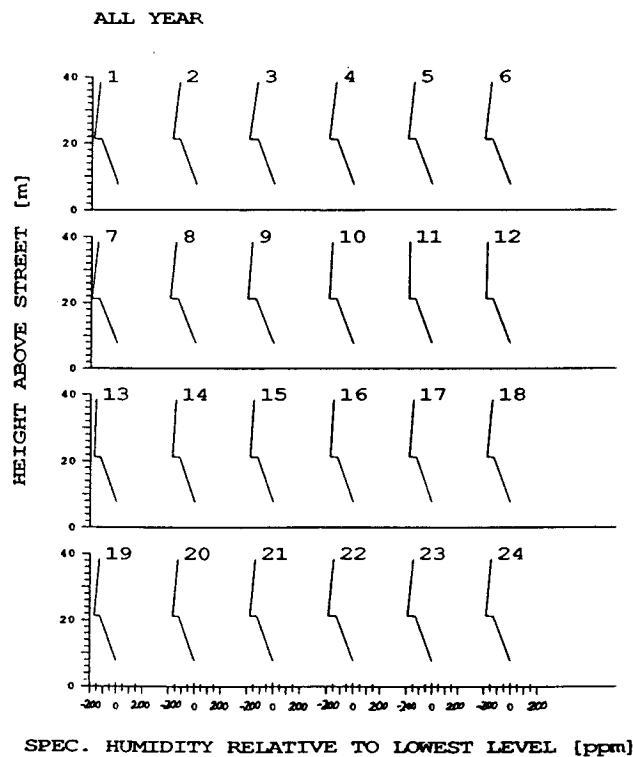

Figure A3.19   Average profiles of mean specific humidity difference between height z and the lowest level (position 5). Unit are parts per million (ppm) = 10^{-6} kg H_2O/kg wet air. Data used: all reliable data from the whole period of measurements.
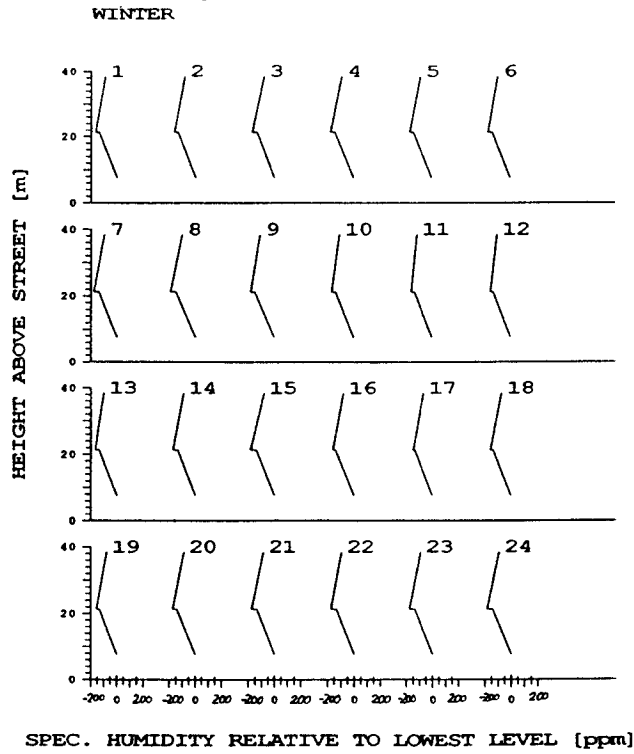
WINTER

SPEC. HUMIDITY RELATIVE TO LOWEST LEVEL [ppm]

Figure A3.20a   As Fig.A3.19, but for months December, January and February.

FEBRUARY

SPEC. HUMIDITY RELATIVE TO LOWEST LEVEL [ppm]
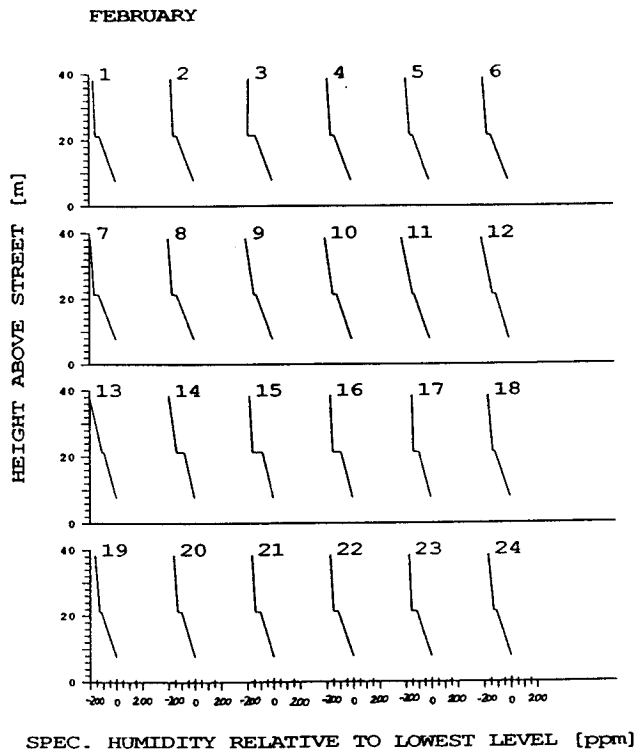
Figure A3.20b   As Fig. A3.13, but for February, 1988.

OCTOBER & NOVEMBER

SPEC. HUMIDITY RELATIVE TO LOWEST LEVEL [ppm]
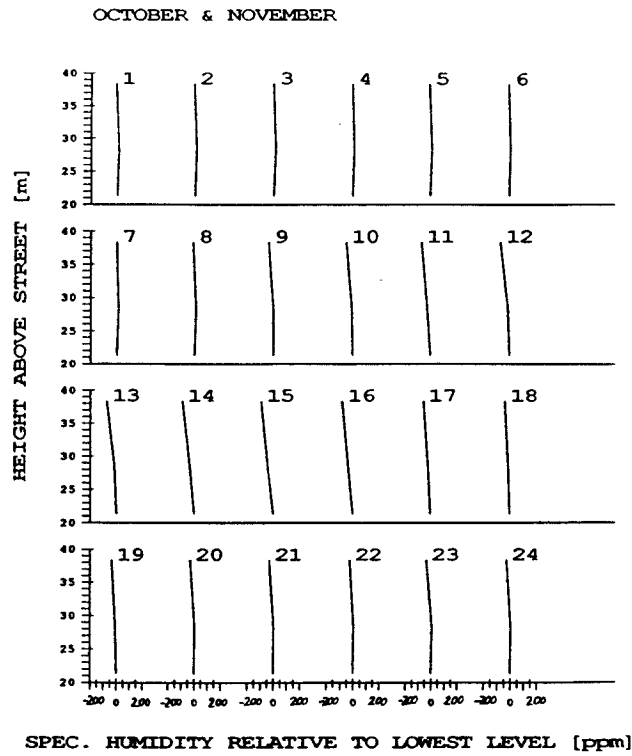
Figure A3.21a   As Fig.A3.19, but for October and November 1987 and positions
                 9,11 and 12.

APRIL & MAI

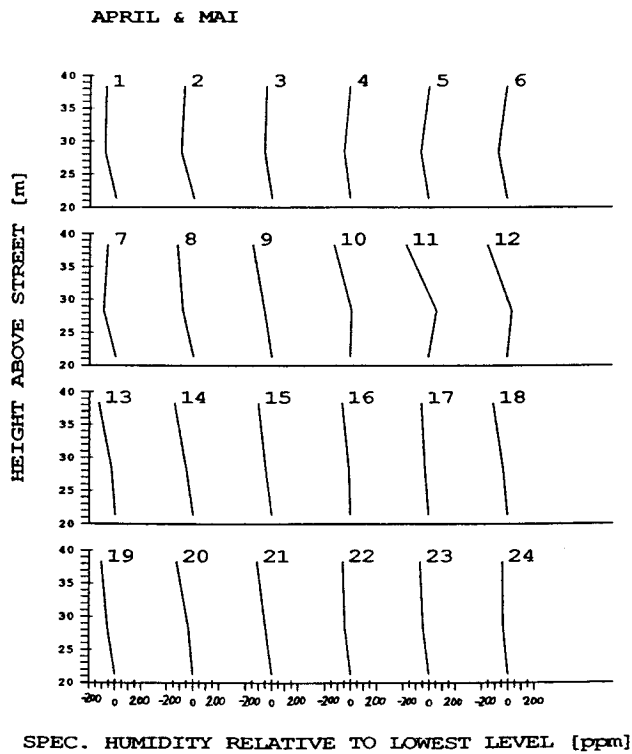SPEC. HUMIDITY RELATIVE TO LOWEST LEVEL [ppm]

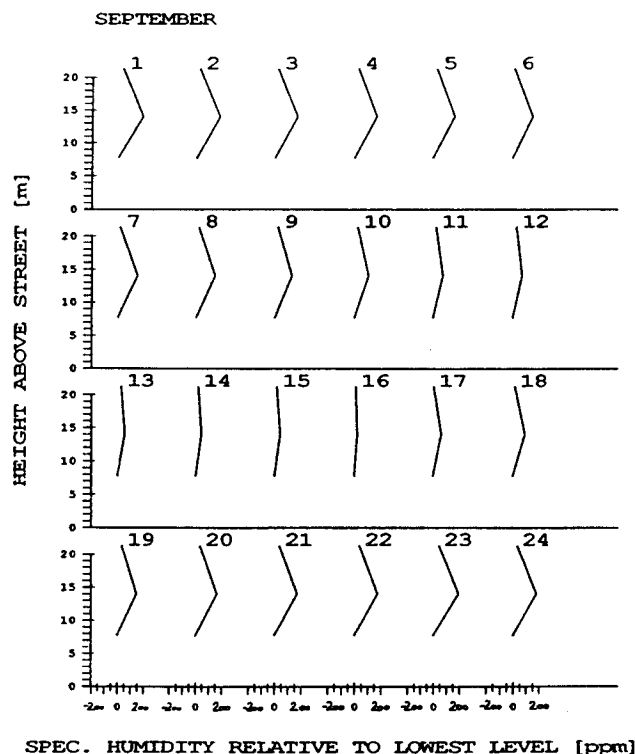Figure A3.21b   As Fig. A3.21a, but for April and May, 1988.

Figure A3.22 As Fig.A3.19, but for September, 1987 and positions 5,7 and 8.

Within the canyon, a third level was measured in September 1987 (Fig. A3.22). The slightly positive over-all gradients seem to be characteristic for this season, even if they are of the order of measurement accuracy. The significant maximum at the mid-canopy level, on the other hand, is astonishing. From the relative calibrations (see Appendix 1.2) it can be excluded that the instrument systematically read high. This maximum is associated with an almost uniform temperature distribution (Fig. A3.16) and occurs predominantly during the night. This phenomenon could be due to the vortex circulation within the canyon, transporting moist air from the surface (small strips of grass between the houses and the sidewalks) to the intermediate level rather than to position 5 (which lies in the height range where the vortex center might be expected, c.f. Yamartino and Wiegand, 1986). This hypothesis, however, cannot be tested with the data available from the present measurements.

The positive gradient of specific humidity within the urban RS observed in many hourly means and also as the over all average, needs some explanation. If evaporation is considered the dominant source of water vapour close to the surface, one would expect a negative gradient as found within the canyon. At the level close to the roof (positions 8 and 9, respectively) a clear horizontal variation in humidity is seen (Fig. A3.19). For the majority of hourly averages at position 9, a lower specific humidity is observed (evaporation only after rainfall events) than over the street canyon (position

8). At the uppermost level (position 12) on the other hand, humidity lies between that of positions 8 and 9, respectively (for the average profiles, Fig. A3.19, but also for most of the hourly profiles, Fig. A3.23). Therefore, it is suspected that mixing of wetter canopy air and drier "above roof air" results in this positive RS gradient between positions 9 and 12. This finding highlights the importance of measuring true horizontal averages as defined in Chapter 3 in order to obtain valuable gradients of any scalar quantity.
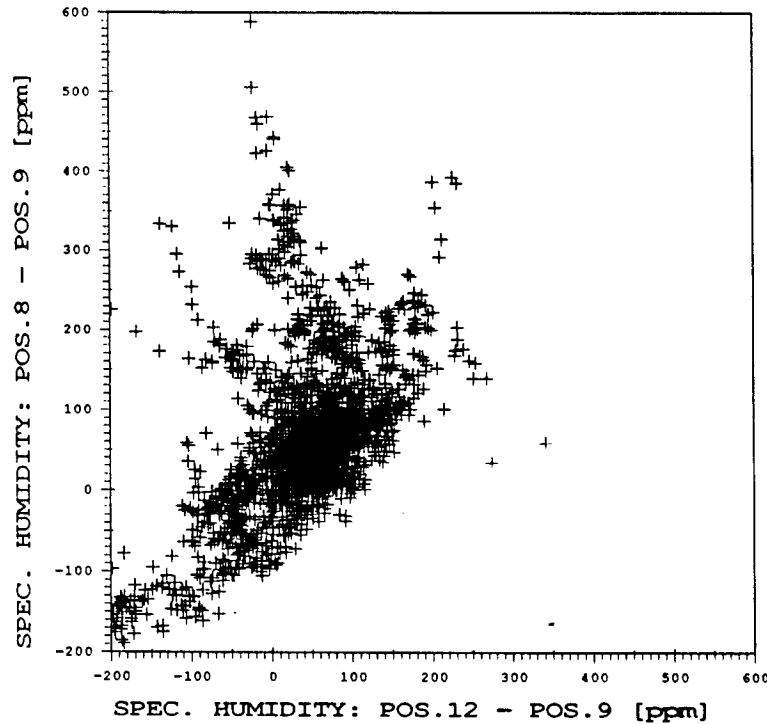

Figure A3.23   Comparison of differences in specific humidity between positions 8 and 9 and positions 12 and 9, respectively..

Gradients of potential temperature and specific humidity are sometimes used to calculate the Bowen Ratio β, defined as

$$\beta = \frac{Q_H}{Q_E} \qquad\qquad (A3.2)$$

where Q_H and Q_E are the turbulent fluxes of of sensible and latent heat, respectively and might be parameterised using K-theory. From the present measurement configuration, however, the application of this concept is questionable due to several reasons:

- the commonly used configuration with temperature and dew point measurements only at positions 9 and 12 allows the calculation of a "bulk Bowen Ratio"over the whole layer at most

- the use of K-theory in equation (A3.2) requires i) that K_H equals K_q and ii) that the turbulent fluxes of sensible and latent heat may be calculated from the

respective gradients. Both assumptions are neither obvious nor verified for an urban RS or canopy layer.

If furthermore the Bowen Ratio is calculated from the present data after

$$\beta = \frac{\overline{\rho} c_p \frac{d\overline{\theta}}{dz}}{\overline{\rho} L_v \frac{d\overline{q}}{dz}}, \quad K_H = K_q, \tag{A3.3}$$

where the derivatives are obtained using the differences of potential temperature and specific humidity at positions 9 and 12, an error analysis shows that the relative error $d\beta/\beta$ is close to unity for typical conditions. In addition, the small gradients that are often observed request that a large portion of the data are rejected due to objective criteria (Ohmura, 1982). No attempt is made, therefore, to estimate the ratio between the turbulent fluxes of sensible to latent heat from the present profile data.

Curriculum Vitae

Name	Rotach, Mathias Walter Jakob	
Date of Birth	March 31, 1960	
Place of Birth	Zürich	
Citizenship	Swiss	
Education	1967	Primary School, Zürich and Erlenbach
	1973	High School, Zürich
	1980	Swiss Federal Institute of Technology (ETH), Faculty of Natural Sciences (Atmospheric Physics)
	1983	"Project Oriented Studies" (POST), a course in applied scientific work. Project: "Smog and Ozone" (measurement techniques and investigations to quantify transport mechanisms of smog constituents)
	1985	Diploma in Natural Sciences (ETH), Thesis: "Die Smog Chamber"
	1985	Research assistant and Ph.D. student, Department of Geography, ETH
	1986	Participant of NATO Advanced Study Institute on "Physically-based Modelling and Simulation of Climatic Change", 11-23 May, Erice, Sicily
	1988	Participant of the Workshop (Fall School) on "Measurement and Parameterization of Land-Surface Evaporation Fluxes", 10-21 October, Banyuls, France.
	1989	Part time job as an air quality consultant (INFRAS, Zürich)
	1990	Participant of the ETH Greenland Expedition